# Optical Assessment of Middle Ear Inflammation

by

David Samuel Jung, M.Sc.

submitted to The University of Nottingham for the degree of Doctor of Philosophy

June 2016

**Abstract**

This thesis describes the development of an optical device to assess the inflammatory state of the middle ear mucosa through the ear canal, after ventilation tube insertion in otitis media with effusion in children.

An optical phantom of the middle ear was developed in order to allow repeatable experiments. The phantom consists of eardrum and mucosa while all other structures are neglected. The optical properties of the phantom were determined based on literature review and experiments on an animal model. The middle ear mucosa phantom is based on a polyester resin, with dyes added to introduce absorption and a titanium dioxide based white colour to introduce scattering. Four phantom are created to model healthy, intermediate, and diseased mucosa. Several approaches are taken for the eardrum phantom, either a grid glass diffuser or a resin phantom with scattering introduced by fibre glass is used.

Middle ear inflammation affects the mucosa while the eardrum might not be affected. Hence, the mucosa must be assessed and signals resulting from the eardrum, blocking the direct light path, filtered, in order to reduce background signals. During literature research and preliminary experiments, multi-wavelength measurements were selected to assess the mucosa and confocal techniques to allow measurements through the eardrum. The tissue is illuminated with two wavelengths and the reflected signal analysed. Appropriate selection of the wavelengths at characteristic point of the absorption spectrum of blood allows assessment of the inflammation via the blood concentration in tissue. The confocal idea was adopted leading to the "anti-confocal" system, where a central stop replacing the pinhole rejects light from the plane in focus rather than rejecting all out of focus light. With the eardrum in focus and a stop radius larger than the confocal pinhole radius ($r_{\text{stop}} = 0.48\,\text{mm}$), most light from the eardrum is rejected (reduced to 0.2 %) while signal from the mucosa are still detected (reduced to 25.6 %), according to simulations.

Simulations of the anti-confocal system showed an increase of the signal level by a factor of 3.2 or a 1.5 times higher background rejection ratio (SBR) compared to the conventional confocal system, when keeping the respective other value constant. This advantage still holds and is even improved in some cases when increasing the scattering coefficient (from 11 up to $44\,\text{mm}^{-1}$), reducing the scattering anisotropy (from 0.99 to 0.6), changing the distance between eardrum and mucosa (0.5 to 8 mm), inaccurate focus (up to 3 mm out of focus), and changed NA (0.055-0.27). Further, best wavelengths for measurements of the blood concentration and thus inflammation of the mucosa have been determined in simulations to be 730 and 546 nm. In the investigated range of wavelengths (500 to 940 nm), the relation of near infra-red signal at 730 nm to green reflection signal at 546 nm

gives the highest response to a change in the total blood level in tissue while showing a low response to changes in blood oxygenation.

The anti-confocal system was built as bench-top system and characterised. Instead of using a physical stop, a CCD camera was used and anti-confocal filtering done during post-processing, by selecting certain pixel on the camera. Experimental results confirmed the simulations and showed an increased signal and easier use of the anti-confocal system compared to the confocal system as no exact focus is required. An anti-confocal stop with 0.48 mm radius showed best performance, showing a high contrast and low variation during the measurement. Measurements were possible with increased scattering (simulated by the stronger scattering grid glass diffuser) and attenuation (simulated by absorbing dyes added to the resin eardrum phantom) of the eardrum, increased distance between eardrum and mucosa (2–6 mm), defocus of the system, and altered orientation of the phantom surface (0–10 deg) with differences in the mucosal blood level still detectable. But the measured inflammation index is influenced by the transmission properties of the eardrum. While the influence of absorption can be accounted for by confocal detection of the properties of the eardrum during the same measurement, improved signal processing and modelling of light propagation are necessary to account for changed scattering of the eardrum.

Tests on the hand of healthy volunteers showed that the proposed system is able to detect a change in the concentration of haemoglobin of living tissue measured through an eardrum simulating scattering layer. The next steps are the improvement of signal processing to account for changes of the measured inflammation index due to scattering of the eardrum. Once this is achieved, the optical system can be minimised to allow measurements on the ear and pilot trials for evaluation and calibration of the system.

**Publications Resulting from this Project**

1. David S. Jung, John P. Birchall, John A. Crowe, Chung W. See, and Michael G. Somekh, "Monte Carlo Photon Simulation of an Anti-Confocal System to Monitor Middle Ear Inflammation," in Optics in the Life Sciences, OSA Technical Digest (online) (Optical Society of America, 2015), paper JT3A.41.

2. David S. Jung, John A. Crowe, John P. Birchall, Michael G. Somekh, and Chung W. See, "Anti-confocal versus confocal assessment of the middle ear simulated by Monte Carlo methods," Biomed. Opt. Express 6, 3820-3825 (2015).

The publications are attached in Appendix G.

**Acknowledgements**

I want to thank my supervisors John Birchall, John Crowe, Chung See, and Mike Somekh for the support and discussions during the PhD.

Thanks go to Emma Hoskison and Mike Milheran (University of Leicester) for supplying guinea pig eardrums as animal models, thanks to Sameer Mallick (University of Sheffield) for supplying gerbil eardrums, Mark Wallace and Alan Palmer (MRC IHR, University of Nottingham) for help and providing equipment dissecting the animal eardrums and providing a freshly killed guinea pig to acquire fresh eardrums.

I also want to thank Denise Mclean (Advanced Microscopy Unit) for support preparing histological samples of the guinea pig eardrums, Emily Hogan (Ophthalmology, QMC) for supporting us with experiments on commercial OCT systems, and Kevin Webb (University of Nottingham) for support and guidance using the confocal microscope and tissue specimen preparation, Richard Smith for guidance on producing the safety data sheet for the optical system.

Thanks to Professor Jeremy Hebden (Biomedical Optics Research Laboratory, University College London) for instruction, providing the recipe, and facilities for production of optical tissue phantoms.

Finally, I want to thank the people who volunteered to participate on the experiments conducted during the PhD and all other people who supported me with discussions and feedback during this project.

David Jung

Nottingham, June 2016

# Contents

# List of Figures

# List of Tables

# Chapter 1

# Introduction

The aim of this project is to develop an optical diagnostic device for the improved diagnosis of the inflammatory state of the middle ear mucosa during otitis media with effusion (OME) in children. To understand this task, the anatomy of the middle ear, the clinical state of OME and its consequences are explained first. Based on this knowledge, the task is then explained in detail in Section 1.5 and the outline of this report presented in Section 1.6.

## 1.1 Anatomy of the Ear

The ear is divided into three parts, the outer, middle, and inner ear as shown in Figure 1.1. The outer ear consists of the pinna and the external ear canal, also called external auditory meatus, which has a length of about 25 mm from pinna to eardrum. The ear canal is circular in children and has an approximate diameter of 6 mm. It has the shape of a lazy "S", so it is possible to see the eardrum, also called the tympanic membrane (TM), from the outside using an otoscope (a diagnostic instrument to investigate the appearance of the eardrum described later in Section 2.1) to straighten the ear canal and illuminate and image the eardrum [1].

The eardrum is a translucent structure, dividing the outer and middle ear which contains the ossicles, called the malleus, incus, and stapes. The ossicles transfer and amplify the pressure variations from the eardrum to the cochlea in the inner ear. The system of eardrum and ossicles provides impedance matching of air (environment) to liquid (inner ear) and prevent the reflection of the majority of the energy at the interface of both media which would be the case otherwise. The cavity of the middle ear, called the tympanic cavity, has a volume of about $0.5\,\mathrm{cm}^3$ [2]. The vertical (height) and anterior-posterior (length, into the paper in Figure 1.1) dimensions of the middle ear cavity are 15 mm and the transverse diameter (width, horizontal dimension in Figure 1.1) is about

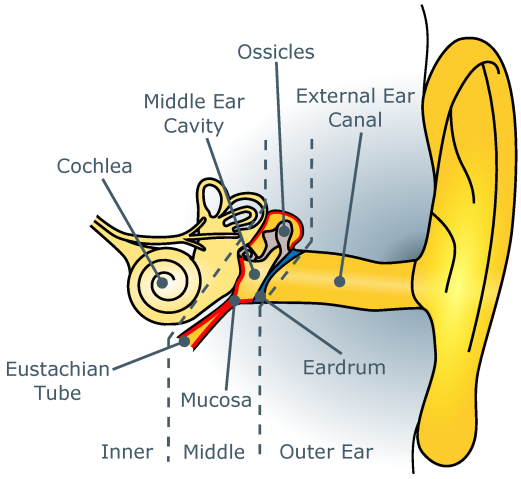


Figure 1.1: Anatomy of the Ear.

6 mm above, 4 mm below, and 2 mm opposite the centre of the eardrum [3]. The middle ear cavity is lined by mucosa and connected to the nasopharynx (back of the nasal cavity) by the Eustachian tube.

The eardrum has a shallow cone shape with oval base and a longest diameter of 9-10 mm and shortest diameter of 8-9 mm [3]. The cone has a depth of about 2 mm and points inward to the middle ear [1]. Figure 1.2 shows a drawing of the eardrum seen from the external ear canal, while Figure 2.1 shows photos of the earadrum. Three main features are obvious: the outline of the handle of the malleus attached to the medial (side facing the middle ear) of the eardrum in the middle, the pars flaccida above, and pars tensa attached to the malleus. Also visible in most images of the eardrum is a cone of light in the lower part resulting from direct reflection of the illumination. The pars tensa, a thin translucent layer, constitutes the main part of the eardrum. It consists of an epidermal layer laterally (towards the external ear canal), radial fibrous layer, circumferential fibrous layer, and mucosal layer medially, forming part of the lining of the middle ear cavity. The two fibrous layers give the eardrum its mechanical strength. The radial fibres, leading from the hand of malleus in the middle to the edge (annulus), are present in all regions of the pars tensa while circular fibres are less prominent in the centre. In humans, the pars tensa's thickness measurements vary from a minimum value of 20 µm to a maximum value of 500 µm [4] with average values of the thinnest part which is central between annulus and malleus of 50 to 70 µm [5]. The pars flaccida is thicker than the pars tensa, up to 600 µm [4] and is not under tension.

The best position to perform measurements on the middle ear is marked in Figure 1.2 in green. The reasons for this are that the eardrum is thinnest in the middle between malleus and annulus,

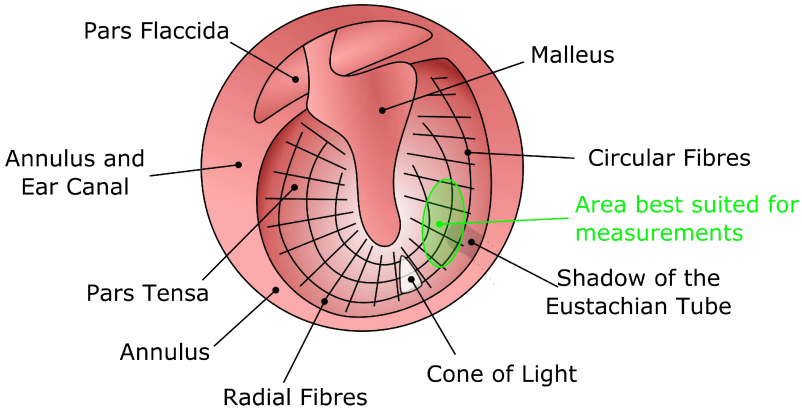


Figure 1.2: Eardrum as seen from the ear canal.

there are no ossicles obscuring the view on the mucosa in this area, and last, this area is close to the Eustachian tube where the inflammation when present is most severe.

The inner ear contains the cochlea which converts the mechanical vibrations of sound into electrical signals by use of the inner hair cells. These signals are then transferred to the brain via a neural nerve relay for further processing. The round and oval window form two flexible fibrous boundaries between the cochlea and middle ear, the remaining boundary is bone. The oval window is in direct contact with the stapes and transmits vibrations, while the round window is necessary to allow the incompressible fluid inside the cochlea to move and the hair cells to be stimulated.

## 1.2 Middle Ear Inflammation

Otitis media (OM) is inflammation of the mucosal lining of the middle ear cavity. Several different types of otitis media are recognised, with acute otitis media (AOM) and otitis media with effusion (OME, also called glue ear) being the most common forms. AOM is an acute viral or bacterial infection mostly affecting only one ear (unilateral) resulting in ear pain, deafness, fever, tiredness, and unease of the patient. OME in contrast is a chronic inflammation with only deafness as a symptom. The hearing loss is present due to liquid accumulation in the middle ear cavity of normally both ears (bilateral) and biofilms (group of bacteria in lower metabolic state adherent to mucosa) are present [6]. This work focuses on the diagnosis of OME.

## 1.3 Diagnosis of Otitis Media with Effusion

OME is a common condition that 80 % of British children experience by the age 10 [7]. It leads to hearing loss which in turn may affect their speech and education if persisting for an prolonged

time. It is a chronic inflammation of the middle ear and may persist up to several years. This inflammation is caused by an irritation of the mucous membrane in the middle ear and Eustachian tube increasing the production of secretion with higher viscosity and swelling of the mucosa in the Eustachian tube and thus impaired clearance of the middle ear cavity. According to the surgeons, the inflammation is more severe in the lower part of the middle ear close to the Eustachian tube and less severe above the eardrum, as shown in Figure 1.1 with a thicker marked mucosa near the Eustachian tube. The secretion filling the middle ear cavity damps the movement of the eardrum leading to decreased sound transmission to the cochlea and thus hearing loss.

In 63 % of the cases OME resolves spontaneously within three months making surgery unnecessary. But if a significant hearing loss is present for more than three months and the child's speech and education is affected, a surgery is recommended by NICE (The National Institute for Health and Care Excellence) guidelines [8]. In these surgeries, called myringotomy, the eardrum is punctured and the effusion is aspirated while the child is under general anaesthetic [7]. Then a ventilation tube also called grommet is inserted into the eardrum to replace the function of the blocked Eustachian tube by ventilating the middle ear. After six month or longer, depending on the type of the ventilation tube, the eardrum grows back closing the hole extruding the grommet. In England, more than 30,000 of these surgeries are performed each year (data from 2005/06) [9] and this is one of the most common surgeries performed on children in the developed world [10]. But this operation is far from ideal, in 25 % of the cases, further surgery is necessary within two years due to recurrence of OME. The recurrence of OME is due to persistence of the inflammation, currently biofilms are considered the probable cause [10]. Additionally, a ventilation tube increases the risk of persistent perforation of the eardrum, the longer it stays in place [11, 12].

## 1.4 Motivation for this Project

OME is diagnosed by a history of hearing loss and otoscopy and is confirmed by tympanometry (Measurement of the pressure dependent sound signal reflected off the eardrum. For more detail see Section 2.1.2). The diagnosis by otoscopy requires an experienced clinician to give a definite and correct diagnosis. Further, there are only guidelines suggesting when to perform a surgery and these are often ignored [13, 14]. These facts ask for improved and standardised techniques for the diagnosis of otitis media [9].

To date there is no way of predicting in which cases OME will recur and in which it will not. We hypothesise that in the recurrent cases the mucosa does not return to normal but stays inflamed resulting in a new fluid build-up after the grommet is expelled from the eardrum. But at the moment there are no diagnostic devices available to assess the inflammation in the middle ear and

test this hypothesis.

This motivates the development of a diagnostic device able to assess the inflammation of the middle ear mucosa after myringotomy. If the hypothesis is proven correct, the device could be used to predict the course of OME and recurrence. This would reduce stress for the child and decrease costs and save time for the NHS and parents by avoiding unnecessary visits to a doctor for non-recurrent cases. Further, it would increase the credibility of the diagnosis when being able to perform a more accurate statement of the course of OME.

## 1.5 Definition of the Problem

The task is to develop a device able to perform assessment of the middle ear inflammation and characterise its severity and course over time. The device must be similar to the current diagnostic devices with respect to size, handling and contact with the patient in order to be easily accepted into clinical use. Thus the device should have a small handheld head, use the same specula as standard otoscopes, while an additional table top setup is acceptable. The table top setup may include a display, signal processing, light sources, and other components and must be connected to the optical head via optical fibres and signal cables to allow easy movement and alignment of the optical head with the patient's ear. The measurement time needs to be short for it to be practicable in the clinical examination of children. Further, no invasive techniques such as the use of biomarkers, or approach through the Eustachian tube are allowed in order to enable quick and cheap diagnosis. Assessment must happen through the external ear canal. Thus, a second problem is introduced – performing measurements and assessment through the eardrum. Puncturing of the eardrum is not an option as a non-invasive diagnostic device is desired. Also, imaging through the ventilation tube is not possible as it is not always aligned with the ear canal. Fixation of a ventilation tube's position is not possible as this requires contact with the eardrum and a movement of the patient might cause rupture of the eardrum. Thus, the system must be able to optically penetrate the eardrum without damaging it and be able to filter signal components resulting from the mucosa from signal components resulting from the eardrum or other structures not involved in the inflammation. Image reconstruction is not necessary as long as information about the inflammation is collected.

The device to be developed has to perform according to the following requirements:

**Show the inflammation** To give information about the degree of the inflammation.

**Imaging depth** The inflamed tissue is the middle ear mucosa hidden behind the eardrum with a thinnest area of 50 to 70 µm and average thickness of 100 µm with the cavity having a

2–4 mm depth. As reflection signals are measured, the signal must penetrate the eardrum and the middle ear cavity and return the same path in order to be detectable. In healthy ears the middle ear cavity is air filled and does not add signal or attenuation. While OME cavities can be filled with a fluid, this fluid is removed during ventilation tube insertion and thus a air filled cavity present in the investigated cases.

**Imaging resolution** No image is required; only a single indicator for inflammation is necessary. Thus, the only requirement on resolution is to distinguish between mucous tissue and eardrum and other structures not involved in the inflammatory process. A large sampling area of the mucosa is desirable in order to average the mucous membrane properties during the measurement.

**Non-invasive and quick** The inflammation must be assessed from the external ear canal through the eardrum without puncturing of the eardrum or using biomarkers or stains. Accessing through the Eustachian tube is not possible as the inflamed tissue would be traumatised increasing the risk of scarring. The image acquisition time may not exceed a few seconds, and the system must be similar in use to ordinary otoscopes.

**Cheap** To be usable in clinics without high investments. (This requirement must not be met for the prototype during the research phase but must be considered with regard to a later stage of this project.)

**Hand-held** The head of the monitoring device should be hand-held to allow easy handling and easy usage by the medical staff. Further, it should not to scare the child by being a bulky and threatening tool.

**Safe** To ensure safety the monitoring device is not allowed to be in contact with the eardrum and the optical radiation must not exceed safety limits.

Figure 1.3 shows a schematic drawing of the problem. The handheld imaging system is placed outside the ear canal and assesses the middle ear through the external ear canal. A standard otoscope speculum is used to align the system with the ear canal and ensures compatibility with clinical standards. The probing light (golden) penetrates the eardrum (blue) and middle ear cavity, reaches the mucosa (red), and propagates back to the detector system. On the way signal is lost due to scattering and absorption in the eardrum. The system then filters signal from the mucosa (red), carrying information about the inflammation, and signal from the eardrum (blue), without information. Thus the background is rejected and only the signal from the mucosa analysed in order to assess the inflammation.

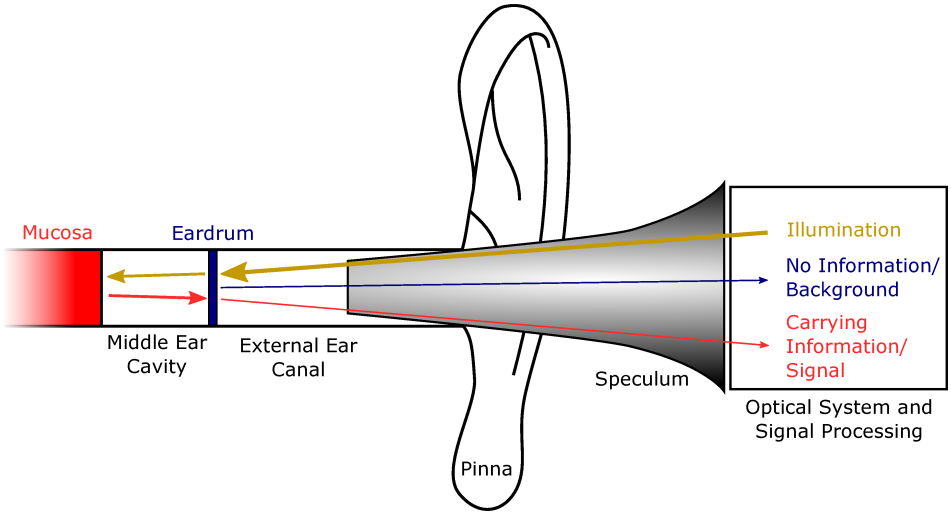


Figure 1.3: Simplified schematics of the ear and imaging problem. Light scattered at the eardrum is not illustrated for simplicity. Thickness of mucosa, eardrum, and middle ear cavity are not to scale.

## 1.6 Further Outline of the Thesis

The problem and task of this project has been presented. In the next chapter, a literature review is conducted in order to identify potentially suitable methods to apply to this task. Then, an optical tissue phantom of the middle ear is developed in Section 3 in order to allow reproducible and standardised experiments and characterisation of the system. The selected method, confocal imaging is presented in Section 4 and first experiments are conducted. This system is then adopted for the current task and the anti-confocal system developed and simulated in Section 5. Spectroscopic measurements using this system are then introduced and simulated in Section 6 with best wavelength for measurements selected based on the simulation results. Afterwards, the system is built, characterised, and its performance tested in Section 7. Finally, the project is summarised and an outlook of future work given in Section 8.

# Chapter 2

# Literature Review

This chapter aims to identify possible techniques to assess the middle ear inflammation. Signs of an acute inflammation are redness and increased heat, resulting from increased blood flow due to a higher metabolism of the tissue; swelling, due to an accumulation of liquid; pain, and a loss of function [15]. OME is a chronic, not an acute inflammation and only some of these signs are present. According to surgeons, the normally white middle ear mucosa (see Figure 3.2) turns red during inflammation and is more severe close to the Eustachian tube. While this is a marker that can be used to assess the middle ear inflammation it is not easy to acquire as hidden behind the eardrum and most research and currently used diagnostic methods focus on the appearance of the eardrum as it is easily observable.

This chapter first explains the currently used tools for diagnosis of otitis media, and then presents current research in imaging the middle ear in the context of otitis media. Third, possibilities to characterize inflammation as well as findings of research projects, and last 3D tissue imaging methods are presented. The chapter concludes with an evaluation of the methods with respect to the task of assessment of the inflammation in the middle ear through the eardrum.

## 2.1 Current Diagnosis of Middle Ear Inflammation

OME is diagnosed by a combination of the following methods: The hearing loss is reported by the children's parents and the loss of function is confirmed by tympanometry (analysis of the response of the eardrum to a stimulating sound, see Section 2.1.2) and pure tone audiometry (determination of hearing levels). The liquid accumulation, reddening of the mucosa, and other signs of OME are observed during otoscopy (visual inspection of the eardrum) and the movement of the eardrum can be observed during pneumatic otoscopy.

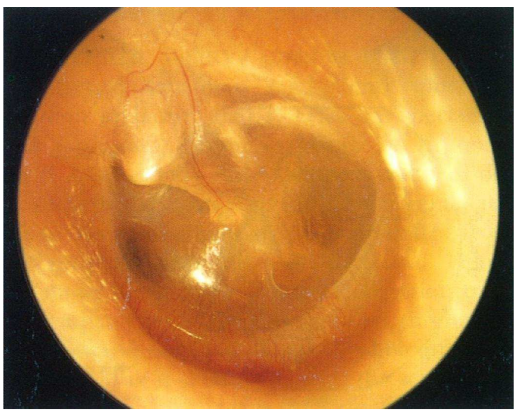

(a) Healthy left eardrum.

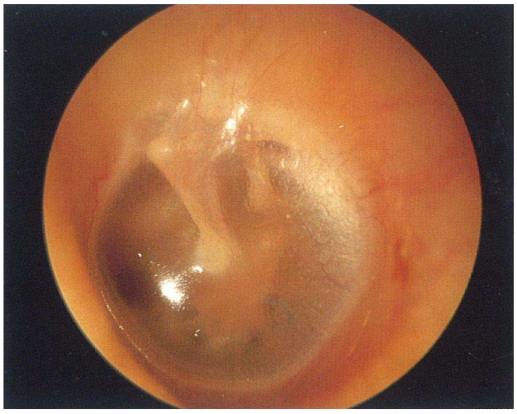

(b) OME in the left ear. Malleus handle in normal position.

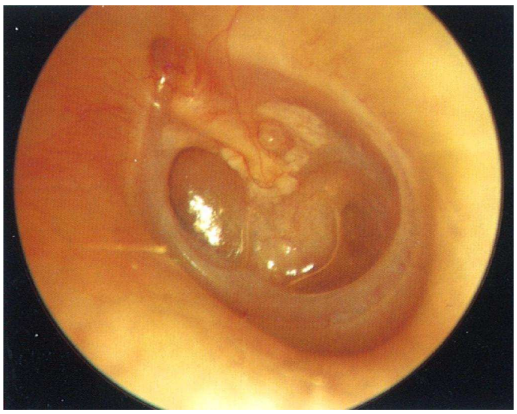

(c) Liquid level in left ear with OME.

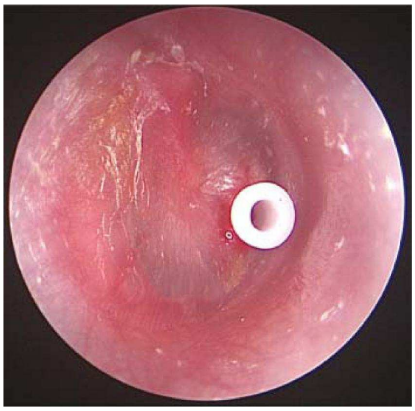

(d) Eardrum with grommet inserted.

Figure 2.1: Examples of otoscopic findings in healthy and OME ears taken from [17] (a, b, and c) and [18] (d).

### 2.1.1 Otoscopy

As standard diagnostic tool, an otoscope is used for optical examination of the eardrum. Based on the appearance of the eardrum, the type of OM is diagnosed. Signs for OME are decreased translucency of the eardrum, increased vascularity, presence of bubbles behind the eardrum, colour change, and no concavity or even convexity of the eardrum. In different patients, different combinations and developments of these signs are present complicating a correct diagnosis [16].

Figure 2.1 shows four examples of otoscopic findings. Subfigure (a) shows a healthy eardrum, while (b) and (c) show OME ears. For a layperson it is hard to detect inflammation in case (b) while the presence of bubbles (a sign of resolution) and liquid in (c) allow an easier detection of OME. Subfigure (d) shows an eardrum with a grommet inserted.

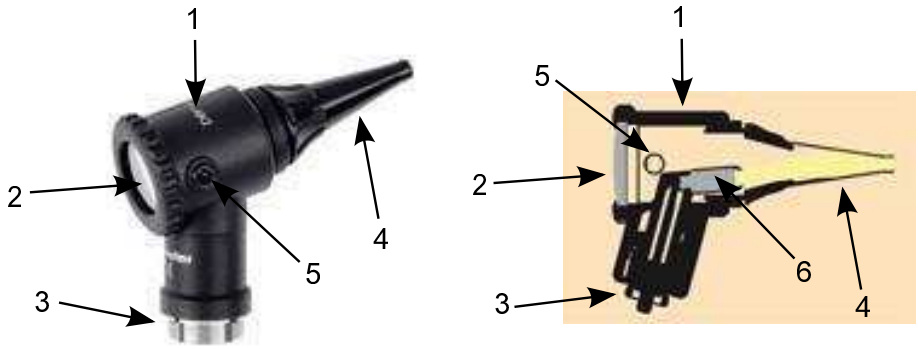


Figure 2.2: Basic otoscope [19].

Basic otoscopes are simple devices for viewing of the eardrum with a light source for illumination; speculum to fit into the ear canal; and a magnifying lens with magnification of around 2.5 [19]. More sophisticated types have an improved illumination structure, higher magnification, and a camera to allow presentation of the eardrum on a screen.

Figure 2.2 shows a picture (left) and structural drawing (right) of the head of a basic otoscope (Riester Pen-Scope, Rudolf Riester GmbH & Co. KG, Germany). The head consists of the housing (1), removable magnifying lens (2), screw fitting to attach the handle (3), and reusable speculum (4). Located at the side of the head is an adapter for an inflation bulb (5) for pneumatic otoscopy. The lamp for illumination (6) of the eardrum is placed inside the hollow head. Visual inspection of the eardrum is possible though the magnifying lens.

Figure 2.3 shows a video otoscope (Digital Macroview$^{TM}$ Otoscope, Welch Allyn, Skaneateles Falls, NY, USA) for video recording and image acquisition of otoscopic images for presentation on a PC. The dimensions of the head are $70 \times 102 \times 37$ mm and the image is focussed manually by the use of a focussing wheel [20]. The basic setup is similar to the previously presented otoscope, except for more elaborate optics and the camera replacing visual observation. Cables will be attached to the otoscope head to allow visual inspection of the middle ear on a screen.

During pneumatic otoscopy pressure is applied to the eardrum using an inflation bulb attached to the otoscope head and its movement can be observed through the otoscope. Liquid in the middle ear changes the reaction of the eardrum to a changed pressure as it hampers the movement. This gives an additional indicator to improve the diagnosis. According to [21], pneumatic otoscopy yields an accuracy of 72 to 92 % of predicting the presence of liquid in the middle ear. Pneumatic otoscopy is useful in general practices or nurse clinics where no tympanometry is available, in ENT clinics tympanometry is preferred.

Figure 2.3: Video otoscope [20].

### 2.1.2 Tympanometry

Tympanometry is used to measure the mobility of the eardrum. The tympanometer is placed on the ear to seal the ear canal to be able to change the pressure in the ear canal. A tone of 226 Hz is generated and the from the eardrum reflected energy is measured as a function of ear canal pressure. As a result the admittance (a measure of how sound is transmitted through the middle ear) of the eardrum is plotted over the pressure range in the tympanogram as shown in Figure 2.4. Most sound is transmitted through the middle ear when the pressure in the external ear canal equals the pressure in the middle ear cavity. In a healthy ear this is the case at atmospheric pressure, and the tympanogram shows a sharp peak at atmospheric pressure (Type A). In ears with effusion the peak may show a flat tympanogram (Type B) or a shifted peak to lower pressures (Type C). The test takes less than 10 s and is easy to conduct except for difficulties when the sealing of the ear canal in some of the patients [22].

A flat tympanogram and a shift of the peak in the tympanogram can also result from perforation of the eardrum, a tumour in the middle ear, or other diseases. Thus, tympanometry must not be used as the only tool for diagnosis. Tympanometry yields an accuracy of 76 to 94 % of predicting the presence of liquid in the middle ear [21].

### 2.1.3 Spectral Gradient Acoustic Reflectometry

Spectral gradient acoustic reflectometry is a relatively new technique to assess the presence of middle ear liquid. The sound reflected from the eardrum is measured over the range 1.8–4.4 kHz. A maximum cancellation of the sound appears if 1/4 of the wavelength equals the eardrum to detector distance as the reflected sound is then out of phase. Presence of a liquid in the middle ear causes increased reflection of sound energy, narrowing the bandwidth of cancellation. This causes

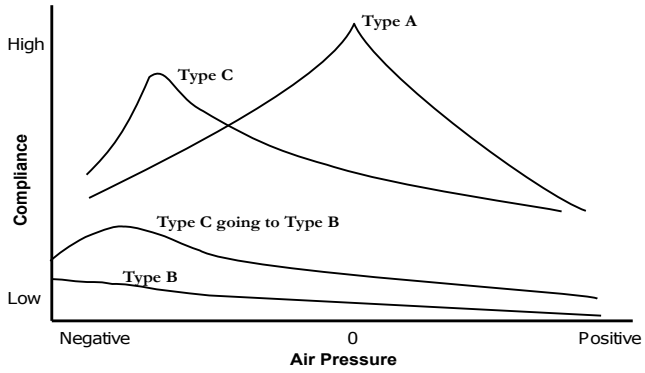


Figure 2.4: Example tympanograms. Type A – normal, Type B – advanced OM with liquid or perforation, Type C – early OM [23].

the reflectivity plot to show a narrow minimum which can be used to detect liquid. The advantage in contrast to tympanometry is that there is no need for an airtight sealing in the ear canal and thus an easier application. But its accuracy is lower than in tympanometry and pneumatic otoscopy with values of 58 to 95 % [22]. Hence, tympanometry is the most widely used technique.

## 2.2 Current Research in Imaging of the Middle Ear

As seen above none of the current methods is satisfying. Diagnostic accuracy is subjective and dependent on personal experience. Consequently, there are several groups trying to improve the diagnosis of OM. This section summarises research that deals directly with the imaging of the middle ear in context of otitis media.

### 2.2.1 Image Processing for Enhanced OM Diagnosis

The simplest and cheapest approach to improving OM diagnosis is to use state of the art otoscopes or endoscopes for image acquisition and to improve diagnosis using digital image processing. One idea is to use image processing to enhance important features to aid the surgeon in diagnosing and the other is to provide automated classification algorithms to standardise the diagnosis procedures and help inexperienced otoscopists.

Vertan et al. [24,25] performed colour analysis on otoscopic images of the eardrum to distinguish between healthy subjects and subjects with OME. The colour of the ear canal is used for colour correction to improve the algorithm. The algorithm was tested on 100 images and showed correct classification for 74 % in normal and 62.5 % in eardrums with effusion. This shows that colour alone is not a sufficient feature for correct diagnosis but also other information such as texture,

air or liquid bubbles, light reflections, and contrast between eardrum and ear canal have to be considered.

Kurvilla et al. [16,26] propose an automated classification system for the three classes of acute otitis media (AOM), otitis media with effusion (OME), and no effusion (healthy person). The diagnosis is made based on the features of concavity and bulging of the eardrum, translucency, colour tone, grayscale variance, and bubble presence in acquired images of the eardrum. The algorithm was tested on 181 eardrum images and reached an accuracy of 84 % in a first study [16] and 90 % with improved algorithms [26], increasing the accuracy seen in [24,25] by including more information than just colour.

Cheng et al. [27] used a camera mounted on a standard otoscope for image acquisition and performed image processing to enhance important features to facilitate the diagnosis. Contrast enhancing and segmentation algorithms were employed and promised better diagnosis although no evaluation was conducted yet.

Shiao et al. [28] propose the use of videotelescopy instead of otoscopy as better illumination, higher magnification, and a smaller head allowing closer examination of the eardrum enable a better diagnosis. The disadvantages are the use of more expensive and non-portable endoscope systems and the danger of rupturing the eardrum when the patient moves their head as the endoscope is close to the eardrum. This cannot happen during normal otsocopy as the tip of the speculum is about 13 mm apart from the eardrum and its position is fixed by the speculum being in contact with the ear canal. The study reports an improvement compared to pneumatic otoscopy and tympanometry with an accuracy of 98 % (197 out of 201) in OME diagnosis compared to 89.1 % (179/201) and 88.6 % (178/201), respectively.

These examples show that image processing on eardrum images might help to improve the diagnosis of otitis media but cannot be the only approach as it does not lead to a certain diagnosis. Further, only the type of the middle ear inflammation is diagnosed (AOM or OME compared to healthy ears) but not the state of the inflammation itself.

### 2.2.2 Spectroscopy or enhanced Illumination for Improved Otitis Media Diagnosis

Valdez et al. [29] investigated the influence of illumination colour on diagnostic accuracy of AOM. A video otoscope as presented in Section 2.1.1 was used for imaging and the standard white light illumination was replaced by colour LEDs in order to change the illumination colour. The images recorded with green and blue illumination show improved contrast of blood vessels and the material behind the eardrum allowing easier diagnosis of pathological states. Figure 2.5 shows

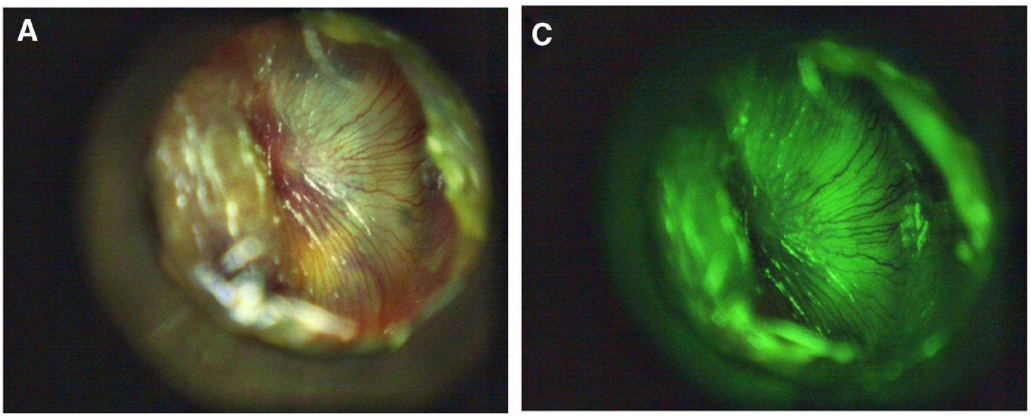


(a) Normal white light illumination (b) Illumination by a green LED

Figure 2.5: Image of an AOM eardrum with different illumination colours. The green illumination shows increased contrast of blood vessels and the material behind the eardrum [29].

images recorded with green versus white light illumination for illustration.

Sundberg et al. [30, 31] analyse the reflectance spectrum of the eardrum in the visible range of 450 to 600 nm (600 to 800 nm is also measured but does not give additional information) to classify the cases of mucous, serous, or no effusion, eardrums after myringotomy, and healthy ears. Using this measurement it is possible to distinguish the groups "in statistical terms". As the eardrum is translucent it is assumed that the eardrum itself does not contribute to the changing spectra but the medium behind the eardrum, namely middle ear liquid and mucosa. This work shows that spectroscopic data of the ear contains information about the disease but spatial filtering of the signal is necessary for improved precision of the measurements in order to determine the origin of the signal.

### 2.2.3 Confocal Fluorescence Imaging for Bacteria and Biofilm Detection

Stoodley et al. [32] and Ehrlich et al. [33] show the application of confocal microscopy to visualize bacteria and biofilms in the mucosa of chinchilla and human *ex vivo*, techniques that require staining of the investigated samples.

Wekhaven et al. [34] and Spector et al. [35] on the other hand do not require the use of dyes as the auto-fluorescence profile of bacteria present in the OM model ear of chinchilla *ex vivo* was investigated. Only seven samples were investigated with each picture recording taking 40 min but the results show a 100 % accuracy when classifying three kinds of bacteria and no bacteria.

None of these methods are suitable for this project as either staining is necessary or the acquisition time is too long. Valdez et al. [36] on the other hand managed to quickly record auto-

fluorescence images of the middle ear. The system was described earlier in Section 2.2.2 [29] and uses filters in the imaging path to detect fluorescence instead of reflected light. This allows recording of autofluorescence spectra and differentiation of pathological from healthy regions in case of cholesteatoma (destructing and expanding growth of tissue).

### 2.2.4 3D Shape Extraction of the Eardrum

Extraction of the shape of the eardrum adds information to the image of the eardrum. Conventionally this is achieved by pneumatic otoscopy. Several groups have developed enhanced otoscopes to directly extract this information without the need for pneumatic measurements.

Bedard et al. [37] made use of a light field otoscope (a lens array allowing the recording of multiple images with different viewing angles but reduced resolution) to measure the shape of the eardrum in order to improve the diagnosis of AOM. Anshuman et al. [38] made use of structured light illumination to extract the shape of the eardrum. In [39] the movement of the eardrum is recorded at video rate while a microphone creates stimuli similar to pneumatic otoscopy. The movement of the eardrum are recorded and can be used for diagnosis. These methods add no information compared to pneumatic otoscopy, but do allow easier handling and diagnosis as two steps are combined into one system.

### 2.2.5 Optical Coherence Tomography

Optical coherence tomography (OCT) is a technique comparable to ultrasonic imaging but uses light instead of ultrasound. Light is emitted into a tissue and the depth information of the back reflected light used to localise scattering particles. While depth information is acquired via delay of the signal in US, interferometry is used in OCT. The signal is superposed with a reference path and depth information is extracted from the resulting interferometric pattern. A 3D image is acquired by scanning the beam across the sample. As light is used instead of ultrasound the resolution increases to less than 10 µm but also the penetration depth decreases to 2–4 mm. A common application of OCT is in ophthalmology (assessment of the eye) to image the tissue layers of the retina. However, several groups have developed OCT systems to acquire images of the middle ear [40–48].

Nguyen et al. [45] use a hand held OCT-otoscopy system to acquire OCT images of the eardrum and detection of biofilms adherent to it. This OCT system is able to determine the absence or presence of biofilms with a sensitivity of 83 % and specificity of 98 % in adult patients. A future aim of the project is to differentiate between different cases of OM based on the structure of the biofilm. Figure 2.6 shows OCT images of a healthy eardrum and one with biofilm acquired by this

OCT system. A normal eardrum shown in the upper image shows a sharp contrast between outer ear canal, eardrum, and middle ear cavity. In presence of biofilm a thick layer adherent to the eardrum is visible and a less distinct transition from biofilm to middle ear cavity is observed.

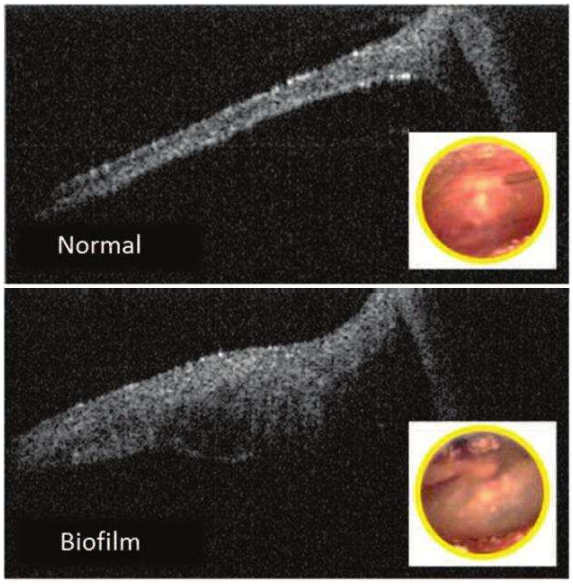


Figure 2.6: OCT images of an healthy eardrum and one with biofilm [46].

Pitris et al. [44] use a bench top system to show the feasibility of imaging the ossicles in the middle ear using OCT. Images acquired with this system area shown in Figure 2.7. The field of view is 5x5 mm (width x depth) and the resolution 15 µm. As Figure 2.7 B shows, structures up to 2.5 mm below the eardrum, such as the incus (I), are clearly visible.

Hubler et al. [47] developed an OCT system to measure the thickness of the eardrum. This is a possible marker for different cases of OM where inflammation and biofilms change the eardrum thickness. Cho et al. [41] for example report the mean thickness of the eardrum in healthy cases (122 µm), OME cases (108 µm), chronic OM (326 µm), and adhesive OM (251 µm), also measured by OCT. Pawlowski et al. [48] developed a small OCT with tunable focus for extended field of view to image middle ear structures and record sound induced movement of the eardrum.

OCT has proven to be suitable to visualise structures within the middle ear. Disadvantages are that no inflammation is visualised and the system is quite complex and expensive. An improvement would be the use of spectroscopic OCT as described later in Section 2.3.8 in order to detect inflammation as well as structures.

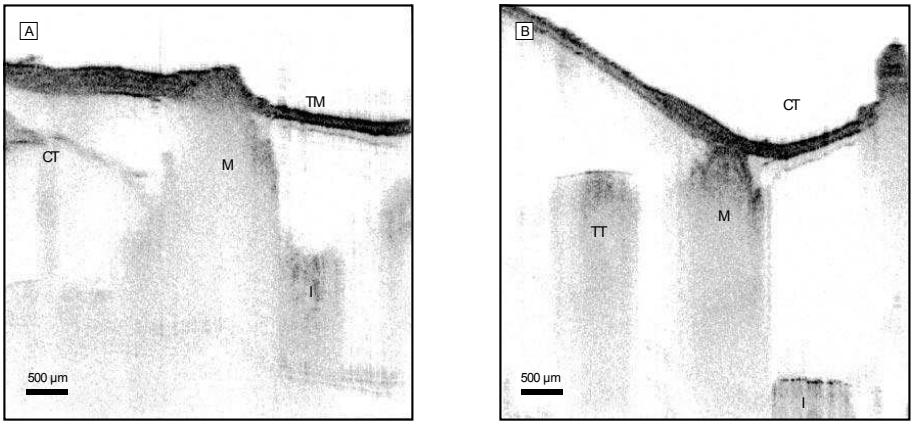


Figure 2.7: OCT images the eardrum and underlying structures; TM – tympanic membrane/eardrum, M – malleus, I – incus, CT – chorda tympani nerve, and TT – tensor tympani muscle [44].

### 2.2.6 Ultrasound

Ultrasound is a cheap, fast, and safe imaging modality and widely used for non-invasive imaging. Seth [49], Discolo [50], and Abramson [51] show the application of ultrasonic imaging to detect liquid in the middle ear. Different liquid states result in different observed reflection peaks. An empty ear shows a single peak for the eardrum whilst the presence of liquid results in further peaks. The amplitude of these peaks is dependent on the thickness of the effusion. Thus it is possible to assess the thickness of the liquid and also to detect bubbles within the liquid.

Landry et al. [52] use high frequency ultrasound to visualize structures in the middle ear. In contrast to the previous papers images are recorded instead of only single scans. An example image taken from an cadaveric eardrum is shown in Figure 2.8. The middle ear cavity was filled with a liquid and also a contact medium between eardrum and probe was required to record the image.

Water or gel in the external ear canal is used as contact medium from transducer to eaerdrum and due to low cooperation of the children, anaesthetisation is necessary [50]. Junho et al. [53] present the development of an ultrasound probe that allows application without anaesthetization but still needs a short low-pressure water pulse to provide the contact medium. The use of a contact medium for imaging is undesirable, furthermore, only the presence and state of the liquid are imaged, but not the inflammation. Consequently ultrasound imaging is not suitable to assess the middle ear inflammation.

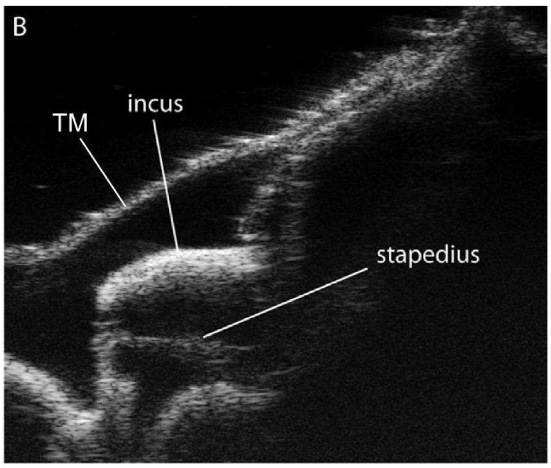


Figure 2.8: US image of the middle ear [52].

### 2.2.7 Temperature

One effect of inflammation is increased blood flow and thus an increased temperature of the tissue if its normal temperature is lower than body core temperature. Derowe and Fishman [54, 55] investigate this effect to enhance the diagnosis of OM by measuring the temperature of the eardrum using a fibre optic infra-red radiometer. The measurements show an increased temperature of eardrums with AOM with contrast to healthy eardrums of $0.68 \pm 0.27\,^{\circ}\mathrm{C}$ in one sided OM. It is stated that this measurement could be used as diagnostic tool when combined with other data and that it is not intended to be a sole diagnostic measure. Further, OME is mostly present on both ears in contrast to mostly unilateral AOM, hence a reference measurement is not available.

### 2.2.8 Magnetic Resonance Imaging and Computed Tomography

The diagnosis of otitis media in dogs using magnetic resonance imaging (MRI) [56] and computed tomography (CT) [57] is investigated. Both methods show the ability to diagnose OM with MRI providing more information as it has higher contrast for soft tissues. But both methods are not suitable for the quick diagnosis of OME due to high costs, radiation exposure, and the complicated imaging procedures.

### 2.2.9 Evaluation of the presented Methods

Different approaches to improve the diagnosis of OM have been described. Image enhancing methods were presented first. Improved imaging methods (wider field of view or improved illumination) or image processing are able to enhance important features and allow easier diagnosis. Other

projects use computer programs to perform automated diagnosis. While these methods may make diagnosis easier and more objective they do not add new information. Further, these methods are used to diagnose different OM cases but are not able to assess the inflammation of the middle ear mucosa itself.

OCT, US, CT, MRI, and improved otoscopes for eardrum shape extraction visualise structures inside the middle ear such as the shape of the eardrum, liquid inside the middle ear, and biofilms attached to the eardrum. While these methods add some additional information to standard otoscopic images they only replace previously used methods such as pneumatic otoscopy or tympanometry that are already able to detect liquid and increased pressure in the middle ear. Further, these methods are not able to detect inflammation itself. The only exception is OCT that can be extended to spectroscopic OCT able to pick up spectroscopic information as explained later in Section 2.3.8.

Fluorescence imaging adds new information but requires long acquisition times, the use of dyes, or has only been applied to other pathologies in the ear such as cholesteatoma, but not OME. Hence, its suitability to diagnose the middle ear inflammation is questionable.

According to Chandrasoma [15] the signs of an acute inflammation are redness, increased heat, swelling, pain, and a loss of function. The first two signs are a result of increased blood flow and swelling is due to an accumulation of liquid. OME is a chronic, not an acute inflammation and only some of these signs are present. The only methods assessing the inflammation using these signs are temperature and spectroscopic measurements. Since temperature measurements need a healthy ear as a reference and are not intended as a sole measure the only method left is spectroscopy.

In the next section literature research is expanded to diagnostic methods to assess inflammation in general, rather than those restricted to the middle ear in order to find methods that could be transferred to this application.

## 2.3 Current Research and Clinical Practice in Detecting Inflammation

Most of the above techniques do not assess the state of the inflammation of the middle ear. Rather they aim to improve the discrimination of different types of OM, determine the state of the liquid in the middle ear, or to show the presence of bacteria. In this section, other areas of medicine are investigated in order to find techniques to assess the state of inflammation as these techniques might be applicable to the middle ear.

The metabolic state of an inflamed tissue is increased and so too is the blood supply due to a

higher oxygen demand. Hence, many methods are based on the blood content and oxygenation in tissue. Thus, the oxygen transport and circulatory system in the human body is explained first. Also the water content in inflamed tissue is increased, and the absorption of water instead of blood can be used as indicator as well.

### 2.3.1 Oxygen Transport System in the Human Body

Oxygen is transported in the human blood system in two ways. It is either bound to haemoglobin (about 98 %) or dissolved in the blood plasma (about 2 %) [58]. This description and most literature focuses on the portion bound to haemoglobin as this constitutes the vast majority of oxygen in the blood. The haemoglobin is loaded with oxygen in the lung and pumped through the arteries into the body. The arteries branch out and decrease in diameter to reach every part of the body. The small branches leading to the capillaries are called arterioles. While most of the exchange of oxygen happens within the capillaries, some portion of the oxygen leaves the blood while in the arteries. A pressure difference due to the heart beat is visible in the arteries and arterioles. After passing the capillaries, the deoxygenated blood is collected by the venules and led back to heart and lungs by the veins. No pulse is present in venules or veins. The biggest diameter of the arterioles and venules is about 100-200 µm and decreases to a diameter of 5 µm in the capillaries [58]. The oxygenation in the arteries is between 95 to 98 % in a healthy person. This value decreases slightly in the arterioles and shows a linear falloff in the capillaries as oxygen is dispensed into the tissue. The oxygenation of the venous blood in a healthy subject is between 60 to 80 % [59].

### 2.3.2 Spectroscopy

Several groups have investigated the use of far infra-red (15 µm to 1 mm) spectroscopy to analyse the state of different tissues. Li et al. [60] use the infra-red spectrum at wavelength from 15 to 78 µm to classify gastric cancer, gastritis (inflammation in the stomach), and healthy tissue and yield an overall accuracy of 77 %. The image acquisition time is 1 to 2 min. In *ex vivo* tests in mice Katukuri et al. [61] reach an accuracy of 90 % (sensitivity 92 %, specificity 88 %, and predictive value of 88 %) when differentiating colitis (inflammation of the colon) and healthy colonic mucosa. The wavelengths used were 35 to 70 µm. Shaw et al. [62] use the spectrum from 42 to 70 µm to classify tendon, healthy muscle, and inflamed muscle tissue in mice *ex vivo* and classify 27 out 36 cases correctly. The observed changes in the spectra stem from changes in the structure of the tissue and composition of the molecules proteins, fats, and nucleic acids in the tissue [60].

De Veld et al. [63] analysed the diffuse reflectance of oral mucosa for healthy and cancerous tissue in the wavelength range of 400 to 700 nm. The reflection spectra enabled distinguishing

between healthy tissue and malignant lesions (cancerous tissue) with a sensitivity of 82 % and specificity of 88 %. The cancerous tissue analysed here is benign and malignant (benign - tumour that does not have the ability to spread and infect other tissues; malignant - can spread) lichen (chronic inflammatory disease of mucosa or skin [64]).

Liu et al. [65] analysed the absorption spectrum of healthy oral tissue, gingivitis (inflammation of the gum tissue), and periodontitis (inflammation of the periodontium, tissue supporting the teeth) in the wavelength range of 500 to 1100 nm as shown in Figure 2.9. The absorption $A = \log\left(\frac{1}{R}\right)$ is used to determine the oxygenation of the tissue and a significantly decreased oxygenation and significant increase in deoxyhaemoglobin of inflamed tissue is found.

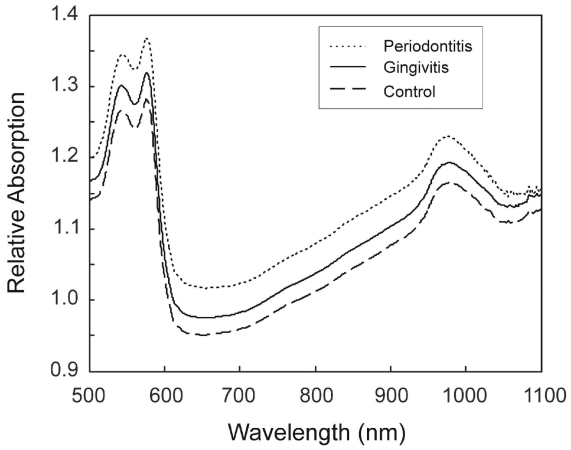


Figure 2.9: Mean absorption spectra from healthy, gingivitis, and periodontitis sites [65].

Another approach to enhance the visualization and detection of inflamed tissue is proposed by Wang et al. [66, 67]. The idea is to find an optimal illumination colour to improve the contrast between normal and inflamed tissue. This method is applied in the oral cavity and a good combination of multicolour RGB LEDs with a colour temperature of 4000 to 5000 K improves the colour difference by 42 % compared to the standard fluorescent lamp illumination.

According to Wang et al. [68], tissue oxygenation is an important biological indicator in inflammatory diseases. Several groups use spectroscopy to determine the concentration of oxygenated ($HbO_2$), de-oxygenated haemoglobin (Hb), and absolute concentration of haemoglobin ($HbO_2$ + Hb) [69–71]. These measurements are based on the different absorption coefficients of oxy- and de-oxygenated haemoglobin. Taking measurements at different wavelengths including one isobestic point (a wavelength where both types show the same absorption coefficient) all three values can be determined. Measurements are done in the visible and near infra-red (NIR) wavelength region of 475 to 1000 nm and make use of the isobestic points at 500, 530, 570 or 797 nm. Similarly, Liu et al. [72] uses the NIR spectra to detect the accumulation of water in the tissue to distinguish

healthy gum tissue and gingvitis with an accuracy of 60 % and specificity of 85.7 % in the control set.

Persson et al. [73] investigate a problem similar to the middle ear, the diagnosis of inflammation in human sinus cavities. The sinus cavities are illuminated by a single wavelength laser diode whose wavelength is temperature tuned across the molecular oxygen absorption line at 761.003 nm. During inflammation the air in the sinus cavity is replaced by liquid as a result of swelling of the mucosal tissue and occlusion of the cavity similar to the fluid build up in OME. The reflection signal backscattered from tissue layers below the sinus cavity is used to determine whether the sinus cavity is filled with air or fluid. An air filled cavity results in strong absorption at the molecular oxygen line while a fluid filled cavity does not show this characteristic. Other wavelengths are less affected by the fluid and can be used as reference. Spatial filtering of the reflection signal is necessary to reject photons scattered in the bone and skin layers above the sinus cavities. It is mentioned that measurements in the ear should be straight forward, but again, this method is not suitable for the problem treated here as the detection of liquid does not give information about the grade of the inflammation and can be detected using other methods. In contrast, the other presented spectroscopic methods are able to detect and classify inflammation.

### 2.3.3 Pulse Oximetry

Pulse oximetry makes use of the different light absorption spectra of oxygenated $HbO_2$ and deoxygenated Hb blood as well as the pressure and thus volume change of the arteries and arterioles. Conventional pulse oximeters measure the oxygenation of arterial blood at peripheral body parts such as fingertips, toes, or earlobes. The tissue is illuminated by LEDs of different wavelengths (normally 660 and 940 nm [74]) and the transmitted light is measured opposite the illumination point. The light is absorbed by tissue, venous, and arterial blood. To extract only the desired absorption due to the arterial blood the measured signal is analysed over time. The absorption due to tissue and venous blood does not change over time (except for motion artefacts) but the arterial absorption does. This is due to the pressure change induced by the heart beat and pulse. This in turn results in an expansion of the arteries and thus higher contribution to the total absorption. This pulsation component is about 1 to 5 % of the total signal [75] and can easily be extracted.

Pulse oximeters are calibrated by measurements on healthy subjects breathing different oxygenated air to artificially change their blood oxygenation. As levels below 80 % are dangerous, the calibration cannot be done below this level and the measurements are interpolated and thus less accurate [75]. Further factors decreasing the performance of pulse oximeters among others are abnormal levels of other haemoglobin derivatives such as methaemoglobin MetHb (normally

less than 1 %) and carboxyhaemoglobin HbCO (normally less than 2 %), ambient light, vasoactive drugs [76], and an inaccurate peak wavelength of the illuminating LEDs [74]. The accuracy of pulse oximeters is about 2-4 % [74].

As these conventional oximeters measure transmission they can only be used at thin samples such as an earlobe. In some cases such as badly perfused limbs these measurements are inaccurate thus new devices based and reflection measurements are developed. Using reflection measurements the sensors can be placed at any part of the body. Transmission and reflectance based sensors are compared in [77] and [78] showing similar performance in normal patients and improved performance of the reflectance sensors in badly perfused limbs.

Pulse oximeters can also be used to diagnose inflammation. For example, Setzer et al. [79] use a modified pulse oximeter to assess the tissue oxygenation in different forms of pulp inflammation. The only relevant modification of the system is an amplification of the pulsed signal by a factor 2.5 to compensate the worsened signal in this application. A statistical difference between the oxygenation of healthy and inflamed cases is discovered, showing that also arterial/arteriol blood is less oxygenated during inflammation.

### 2.3.4 Pulse Co-Oximetry

Pulse oximeters are only able to measure the oxygenation of tissue but not the total blood content or concentration of other haemoglobin derivatives. The Masimo rainbow Pulse CO-Oximeter (Masimo, Irvine, CA) solves this problem and is able to measure total haemoglobin concentration as well as oxy-, carboxy-, and methaemoglobin content. In [80] it is shown that these measurements have “acceptable” accuracy for clinically use. The measurement principle is similar to that of conventional pulse oximeters, but instead of only 2 more than 7 wavelengths are used [81] and allow for the identification of multiple haemoglobin components.

### 2.3.5 Camera Images for Oximetry

Another option to perform oximetry is to take multi-colour images of the tissue and analyse its spectral components or change the spectral characteristics of the illumination in different images [82]. This is done for the retina, using illumination with wavelengths of 586 nm and 605 nm. At 586 nm both oxygenated and deoxygenated blood have the same absorption coefficient. This isobestic case is used as reference measurement. At 605 nm the absorption coefficient of deoxygenated blood is higher than the one of oxygenated blood. A measurement at this wavelength is then used to determine whether the amount of oxy- or deoxygenated blood is higher. The group finds mean values for the oxygenation of arterioles of 99 % and of venules of 52 %. The standard deviation is

3.7 % and 5.3 %, respectively. These results show the feasibility of oxygenation measurements by camera images but this method cannot be applied to the middle ear as the eardrum obscures the light path and no clear image of the vessels will be available.

### 2.3.6 Optical Coherence Tomography

Besides the application of OCT in ophthalmology and research in imaging the eardrum, there is also research in diagnosing inflammation using OCT. Shen et al. [83] for example investigate the use of OCT in colonoscopy to distinguish the two major types of inflammatory bowel diseases (IBD) Crohn's Disease (CD) and Ulcerative Colitis based on the tissue structure. Transmural (spanning the whole depth of the intestine wall) inflammation, a hallmark of CD, can be detected by OCT as the layered structure of the tissue disappears and its presence or absence helps deciding which form of IBD is present. A light source with centre wavelength of 1270 nm is used, a spatial resolution of 10-20 µm, and an imaging depth of 1.5 mm (up to 3.5 mm when compressing the tissue) achieved. A study of 70 patients results in a specificity of 83.3 % and a sensitivity of 90 % in diagnosing CD.

### 2.3.7 Doppler Optical Coherence Tomography

Doppler optical coherence tomography (DOCT) is an advancement of OCT aiming to visualise blood flow in addition to the structure of the tissue. The velocity of a particle is extracted from the OCT signal using the phase difference between two adjacent z-scans. This method was successfully used to measure retinal blood flow and is a promising non-invasive alternative for other applications such as angiography [84]. In the investigated application it could be used to visualise the blood flow in the middle ear mucosa in addition to structures in the middle ear.

### 2.3.8 Spectroscopy Optical Coherence Tomography

Rather than using the spatial information of OCT only, the addition of spectroscopic information would enhance the system and allows assessing the blood oxygenation. Spectroscopy Optical Coherence Tomography (SOCT), an enhancement of OCT, is capable of this. The basic idea of SOCT is to combine OCT and Fourier Transform Infra-Red Spectroscopy (FTIR) as both techniques are based on an interferometer.

Similar to conventional spectroscopy, light is passed through a sample and the transmitted light recorded. But instead of scanning the wavelength though the desired range, a broadband pulse is used and the transmitted light brought to interference with a reference beam. The interference signal is Fourier transformed and allows to detect all frequencies at once reducing the measurement time [85]. The spectrum within the bandwidth of the source, which is normally about 50 to 100 nm,

is analysed. This spectral bandwidth is broad enough to determine the oxygen and de-oxygen level of haemoglobin in tissue to asses inflammatory diseases [68].

As OCT is clinically used for diagnosis in the eye it is obvious to facilitate SOCT for retinal oximetry. For example, the group of Kageman [86] use wavelengths from 805 to 855 nm for oximetry and find statistical differences between arterial and venous blood. This study demonstrates the theoretical feasibility of oximetry using SOCT but as [87] states, it is not ready for clinical use yet.

Further examples are the work by Liu [88] and Faber [89] who investigate the use of SOCT to determine the oxy-haemoglobin content of blood *in vitro* and *in vivo*, respectively. Lui [88] measures the properties of both fully ox- and de-oxygenated, diluted (to reduce the scattering coefficient) sheep blood and the spectroscopic results show good correspondence to the oxygen level. *In vivo*, the measurement would be less accurate due to the strong scattering of blood. But still they conclude that it is possible to do real time $HbO_2$ assessment using spatial filtering. In contrast [89] states that current models for light transport are not sufficient to extract the absorption coefficient from SOCT measurements. Only careful calibration of the system may lead to quantitative measurements taking the path length of the detected light into account. The optical properties of the surrounding tissue in the optical path has to be taken into account to compensate for errors [86].

The resolution of SOCT is about the size of red blood cell. Thus, a single OCT scan can assess only very few blood cells. Yi and Li [90] investigate the possibility to assess the haemoglobin oxygenation by the measurement of single cells. The *in vitro* experiments show that this is possible although more elaborate models for scattering and signal processing are necessary.

In conclusion, SOCT could be used to assess the oxygen saturation in blood if appropriate light transport models are used, the optical properties of the surrounding media are taken into account, and the system is calibrated properly. But none of the presented works achieves this in a reliable way in order to transfer this technique into clinics.

### 2.3.9 Raman Spectroscopy

Lieber at al. [91] develop a portable confocal Raman spectroscopy system to classify inflamed scar tissue, two kind of cancerous tissue, and healthy skin. In case of Raman scattering the frequency of the scattered photon is shifted due to interaction with a vibrating molecule. The resulting frequency depends on the interacting molecule and can be used to determine substances or classify tissues. The proposed method uses a 825 nm, 40 mW laser for illumination, an image acquisition time of 30 s, and collects the Raman spectra from 500 to 1800 nm. The different tissues can be distinguished with an overall accuracy of 95 % (40 out of 42 cases, 100 % sensitivity, and 91 %

specificity).

### 2.3.10 Laser Doppler Flowmetry

In laser Doppler flowmetry (LDF) the Doppler shift of a laser beam reflected from the moving blood is used to measure its velocity. The blood velocity can be related to the metabolism which in turn is connected to inflammation in the tissue. Baab [92], Quinn [93], and Gleissner [94] use LDF to assess inflammation of for example gingvial sites. The results are not reliable [94] and are less accurate than conventional techniques [93]. During measurements in the middle ear, the eardrum would pose another source of error and unreliable results are expected. Hence, LDF is deemed not suitable for the proposed task.

### 2.3.11 Evaluation of the Presented Methods

Most of the above presented methods are based on spectroscopic measurements making use of the changed absorption spectrum of the tissue under investigation. Either the total blood content or the oxygenation is assessed. The full spectrum or only single wavelengths can be analysed.

Pulse oximetry is widely used in clinics and is a reliable method as background signals are filtered by use of the pulsating nature of the blood absorption due to volume changes of vessels. While it is mostly used for oxygenation measurements, it also shows statistical differences when analysing inflamed tissues. LDF is used to measure blood flow instead of blood oxygenation. This gives information about the blood content in the tissue and thus the metabolism, but results are not reliable.

Spectroscopic measurements using a wide wavelength range are also promising as more information is extracted than in single wavelength measurements. The problem when doing measurement in the middle ear is that the eardrum prevents direct measurements. Spatial discrimination/3D imaging techniques become necessary in order to filter background from the eardrum and signal from the mucosa.

SOCT is a technique that combines spectroscopy and 3D imaging and is used to assess blood oxygenation. The analysed wavelength range is restricted to the bandwidth of the source (about 100 nm or less) and also the analysed volumes are small. This results in inaccurate results and improved signal processing is necessary. The next section investigates other 3D imaging techniques that allow resolving signal from mucosa and eardrum and can be combined with spectroscopic methods in order to assess the inflammation.

## 2.4 Current Research in Imaging 3D Volumes

This section summarizes 3D imaging techniques used to visualize tissue volumes. OCT and its enhancement SOCT have been described earlier. Other techniques are Diffuse Optical Tomography [95, 96], Laminar Optical Tomography [95], Low Coherence Enhanced Backscattering (LEBS) [97, 98], confocal microscopy [99, 100], Photo-Acoustic Tomography (PAT) [101–105], Acousto-Optic Imaging [106], Orthogonal Polarisation Spectral Imaging (OPS) [107, 108], and Side Stream Dark Field Imaging (SSD) [109, 110]. These techniques might be useful to separate background from signal to facilitate the assessment of inflammation in the middle ear.

### 2.4.1 Diffuse Optical Tomography

In Diffuse Optical Tomography (DOT) the tissue is illuminated by near infra-red radiation and light exiting the medium is recorded by spatially distributed detectors. While photons propagate through the media they experience scattering and absorption. Using a photon propagation model, the spatial distribution of absorbers is reconstructed from the detected signal. In this way the distribution of the main absorbers (haemoglobin, water, and melanin) in tissue and thus the distribution of different tissues is identified. The imaging depth is several centimetres and the resolution 5 to 10 mm [95]. It is used for example in breast imaging for cancer detection and brain imaging [96].

This method is not applicable to the middle ear as distributed detectors are necessary and thus the system cannot be placed in the ear canal. Further the resolution ($> 5$ mm) is too coarse for the small structures inside the ear.

### 2.4.2 Laminar Optical Tomography

Laminar Optical Tomography (LOT) evolved from DOT and achieves higher resolutions of about 100 to 200 µm but smaller penetration depths of about 2 to 3 mm [95]. The improvement in resolution is achieved by smaller source detector separation. Further, the spatial source and detector grid in DOT is changed to a single source surrounded by several detectors and images are achieved by scanning of the system across the sample. It is assumed that light emerging far away from the illumination experienced more scattering events and thus has travelled deeper into the tissue. Using light propagation models, the spatial distribution of scatterers and an image are reconstructed. The penetration depth is of the same order as the source-detector separation which varies between 200 µm up to 3 mm. As for DOT, this method is not suitable for this task as the required detector separation is to larger to be used within the ear and contact with the tissue is required.

### 2.4.3 Low Coherence Enhanced Backscattering

Low Coherence Enhanced Backscattering (LEBS) is based on interference of directly backward scattered light. Scattered photons travelling in inverse direction in the tissue form an interference pattern at small angles with up to twice the intensity than incoherent scattered light. The first and last scatterer of the path act similar to pinholes in the double slit interference experiment resulting in constructive interference causing the increased signal. At higher angles from the direct backward direction this signal disappears as no constructive interference is possible. The penetration depth is restricted to the coherence length of the illumination (approx. 150 µm) as no interference is observed if photons travel further than the coherence length [98]. Depth resolution is obtained by analysing the interference pattern at different angles, high penetration depths affect the centre of the interference pattern and shorter paths affect the periphery [97]. Spectroscopy is for example done in the wavelength range of 400 to 700 nm [98]. The penetration depth of 150 µm is high enough to penetrate the eardrum with average thickness of 100 µm but still has to penetrate the middle ear cavity of 2 to 4 mm depth. Further, the system is only used in research, making this an experimental, less reliable system.

### 2.4.4 Confocal Microscopy

In confocal systems a pinhole is placed in the plane of focus so that only light resulting from the intersection of optical axis and image plane passes through the pinhole to the detector. At the same time, the illumination light is focused on the same spot. In this way a very good resolution of less than 1 µm is achieved [99] and light from out of the focus planes is rejected. As only a tiny area is imaged, scanning is needed to reconstruct an image of an area or volume. The penetration depth is up to 250 µm depending of tissue type and the wavelength used. As most of the light is blocked by the pinhole the signal intensity is low and high illumination power is needed. Confocal systems are used in reflection mode as well as for fluorescent imaging.

Dunbar et al. [100] show the application of confocal endomicroscopy used to investigate gastrointestinal mucosa. One presented system shows imaging depth of 250 µm, lateral resolution of 0.7 µm, axial resolution of 7 µm, and field of view of $475 \times 475\,\mu m^2$ at an outer diameter of the endoscope of 12.8 mm. An alternative system shows a penetration depth of 130 µm, resolution of $3.5 \times 15$ µm, and field of view of 600 µm while the endoscope has an diameter of 2.7 mm. Both systems need contrast agents for fluorescent image acquisition [100].

While the use of dyes is not allowed in this project due to requirement of a quick and non-invasive technique, confocal imaging is still possible when used in absorption mode where the reflected or transmitted light with original wavelength is analysed. Spectral measurements can

easily be conducted by the use of different illumination wavelengths and subsequent measurements as for example done by Itzkan et al. [111] when imaging cells and Reinholz et al. [112] to image the retina. As the wavelength can be chosen freely this method is easily combined with spectroscopy to assess the blood concentration and oxygenation. Similarly to SOCT, the signal processing is expected to be a main issue as tissue in the light path affect the measurement at the sampled area by wavelength dependent scattering and absorption.

### 2.4.5 Photo-Acoustic Tomography

In Photo-Acoustic Tomography (PAT) laser pulses (with e.g. 5 ns pulse duration and 10 to 20 Hz repetition rate [101]) are absorbed by tissue resulting in heating of the absorbing tissue and pressure $P$ increase according to

$$P = \frac{\beta c^2}{C_p} \mu_a F \tag{2.1}$$

where $\beta$ is the thermal coefficient of volume expansion, $C_p$ the heat capacity, $c$ the speed of sound, $\mu_a$ is the absorption coefficient, and $F$ is the laser fluence [101]. This pressure change in turn leads to ultrasonic (US) emissions. Depth information is achieved by evaluating the relative time of arrival of the US signals and spectroscopic information by evaluating the amplitude of the recorded signal dependent on exciting wavelength. Penetration depth is higher than in OCT (up to 84 mm have been demonstrated in experiments) as the radiation only travels in forward direction, while the less attenuated ultrasound signal travels back. The spatial resolution is about 1/200 of the imaging depth [102]. Figure 2.10 illustrates this relation and also shows example images recorded with different scales. PAT shows a good contrast of capillaries as the signal is dominated by absorption and haemoglobin is a main absorber in tissues. Thus this imaging modality is well suited for blood analysis [103].

The signal amplitude of the PAT signal is related to the volume expansion coefficient $\beta$ and the speed of sound $c$ which both are dependent on the temperature. Thus the signal amplitude is temperature dependent and using calibration for a particular tissue the temperature of the tissue can be determined [101]. The sensitivity is about 0.1 °C. Further, PAT can assess the blood flow. Thus, PAT can measure all metabolic parameters of blood circulation: vessel structure, haemoglobin concentration, temperature, and flow velocity [102].

To record the ultrasonic emissions traditional sensors must be in contact with the tissue to avoid attenuation in air and reflection at the tissue to air interface. But contact with the eardrum is not permitted here. Recently, several groups have developed non-contact sensors using laser interferometry [104] and Low Coherence Interferometry [105] overcoming this problem. As interferometric system are used for US detection it is straight forward to include OCT in the system,

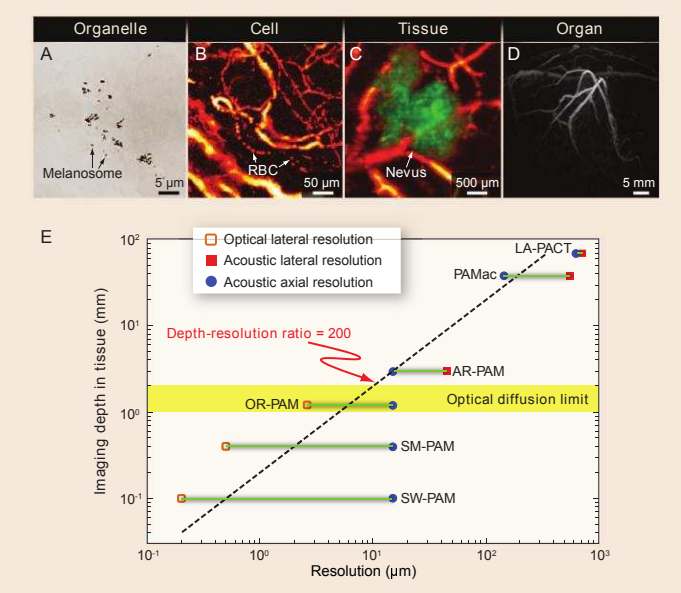


Figure 2.10: Resolution versus imaging depth of PAT shown in subfigure E) [102]. Subfigure A) shows an image recorded with SW-PAM (Sub-Wavelength Photo-Acoustic Microscopy), B) was recorded with OR-PAM (optical-resolution PAM), C) with AR-PAM (acoustic-resolution PAM), and D) with PACT (photoacoustic computed tomography).

as done by [103] developing a combined PAT and OCT system.

On a first glance, PAT seems to be suitable for this task as it allows to assess vessel structure, haemoglobin concentration, temperature, and flow velocity. But expensive equipment is necessary making the system less suitable.

### 2.4.6 Acousto-Optic Imaging

Acousto-Optic imaging (AOI) [106] increases the imaging depth in scattering tissue to depths deeper than the ballistic path length of photons. This is done by use of acoustic modulation of the light wavelength making use of Doppler shift.

When light propagates through a scattering medium an area with high absorption cannot be seen when buried deep inside the tissue as photons are scattered resulting in random light paths. Doppler shift modulation of the light passing through the tissue, changes the wavelength of some of the photons. When restricting the area of modulation, this small area acts as a virtual source of light with the modulated wavelength. If this modulation area is placed on tissue with high absorption, less light will pass through the modulation area and the detected modulated light is reduced, compared to an area with low absorption. This allows measurement of the optical absorption of

the tissue inside the modulation area. Imaging depth is increased to several centimetres as the area is determined by the US and not by the ballistic path length. Resolution is around 1.5 mm traverse and 15 mm along the US axis, defined by the US focus. By scanning the modulation area through the sample, an image is reconstructed with resolution according to the US focus. Light and US source need to be orientated orthogonally as the unfocussed signals overlap otherwise, adding an offset to the modulated signal. Orthogonal orientation is not possible inside the ear.

### 2.4.7 Orthogonal Polarisation Spectral Imaging

Orthogonal polarisation spectral imaging (OPS imaging) uses the effect that polarised light keeps its polarisation state when reflected but loses its polarisation after several scattering events. Using an analyser orientated orthogonal to the polarised illumination, reflected and superficial scattered light can be filtered from deeper penetrated and multiple scattered light. This is used to image and enhance the contrast of subsurface structures such as blood vessels [108]. Mathura et al. [107] report an improved image quality of capillaries using OPS imaging compared to capillary microscopy while measurements of blood cell velocity and capillary diameter shows similar results.

This method would allow reducing reflections from of the surface of the eardrum but light is still scattered when passing though the eardrum. This cannot be corrected resulting in a blurred image of the mucosa. A recorded image would be similar to normal otoscope images with specular reflections rejected and reduced signal from the eardrum but still would not show a clear image of the middle ear.

### 2.4.8 Side Stream Dark Field Imaging

Similarly to OPS, side stream dark field imaging (SSD Imaging) is used in capillaroscopy to enhance the contrast of images of blood vessels [109, 110]. Illumination beam and detection are spatially separated as shown in Figure 2.11 where the sample is illuminated with an annular ring and the detection aperture is inside the illumination ring so that no direct reflections are detected. Only scattered light is detected and the contrast of subsurface structures improved compared to normal detection.

This method cannot be applied inside the narrow ear canal as the spatial separation of illumination and detector requires contact of imaging device and sample.

### 2.4.9 Evaluation of the Presented Methods

Confocal microscopy, SOCT, and PAT seem to be the most promising techniques to image the middle ear. While PAT shows high contrast for blood vessels it requires a complex system. SOCT

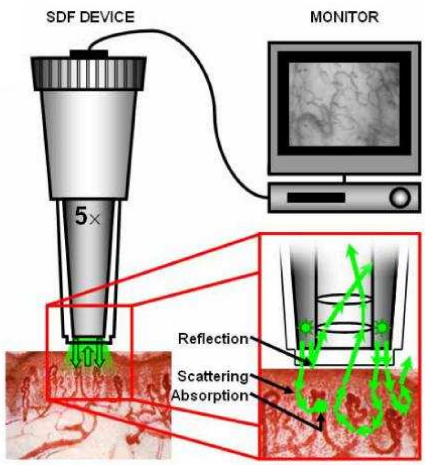


Figure 2.11: Concept of side stream dark field imaging [110].

is also a promising technique as OCT systems have been shown to be usable in the ear and spectroscopic measurements would add information. The system is simpler than in PAT but the spectral measurements require improved signal processing. Last, confocal microscopy systems are simpler than both PAT and SOCT which is of advantage considering the possible further use of the system requiring cheap and simple devices. Furthermore, the wavelengths used for spectroscopy can be freely chosen in contrast to SOCT. Hence, we think that confocal microscopy is the best alternative.

## 2.5 Conclusion

Table 2.1 and 2.2 summarise the presented methods and give short comments about the usefulness for the assessment of middle ear inflammation.

Current research projects do not focus on the assessment of the inflammation of the middle ear mucosa. Projects either aim to improve the discrimination of different cases of middle ear inflammation or to detect signs of middle ear inflammation such as biofilms, middle ear effusion, or bulging shape of the eardrum. Hence, the literature search was widened to find techniques to assess inflammation in general. The mostly used method is spectroscopy making use of the changed absorption spectrum of the tissue due to changed blood content. While promising results are achieved, the problem in the ear remains to overcome the eardrum in the light path. 3D imaging techniques that can be combined with spectroscopy will be able to achieve this. While OCT and PAT seem promising alternatives, we argue that confocal microscopy is the best alternative due to a simpler and cheaper system and free choice of wavelengths for spectroscopic measurements. Consequently, a spectroscopic confocal system is developed and tested after a middle ear phantom

has been developed.

Table 2.1: Overview of the Presented Imaging Methods

| **Method** | **What is shown** | **Penetration depth [mm]** | **Resolution [µm]** | **Detects inflammation** | **Rejects background** | **Comments** | **References** |
|---|---|---|---|---|---|---|---|
| Image processing | Eardrum in improved quality | | | No | No | | [16, 24, 25, 27, 28] |
| Spectroscopy | Spectrum of area/volume | | | Yes | Not on its own | able to reject background when combined with 3D method | [30, 31, 60–62, 66–71, 113] |
| Fluorescence | Bacteria & Biofilms | *see confocal* | *see confocal* | No | Yes | used in combination with Confocal Microscopy | [32–35] |
| Shape extraction of TM | 3D image of TM | | | No | No | | [37–39] |
| Ultrasound | Structures, liquid in the middle ear | 150 | $> 200$ | No | Yes | | [49–51, 53] |
| Temperature | IR Radiation | | | Yes | No | healthy ear as reference needed | [54, 55] |
| MRI | Structure | $> 210$ | 400 | Yes* | Yes | very expensive system; *via structural changes | [56, 114] |
| CT | Structure | $> 350$ | 500 | Yes* | Yes | x-radiation; *via structural changes | [57, 115] |
| Raman Spectroscopy | Structure & Spectrum | *see confocal* | *see confocal* | Yes | Yes | used in combination with Confocal Microscopy; high power/long exposure time | [91] |
| Pulse Oximetry | blood oxygenation | | | No | Yes | no clear relation of inflammation and oxygenation (see Section 3.3.2) | [74–79] |
| Pulse Co-Oximetry | blood oxygenation and total blood content | | | Yes | Yes | no access to the signal processing and used wavelengths | [80, 81] |

Table 2.2: Overview of the Presented Imaging Methods, Continued

| **Method** | **What is shown** | **Penetration Depth [mm]** | **Resolution [µm]** | **Detects inflammation** | **Rejects background** | **Comments** | **References** |
|---|---|---|---|---|---|---|---|
| LDF | Blood flow | | | Yes | No | not accurate enough | [92–94, 116] |
| DOT | Structure & Spectrum | $> 10$ | $> 5000$ | Yes | No | resolution too low | [95, 96] |
| LOT | Structure & Spectrum | 3 | 100 - 200 | Yes | Yes | does not fit in the ear canal | [95] |
| SOCT | Structure & Spectrum | 4 | 5 | Yes | Yes | improved algorithms necessary | [40, 43–45, 68, 86, 88, 89] |
| LCEB | Structure & Spectrum | 0.15 | 9 | Yes | Yes | only research projects, unreliable | [97, 98] |
| Confocal Microscopy | Structure | 0.25 | $< 15$ | Yes* | Yes | *combined with spectroscopy | [100, 111, 112] |
| PAT | Structure & Spectrum | $> 4$ | 1/200 of penetration depth | Yes | Yes | expensive and complex | [103–105, 117] |
| AOI | Structure & Absorption | several cm | $(1{,}5 \times 15) * 10^3$ | Yes | Yes | does not fit in the ear canal | [106] |
| OPS | spectrum, reflection reduced image | | | No | Yes | improves contrast of subsurface structures only | [107, 108] |
| SSD | spectrum, reflection reduced image | | | Yes | Yes | does not fit in the ear canal | [109, 110] |

# Chapter 3

# Development of a Middle Ear Phantom

The optical system that will be developed later has to be tested before being used on human subjects. These test will have to be conducted on a sample with known optical properties in order to validate the results. Further, stable optical properties are desired in order to be able to compare results when improving and changing the optical system. Hence, an optical tissue phantom of the middle ear is developed in this section.

The middle ear phantom will consist of two main layers, the eardrum and the middle ear mucosa, both separated by an air gap simulating the middle ear cavity. A phantom holder is designed as well in order to align and position the middle ear phantom with the optical system. The eardrum phantom will be simulated by a thin layer introducing scattering and absorption in the light path, while the mucosa phantom is a sample thicker than the penetration depth of light. The layered structure of the middle ear tissue (mucosa, sub-mucosa, and underlying tissue) will be neglected and simulated by a single layer. This is valid as the penetration depth is expected to be lower than the thickness of mucosa and sub-mucosa. A change in the mucosa tissue will then be simulated by different exchangeable mucosa phantoms simulating healthy and diseased mucosa. All other components of the middle ear, such as ossicles or the ear canal, are neglected in the phantom as the selection of an appropriate measurement area in combination with the small detection aperture in the ear canal rejects light originating from these components.

This chapter first presents several approaches to create optical tissue phantoms and selects the most appropriate approach. Then, the background of light propagation in tissue and optical properties of tissues are explained. Optical properties of mucosa are collected from literature in order to design a mucosa phantom. Then literature is scanned for optical properties of eardrums and

animal eardrums are characterised to enable the creation of realistic eardrum phantoms. Finally, the middle ear phantom is designed and presented.

## 3.1 Possible Models

There are several alternatives to design a middle ear phantom, which have to be evaluated by the following criteria. First, the model has to be as close as possible to reality, second, its properties must be reproducible to allow comparable and repeatable experiments, and third, the approach must be feasible within this project and time scale.

**Animal Model:** An animal model for middle ear inflammation as for example used in [33, 118, 119] would be closest to the human case but is also most difficult to work with. First a model has to be found and all the ethical obstacles overcome. Further, results would not be repeatable as the disease in animals changes over time and different animals will show different characteristics. This approach is not feasible during this project, but could be an alternative to test a fully developed system before testing it in clinics.

**Human Model:** While tests on patients are not feasible at this stage another option would be to simulate inflammation on a healthy volunteer by either inducing inflammation (as done by [120] in rats or [121] on humans using histamine) or occlusion of limbs as done in [122]. Results are not reproducible but this provides an option for tests of the system once it is characterised.

**Tissue Phantom:** The next possibility is to develop homogeneous tissue simulating phantoms with properties defined by the mixture of the phantom material. Only static properties are achieved but different phantoms simulating different metabolic states can be produced.

**Phantom with Real Blood:** The use of a tissue phantom with capillaries to conduct blood with different oxygen contents as presented in [123] would mimic the real live mucosa closer than a static tissue phantom. This would allow reproducible properties, but setting the oxygenation is a problem and requires a complicated setup. Further, the sample will not be homogeneous as small vessels cannot be produced and measurements would be dependent on the sampled area.

Static tissue samples will be used as this option will give most reproducible properties and is easiest to handle. The optical properties of mucosa will be collected from literature, while animal eardrums are characterised in order to define optical properties of an eardrum phantom. This

middle ear phantom will be used to characterise and test the optical system. Once this is done other phantoms can be considered.

## 3.2 Background

When light interacts with tissue, several phenomena can be observed: reflection at the air tissue interface and attenuation within the tissue. The attenuation is composed of scattering and absorption of the light. Scattering is a result of refraction at interfaces within the tissue such as cells, cell organelles, and fibre structures that exhibit a different refractive index than the surrounding medium [124]. Absorption appears when the photon interacts with a molecule and its energy is transformed into internal energy (such as thermal energy) of the absorbing molecule.

The mathematical description of light propagation in tissue is presented first and then these properties are linked to physical parameters of the tissue and their origin explained.

### 3.2.1 Light Transport in Tissue

The optical properties of tissue are given by the absorption coefficient $\mu_\mathrm{a}$, scattering coefficient $\mu_\mathrm{s}$, scattering anisotropy factor $g$, and refractive index $n$. Derived units are the reduced scattering coefficient (also called transport scattering coefficient) $\mu_\mathrm{s}' = (1-g)\mu_\mathrm{s}$ and attenuation coefficient $\mu_\mathrm{t} = \mu_\mathrm{a} + \mu_\mathrm{s}$. The anisotropy factor $g$ is the mean cosine of the scattering angle $\theta$, a value of 0 means isotropic scattering, a value close to 1 means forward scattering, and a value close to -1 describes backward scattering. The Henyey-Greenstein function is often used to model the probability distribution of the scattering angle $p(\theta)$ as a function of $g$ as it describes a typical phase function for light interacting in tissue.

$$p(\theta) = \frac{1}{4\pi}\frac{1-g^2}{[1+g^2-2g\cos(\theta)]^{3/2}} \tag{3.1}$$

The mean free path $MFP$ of photons in tissue before scattering or absorption occurs is given by the inverse of the attenuation coefficient $MFP = \frac{1}{\mu_\mathrm{t}}$.

Light transport through a non-scattering but absorbing media is described by the Lambert-Beer Law

$$I(z) = I_0 \exp(-\mu_\mathrm{a} d) \tag{3.2}$$

where $I_0$ is the incident intensity, $I$ the exiting intensity, and $d$ the thickness of the medium. Including the reflection at the interface this equation becomes

$$I(z) = I_0(1-R_\mathrm{F})\exp(-\mu_\mathrm{a} d) \tag{3.3}$$

with the Fresnel Reflection $R_\mathrm{F}$ at the tissue to air interface

$$R_\mathrm{F} = \left(\frac{n-1}{n+1}\right)^2 \tag{3.4}$$

In case of weak scattering media ($\frac{\mu_\mathrm{s}'}{\mu_\mathrm{t}} < 0.5$) as well as for a thin sample ($\mu_\mathrm{t} \cdot d < 1$) with more scattering ($\frac{\mu_\mathrm{s}'}{\mu_\mathrm{t}} < 0.9$) and a collimated laser beam also scattering can be included into the Lambert-Beer Law as follows [124]

$$I(z) = I_0(1 - R_\mathrm{F}) \exp(-\mu_\mathrm{t} d) \tag{3.5}$$

For higher scattering coefficients a more complex theory must be used as photons travelling through the media have different path lengths, dependent on scattering events and angles, and thus the path length used in the exponential Lambert-Beer law changes. Another approximation is the modified Lambert Beer Law given by [125]

$$I(z) = I_0(1 - R_\mathrm{F}) \exp(-A_\mathrm{s} - \mu_\mathrm{a} d) \tag{3.6}$$

where $A_\mathrm{s}$ is an offset due to scattering. More terms can be included for a better approximation [125].

The time photons need to travel through a media is described by the diffusion approximation and their path through the media can be simulated by Monte-Carlo simulations. The fluence rate $\phi(r,t)$ of photons through a tissue at a set time $t$ and distance $r$ from the incident point, is described by

$$\frac{1}{c}\frac{\partial}{\partial t}\phi(r,t) - D\nabla^2\phi(r,t) + \mu_\mathrm{a}\phi(r,t) = S(r,t) \tag{3.7}$$

where $S(r,t)$ describes the illumination source and $D$ is the photon diffusion coefficient

$$D = \frac{1}{3(\mu_\mathrm{s}' + \bar{a}\mu_\mathrm{a})} \tag{3.8}$$

with $\bar{a}$ being a scaling parameter with values between 0 and 1. This equation applies if scattering is greater than absorption and the photon travelled many mean free paths $MFP$ [125].

In case of an infinite space and an ultra short illumination pulse $S(r,t) = \delta(0,0)$, the approximation of the diffusion equation Equation (3.7) is given by

$$\phi(r,t) = c(4\pi Dct)^{-3/2} \exp\left(-\frac{r^2}{4Dct} - \mu_\mathrm{a} ct\right) \tag{3.9}$$

with $c$ the speed of light in the tissue [125].

Monte Carlo methods are described in more detail in Section 5.3 so only a short description is given here. The path of a single photon in tissue is simulated as follows: The photon is send into the media, and after it has travelled a distance according to the mean free path it experiences a scattering event. The intensity is reduced according to the absorption coefficient and the direction

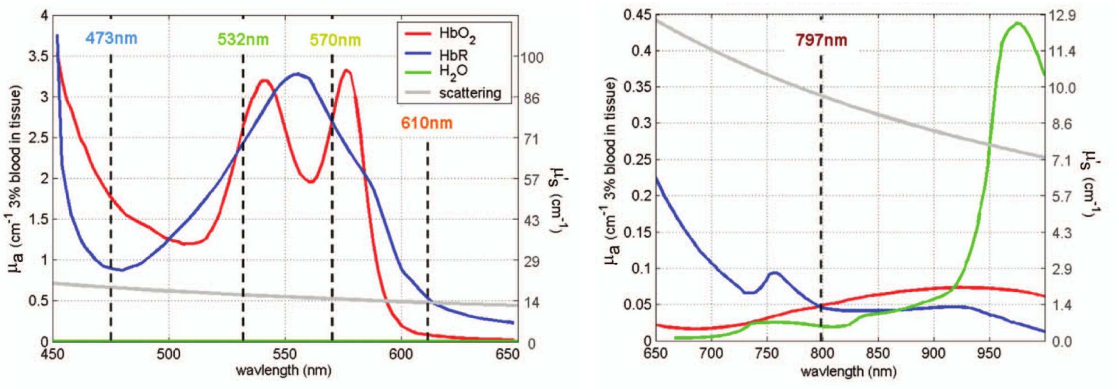


(a) Visible range

(b) NIR range

Figure 3.1: Absorption spectra of main absorbers in tissue and typical scattering spectrum of brain tissue [126]. Note the different scaling of both graphs.

is changed using a random scattering angle calculated by the Henyey-Greenstein function. Then the photon travels further into the new direction until it experiences another scattering event or exits the medium. The addition of multiple random photons paths results in a distribution approximating the real case. The more photons are simulated the more accurate are the results.

### 3.2.2 Origin of Optical Properties of Tissues

The main absorber in tissue are water, blood (oxygenated haemoglobin $HbO_2$, de-oxygenated haemoglobin Hb/HbR, and other less common haemoglobin derivatives), lipids, and melanin. Figure 3.1 shows the absorption spectra of water and haemoglobin in the visible and near infra-red range. The spectra of lipids and melanin are omitted neither of both is present in the middle ear. The final absorption of tissue is a sum of the single components multiplied by their concentration. Haemoglobin shows absorption peaks in the UV and blue range (not shown in the graph) and in the green range and then decreases with wavelength. Oxygenated and de-oxygenated haemoglobin generally show a similar course on a larger scale but show differences on a more detailed investigation. For example oxygenated haemoglobin shows two peaks in the green range while de-oxygenated haemoglobin shows only one peak. These differences are used for the measurement of blood oxygenation. The generally low absorption in the red wavelength range allows more red than green and blue light to be scattered from tissues, resulting in the red colour of blood. Water in contrast shows a low absorption in the visible range but increasing absorption above 900 nm. This results in an absorption window in tissues in the red and NIR range with low absorption coefficient.

Figure 3.1 also shows the course of the scattering coefficient in brain tissue, which is much

higher than the absorption coefficient and decreases with increasing wavelength. Other tissue exhibit similar spectral dependence but can vary more than one order of magnitude in absolute values. Scattering results from random refractions of light at interfaces within the tissue, such as cells and fibre structures. The scattering characteristics (coefficient and angle) are dependent on the wavelength and size of the scattering particles. Structures such as collagen bundles with dimensions of 1 to 10 µm are bigger than the used wavelengths and result in Mie scattering which decreases with wavelength and can be described by $\mu_s = a\lambda^{-b}$ with $b$ having values around 0.5 to 1.5. This approximation is used to calculate the scattering spectum shown in Figure 3.1, with $a = 1.14 \cdot 10^{-7}$ and $b = 1.3$. Membranes and organelles on the other hand are much smaller, around 100 nm, and result in Rayleigh scattering that is scaled with $\lambda^{-4}$ [127]. In general, scattering in the visible and near-infrared range decreases with increasing wavelength.

The scattering anisotropy is dependent on the diameter of the scattering particles as well. Larger structures (similar or larger than the wavelength) result in mainly forward scattering ($g$ close to 1) and smaller structures show more isotropic scattering ($g$ closer to 0) [128].

The absorption coefficient is minimal in the range of 700 to 900 nm and the scattering coefficient relatively small forming an "optical window" with highest penetration depth and low attenuation in tissue in the NIR range (700 to 900 nm).

A wide range of optical properties in the visible and NIR range are reported. Values for the absorption coefficient range from 0.01 to 4 $mm^{-1}$, scattering coefficient from 1.09 to 45 $mm^{-1}$, scattering anisotropy of 0.8 to 0.97, and refractive index of 1.4 to 1.5 [124]. The reported properties depend on the method of measurement (optical setup), preparation of the samples (*in vivo* or *ex vivo* and storage), and the type of tissue itself. Values for mucosa and the eardrum are reported in more detail in the following sections.

### 3.2.3 Scattering on Collagen Fibres

Mostly, the tissue is assumed to be isotropic resulting in an isotropic scattering coefficient but this is not the case for tissues such as muscles or the eardrum. Cylindrical aligned collagen fibres in the tissue cause anisotropic scattering that can be described using a direction dependent scattering coefficient [129]. In calculations, these fibres are assumed to be infinite long (justified as the diameter is smaller than the length of the fibres) and the scattering calculated by the Mie Theory for infinite cylinders (as described by [130]). A mean diameter and main orientation direction are assumed and Gaussian distribution of these parameters can be applied to give more accurate results when simulating a tissue volume [131].

Light incident on a single fibre is scattered into a cone around the original propagation direction.

The scattering angle of this cone is dependent on the diameter of the cylinder, the wavelength, the refractive indices, and the angle of the incident beam towards the fibre. With increasing incident angle, the scattering cone cylinders' base turns into an ellipse with longer axis perpendicular to the cylinder, and finally into a single plane for a perpendicular incident beam. This means the direction dependent scattering coefficient has a small value in direction of fibre orientation and a high value orthogonal to its orientation [129].

## 3.3 Optical Properties of Mucosa

Optical properties of mucosa are reported in this section in order to develop a model for healthy and inflamed middle ear mucosa.

For illustration, a not inflamed middle ear cavity is shown in Figure 3.2 as seen from the external ear canal with the eardrum removed [132]. The image was recorded during stapedotomy (surgical replacement of the stapes) and shows the incus (RLB), oval window (O), and the entrance to the Eustachian tube (E). The mucosa appears mostly white with local blood vessels. When inflamed, the middle ear mucosa shows more blood vessels and appears in general redder, according to surgeons. Effects of inflammation are described later in more detail.

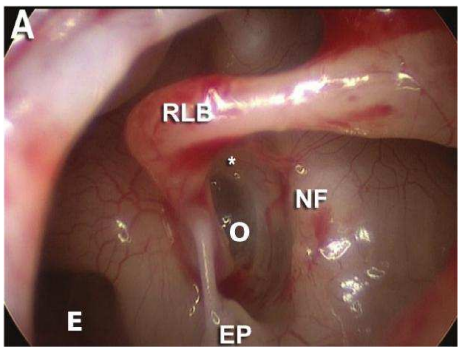


Figure 3.2: Middle ear during stapedotomy seen from the external ear canal with the eardrum removed [132]; RLB – long process of the incus, NF – facial nerve canal, EP – pyramidal eminence, E – eustachian tube, O – oval window.

### 3.3.1 Optical Properties

Literature report little about optical properties of middle ear mucosa, especially during inflammation. Hence, other mucous tissues in human as well as middle ear mucosa in animals, and other inflammatory diseases and cancers are considered. A wide variety of optical properties of mucous tissues are reported. These variations are due to differences in the measurement setups (integrating

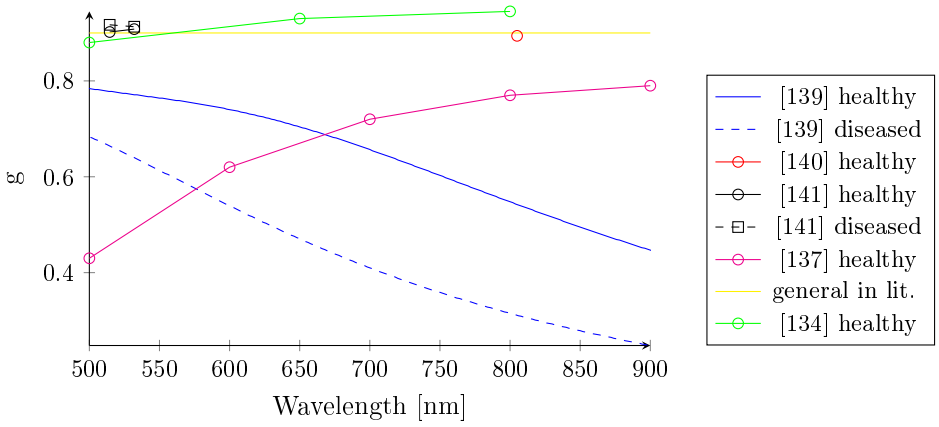


Figure 3.3: Scattering anisotropy of mucosa reported in literature.

sphere, fibre probes, ...), tissue sites (colon, oral, ...), state of tissue (ex vivo, in vivo), and disease (cancer, polyp, bowel disease). All the diseased cases can be described as inflammatory diseases or similar diseases showing higher metabolism. Figure 3.3, Figure 3.4, and Figure 3.5 summarise the scattering coefficients, absorption coefficients, and scattering anisotropy found in literature, dependent on the wavelength. Different references are shown in different colours, healthy tissues are shown with circles and solid lines and diseased cases with squares and dashed lines. Full spectra can be found in [133–138]. If the values for the whole spectrum are given then only lines are shown. Otherwise the given values are indicated by the markers and connected via lines in order to show the approximate course over the whole range. Average tissue properties are summarised in Table 3.1 where no distinction is made between different diseased cases and all changes are summarised into one value. The table indicates a decrease in scattering during disease but this is not the case for all diseased cases as indicated in Table 3.2 and hence a no change in scattering due to inflammation is assumed later.

### 3.3.2 Effect of Inflammation

Effects of inflammation are an increased blood flow and water content in the tissue. The increased blood flow results in a higher haemoglobin concentration in the affected tissue and hence increased absorption coefficient. First, changes of the tissue structure are presented and then a list summarising literature reporting changes of optical properties during inflammation is given.

The middle ear mucosa of rats shows a doubled thickness in inflamed ears compared to healthy ones, changing from about 21 µm to 48 µm. The number of vessels showing a diameter bigger than 10 µm doubles in rats [118]. In contrast, Amelink et al. [145] report a constant vessel diameter of human oral mucosa during cancer. Matanda et al. [146] report a decreased distance of the centre

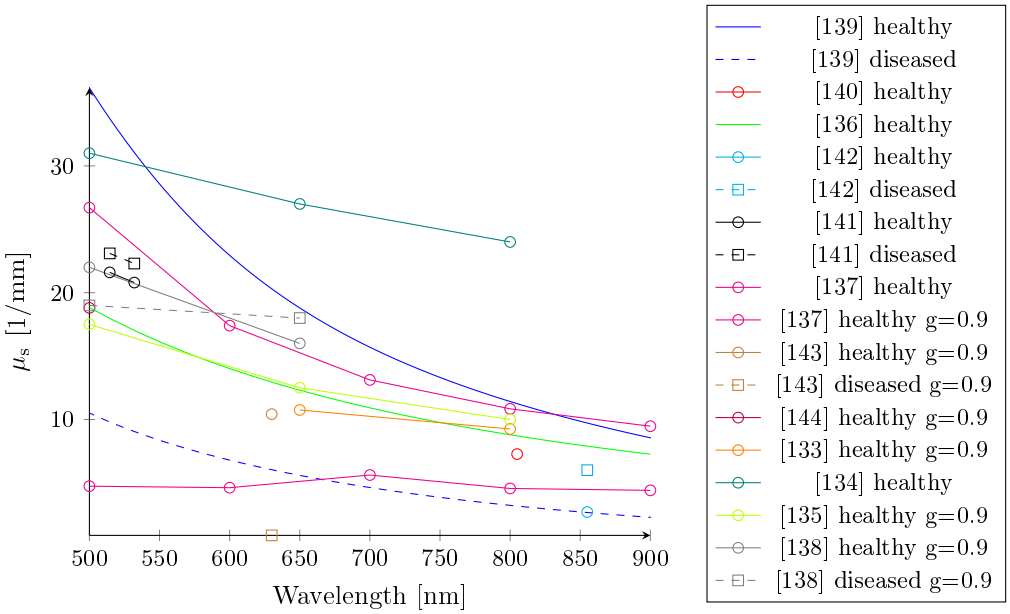


Figure 3.4: Scattering coefficient of mucosa reported in literature. For data labelled with "$g = 0.9$" the reduced scattering coefficient was given and $g$ of 0.9 assumed for calculation.

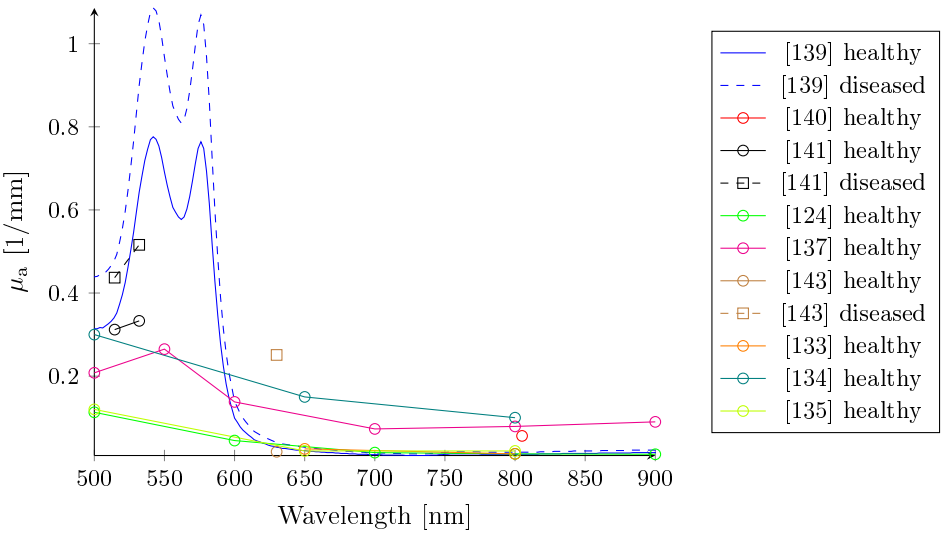


Figure 3.5: Absorption coefficient of mucosa reported in literature.

Table 3.1: Average optical properties of mucosa taken from literature partly presented Figure 3.4 and Figure 3.5. As not much data about changes during inflammation is available, data is also taken from other inflammatory diseases and summarised as 'diseased'.

| **Wavelength [nm]** | | **500** | **650** | **800** |
|---|---|---|---|---|
| **Reflectance** | healthy | 21.4 | 26.4 | 22.3 |
| **[%]** | diseased | 12.3 | 17.0 | - |
| **absorption** | healthy | 0.23 | - | 0.04 |
| **[1/mm]** | diseased | 0.44 | - | 0.02 |
| **scattering** | healthy | 24.8 | - | 11.7 |
| **[1/mm]** | diseased | 17.5 | - | 3.6 |

of the blood vessels to the surface of the mucosa in humans. In healthy ears the distances are 42±1 µm (mean±standard error) in the upper part of the middle ear and 61±2 µm in the lower middle ear compared to the distances of 22±1 and 45±1 µm in inflamed ears.

Table 3.2 summarises a list of literature reporting tissue parameter changes in diseased mucous tissues. A "+" indicates a increase in the parameter while a "–" indicates a decrease. Trends are reported for blood content $V_{\mathrm{Hb}}$, Oxygenation $Oxy$, absorption coefficient, and scattering coefficient. If not listed, the changes are true for the whole wavelength range (red and NIR). The investigated tissue type and disease are listed as well. Information is taken from literature either reporting the optical parameters directly or reporting parameters such has the blood concentration or reflectance. Full spectra of reflectance and absorption are reported in [30, 63, 65, 135, 137–139, 145, 147–151].

The table shows clearly that the blood level increases, as does the absorption coefficient. Literature is less clear on tissue oxygenation and scattering coefficient. Hence, the latter parameters are assumed to be unaffected by inflammation and only the blood content and thus absorption coefficient is changed. Additionally to these properties, [141] reports increased scattering anisotropy $g$ for tumours in the colon. A mathematical model used for simulations and design of optical tissue phantoms is presented later in Section 3.3.3.

### 3.3.3 Mathematical Model for Scattering and Absorption

Rowe et al. [139,153] use Monte Carlo methods to recover the optical and metabolic properties from *in vivo* reflectance measurements of human colon mucosa. The parameters of the MC simulations are varied within plausible pathological limits to fit the reflectance measurements. The optical parameters scattering coefficient, absorption coefficient, and scattering anisotropy are derived from the metabolic tissue parameters volume fraction of blood $V_{\mathrm{Hb}}$, haemoglobin saturation $\alpha$, mean size

Table 3.2: Influence of disease on metabolic parameters of mucous tissues. Blood Content – $V_{\mathrm{Hb}}$, Oxygenation – $Oxy$. No information given for empty fields, changes are true for listed wavelengths and if none is given they are true for the whole range of interest. *not directly stated but gathered from reported increase in blood content, **reduced reflection in diseased cases reported and hence increased absorption expected.

| Ref. | $V_{\mathbf{Hb}}$ | $Oxy$ | $\mu_{\mathbf{a}}$ | $\mu_{\mathbf{s}}$ | $\lambda$ [**nm**] | **Tissue** | **Diseased Case** |
|---|---|---|---|---|---|---|---|
| [145] | + | - | +* | | | oral | cancerous |
| [152] | | | - | - | | duodendal | pancreatic cancer |
| [124, 142] | | | | + | 855 | oral | cancerous |
| [141] | | | + | + | 500 | colon | tumour |
| [139, 153] | + | const. | + | - | | colon | cancer |
| [138] | | + | + | - | $< 600$ | colon | polyp |
| [138] | | + | + | + | $> 600$ | colon | polyp |
| [154] | + | + | +* | | | colon | inflammatory bowel disease |
| [69] | + | - | +* | | | colon | ulcerative colitis |
| [155] | + | - | +* | | | colon | ulcerative colitis |
| [65] | + | - | +* | | | gum | gingivitis, periodontitis |
| [79] | | - | | | | pulp | inflammation |
| [143] | | | + | - | 630 | bowel & Peritoneum | tumor |
| [63] | | | +** | | | oral | cancerous |
| [15] | + | | +* | | | general | inflammation |
| [72] | | - | | | | gum | gingivitis, periodontitis |
| [149] | | | +** | | | oral | carcinoma |
| [118] | + | | | | | middle ear (rat) | inflamed |
| [113] | + | - | +* | | | gingiva | inflamed |

of scattering particles $d_s$, mean volume fraction of scattering particles $V_s$, according to [139,156–158]

$$\mu_a(\lambda) = \frac{V_{Hb}\ln(10)c_{Hb}\cdot(\alpha\epsilon_{HbO2}(\lambda)+(1-\alpha)\epsilon_{Hb}(\lambda))}{64500[g/mol]} \quad (3.10)$$

$$\mu_s(\lambda) = \rho_s(\lambda)\sigma_s \quad (3.11)$$

where $\epsilon_{HbO2}$ is the molar extinction of oxyhaemoglobin, $\epsilon_{Hb}$ the molar extinction of haemoglobin (data available from [156]), $c_{Hb} = 120\,\mathrm{g/l}$ the concentration of haemoglobin per litre of blood, $\sigma_s$ the density of scattering centres, and $\rho_s$ is the scattering cross section. The density of scattering centres is given determined by the volume fraction of scattering particles as follows

$$\sigma_s = V_s\frac{1}{4/3r^3\pi} \quad (3.12)$$

The scattering cross section is calculated by Mie theory (codes available online [159] or for MATLAB [160]). Inputs to the code are the relative reflective index between particle $n_p$ and medium $n_m$ given by $n_{rel} = \frac{n_p}{n_m}$ and the size parameter given by $x = \frac{2\pi d_s/2}{\lambda/n_m}$, where $d_s$ is the mean diameter of the scattering particles. The scattering efficiency $Q_s$ as output of the Mie calculation is then used to determine the scattering cross section as follows [161]

$$\rho_s = Q_s\pi(d_s/2)^2 \quad (3.13)$$

The tissue model in the MC is composed of three layers: mucosa, submucosa, and underlying muscle tissue. The optical measurement geometry is simulated as well as it is affecting whether photons are detected or not. The blood volume concentration in mucosa varies from 2 to 10 % while the variation is 5 to 20 % in submucosa. The oxygenation varies from 50 to 75 %. The thickness of the mucosa is 400 to 600 µm and that of the submucosa 400 to 850 µm [139, 153].

Zonios et al. [138] uses a similar approach to determine the attenuation coefficients by metabolic parameters but uses the diffusion approximation instead of MC methods to determine the optical parameters. Yudovsky et al. [158] uses a similar model to determine the absorption and scattering coefficient for skin in MC simulations. They introduce background absorption of tissue while the previous references only using blood as absorber. Further, the scattering coefficient is approximated by a power law as introduced in Section 3.2.2 instead of using Mie Theory.

### 3.3.4 Final Model for the Optical Properties

The average properties of mucosa found in literature are listed in Table 3.1. Only few values were given for the diseased cases so these values are less reliable. While these values give the optical properties for single wavelengths, the model of [139] presented in the previous section gives the ability to simulate the complete spectrum in the visible and NIR range. But as the properties

calculated by the mathematical model vary from the average values in literature, the model is scaled to fit the average values.

A linear scaling is chosen and the offset can be seen as background absorption caused by water (spectrum given by [162]) or other tissue absorbers. This choice is supported by [158] using a tissue background absorption in their model. The scaling coefficients are set so that the model fits the average literature values at 500 and 800 nm.

$$\mu_{\mathrm{a,scaled}} = 0.62 \cdot \mu_{\mathrm{a,original}} + 0.03 \tag{3.14}$$

$$\mu_{\mathrm{s,scaled}} = 0.53 \cdot \mu_{\mathrm{s,original}} + 5.57 \tag{3.15}$$

The oxygenation and scattering are held constant in the inflamed case as literature was not consistent about this change as seen in Table 3.2. The blood volume fraction on the other hand is consistently reported to increase with disease. A maximum change of 2 % in healthy to 20 % in the inflamed case is assumed. These values are taken from [153] reporting 2-10 % in mucosa and 5-20 % in submucosa. As both layers will be sampled, the maximum range is used for the model.

This model is used later to determine properties for the construction tissue phantoms and to simulate the optical system using Monte-Carlo models in order to determine best wavelengths to detect inflammation.

## 3.4 Optical Properties of the Eardrum

This section first presents the optical properties of the eardrum reported in literature and then experiments are conducted to characterise the transmission through eardrum samples.

### 3.4.1 Properties Reported in Literature

Figure 3.6 shows the reflection spectra of a frozen cadaveric eardrum and three eardrums of living persons taken from [163]. As light penetrates through the eardrum the spectra does not only result from the eardrum but also from reflections from the middle ear cavity (left graph, plot 1 and 2). To investigate the influence of the middle ear on the spectrum, the tympanic cavity of cadaveric ears was dyed with black ink to decrease its reflection to zero (left graph, plot 3 and 4). The measurements show a decrease of the reflected intensity but a similar course especially between 400 and 600 nm. The spectra show characteristics of the haemoglobin spectrum indicated the presence of blood in the eardrum.

MacDougall et al. [164] present a model for the absorption in the human eardrum. A scattering coefficient of 22 $\mathrm{mm}^{-1}$ is given for 1310 nm. This value is derived from optical properties of dermis [165] but not directly derived from measurement on the eardrum. From this value and an assumed

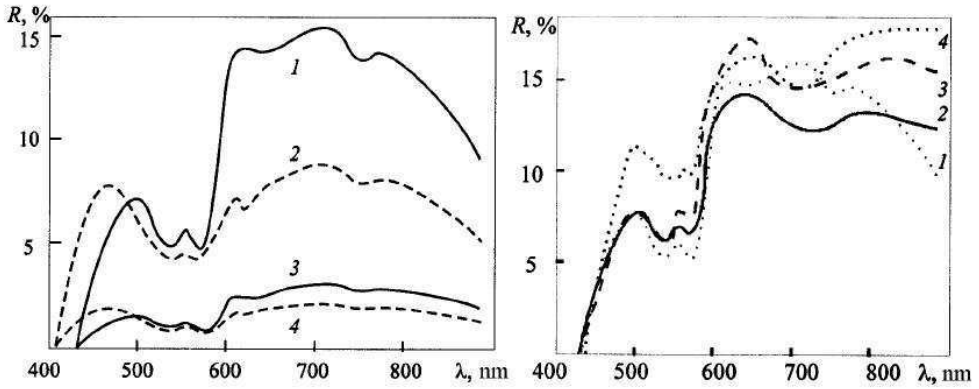


Figure 3.6: Diffuse reflection spectrum of the eardrum [163].
Left: 1) eardrum and middle ear of frozen cadaveric specimen, 2) eardrum and middle ear of cadaveric specimen kept in stabilizing solution, 3) eardrum of frozen cadaveric specimen alone, 4) eardrum of specimen kept in stabilizing solution alone.
Right: 1) eardrum and middle ear of frozen cadaveric specimen, 2)–4) eardrum and middle ear of living volunteers.

thickness of the eardrum of 100 µm the transmission of ballistic photons is calculated to be 11 %. A double pass would result in 1.2 % transmitted light, equal to a 19 dB loss. Measurements with an OCT systems show a 13.5 dB loss, equivalent to 21 % unscattered light on a single pass. Hence the actual scattering coefficient is smaller than 22 $mm^{-1}$. Absorption is neglected in this model. The reflection from an eardrum were measured to be 11.6 % [165].

### 3.4.2 Effect of Inflammation on the Eardrum

Middle ear inflammation can influence the thickness of the eardrum, which will influence the transmission and measurements. Cho et al. [41] report an average thickness of healthy eardrums of 122 µm, OME eardrums of 108 µm, chronic OM eardrums of 326 µm, and adhesive OM eardrums of 251 µm. Other groups report the attachment of biofilms to the OME eardrum [45]. The thickness of rat eardrums increases 2 fold during AOM [166].

While the eardrum thickness can increase during certain cases of OM, it does not increase during OME. Only a biofilm gets attached to the eardrum. This biofilm should be mostly removed during clearing of the tympanic cavity and hence not decrease the transmission significantly.

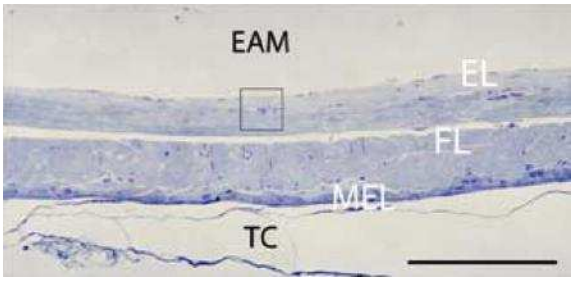


Figure 3.7: Light micrograph of a histological sample of an human eardrum [168]; EAM – external acoustic meatus/outer ear canal, EL – epidermal layer, FL – fibrous layer, MEL – mucosal epithelial layer, and TC – tympanic cavity; the capillary indicated by the box is located between EL and FL; scale bar corresponds to 100 µm.

### 3.4.3 Animal Eardrum Model

As the literature does only report little optical properties of eardrums (and the only reference reporting scattering properties of the eardrum [164] was published in 2015), experiments are conducted in order to determine the optical properties. As human eardrums are not accessible, animal eardrums are characterized. To allow a transfer of the measurements to the human eardrum, thickness and other parameters are compared first. The surface area of mammalian eardrums does not differ a lot despite the huge size difference of the individual species [4]. The structure of the eardrums is also similar, the only remarkable differences between eardrums of different mammal species is their thickness and number of fibre layers.

The human eardrum shows a thickness of 50 to 70 µm in the thinnest central region, with increasing thickness towards the malleus and annulus, and around 100 µm average thickness [5]. The human eardrum shows a radial and a circumferential fibre layer. The cross section of the human eardrum is shown as a histological sample in Figure 3.7. The eardrum consists of an epidermal layer, showing several cell layers, the radial collagen fibre layer, circumferential fibre layer, and finally a few call layers thick mucosal layer on the inside facing the tympanic cavity [167].

Figure 3.8 shows the surface of a human eardrum recorded with a scanning electron microscope when seen from the middle ear [169]. Both fibre layers are clearly visible. [170] reports a diameter of the radial fibres around 22 µm and 12 µm for the circumferential fibres. [171] on the other hand reports an average diameter of 8 µm.

Several animal eardrums have been investigated. For example the guinea pig eardrum shows similar colour and shape as the human one but is thinner and shows little collagen fibres resulting in a higher transparency [172]. Table 3.3 summarised the structure of human and animal eardrums for easy comparison.

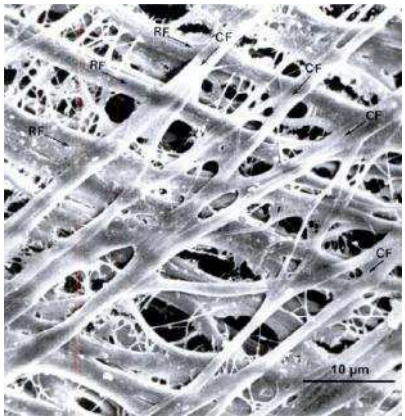


Figure 3.8: Scanning Electron Microscope image of the human eardrum seen from the middle ear [169]. Radial fibres (RF) and circular fibres (CF) are visible.

Table 3.3: Comparison of human and animal eardrums.

| | **Thickness [µm]** | **Fibres & Diameter** | **Other layers** |
|---|---|---|---|
| **Human** | 50–70 in thinnest area, 100 average [5] | radial (22 µm) and circumferential (12 µm) [170] | several cells of epidermal externally, and few cells of mucosal layer internally [167] |
| **Guinea Pig** | 10–20 [Appendix A], 10 according to [173] | circular scarcely encountered, except near annulus [172]; circular ∼2 µm, oblique fibres 0.8–1.2 µm, radial 3–4 µm [174]; radial fibres (8 µm) seen everywhere, scarcely circumferential fibres | 1 layer of epithelium internally and externally [175] |
| **Gerbil** | 7 in central region, 20 near manbrium, 35 near annulus [176] | densely packed collagen fibres, strictly arranged radial and circular [177], [178]; ∼5 µm [Appendix A] | |
| **Chinchilla** | | one fibre layer visible [171] | |
| **Cat** | 30–50 [173] | radial (16 µm) and circumferential (8 µm) [171, 179] | epidermal and mucosal layer [179] |
| **Pig** | 80 [165] | anatomy similar to human [165] | |
| **Sheep** | | no fibres [180] | |

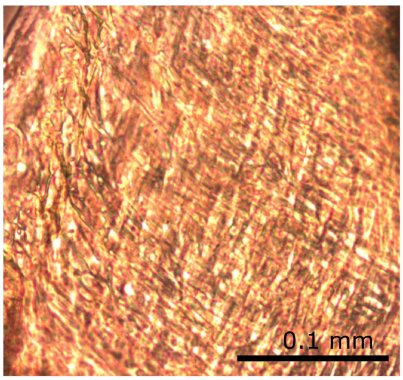


Figure 3.9: Microscope image of a gerbil eardrum with two fibre layers visible.

Pig would make a good animal model as the eardrum shows similar thickness to the human one and the anatomy is very similar [165]. Further, pig heads can be acquired from a local butcher. This was done but we were not able to dissect an eardrum sample as dissection is not trivial due to the deep placement of the eardrum inside the skull.

Gerbil middle ears were provided in frozen state by Sameer Mallick (University of Sheffield). Animals were treated and killed according to their procedures and only middle ears of dead animals used here.For imaging, the eardrums were thawed, the eardrum dissected and placed on a microscope slide, suspended in saline solution to avoid drying, covered with a cover-glass, and imaged. Figure 3.9 shows a microscope image of a gerbil eardrum recorded with a wide-field microscope at 10 times magnification. Two orthogonal fibre layer structures are visible. These fibres are densely packed and smaller than in human. We were only able to dissect small useful samples and hence experiments were not easy to conduct.

Stored guinea pig eardrums were provided by Emma Hoskinson and Mike Milheran (University of Leicester) and a recently killed guinea pig eardrum was provided by Mark Wallace and Adam Palmer (MRC IHR, University of Nottingham). In all cases animals were treated and killed according to the procedures of the respective institutes and only middle ears of dead animals used.

Guinea pig eardrums were acquired in either frozen state, suspended in formaldehyde, or freshly dissected from a just killed animal. Figure 3.10 shows a photograph of an eardrum stored in a frozen state and thawed still attached to the annulus and middle ear. The eardrum is visible as round area with the malleus in the middle. It is surrounded by the bony annulus and shows a puncture above the malleus. The Eustachian tube is visible through the eardrum as dark shadow. During dissecting the eardrum was cut loose from the annulus, placed on a microscope slide, suspended in saline solution, and covered by a cover slip to prevent drying.

Figure 3.11 shows widefield images of a guinea pig eardrums, a single layer left, and two stacked

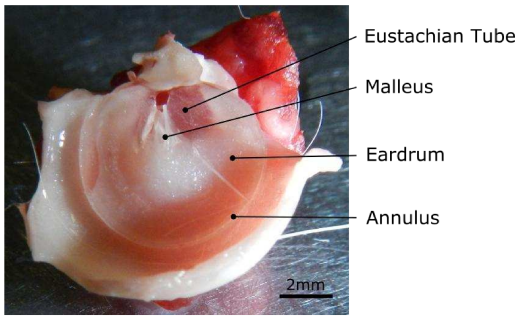


Figure 3.10: Photograph of a guinea pig eardrum still attached to the annulus and middle ear. The diameter of the eardrum is around 6 to 7 mm.

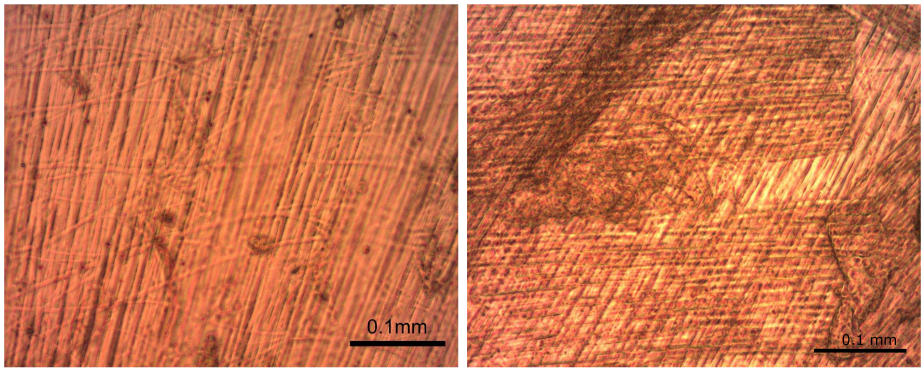


(a) Single layer (b) Double layer

Figure 3.11: Microscope images of guinea pig eardrums.

layers on the right. The prevalent radial fibre structure is visible in subfigure (a) and scarce circular fibres are also observed. The fibre diameter is around 8 µm. As this is not a good model for the human eardrum showing two fibre layers, two guinea eardrum sections are placed on top of each other with orthogonal fibre orientation as shown in subfigure (b). Histological images of a guinea pig eardrum and middle ear are presented in Appendix A for more detailed analysis.

The gerbil eardrum structure resembles the human eardrum structure more closely than the guinea pig, but is much thinner. Also, samples are not easy to dissect, bigger samples of the guinea pig eardrums were easier to dissect. Further, the guinea pig eardrum is thicker and the double layer can be achieved by placing two eardrums on top of each other. In this way, also the thickness is closer to the thickness expected in a human eardrum. Hence, the double layered guinea pig eardrum will be used as model for the human eardrum. The transmission through this model will be measured in the following section.

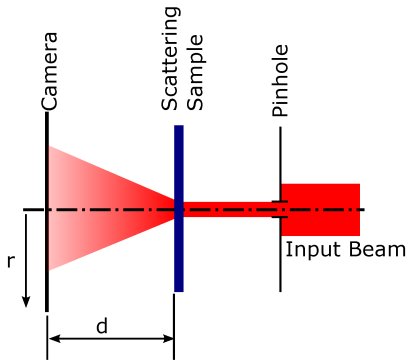


Figure 3.12: Experimental set-up used to characterise the transmission of the eardrum and other samples.

### 3.4.4 Measurement of the Transmission

This section describes the characterisation of the animal eardrum model in order to determine its transmission characteristics. First, the experimental set-up is described, then the system calibrated on a sample with known characteristics, the eardrum characterised, and finally a model derived.

#### Experimental Set-up

The experimental set-up for transmission characterisation is shown in Figure 3.12. A collimated light beam of 200 µm diameter is directed on the sample and a camera (PL-B955U, PixeLink, Ottawa, Ontario, Canada) placed behind the sample to record the transmitted light. A reference measurement is taken with a microscope slide in place to characterise the input beam and make the measurements independent of the reflections from the surface.

The camera records light scattered in an angular range of $\arctan(r/d) = \pm 6.6\,^\circ$ with the distance $d$ between the camera and the scattering layer and $r$ the maximum possible radius on the detector area. This means, strongly scattered light ($\alpha > 6.6\,^\circ$) is not detected, for this a larger detector would be necessary. Possible set-ups for improved measurements would be the use of integrating sphere in order to detect all signals without spatial distribution as in [141] or spatial scanning of the detector as done in [181] in order to cover a bigger area and measure total transmission and reflection. But as measurements in the ear are restricted to a NA of 0.08 corresponding to an angle of 4.6 °, a complete characterisation is not necessary. Further, the scattering of the eardrum is very forward directed and most light is detected with the current setup.

The recorded camera images are analysed using MATLAB. The input power is defined as the sum over all pixels in the reference image with no scattering sample in place. The central portion of unscattered light is defined as the area illuminated by the reference beam with power more than

$\frac{1}{e^2}$ of the maximum. The relation of input power to the sum over all pixels approximates the total transmission of the sample (neglecting widely scattered light) and the power in the central portion divided by the input power approximates the unscattered transmission.

$$T_{\text{total}} = \frac{\sum_{\text{all}} I_{\text{sample}}}{\sum_{\text{all}} I_{\text{ref}}} \tag{3.16}$$

$$T_{\text{unscattered}} = \frac{\sum_{\text{central}} I_{\text{sample}}}{\sum_{\text{central}} I_{\text{ref}}} \tag{3.17}$$

Three lasers are used for illumination, one with 532 nm (BWN-532-30, B&W Tek, Newark, DE, USA), the second at 632 nm, and the third at 808 nm (L808P010, Thorlabs, Newton, New Jersey, USA, controlled by the power and temperature controller kit LTC100-B LD, Thorlabs, Newton, New Jersey, USA) to allow measurements of the transmission characteristics in dependence of the wavelength in the visible and NIR.

### Influence of Storage

In a first version of this experiment a white light source was used for illumination and a RGB camera (DCC1645C, Thorlabs, Newton, New Jersey, USA) used as detector. As the light is not collimated a wider pinhole was necessary to allow enough light to pass through the system. This measurement allowed the easy measurement of three wavelength ranges (red, green, and blue) but no accurate measurement of the unscattered light due to the large beam diameter.

The transmission through eardrum samples stored in frozen state, preserved in formaldehyde, and one just killed guinea pig is measured. The fresh sample shows a total transmission of 72 % in the red, 70 % in green, and 66 % in the blue region. When converting the RGB colour map into LUV and using the lightness a transmission value of 67 % is measured. The lightness transmission value of a frozen sample is measured to be 58 % and the transmission of three samples stored in formaldehyde are 15, 41, and 36 %.

This shows a wavelength dependent attenuation with higher wavelengths being less attenuated. It further shows less attenuation of the fresh sample, with the frozen following, and lowest transmission of the formaldehyde samples. When using stored samples for further experiments, the attenuation will be higher than for *in vivo* eardrums. All further experiments are conducted on eardrums stored in formaldehyde.

### Calibration

The transmission of a 1500 grid ground glass diffuser (DG20-1500, Thorlabs, Newton, New Jersey, USA) with known scattering characteristics is measured in order to test and calibrate the system. The transmission pattern recorded by the camera is shown in Figure 3.13 (a) with the white

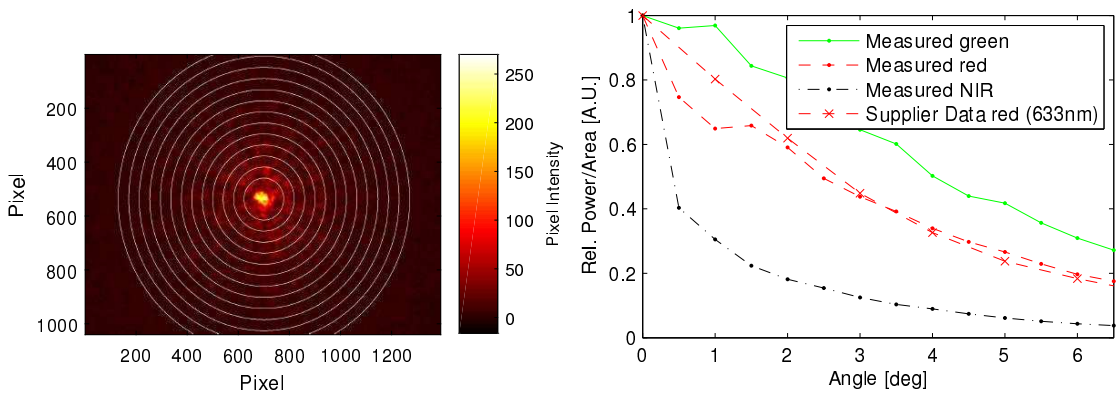


(a) Power distribution on the camera (NIR)

(b) Radial power distribution

Figure 3.13: Transmission calibration using diffuser with known scattering characteristics

circles marking steps of 0.5 deg scattering angle $\alpha$ from the central spot, calculated by distance between scattering layer and detector surface $d$ and distance from the edge of the unscattered beam $r$ according to $\alpha = \arctan\left(\frac{r}{d}\right)$. Subfigure (b) shows the power divided by area for each angle measured at 3 different wavelengths, 532 nm (green), 632 nm (red), and 808 nm (NIR). The reference data is shown as red, dotted line and taken from the supplier data sheet [182], measured at 633 nm.

The central unscattered beam has a diameter of 0.2 mm and is not an ideal point source. This means light with a small scattering angle is still detected within the central spot and registered as unscattered light. To account for this, the central power (0 deg) is scaled and the power added to 0.5 and 1 deg scattering angle resulting in the scaling

$$P(0\,\text{deg}) = P(0\,\text{deg}) \cdot 0.85 \tag{3.18}$$

$$P(1\,\text{deg}) = P(1\,\text{deg}) + P(0\,\text{deg}) \cdot 0.11 \tag{3.19}$$

$$P(2\,\text{deg}) = P(2\,\text{deg}) + P(0\,\text{deg}) \cdot 0.04 \tag{3.20}$$

This scaling results in the good accordance of measurement and supplier data shown in Figure 3.13 (b) and is used for all further measurements.

### Results

The transmission through a single layer guinea pig eardrum and two orthogonally stacked layers are measured and the transmission pattern are shown in Figure 3.14. A speckle pattern is visible as the small collimated laser beam and scattering particle in the eardrum cause interference of the transmitted light. Main scattering directions are visible as a result of the light being mostly

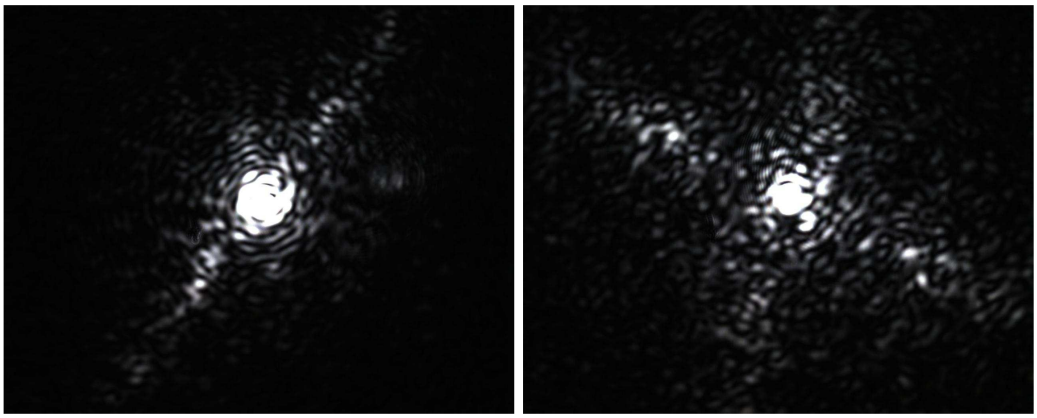

(a) Single layer (b) Two orthogonal layers

Figure 3.14: Transmission pattern through guinea pig eardrum samples. Speckle pattern and main scattering directions are visible.

scattered at the collagen fibres in the eardrum as explained previously in Section 3.2.3. The collagen fibres act as a grating and diffraction profiles can be seen when illuminating with a beam of larger diameter.

The radial power distribution for both cases is shown in Figure 3.15, independent of the scattering direction as the optical system is symmetric around the optical axis. The blue dotted curve shows the power of the unscattered reference beam while the measurement of the eardrum is shown in black. 5 measurements at different positions are taken, with the mean shown here and the standard deviation indicated by the errorbars. The used wavelength is 808 nm. Light is more scattered by the double layered model (TM 2x) than by the single model (TM 1x) indicated by the lower power in in the centre and higher power at higher scattering angles. The total detected power on the camera is 80 % for the single and 73 % for the double eardrum. This shows that the scattering does not scale linearly with thickness. This is due to the fact that scattering mostly results from the fibre structure and surface roughness of the eardrum which does not have the same effect on a second layer.

Next, the wavelength dependent scattering is analysed using transmission measurements at 532, 632, and 808 nm through a single eardrum. As Figure 3.16 shows, scattering is lowest for 808 nm and highest for 532 nm. The transmitted light at 808 and 633 nm is similar at wider angles but the NIR shows higher unscattered transmission indicated by higher power at 0 and 0.5 ° scattering angle. The transmitted intensity at 532 nm is lower in all regions. This is in accordance with theory describing wavelength dependent scattering by a power function $\mu_s = a\lambda^{-b}$ resulting in the scattering coefficient decreasing with wavelength.

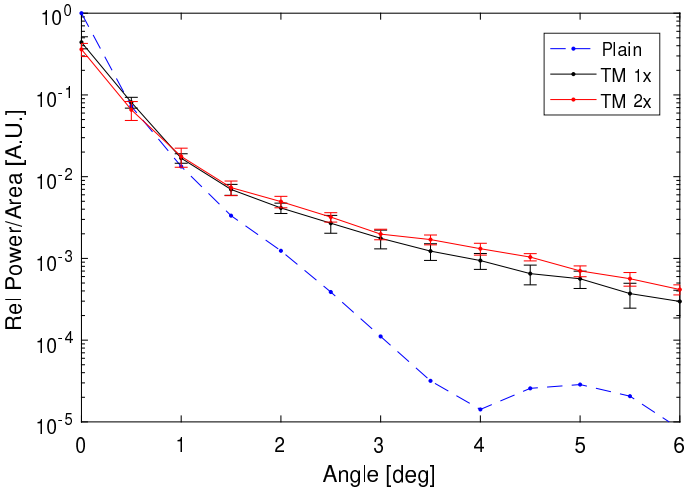


Figure 3.15: Angular power distribution of direct illumination (plain) and transmission through a single (TM 1x) and two layer (TM 2x) eardrum measured at 808 nm.

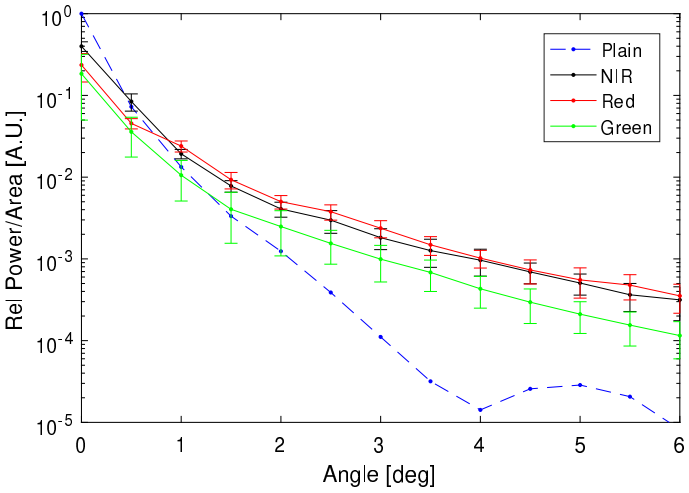


Figure 3.16: Wavelength dependent transmission through a single layer eardrum measured at 532 (green), 632 (red), and 808 nm (NIR).

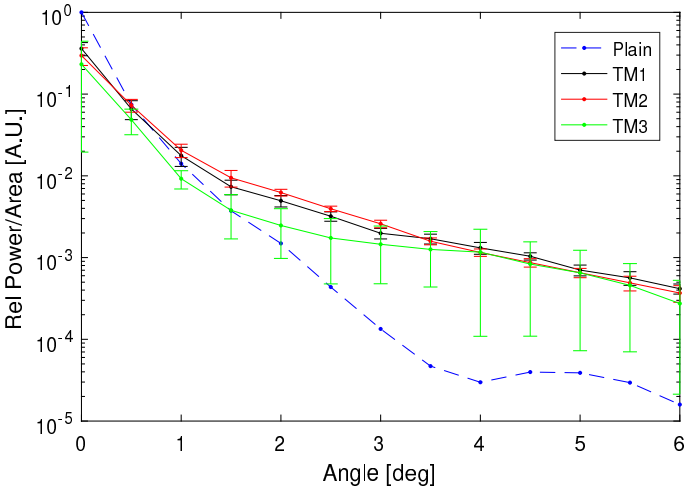


Figure 3.17: Transmission through three different double eardrum samples measured at 808 nm.

Figure 3.17 compares the transmission measurement of 3 different guinea pig eardrums stored in formaldehyde, measured at 808 nm with two stacked eardrum layers, identified earlier as best model for the human eardrum. All samples show similar results at larger scattering angles, with sample 3 showing lower direct transmission. In overall the transmission of all three eardrums is similar and variations between different eardrums are close to variations between different positions of a single eardrum, indicated by the errorbars of each plot.

### 3.4.5 Simulation Model

In order to allow simulation of the middle ear system and to derive optical properties of the eardrum, a computer model was varied to match the scattering characteristics. The experimental geometry was simulated and the scattering in the eardrum simulated using Monte Carlo Models (presented later in Section 5.3). The scattering coefficient, scattering anisotropy, and absorption coefficient are varied to match the angular distribution of simulation and measurements on the double layered guinea pig eardrum. The direction dependent scattering of the eardrums is not considered in this simulation model or later in the construction of the eardrum phantoms as the optical system is symmetrical about the optical axis and hence only the deflection angle from the optical axis is important.

Simulated distributions are shown in Figure 3.19 and Figure 3.18 where first the scattering anisotropy and then the scattering coefficient is varied. A low scattering anisotropy results in high scattering angles and the light scattered outside the camera area, shown by the fast decay of the power distribution in Figure 3.18. A anisotropy factor of 0.99 fits the measurements best. This high anisotropy is a result of the large dimension of the fibres compared to the wavelength

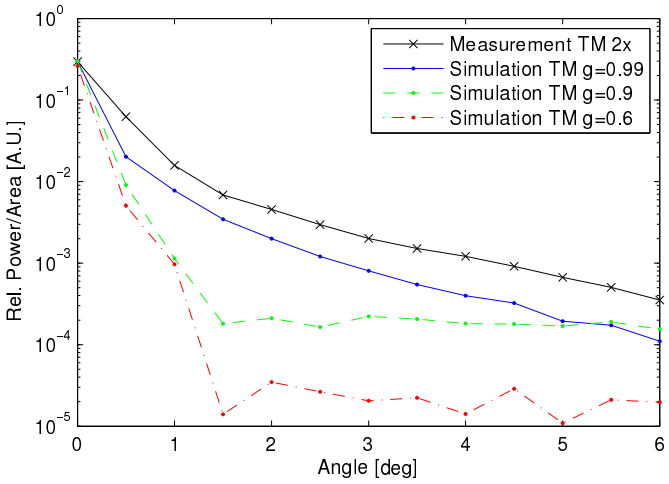


Figure 3.18: Simulated transmission with varied scattering anisotropy.

resulting in strong forward scattering as explained earlier in Section 3.2.2. An increasing scattering coefficient decreases the unscattered light portion and causes more light being scattered away from the optical axis. A coefficient of $11\,\mathrm{mm}^{-1}$ is selected here and the absorption coefficient of $1.8\,\mathrm{mm}^{-1}$ is found. As this model is only an approximation, the properties of the eardrum are later varied in simulations in order to account for an inaccurate model and changes between different eardrums.

## 3.5 Design of the Middle Ear Phantom

There are many different approaches to create tissue phantoms, an overview is given in [183]. Epoxy resin based tissue phantoms are used here for the mucosa, for two reasons. First, the phantoms are solid and show stable properties over years, and second a recipe is available from the Biomedical Optics Research Laboratory, UCL, published in [30,31]. Different options are investigated for the eardrum phantom, but all show stable characteristics as well.

### 3.5.1 Mucosa - One Wavelength

The first set of phantoms is produced at and with help of the Biomedical Optics Research Laboratory, UCL and matches the optical properties of mucosa at 650 nm only as at this stage of the project only one red laser was used. A second set of phantoms matching the optical properties of mucosa at 808 and 532 nm is produced in Nottingham, and based on the recipe provided by the Biomedical Optics Research Laboratory, UCL.

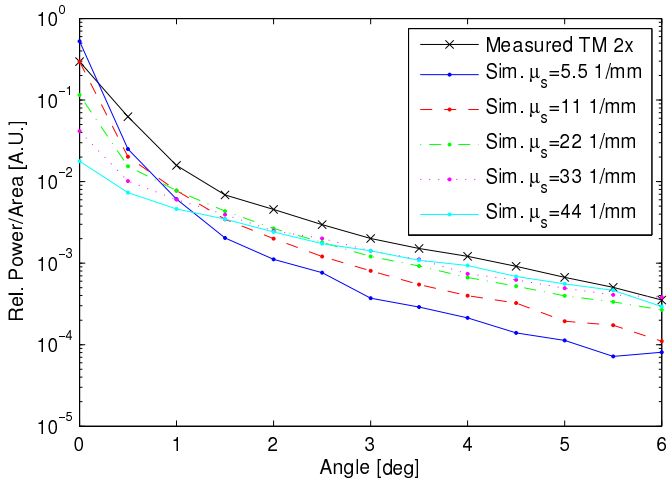


Figure 3.19: Simulated transmission with varied scattering coefficient.

**Recipe**

The recipe was provided by the Biomedical Optics Research Laboratory, UCL. The base material is the clear polyester casting resin (405-210, Tiranti Ltd., Thatcham, UK) which is mixed in a relation of 99:1 (in weight) with the Liquid Hardener (405-810, Tiranti Ltd. Thatcham, UK). Superwhite ($TiO_2$ particle based white colour; 407-220, Tiranti Ltd. Thatcham, UK) is used as scattering agent and the dye Pro Jet 900 NP (in solution with the epoxy resin MY753, Ciba-Geigy Ltd., Switzerland, to give absorption coefficient of $20.5\,\mathrm{mm}^{-1}$ at 800 nm [184]) as absorbing agent. The required weight of dye and scattering agent is calculated by the desired phantom volume and the density of the resin of $1.15\,\mathrm{g/cm}^3$.

The required weight of dye $m_{\mathrm{dye}}$ (in grams) is given by the absorption coefficient $\mu_{\mathrm{a}}$ as follows

$$m_{\mathrm{dye}} = \frac{\mu_{\mathrm{a}} - \mu_{\mathrm{a,resin}}}{\mu_{\mathrm{a,dye}}} \cdot \frac{m_{\mathrm{total}}}{1000} \cdot \frac{1}{c_{\lambda,\mathrm{a}}} = \frac{\mu_{\mathrm{a}} - 0.001}{0.0205} \cdot \frac{m_{\mathrm{total}}}{1000} \cdot \frac{1}{0.36} \tag{3.21}$$

with absorption coefficient of the pure resin $\mu_{\mathrm{a,resin}} = 0.001\,\mathrm{mm}^{-1}$, absorption coefficient of the dye mixture $\mu_{\mathrm{a,dye}} = 0.0205\,\mathrm{mm}^{-1}$ at 800 nm, total mass of the mixture $m_{\mathrm{total}} = m_{\mathrm{resin}} + m_{\mathrm{hardener}}$ in grams, and the lambda factor $c_{\lambda,\mathrm{a}}$ accounting for the wavelength dependent absorption of the dye and the recipe being characterised for 800 nm. The absorption coefficient at 650 nm is 0.36 of the value at 800 nm, resulting in $c_{\lambda,\mathrm{a}}(650) = 0.36$.

The required weight of scattering agent $m_{\mathrm{scattering}}$ is given by a very similar formula

$$m_{\mathrm{scattering}} = \frac{\mu'_{\mathrm{s}}}{\mu'_{\mathrm{s,SW}}} \cdot \frac{m_{\mathrm{total}}}{1000} \cdot \frac{1}{c_{\lambda,\mathrm{s}}} = \frac{\mu_{\mathrm{a}}}{0.8} \cdot \frac{m_{\mathrm{total}}}{1000} \cdot \frac{1}{1} \tag{3.22}$$

where $\mu'_{\mathrm{s}}$ is the desired reduced scattering coefficient in $\mathrm{mm}^{-1}$, $\mu'_{\mathrm{s,SW}} = 0.8\,\mathrm{mm}^{-1}$ is the reduced scattering coefficient of the superwhite scattering agent. The lambda factor $c_{\lambda,\mathrm{s}} = 1$ is used here

Table 3.4: Desired optical coefficients and required concentration of scattering and absorbing agent for the one-wavelength mucosa phantoms at 650 nm.

| Phantom | $\mu_s'$ [mm$^{-1}$] | $c_{\text{scattering}}$ [g/kg] | $\mu_a$ [mm$^{-1}$] | $c_{\text{dye}}$ [g/kg] |
|---|---|---|---|---|
| 1 - Healthy | 1.341 | 1.675 | 0.061 | 8.130 |
| 2 - Intermediate | 1.341 | 1.675 | 0.1 | 13.415 |
| 3 - Intermediate | 1.341 | 1.675 | 0.18 | 24.255 |
| 4 - Diseased | 1.341 | 1.675 | 0.264 | 35.637 |

even though a factor of about 1.34 would be correct [185]. This is corrected in the next set of phantoms. The designed optical properties are accurate to 5-10 %, depending on the accuracy of the measured weights of the ingredients. The $g$ factor of the scattering agent is 0.5 to 0.7 [185].

Four phantoms are produced; one simulating healthy mucosa, another one simulating inflamed mucosa, and two intermediate ones. The properties and calculated concentrations are given in Table 3.4. According to Monte Carlo Simulations this results in a total reflectance of 39.6, 32, 23.4, and 20 % for the four phantoms.

### Production Process

In the first step an excess amount of the resin is poured in a container by weight, the scattering agent added, also measured by weight, and the whole resin stirred manually until the mixture is homogeneous by eye inspection. A quarter of this mixture is then poured into a second container and the absorbing agent added. An excess amount of the initial mixture is necessary as not all of the mixture can be scraped out of the containers when poured into the second container. The mass of each individual phantom mixture is measured and the required amount of dye added. Again, the mixture is stirred by hand and finally the hardener added, the mixture stirred again, and poured into the mould. In this way four different phantoms with the same scattering coefficient but different absorbing coefficients are produced. The phantoms are left at normal room temperature to harden for 2 days before extracting from the mould and machining into the final shape. Tupperware boxes are used as containers and the phantom can easily be removed from the mould and the mould be reused.

Machining is necessary for three reasons, firstly to achieve a diffuse scattering surface instead of a specular one as is the case after casting without any further processing. Secondly, there is a low concentration of particles at the surface of the phantom. When removing the top layer this low concentration is removed and a cut through some of the particles is done. This results in more homogeneous properties of the phantom. Third, flat surfaces are needed for a defined orientation

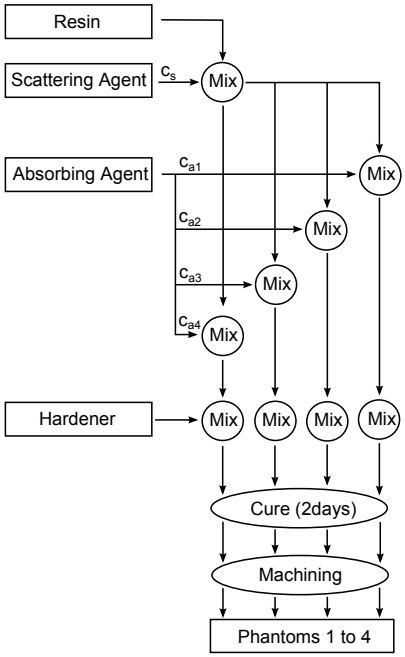


Figure 3.20: Production process for the four mucosa phantoms with same scattering and different absorption coefficients. $c_\mathrm{s}$ is the concentration of scatterer and $c_{\mathrm{a}1}$–$c_{\mathrm{a}4}$ the four different concentrations of absorbing agent.

of the phantom towards the sampling beam. This is not given without machining as the mould is not rectangular.

Figure 3.21 shows the 4 phantoms after curing and machining. All phantoms are grey as they match the optical properties of tissue at 650 nm only and otherwise exhibit the spectrum of the used dye. But a difference in the grey level of the phantoms is visible, according to the absorber concentration. The absorber concentration increases from phantom 1 to 4.

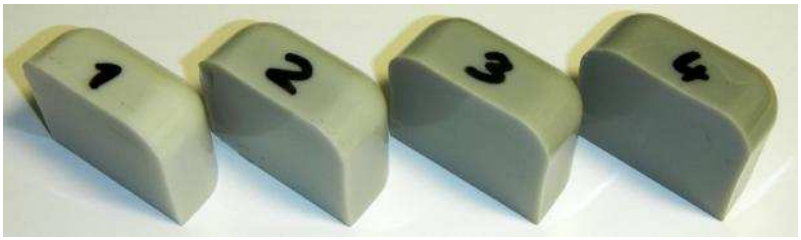


Figure 3.21: Photograph of the cured and machined phantoms.

Table 3.5: Surface roughness of the mucosa phantoms

| | $R_a$ [A.U.] | | | |
|---|---|---|---|---|
| **Surface** | **Phantom 1** | **Phantom 2** | **Phantom 3** | **Phantom 4** |
| machined | 1.91 | 2.04 | 3.57 | 4.62 |
| polished | 1.41 | 0.94 | 1.90 | 1.70 |

**Surface Characterisation and Polishing**

The surface of the phantoms is characterised using a confocal microscope (TCS SP2, Leica, Wetzlar, Germany) in reflection mode and probing wavelength of 488 nm and 10× objective. A z-stack of the surface is taken with 512×512×50 pixel resolution corresponding to a volume of 1.5×1.5×0.104 mm. Vignetting of the image is visible, thus the 100 outer pixel are removed resulting in images of 312 × 312 pixel. These images are then processed in ImageJ (Wayne Rasband, National Institutes of Health, Public Domain program, `imagej.nih.gov/ij/`) as presented in a note by the Otago Centre for Confocal Microscopy [186].

The plug-in "Extended Depth of Field" (available from [187] and described in [188]; Settings 'Expert mode' with standard parameters and 'denoising' in post processing) is used to create a height map and completely focused composite image of the stack. The composite images are displayed in Figure 3.22 (a) to (d) for phantoms 1 to 4. In the next step the surface characteristics are calculated using the plug-in "SurfCharJ" (available from [189] and reported in [190]). The surface roughness is then characterised by the arithmetic average $R_a$ of the deviation of the surface to the mean surface given by

$$R_a = \frac{1}{n}\sum_{i=1}^{n} |y_i - y_{mean}| \tag{3.23}$$

where $n$ is the number of measured points, $y_i$ the current surface height, and $y_{mean}$ the average surface height. All standard parameters of the plug-in are used, except for levelling the surface. The surface roughness values $R_a$ given in Table 3.5 quantify the roughness of the surface visualised in the images.

As the surface of the phantoms show different roughness, one surface of the phantoms is polished and the surface recorded again. Polishing was done on the wheel polishing machine "LabPol 21" (Struers, Catcliffe, UK) in two steps, first a wet 4000 grit grinding (Microcut, Silicone Carbite, P4000, Buehler, Lake Bluff, IL, USA) and second the a polishing suspension (Master Met$^{TM}$2, Non-Crystallizing Colloidal Silica, 40-6380-064, Buehler, Lake Bluff, IL, USA) were used to polish the surface for about 1 minute for each step. Figure 3.22 shows the resulting surfaces of all four phantoms in subfigures (e) to (h) and Table 3.5 lists the $R_a$ values.

Bright regions of the images in Figure 3.22 are in focus while dark regions are not. When

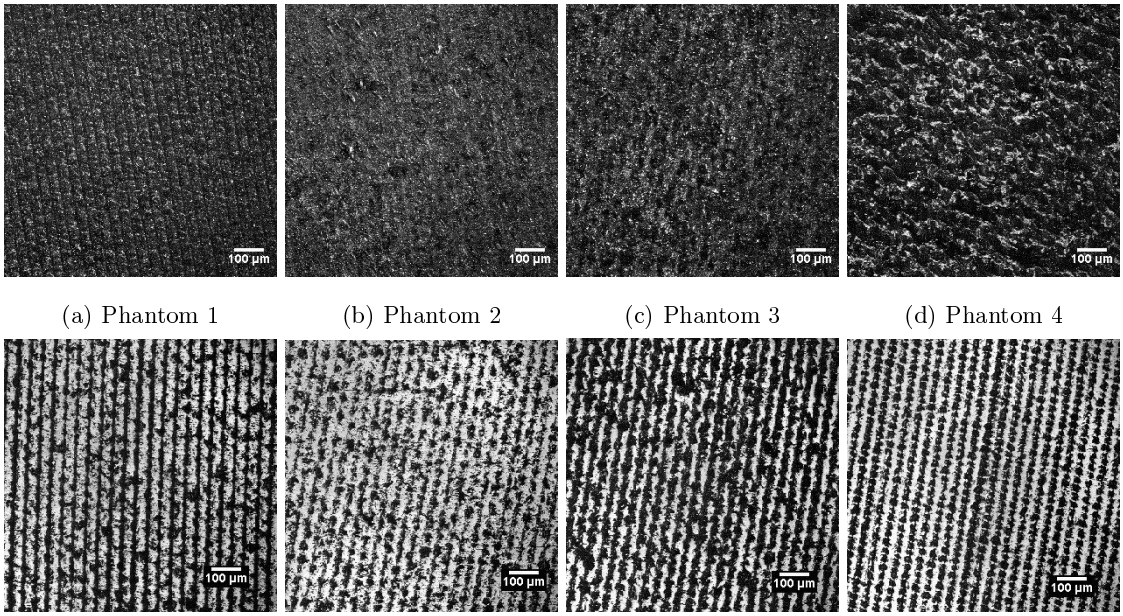


(a) Phantom 1 (b) Phantom 2 (c) Phantom 3 (d) Phantom 4

(e) Phantom 1, polished (f) Phantom 2, polished (g) Phantom 3, polished (h) Phantom 4, polished

Figure 3.22: Composite surface image of the phantoms recorded with confocal microscopy. Subfigures a) to d) show the unpolished while e) to h) show the polished surface.

comparing the polished surface to the machined surface, large white areas are visible at polished surfaces. This means large flat areas are present and in focus in the image. These areas result from polishing with a very fine grid and cause specular reflection on the phantom surface, visible by eye. The dark groves result from roughness due to earlier processing with a coarse grid and could be removed by extended polishing. But as all treated surfaces show specular reflections indicating a very smooth surface no further treatment is done. The unpolished surfaces do not show specular reflections and no flat areas indicating a rougher surface. This is confirmed by the $R_\mathrm{a}$ values given in Table 3.5, decreasing from machined to polished surface.

### 3.5.2 Mucosa - Two Wavelengths

A second set of phantoms is produced matching the optical properties of mucosa at 808 and 532 nm. For this, a red dye with similar absorption spectrum to blood has to be found and characterised. The specific absorption coefficient $\epsilon(\lambda)$ of a dye can be characterised using a spectrometer and the formula [191]

$$A = \ln\left(\frac{I_0}{I}\right) = \ln\left(\frac{I_0}{I_0 \exp(-\mu_\mathrm{a}(\lambda)d)}\right) = \mu_\mathrm{a}(\lambda)d = \epsilon(\lambda)cd \tag{3.24}$$

The attenuation $A$ is measured by the spectrometer, the concentration $c$ given by the mixture, and the pathlength $d$ given by the sample. This calculation uses the Lambert-Beer Law for light

propagation in absorbing media and is valid as no scattering is present. The spectrometer Libra S32PC (Biochrom, Cambridge, UK) was used for measurements and gives attenuation reading from -3 to 3 over the wavelength range of 190 to 1100 nm (only 450 to 1100 nm could be used, error in reading below 450 nm). Negative attenuation readings indicate fluorescence while positive values indicate absorption. Only positive values occur during the absorption measurements here and Equation (3.24) can be applied. The used cuvettes have a pathlength of 10 mm.

The selected dye are the previously used dye "Pro-Jet 900NP" (Fujifilm, Minato, Tokyo, Japan; Fujifilm kindly provided a free 5 g sample of the dye) [185], later called NIR dye, and "Polyester Pigment: Translucent Red" (407-330, Tiranti Ltd. Thatcham, UK), later called red dye, supplied by the same supplier as the epoxy resin.

The supplier has "translucent" and "opaque" colours in stock, hence it is assumed that translucent colours do not contain scattering particles while opaque colours do. This assumption is tested by measuring the transmission of a collimated laser beam through the dye solution using the same setup used before to characterise the scattering characteristics of the eardrum (see Section 3.4.4). Figure 3.23 shows the radial power distribution for both green and NIR laser without a sample as solid line and with the dye in the path as dashed line, all normalised to the maximum value to allow easy comparison of the distribution. Only small angles (compared to the previous experiments) are shown as the camera had to be placed further away to accommodate the container with the dye. The characterised sample is about 8 mm of a solution with 2.25 g/kg dye concentration. The angle observed with only air in the beam path ("plain") is a result of the beam divergence. The distribution with sample in the beam path is not widened indicating no scattering particles in the dye. The even slight narrowed distribution is a result of increased exposure time needed to record the image and thus changed noise level after noise subtraction. The green laser is stronger attenuated than the NIR dye (not visible here due to normalisation) according to the absorption spectrum of the dye shown in Figure 3.24.

Four different concentrations are mixed for each dye and the absorption characterised. The measured absorption spectra as well as the original characterisation of the NIR dye [184] are shown in Figure 3.24. The dotted vertical lines indicate the wavelengths (532, 650, and 808 nm) used to test the relation between dye concentration and absorption coefficient. Figure 3.25 shows the calibration curves, where the measured absorption coefficient is shown in dependence of the concentration of the mixture, for three wavelengths indicated in Figure 3.24. The solid line and dots indicate the four measured solutions and the dotted lines show the linear interpolation.

$$\frac{A_{\text{lin}}}{d} = \mu_{\text{a}} = \epsilon(\lambda) \cdot c \tag{3.25}$$

where the slope $\epsilon$ is the specific absorption coefficient of the dye. The interpolation is very good

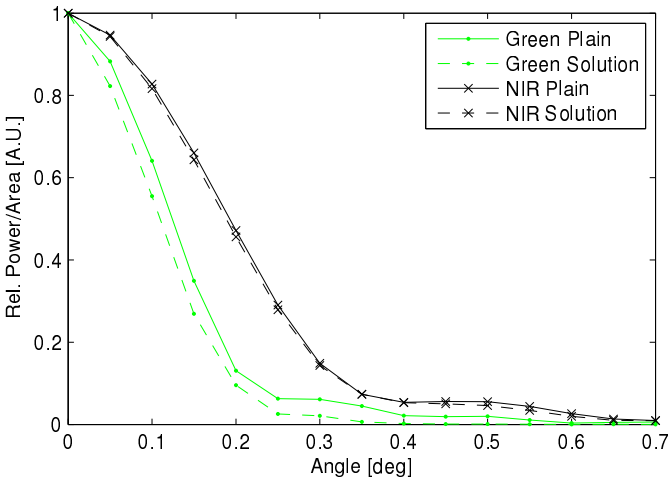


Figure 3.23: Scattering of light passing through 8 mm of red dye measured at 532 and 808 nm.

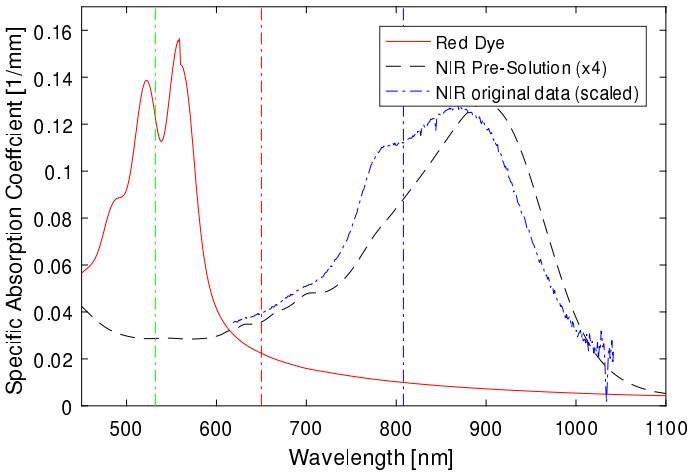


Figure 3.24: Specific absorption coefficient $\epsilon$ of red and NIR dye dependent of wavelength. The specific absorption coefficient for the NIR pre-solution is shown and multiplied by 4 for a more discernible graph. The original data used by [184] is also shown; the concentration of the base solution is different and the data is scaled to match the measurement performed here. The vertical lines indicate the wavelengths of the lasers used in the experiments.

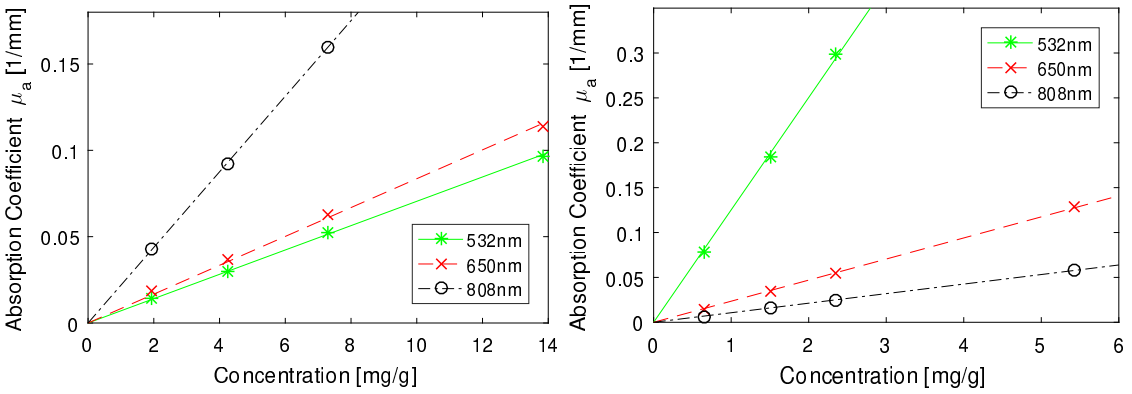


(a) NIR dye (from pre-solution)

(b) Red dye

Figure 3.25: Absorption coefficient versus dye concentration, markers show measurement points and lines the linear interpolation. The fourth concentration is not shown for some of the graphs as reading were out of the range of the spectrometer.

with a $R^2$ value of 0.9977 to 0.9999 showing that both dyes are easily soluble and an accurate determination of the optical properties is possible. Errors in determining the optical properties of the phantom will be caused by inaccurate measurement of the weight rather than dye not being completely dissolved in the base material. To achieve these results, a large stock of high concentration (1:100, dye:resin) of the "Pro-Jet 900NP" dye had to be mixed. This solution was well mixed for over one hour in an ultrasonic bath and intermitted manual mixing. This solution was then further diluted in the final mixtures. Both this second step and mixing of the red dye result in homogeneous mixtures when mixing by hand for less than five minutes. Use of the pro-jet dye directly without the use of a pre-mixture results in less accurate properties as small amounts of the dye are not diluted. This is avoided by the pre-mixture as longer mixing in the ultrasonic bath is possible and the same ratio of unmixed material is present in all further diluted samples.

The needed quantities of the dyes in order to achieve the desired optical properties are determined by

$$\mu_{\mathrm{a}}(\lambda) = c_{\mathrm{red}} \cdot \epsilon_{\mathrm{red}}(\lambda) + c_{\mathrm{NIR}} \cdot \epsilon_{\mathrm{NIR}}(\lambda) \tag{3.26}$$

Using these two dyes it is not possible to achieve the absorption as determined in the model as the absorption coefficient of the red dye is higher at 808 nm than for blood. This results in theoretical negative concentrations of the NIR dye to achieve the desired properties. Hence, the phantoms are adopted by increasing the absorption coefficient in the NIR range to a constant value for all four phantoms. The phantoms were then produced similar to the process described earlier and the final desired properties are given in Table 3.6 and a photograph of the produced phantoms is shown in Figure 3.26.

Table 3.6: Desired optical coefficients and required concentrations of scattering and absorbing agent for the two-wavelength mucosa phantoms.

| Phantom | $\mu_s'(808)$ [$mm^{-1}$] | $c_{scat}$ [g/kg] | $\mu_a(532)$ [$mm^{-1}$] | $\mu_a(808)$ [$mm^{-1}$] | $c_{red}$ [g/kg] | $c_{NIR}$ [g/kg] |
|---|---|---|---|---|---|---|
| 1 - Healthy | 6 | 7.5 | 0.244 | 0.173 | 1.571 | 7.131 |
| 2 - Intermediate | 6 | 7.5 | 0.873 | 0.173 | 6.832 | 4.754 |
| 3 - Intermediate | 6 | 7.5 | 1.502 | 0.173 | 12.093 | 2.377 |
| 4 - Diseased | 6 | 7.5 | 2.131 | 0.173 | 17.354 | 0 |


Figure 3.26: Photograph of the mucosa phantoms matching the absorption at two wavelengths

The scattering anisotropy of the phantoms is 0.6 while the one of mucosa is around 0.9. Hence, the reduced scattering coefficient is adopted accordingly, but this results in a changed reflection of the phantoms than expected for real mucosa. Hence, the reduced scattering coefficient is increased here to match the expected reflections values. Optimising was done using the simulation presented later.

### 3.5.3 Eardrum

The straight forward approach is to produce eardrum phantoms the same way as the mucosa phantoms were produced. The problem is that the scattering anisotropy is given by the scattering particles and is about 0.6 [185] and the scattering distribution of the eardrum with $g = 0.99$ cannot be reproduced. Further, the thickness cannot be set reproducibly as the material shrinks during curing. And finally the surface would need to be machined off as the distribution of particles is not homogeneous at the surface of phantoms. Hence, alternative eardrum phantoms are investigated. The tested samples are a diffuser (used as calibration target earlier), paper, microscope slides whose surface was treated with sand paper to introduce scattering, and fibre glass cast in resin. Photographs of these samples are shown in Figure 3.27.

The transmission of the eardrum samples was measured with the same setup as the transmission of the animal eardrums. The power distribution per angle of the eardrum model and the phantoms

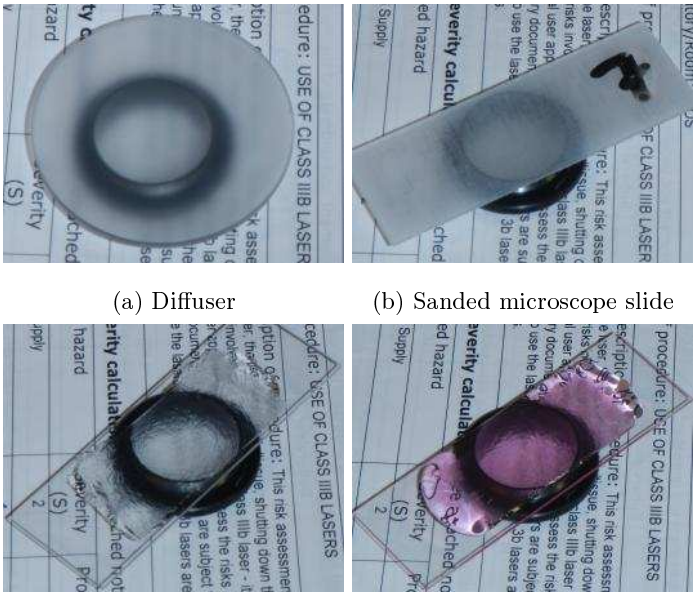

(a) Diffuser (b) Sanded microscope slide

(c) Fibre glass cast in resin (d) Fibre glass cast in resin including dye for absorption

Figure 3.27: Photographs of different eardrum phantoms.

is shown in Figure 3.28, measured at 808 nm. The average distribution of the double eardrum model is shown in black, while the phantoms are shown in different colours. The distribution of the diffuser presented earlier is shown in blue, a grease proof paper (GPP) in green, two different sanded microscope slides (SG3 and SG7) in red and turquoise, and a fibre glass sample (FR1.2) in magenta. All of these samples show higher scattering than the eardrum with the sanded microscope slide being the closest model.

The diffuser is further used as standard sample as its properties are well defined and the transmission characteristics relatively homogeneous. A fault in this model is that scattering appears only at the rough surface of the diffuser instead of inside the whole volume and second, that the scattering is not direction dependent as it is the case in the eardrum. The latter is not a problem as the detection system is rotational symmetrical. Paper is rejected as eardrum phantom because scattering is much higher and almost no unscattered photons pass the sample. The scattering characteristics of the sanded microscope slides depend on the used grid size of the sand paper and the sanding direction, time, and sanded surfaces. The samples shown here are treated with P240 (SG3) and P40 (SG7) grit size at both surfaces, with orthogonal sanding direction. A P40 sandpaper is rough and has an average particle diameter bigger than 250 µm, while a P240 sandpaper is much finer with 63 µm average particle diameter [192]. This explain higher scattering of SG7 as the surface is rougher. In this phantom, the scattering occurs at the surface only but as

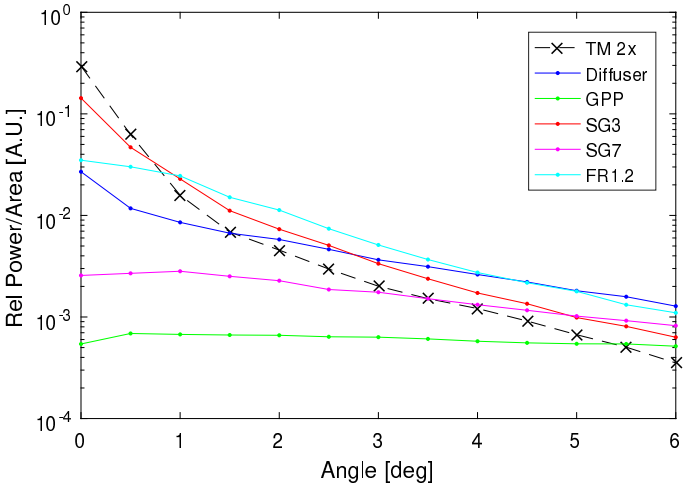


Figure 3.28: Transmission through different eardrum phantoms measured at 808 nm. TM 2x – two layer guinea pig eardrum, GPP – grease proof paper, SG3 – sandpaper 'treated' glass number 3, SG7 – sandpaper 'treated' glass number 7, FR1.2 – fibre glass cast in resin with one fibre glass layer.

two surfaces are treated it is closer to the eardrum than the diffuser.

The last eardrum phantom investigated is a fibre glass mat (406-010, Tiranti Ltd., Thatcham, UK) cast in resin (405-210, Tiranti Ltd., Thatcham, UK). In contrast to the mucosa phantoms, scattering is introduced by the fibre glass rather than $TiO_2$ particles. The advantage of this model is that scattering appears within the sample volume not just at the surface as it is the case for the previous samples. The used fibre glass mat is inhomogeneous and the model could be improved by using more homogeneous fibre glass mats with fibres matching the diameter and refractive index of collagen fibres in the eardrum and the resin matching the refractive index of the connecting tissue in the eardrum. The surface roughness of the phantoms depends on the amount of used resin. When little resin is used the fibre glass is close to the surface causing a rough interface, while it is flat when more resin is used completely covering the fibre glass. Hence, the surface of all produced fibre glass sample is sanded with a P1200 grid paper to achieve comparable surface characteristics.

In order to test the influence of absorption of the eardrum on measurements, a set of phantoms with dyes mixed into the resin were produced. Figure 3.27 (c) shows a clear fibre glass sample without dye and (d) one with red dye added. This will have an effect on the transmission of different wavelengths through the eardrum and affect the measurements of the inflammation and will be tested later. One clear phantom, 4 phantoms with different concentrations of red dye, and two phantoms with NIR dye are produced. The concentration and resulting absorption coefficients for these coloured samples is given in Table 3.7. The measured transmission at 532 and 808 nm

Table 3.7: Dye concentration and resulting absorption of the fibre glass eardrum phantoms

| | $c_{\mathbf{dye}}$ | $\mu_a$ [1/mm] | |
|---|---|---|---|
| **Sample** | [g/kg] | $\mu_a(532)$ | $\mu_a(808)$ |
| Coloured Fibre Glass NIR2 | 22.5 | 0.161 | 0.496 |
| Coloured Fibre Glass NIR1 | 11.1 | 0.080 | 0.244 |
| Coloured Fibre Glass white | 0 | 0 | 0 |
| Coloured Fibre Glass red1 | 0.45 | 0.056 | 0.004 |
| Coloured Fibre Glass red2 | 1.30 | 0.160 | 0.013 |
| Coloured Fibre Glass red3 | 2.27 | 0.279 | 0.023 |
| Coloured Fibre Glass red4 | 4.58 | 0.562 | 0.046 |

and their relation is given later in Table 7.1 to explain observed experimental results. The relation of transmitted intensity at 532 and 808 nm shows the expected decrease from black to red samples when measured at the total area. This is not the case when measured at the centre (unscattered light) indicating inhomogeneities of the scattering coefficient due to the fibre structure.

### 3.5.4 Complete Middle Ear Phantom

The middle ear phantom must be included into the optical set-up, its position, orientation, and distance between eardrum and mucosa defined. For this a sample holder is designed and is machined in the local workshop.

Figure 3.29 shows the holder for the middle ear phantom. The middle ear phantom consists of the mucosa (6) and eardrum (7). The mucosa phantoms is placed on the base (1) and pushed towards the window in the base by use of the pusher (3) and two springs (5). Additionally, a stop (10) is placed at the side of the holder to guarantee reproducible positioning of the sample. The eardrum phantom is placed opposite the window and held by two forceps (9). The distance between eardrum and mucosa is defined by the wall thickness of the window and can be increased by placing additional spacers between wall and phantom. The holder is mounted on a rotational stage and two translation stages to allow variation of the distance from the lens, angle of the surface towards the optical axis and change of sample position.

## 3.6 Compared to Real Middle Ear

The developed middle ear phantom has some differences to the real middle ear. The influence of these differences is discussed.

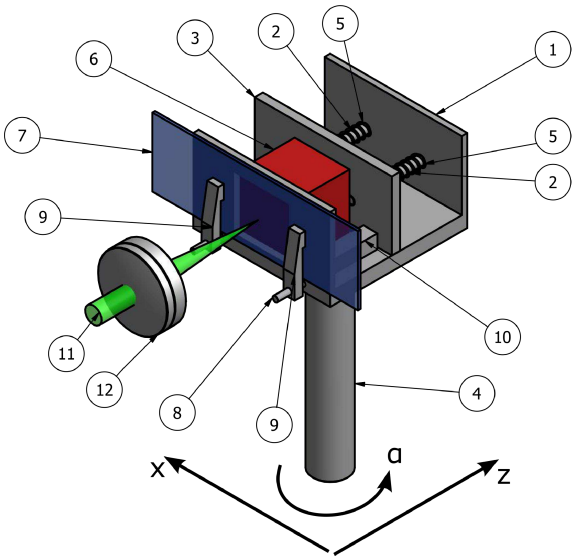


Figure 3.29: CAD model of the middle ear phantom and phantom holder with laser shown to indicate position of optics and illumination. 1 – Base, 2 – Rods, 3 – Pusher, 4 – Post, 5 – Springs, 6 – Mucosa Phantom, 7 – Microscope Slide with eardrum Phantom, 8 – Rods, 9 – Forceps, 10 – Stop, 11 – Laser beam, 12 – Objective Lens. Arrows indicating rotation ($\alpha$) and translation axis (z – along optical axis, x – position on the sample) of the sample.

**Thickness and fibre structure of the eardrum:** The human eardrum has a thickness of 50 to 70 µm at it thinnest part and shows two orthogonal fibre layers while the guinea pig has a thickness of less than 20 µm and shows only one layer and an improved model with two stacked orthogonal orientated fibre layers is used. This model shows a similar fibre structure but the fibres are thinner and the total thickness is lower than in the human case. But as attenuation is mostly caused by scattering at the collagen fibres, the two layer eardrum model is appropriate. As scattering is mostly a result of the fibres and not by particles distributed over the whole thickness, the animal model is appropriate.

**State of the samples eardrum sample *ex vivo*:** As the experiments show it is critical to keep the eardrums moist as the attenuation increases when drying. Also, the stored samples show higher attenuation than a fresh sample. It is not known if there is a similar effect when comparing *in vivo* and *ex vivo* experiments but if so, the scattering would be overestimated in the model compared to the real case.

**Direction dependent scattering of the eardrum:** The eardrum shows direction dependent scattering while some of the phantoms do not. This is not a problem as long as the radial distribution is in accordance, as the optical system is symmetrical around the optical axis

and not selective to the rotation angle.

**Model for absorption of the mucosa:** The model for change of blood flow and absorption in the mucosa during inflammation is based on literature reporting a wide variety of properties. Hence, the model might be inaccurate. To test this, experiments are conducted later in Appendix F to validate that different level of blood can be detected.

**Homogeneity of the mucosa:** While the phantoms are homogeneous over the whole volume, this is not the case for the middle ear. The middle ear mucosa is only around 0.8 to 1.7 mm thick (1-1.7 for chinchilla middle ear [193] and 0.8 to 1.5 total thickness for human colonic mucosa and sub mucosa [153]). Further, the optical properties are not homogeneous, but absorption particles are concentrated in the blood vessels. Nonetheless, the phantom is a valid approximation as a rather large area will be sampled and thus a homogeneous sample can be assumed. Additionally, the reflection from tissue is mostly caused by the superficial layers and hence deeper layers of a multi-layer phantom would only have a small influence on the measurement. Hence, these homogeneous phantoms are valid approximation.

**Influence of other structures in the ear:** The ossicles, the ear canal, and cerumen are not included into the middle ear phantom. This is a valid simplification as measurements at an appropriate position on the eardrum (marked in Figure 1.2) make sure that the ossicles are not within the measured volume. The use of the speculum with small aperture on the tip ensures that light reflected from the ear canal and cerumen in the ear canal is not detected.

In summary, the developed middle ear phantom is a simplified model of the human middle ear allowing repeatable experiments and variation of single parameters of the model. The simplifications are justified and are not expected to change the experimental results.

# Chapter 4

# Confocal Imaging of the Middle Ear

Confocal techniques combined with spectroscopy were selected as most suitable method to assess middle ear inflammation. Hence, a more detailed description of confocal microscopy is given here and experiments on a middle ear model are conducted in order to test the hypothesis that confocal imaging through the eardrum is possible.

## 4.1 Confocal Imaging

Confocal imaging is used to record 3D images of thick sample or to image a single plane within the sample while rejecting out of focus light. The penetration depth is up to 250 µm, depending on the optical properties of the sample. For imaging, the light is focused on the point to be sampled resulting in a high illumination power in this volume and small power everywhere else. Further, a pinhole is placed at the image plane of the sampling area and only light originating from the small sampled volume reaches the detector. Most other light is rejected by the pinhole as shown in Figure 4.1. The combination of focused illumination and pinhole result in an intensity point spread function $psf$ of the confocal system in direction of the optical axis given by

$$psf(\xi, \rho = 0) = \left(\frac{\sin(\xi/4)}{\xi/4}\right)^4 \tag{4.1}$$

where $\xi = \frac{2\pi}{n\lambda} NA^2 z$ is a measure for the z-distance, $\rho = \frac{2\pi}{\lambda} NAr$ is a measure for the radius, both normalised by NA and wavelength [195]. The point spread function is the convolution of two identical functions $\left(\frac{\sin(\xi/4)}{\xi/4}\right)^2$ of illumination and detection optics. This function decreases rapidly

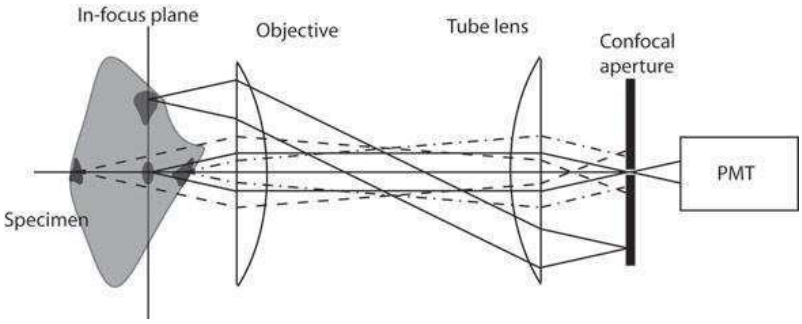


Figure 4.1: Optical set-up of a confocal system [194]. Light from the spot on the optical axis in the focal plane is focused on the confocal aperture and is detected. All other light, such as out of focus (dashed and dash-dotted lines) and off-axis (solid, skewed) is blocked by the aperture and is not detected. Illumination is not shown.

when moving away from the focus $\xi \neq 0$ showing the good background rejection of the confocal imaging system.

The point spread function in traverse direction of the optical axis at $\xi = 0$ is given by

$$psf(\xi = 0, \rho) = \left( \frac{2J_1^2(\rho)}{\rho^2} \right)^2 \tag{4.2}$$

Again, this is a result of the convolution of two identical functions of illumination and detection optics.

In order to create an image of the full sample the focus must be scanned across the sample. This is a "long" process, especially when a 3D image is to be reconstructed. Also, most of the light is rejected by the pinhole resulting in a high radiation exposure of the sample. In most applications, the sample is fluorescent but reflection mode can also be used. A confocal system shows best performance when the radius of the pinhole is just below 4 optical units $OU = \frac{\lambda}{2\pi NA}$ [196]. The axial $r_{\text{axial}}$ and radial $r_{\text{radial}}$ resolution of a confocal microscope are derived from the confocal point spread functions Equation (4.1) and Equation (4.2). The resolution is given by the distance two adjacent point spread functions need to be separated so that a dip by 26 % of the maximum power is observed between both maxima and can be calculated according to [195].

$$r_{\text{axial}} = 1.5n\frac{\lambda}{NA^2} \tag{4.3}$$

$$r_{\text{radial}} = 0.44\frac{\lambda}{NA} \tag{4.4}$$

As example, Figure 4.2 shows the comparison of a wide-field versus a confocal image of a cell aggregate labelled with three fluorescent dyes taken from [197]. The confocal image is much clearer as light from out of focus planes is rejected.

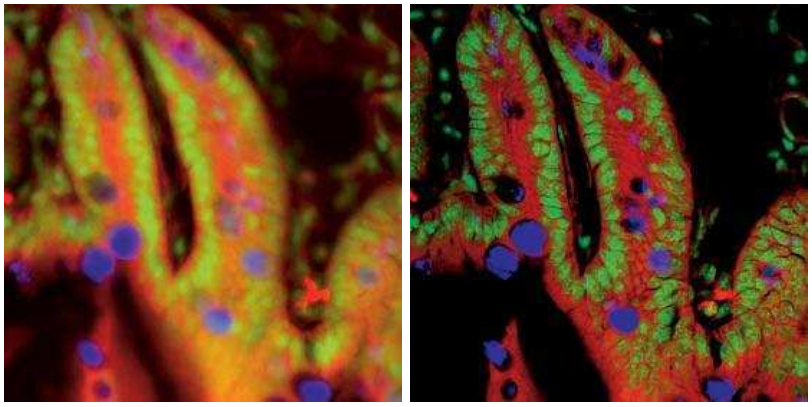

(a) Non-confocal (b) Confocal

Figure 4.2: Non-confocal and confocal microscope image of a triple labelled cell aggregate [197]. Scale not given.

Confocal microscopy is mostly used to image small samples on a microscope but other applications of confocal systems are being researched such as endoscopic imaging of mucosa as earlier presented in Section 2.4.4. A confocal system allows the implementation of spectroscopic measurements as for example shown in [112] implementing a 3 wavelengths system or [111] implementing a broadband system.

## 4.2 Imaging Inside the Ear

Imaging the middle ear through the external ear canal is restricted by the small diameter and length of the ear canal. The diameter of the ear canal in children is about 6 mm and has a depth of 25 mm, as described in Section 1.1. Imaging is done through the speculum of an otoscope in order to straighten the "S" shaped canal and enable view on the eardrum. Figure 4.3 shows a schematic drawing of the speculum of the otoscope presented in Figure 2.2. Eardrum and mucosa are shown as simple lines indicating their position. The reusable speculum can be easily removed and is changed between patients while the fixed speculum is attached to the otoscope. The fixed speculum has an external thread and can be easily attached to other optical components to allow build-up of custom optics while maintaining the normal clinical interface with the patient.

The opening of the fixed speculum poses the smallest aperture with an angle $\Phi = \arctan(r/d)$ ($r$ is the radius of the smallest aperture, and $d$ the distance from sample to the aperture) of about 4.7 deg and a NA of around 0.08. At 808 nm, this results in 4.4 and 187.5 µm radial and axial resolution, respectively.

While these restrictions have to be considered in the optical setup, they will not be considered

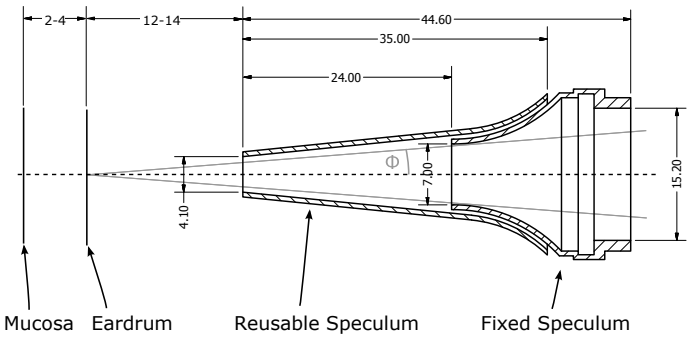


Figure 4.3: Sketch of the otoscope speculum including dimensions.

in the experiments conducted here. Experiments are conducted with an objective with NA of 0.4, the smallest NA available in the system.

## 4.3 Experimental Setup

This section presents experiments using a commercial confocal microscope (TCS SP2, Leica, Wetzlar, Germany) where a target is imaged through animal eardrums showing that confocal microscopy is able to image though an eardrum model. The confocal microscope has several adjustable excitation lasers with wavelengths ranging from 458 to 633 nm. It is designed for fluorescent imaging but the settings can be adjusted for reflectance imaging. The maximum working distance with an objective with 10 times magnification and numerical aperture of 0.4 is 3.6 mm.

The experimental setup on the confocal microscope is schematically shown in Figure 4.4. A "1951 USAF resolution target" covered by a guinea pig eardrum is placed on the microscope. The test resolution target is used instead of the mucosa phantoms developed earlier as an image of the target is to be recorded and the homogeneous mucosa phantoms do not show any contrast within one single phantom. The distance between resolution test target and the eardrum is set to either 1 or 2 mm, by use of a spacer (a distance of 3 mm is expected in the ear but the working distance of the objective restricts the maximum distance). The eardrums are placed on a microscope slide, suspended in saline solution, and covered with a cover slip to prevent drying. Images are either recorded in wide-field transmission or confocal reflection mode.

Several tests of imaging the same target through different eardrum samples are presented, either a single or a double layer of eardrum is used, the distance between eardrum and target is varied, and the illumination wavelength is changed (458, 488, and 543 nm).

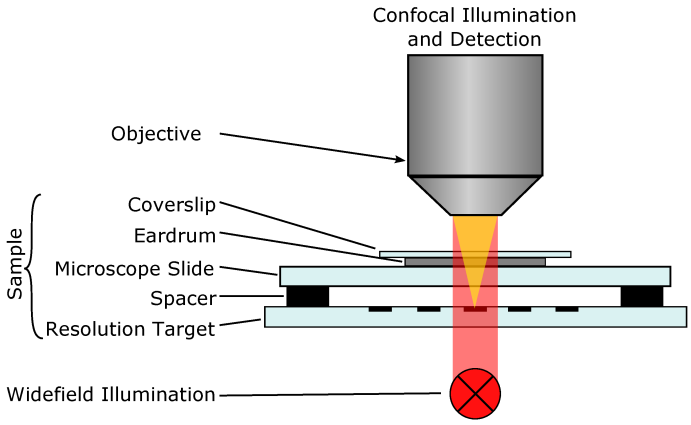


Figure 4.4: Setup of the sample on the TCS SP2 confocal microscope. Yellow indicates confocal light path, used in reflection mode, and red indicates wide-field light paths, used in transmission mode.

## 4.4 Results

Recorded images of the resolution target are shown in Figure 4.5. Subfigure (a) shows a transmission image, focused on the eardrum, and the structure of the eardrum is clearly visible. Subfigure (b) shows another transmission image, this time focussed on the target. The reflective bars of the test target are clearly visible on the top right of the image while the rest of the image shows poor quality as light is scattered by the eardrum placed above the target. Subfigure (c), shows the confocal reflection images when focussed on the target recorded at 543 nm. The transmission images are displayed to explain the confocal image. Subfigure (d) shows an image of the eardrum only, recorded with higher magnification. The white square in subfigure (a) indicates the area displayed in subfigure (d). The yellow lines in the images mark borders between single layered eardrum, double layered eardrum, and no eardrum, best visible in subfigure (a). In the top right area of the image no eardrum is present and the target is clearly visible when focused on the target as done in subfigure (b) and (c). On the bottom right, a single eardrum layer is present and on the bottom left a double layer is present. This transition from single layer to double layer eardrum is clearly visible in subfigure (d). The top left area shows a folded eardrum or some other tissue attached to the eardrum resulting in a thick sample and high attenuation. The squares marked in subfigure (b) indicate areas analysed to measure the contrast as explained below.

A strong confocal signal of the reflective bars is visible in the uncovered area (top right). The gain of the detector is adjusted so that these areas do not saturate in order to allow transmission measurements. The signal in the area of the single layered eardrum (bottom right) is smaller but still obvious and in the area of the double layered eardrum (bottom left), the signal is further

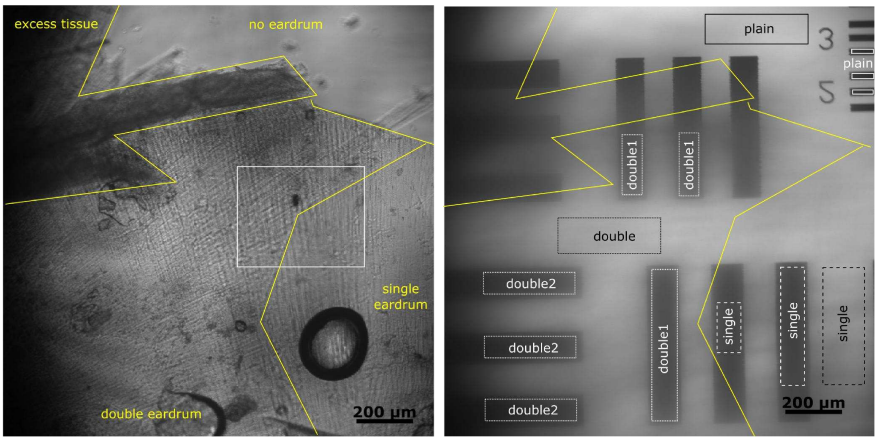


(a) Wide-field transmission image, focused on the eardrum

(b) Wide-field transmission image, focused on the target

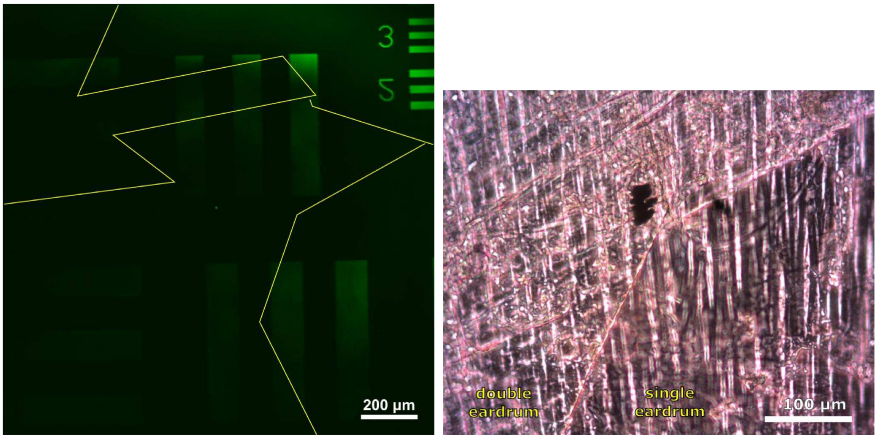


(c) Confocal reflection image at 543 nm

(d) Wide-field image of the eardrum only

Figure 4.5: Target imaged through a double layered guinea pig eardrum. Yellow lines mark borders between different areas of the eardrum sample, no eardrum on the top right, a single eardrum on bottom right, and a double eardrum on bottom left. The boxes marked in (b) indicate analysed areas to measure the contrast.

Table 4.1: Contrast for different wavelengths and eardrum layers. The distance between target and eardrum is 1 mm.

| | Contrast | | | |
|---|---|---|---|---|
| $\lambda$ [nm] | **Unhidden** | **Single** | **Double 1** | **Double 2** |
| 458 | 0.66 | 0.28 | 0.13 | 0.07 |
| 488 | 0.69 | 0.37 | 0.20 | 0.13 |
| 543 | 0.65 | 0.35 | 0.22 | 0.15 |

attenuated.

To measure the unscattered transmission through the eardrum the contrast $C$ is defined, using the definition of the Michelson Contrast [198]

$$C = \frac{I_{\text{signal}} - I_{\text{background}}}{I_{\text{signal}} + I_{\text{background}}} \tag{4.5}$$

is measured. $I_{\text{signal}}$ is the average intensity of the confocal signal of a reflective bar and $I_{\text{background}}$ the average signal detected in the area of the glass substrate. The analysed areas are marked in Figure 4.5 (b) with white boxes for the signal and black boxes for the background. This measure is applied to the unhidden, single, and two double layered areas and the analysed areas labelled accordingly. Two areas are analysed for the double eardrum to show inhomogeneities of the sample. Table 4.1 summarises the contrast values for the presented image.

The contrast is highest (around 0.67) for the uncovered area as expected. For the single layer the contrast is decreased to 0.28 to 0.37, dependent on the wavelength and for the double layer the contrast is even smaller with 0.07 to 0.15 in region 2 and 0.13 to 0.22 in region 1. The attenuation of the eardrum is not homogeneous as shown by the two different analysed areas of the double eardrum sample (double 1 vs. double 2). The contrast is reduced for the second area indicating a higher attenuation. Measurements on an eardrum that is not stored in saline solution shows even more attenuation indicating that drying increases the scattering of the eardrum.

A wavelength dependence of the contrast is visible in Table 4.1. The used wavelengths are relatively close (difference of 85 nm) so the effect is small, but still visible. The contrast generally increases for the hidden cases when imaging with higher wavelengths and the effect is bigger for the double layer. This means the attenuation in the eardrum is higher for lower wavelengths. This is in accordance with the transmission measurements presented in Section 3.4.4. It is expected that the attenuation further reduces going to higher wavelengths allowing better images in the red or NIR.

The distance between eardrum and resolution target also affects the contrast as seen in Ta-

Table 4.2: Contrast for changed distance between eardrum and target.

| | | Contrast | |
|---|---|---|---|
| **Distance [mm]** | **$\lambda$ [nm]** | **Unhidden** | **Single** |
| 1 | 543 | 0.73 | 0.20 |
| 2 | 543 | 0.62 | 0.12 |

ble 4.2. New images were recorded to allow comparison of the same area for both measurements, and only the single eardrum layer is analysed. A higher distance between eardrum and target reduces the signal level even though the eardrum itself does not change. This effect, sometimes called "shower curtain effect", "tracing paper effect", or "t-effect" in literature [199], is observed when imaging a target through a translucent, scattering layer. When moving the scattering layer away from the target towards the observer, the image quality degrades. In the case of confocal imaging the contrast is reduced with increasing distance because scattered light propagates longer to reach the mucosa target and thus the displaced distance orthogonal to the optical axis is bigger. For small distances and forward scattered light, a detection might still be possible as the scattered photons with small angle still reach the sampled volume while for a high distance the light has propagated to far to be detected. Both, the contrast for the single layers as well as for no layer in the light path decrease with distance. This effect is not expected for the plain measurement as no scattering should appear. But as saline solution including small particles is in the beam path, some scattering is introduced and a small decrease in contrast is observed. The effect is bigger for the case when imaging through the eardrum.

## 4.5 Conclusion

When drawing conclusions from the above animal experiments to the proposed application in the human ear the following differences have to be considered:

**Wavelength:** The wavelength used here is in the blue and green range (458, 488, and 543 nm) while the wavelength used later may reach up to the NIR. The scattering and absorption coefficient in tissues decrease from the visible to NIR range resulting in lower attenuation and thus improved signal level when using higher wavelengths.

**Distance between eardrum and target:** In the confocal experiments the distance between eardrum and target is restricted to 1 and 2 mm while in the human ear the distance is higher with 2 to 4 mm. The signal will decrease when increasing the distance.

**Reflection of mucosa compared to the test target:** The target used here is a 1951 USAF resolution test target where the reflection of the target varies from almost completely reflecting to almost no reflections. The mucosa is less reflective and shows a contrast between healthy and inflamed of around 20 % only [63].

**Numerical Aperture** The NA used in the experiments here is 0.4 while the maximum possible NA in the middle ear is 0.08. This will reduce the background rejection ratio of the system and signal power.

As the described experiments show, confocal reflection images of a resolution test target can be taken in the blue and green wavelength range when placed behind a single and double layer of guinea pig eardrum in 1 and 2 mm distance. No image could be acquired for a dry guinea pig eardrum.

The increased thickness, increased distance between target and eardrum, as well as less reflectivity of the mucosa compared to the test target decrease the signal in the human case. A change in wavelength to the NIR range would results in an increased reflection signal. Further, the illumination power and acquisition time can be increased to increase the detected signal, but must be kept within the health and safety limits.

It is assumed that an increase in input power and use of longer wavelengths will allow imaging even with increased attenuation of the eardrum and reduced reflectivity of the mucosa. Hence, a confocal system will be developed in order to assess the middle ear inflammation.

# Chapter 5

# Anti-Confocal System

The previous chapter showed that it is possible to record images through most eardrum samples investigated. Hence it was concluded that confocal techniques are suitable to assess the middle ear and reject background signals from the eardrum.

Confocal imaging is well suited to image a layer embedded within a sample and by selecting one single plane to be imaged and rejecting light originating from all other layers. But the investigated geometry is different, a target volume needs to be sampled (middle ear mucosa) and it is separated from superficial layers (eardrum) by an air gap (middle ear cavity). This means no sharp cut off between rejection and detection planes are necessary and time consuming scanning becomes necessary to cover a representative volume of the mucosa instead of just a single point or plane. Further, confocal imaging has the disadvantage of rejecting most of the light and thus need for sensitive detectors and high illumination power posing a risk to the sample [194]. Another disadvantage in the case considered here is the unknown position of the target layer and the resulting need to scan through the sample along the optical axis in order to find its surface.

All this leads to the idea of an "anti-confocal" system, inverting the confocal idea by rejecting only light from a thin plane while detecting all other light. This anti-confocal system is presented and investigated in this chapter. First, similar ideas in literature are presented, then the concept is explained in detail, and the system simulated. Variations of the properties of the sample (scattering of the eardrum, distance between eardrum and mucosa, surface angle and roughness) and the optical system (position and radius of the stop, position of the focus, detection and illumination NA) are investigated to allow optimisation of the optical system and characterise its behaviour over a wide variety of samples as no ear is like the other. All results are compared to a conventional confocal system with respect to detected signal level and background rejection in order to test whether the anti-confocal system introduces an advantage over the confocal system.

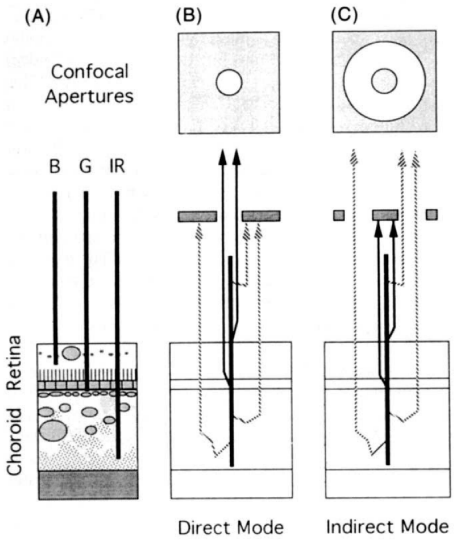


Figure 5.1: Idea of indirect confocal imaging [200]. (A) showing the tissue structure, (B) imaging using a confocal system, and (C) imaging in the indirect mode.

While this chapter deals with the principle of the anti-confocal system, and its ability to separate signal from background, the next chapter is based on this investigation and will introduce multi-spectral measurements to assess the haemoglobin content. Experimental validation is presented later in Section 7.

## 5.1 Literature

A similar idea to "anti-confocal" imaging, called "indirect mode" is presented in [200, 201] where a transmissive annulus, as shown in Figure 5.1 (C) top, is used to reject reflections and directly scattered light. This is in contrast to the confocal imaging or direct mode (B) imaging where only these direct components are detected. This method is applied to imaging the human ocular fundus and enables improved imaging of sub-retinal structures. It is shown that the light detected with indirect mode increases with wavelength (in the investigated range of visible and NIR) as light is penetrating deeper into the tissue and thus the indirect component is increased. In general the amount of detected light is a function of light penetration depth, stop, and aperture/pinhole radius. While confocal imaging emphasises thin or highly reflective and backwards scattering features, indirect mode imaging emphasises features that scatter light laterally, such as liquid accumulation [200] and shows good contrast for large vessels [201].

This idea is also implemented in spectroscopic imaging of the ocular fundus [202] and blood oxygen measurements in retinal vessels [203]. Either the transmissive annulus (central stop and

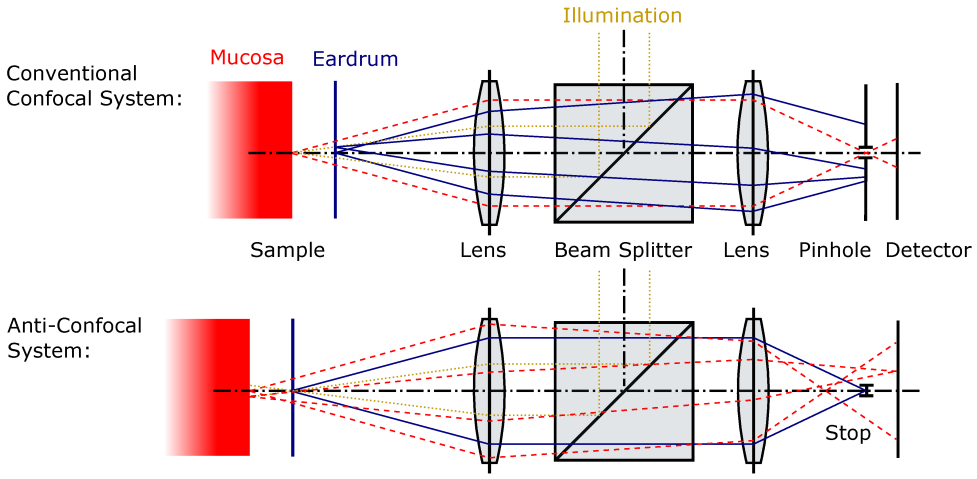


Figure 5.2: Optical principle of the anti-confocal system compared to the conventional confocal system.

large pinhole) or a central stop is used to reject unwanted signal components with the system called "anti-confocal" and "anti-pinhole", respectively.

In all cases the anti-confocal filtering is applied to imaging of the ocular fundus and no other uses have been found. Also, the description and characterisation of the system is minimal. Hence, the system will be investigated and characterised in this chapter. It is encouraging, that the above presented literature use spectroscopy and blood vessel oximetry in context with the anti-confocal system showing that detection of blood content should be possible.

## 5.2 Principle

The schematic setup of the anti-confocal system is compared to a confocal system in Figure 5.2. The sample shown simplified on the left is composed of the mucosa (red), and air gap indicating the middle ear cavity, and the eardrum (blue). In the confocal system the illumination beam (yellow, dotted) is focused on the mucosa. Hence a large area of the eardrum is illuminated, while only a small area of the mucosa surface is illuminated (not considering scattering). Reflected and backscattered light is collected by a lens, passed through a beam-splitter, used to couple the illumination beam in, and focused on a pinhole. Light originating from the mucosa surface (red, dashed) is in focus at the plane of the pinhole and passes through and reaches the detector. Light originating from the eardrum (blue, solid) is out of focus at the pinhole plane and most light is rejected. Light scattered inside the mucosa will be rejected the same way, only that it is focused in front of the pinhole rather than behind. Both the pinhole as well as the focused illumination,

directing most power to the sampling volume, result in the good background rejection ability of the confocal system.

But this shows already a disadvantage of the confocal system applied to diagnosing inflammation in the middle ear mucosa: Light scattered inside the mucosa, and carrying most information about its properties is rejected by the confocal pinhole. Hence, depth scanning would be necessary to acquire information about the inside of the mucosa as well as radial scanning to image an area to acquire average properties instead that of a single small spot. This would result in relatively long imaging times and low signal from inside the mucosa as attenuated by superficial mucosal layers and the eardrum.

In the anti-confocal case the illumination is focused on the eardrum rather than the mucosa, and a central stop blocks all light inside its radius rather than outside. The stop is placed in the focal plane of the eardrum as opposed to the pinhole placed in the focal plane of the mucosa. Thus, light originating from the eardrum is in focus at the stop and does not reach the detector. Light originating from the mucosa is out of focus and most of the radiation reaches the detector. This means a much larger area is sampled and less light lost due to spatial filtering. Hence, scanning might not be required, depending on the homogeneity of the mucosa and its sampled volume. This will be investigated later. On the other hand the resolution is greatly reduced, but this is not of importance here as no image is required, rather a single measure about the severity of the inflammation is desired.

The radius of the stop needed to reject most light from the eardrum depends on several factors. Firstly, it must be bigger than the illuminated area on the eardrum in order to reject all reflections and directly scattered light. When the eardrum gets thicker, the focal spot increases according to the thickness and beam aperture and thus the stop radius must be increased. Finally, increased scattering and increased thickness will result in light being scattered inside the eardrum resulting in light backscattered from outside the directly illuminated area and the stop radius must be increased further to reject these components as well. But an increase in the stop radius results in a decrease of detected signal from the mucosa. A compromise between detection of signal from the mucosa and rejection of signal from the eardrum must be found. This will be investigated in the following section.

Imaging inside the ear is restricted to a small NA of 0.08 by the speculum as illustrated in Figure 4.3. This has the disadvantage of restricting the detectable light. On the other hand it acts as an aperture rejecting light that was scattered far inside the ear and sampled other structures such as ear canal and ossicles that are not included in the model. These structures pose other background sources that cannot be rejected by the anti-confocal stop. But as they are rejected by the small speculum aperture the simplified model of the middle ear composed of mucosa and

eardrum only is valid.

## 5.3 Simulation Methods

The anti-confocal system and the middle ear are simulated using MATLAB in order to allow prediction of its performance and investigate the system itself. First, Monte Carlo Methods for light propagation in tissues and then the geometrical optics code used to propagate the photons inside the optical system are explained and tested, then the simulated geometry, and finally the simulation results are presented.

### 5.3.1 Monte Carlo Method

Monte Carlo Methods are widely used in tissue imaging to simulate light propagation inside a tissue with given optical parameters (absorption and scattering coefficient, scattering anisotropy, and refractive index). Single random paths of photons are simulated inside the tissue, with these paths then combined to give an approximation of light propagation in the tissue. The more photon paths simulated the more accurate the simulation gets.

Monte Carlo simulations are described in detail elsewhere [204,205], with example code available online [206] and a basic structure of the code is shown in Figure 5.3. The steps of the simulation of a single photon path are:

1. First the photon is **launched** into the tissue. The incident position is randomly chosen inside the illuminated area and the direction is given by the illumination system (focus, beam profile, etc.) and the weight $w$ of the photon representing its power is given by 1.

2. The photon **propagates** a random distance $l$ inside the tissue according to an exponential function and the mean free path $MFP$. The distance in the code is given by

$$l = -\log(\xi) \cdot MFP = \frac{-\log(\xi)}{\mu_\mathrm{t}} \tag{5.1}$$

   where $\xi$ is a random variable distributed between 0 and 1.

3. At the new position an **interaction** with the tissue occurs, some of the energy is **absorbed** and the weight of the photon reduced according to the albedo $\alpha$

$$w_\mathrm{new} = w_\mathrm{old} \cdot (1 - \alpha) = w_\mathrm{old} \cdot (1 - \frac{\mu_\mathrm{a}}{\mu_\mathrm{t}}) \tag{5.2}$$

   and the photon is **scattered**. The new propagation direction is given by two random variables, one determining the deflection angle $\phi$ (angle to the original propagation direction)

according to the Henyey Greenstein function

$$\cos(\phi) = \frac{1}{2g}\left(1 + g^2 - \left(\frac{1-g^2}{1-g+2g\xi)}\right)^2\right) \tag{5.3}$$

and the second one determining the azimuthal angle $\psi$ (rotation around the original propagation direction) according to

$$\psi = \xi 2\pi \tag{5.4}$$

4. If the weight of the photon is to small to have a significant effect on the final result (for example $w < 0.001$ as used here) it is either eliminated or its weight increased. The relation of **elimination** and increase of weight keeps the total power in balance, as 9 in 10 photons are eliminated and the weight of one in 10 photons is increased by a factor of 10.

5. When the photon step size is big enough to pass an **interface** between two layers the photon is moved a reduced distance to the interface and no scattering or absorption occurs. According to the reflection ratio given by the Fresnel formula, the refractive indices of the media $n_1$ and $n_2$, and the incident angle $\phi_\mathrm{i}$

$$R = 0.5 \cdot \left(\frac{\sin(\phi_\mathrm{i} - \phi_\mathrm{t})^2}{\sin(\phi_\mathrm{i} + \phi_\mathrm{t})^2} + \frac{\tan(\phi_\mathrm{i} - \phi_\mathrm{t})^2}{\tan(\phi_\mathrm{i} + \phi_\mathrm{t})^2}\right) \tag{5.5}$$

with the transmission angle $\phi_\mathrm{t}$ calculated by $\sin(\phi_\mathrm{t}) = \sin(\phi_\mathrm{i}) \cdot \frac{n_1}{n_2}$. The photon is either reflected or transmitted, again determined by a random variable. If **reflected**, the photon moves the remaining distance backward in reflection direction; if **transmitted** the direction is changed according to refraction and the remaining distance scaled according to the MFP in the new layer.

6. The simulation of one light path is ended when the photons weight is too low or the photon **exits** the medium and is final weight, exit position, direction, and path inside the medium are recorded for further processing.

In the reported code [206] scattering and absorption occur on every interaction with the material. The absorption is scaled by the albedo $\alpha = \frac{\mu_\mathrm{a}}{\mu_\mathrm{t}}$ giving the relation of absorption to attenuation coefficient but the scattering is not scaled. This results in a dependence of the number of scattering events on the absorption coefficient which is not given in this form in reality. Increased absorption of the material results in shorter light paths and this is considered by the weight of the photons. The original form of the code would increase the number of scattering events in this light path as the number of interactions is increased, even though the number of scattering events should be constant during the same propagation distance. This is corrected in this code by introducing

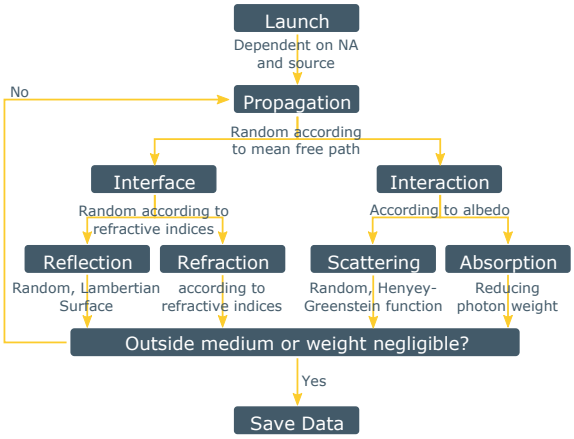


Figure 5.3: Structure of the Monte Carlo code.

scattering only in some of the interactions according to the relation of scattering to attenuation coefficient and using a random number (scatter only if $\xi > \alpha$).

Another change of the code is to replace the specular reflection at interfaces by diffuse reflection. Lambertian reflection is implemented as explained in Appendix B with an option to combine both specular and Lambertian reflection. Further, the time consuming simulation of scattering inside the mucosa is replaced by a model giving the exit angle and exit radius of photons directly. This model is explained and tested in Appendix B and used in this chapter but not in Section 6 which is based on white Monte Carlo simulations explained below.

### 5.3.2 White Monte Carlo

Monte Carlo simulations are time consuming, especially when the same geometry is simulated while changing scattering and absorption coefficient. 'White Monte Carlo' codes try to solve this problem by performing a base simulation and then scaling the results according to the new scattering and absorption coefficient. Alerstam [207] introduces a code for modelling single layered tissue and Liu [208] introduces a code that can be used for the scaling of multiple layers. None of the codes is able to scale the scattering anisotropy.

The codes are explained first and then compared to normal Monte Carlo simulation results to ensure correct implementation. The white Monte Carlo code will be used to simulate the spectral reflectance of the mucosa dependent on blood content presented in the next chapter, while the normal Monte Carlo code is used in this chapter analysing the anti-confocal system.

### Single Layer

The code introduced in [207] is applicable for a single layered medium filling a half space. The Monte Carlo code is similar to a normal Monte Carlo code, except for the following changes:

- The tissue is simulated **without any absorption** ($\mu_\mathrm{a} = 0$) and a **base scattering coefficient** $\mu_{\mathbf{s,0}}$ (a maximum expected scattering coefficient is used in [207] but this is not necessary, any value can be used).
- The **step size** of a photon is chosen according to the scattering coefficient rather than the attenuation coefficient $l = \frac{-\ln(\xi)}{\mu_{\mathrm{s},0}}$ as no absorption is included.
- A photon is **eliminated** after it travelled a predefined distance instead of calculating its weight. This is a source of error as the power of the eliminated photon gets lost. In normal Monte Carlo code a proportion of the photons are kept alive and their weight multiplied by the probability to be eliminated and thus the total power is kept constant. But if the path length is chosen to be long enough, this error is negligible.

The simulation results are then scaled to fit the tissue properties. Dimensions $d$ (path length, exit distance of a photon from the incident point, ...) are scaled according to

$$d = d_0 \cdot \frac{\mu_{\mathrm{s},0}}{\mu_\mathrm{s}} \tag{5.6}$$

where $d$ is the new dimension in the medium with scattering coefficient $\mu_\mathrm{s}$ and $d_0$ is the distance resulting from the simulation with randomly chosen scattering coefficient $\mu_{\mathrm{s},0}$. The weight $w$ of a photon is scaled according to

$$w = \exp\left(-\mu_\mathrm{a} p\right) = \exp\left(-\mu_\mathrm{a} p_0 \frac{\mu_{\mathrm{s},0}}{\mu_\mathrm{s}}\right) \tag{5.7}$$

where $p$ is the path length of the photon inside the tissue scaled by the scattering coefficient as given in Equation (5.6).

### Multiple Layer

Liu et al. [208] (based on [209]) extend this scaling to multiple layers and semi-infinite slabs. Again, the code is based on normal Monte Carlo code and the step size is determined as previously. But here, a photon is terminated after a predefined amount of scattering events [209] instead of using the path length. The power of the eliminated photon is lost and the same error is introduced as previously.

A baseline medium with a single layer is simulated. Virtual interfaces are then placed inside the medium to build up a multi layered tissue. In order to do so, the position of photon must

be tracked over the whole medium to be able to choose the positions of layer interfaces freely. The position of each photon is saved in a grid and the position of the photon at the interface interpolated. This introduces a small error (when the layer surface does not fall onto a grid-line) that can be minimised without increasing the data when using a variable grid size, with smaller grid closer to the surface where the influence of errors is bigger.

Scaling of the photon weight is done according to the scattering events $N$ in each layer $i$ and the attenuation and scattering coefficient

$$w = \prod_{i=1}^{n} \left( \frac{\mu_{\mathrm{s,i}}}{\mu_{\mathrm{t,i}}} \right)^{N_{\mathrm{i}}} \tag{5.8}$$

The distances are scaled separately for each layer and the final distance is a sum of travelled distances in all layers.

$$d = \sum_{i=1}^{n} d_{\mathrm{i}} \cdot \frac{\mu_{\mathrm{t},0}}{\mu_{\mathrm{t,i}}} \tag{5.9}$$

It has to be noted that the attenuation coefficient $\mu_{\mathrm{t}}$ is used here in contrast to the scattering coefficient $\mu_{\mathrm{s}}$ as previously. Further, the thickness $t$ of each layer is scaled according to

$$t_{\mathrm{i}} = t_0 \cdot \frac{\mu_{\mathrm{t,i}}}{\mu_{\mathrm{t},0}} \tag{5.10}$$

It is not explained how refraction at layer surfaces with different refractive index is handled.

### Inaccuracies in the Reported Codes

The first obvious problem is that distances are scaled by $\mu_{\mathrm{t}}$ in [208] while $\mu_{\mathrm{s}}$ is used in [207]. The latter is correct as the path length in the white simulations is only affected by the scattering coefficient, not the absorption. Attenuation is included later using scaling of the weight. Simulations confirm this as shown in Figure 5.4 where simulations scaled by $\mu_{\mathrm{t}}$ match the normal simulation better.

Second, the use of number of scattering events $N$ when scaling the photon weight in Equation (5.8) is invalid. The weight is scaled by the albedo $\alpha$ and thus the relation between scattering and absorption events is considered. But then the scaling is only applied to scattering events, not all possible events including absorption events. Hence, the number of scattering events must be multiplied by $\frac{1}{\alpha} = \frac{\mu_{\mathrm{s}}+\mu_{\mathrm{a}}}{\mu_{\mathrm{s}}}$ in order to get the number of all possible events. This error is similar to the one in the normal Monte Carlo code where scattering was done on every event, including the absorption events.

Third, the minimum weight determining the elimination of a photon determines the spread of the signal. A higher weight results in photons being eliminated earlier and long paths are not simulated. Figure 5.4 c) and d) shows this effect, in the normal simulation a photon was

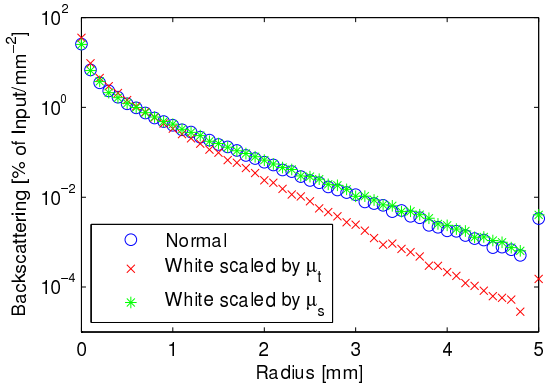


(a) Scaled by scattering events, $\mu_a = 0.5\,\mathrm{mm}^{-1}$

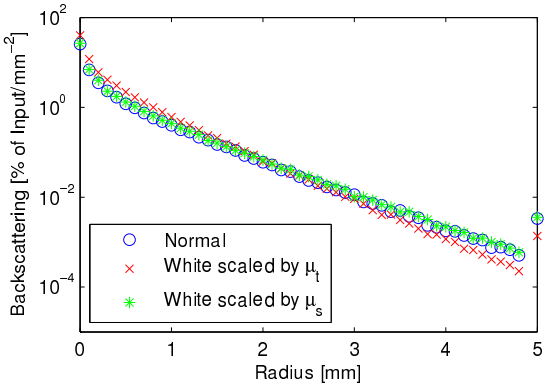


(b) Scaled by path length, $\mu_a = 0.5\,\mathrm{mm}^{-1}$

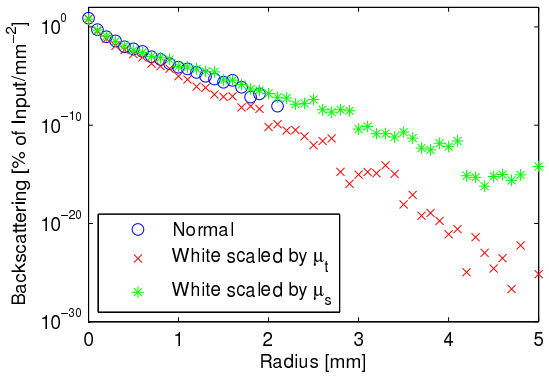


(c) Scaled by scattering events, $\mu_a = 5\,\mathrm{mm}^{-1}$

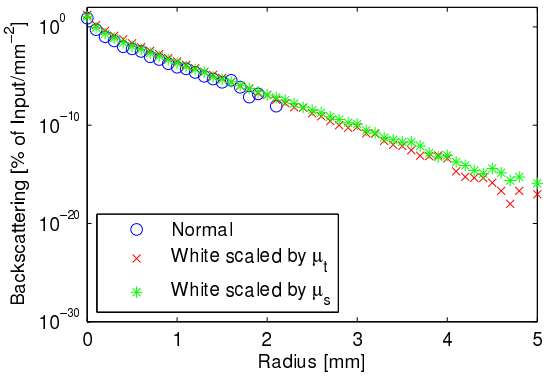


(d) Scaled by path length, $\mu_a = 5\,\mathrm{mm}^{-1}$

Figure 5.4: Test of scaling from $\mu_{s,0} = 20$ to $\mu_s = 10\,\mathrm{mm}^{-1}$ in white MC simulation with $\mu_a = 0.5\,\mathrm{mm}^{-1}$ in the top two graphs and $\mu_a = 5\,\mathrm{mm}^{-1}$ in the bottom figures. The backscattered signal dependent on the distance from incident point on a semi-infinite slab is simulated. The radius from the incident point is sampled from 0 to 5 mm in 0.1 mm steps, all photon with exit radius larger than 5 mm are binned into one value. All values for the white simulation are calculated from the same base simulation.

eliminated when the weight was smaller than 0.00001 and only short paths and small exit radii appear, while in the white simulation a photon was aborted after 1000 scattering events equivalent to $\frac{\mu_s+\mu_a}{\mu_s} \cdot 1000 = 1500$ total events and an elimination weight of $\alpha^{1500} = \frac{\mu_a}{\mu_s+\mu_a}^{1500}$. Thus, longer paths are sampled.

When the absorption coefficient gets much smaller than the scattering coefficient as it is the case for most tissues, the above effects are negligible.

**Code Implemented here**

The code implemented here is a mixture of both the above presented codes and the structure is shown in Figure 5.5. A photon is eliminated after 1,000 scattering events. In [209] a photon is eliminated after 20,000 scattering events. This was tested for geometry 6.1b (explained later) and the difference was not significant but the simulation took 4.2 times longer. Scaling of the photon weight is done according to the path lengths as introduced in [207]. Only the code for a single layer is implemented as scaling of multiple layers is not necessary as only the properties of the mucosa are to be changed according to the blood content. Further, the tracking of photons in the whole medium poses more requirements regarding code, storage, and computation time and the code does not implement refractive index changes between the layers which would be necessary at the air-tissue interface in the ear.

Further, it was discovered that the code for a single medium can be used to scale the absorption coefficient of multiple layers and scattering coefficient of the last layer, a semi-infinite slab. The scattering coefficient of all other layers must be set to the desired one. Hence, this code can be used to scale the absorption coefficient of eardrum and mucosa, and scattering coefficient of the mucosa.

### 5.3.3 Geometrical Optics for Propagation inside the Optical System

The inputs to the Monte Carlo simulations are the entry position on the surface and propagation direction of the photon. The focused input beam is sampled as described in [210]. The input position of the photon is given by a random position within the input beam and the propagation direction is calculated according to the position and NA of the optics. The Monte Carlo simulation implemented here accounts for the refraction at the surface so that the calculation of the depth of focus in the tissue as done in [210] is not necessary.

The output of the Monte Carlo simulations are the exit position of the photon, its direction, weight, and saved path inside the medium (optional). This information is used as input for the simulation of the optical system in order to calculate the incident power at the detector. A paraxial

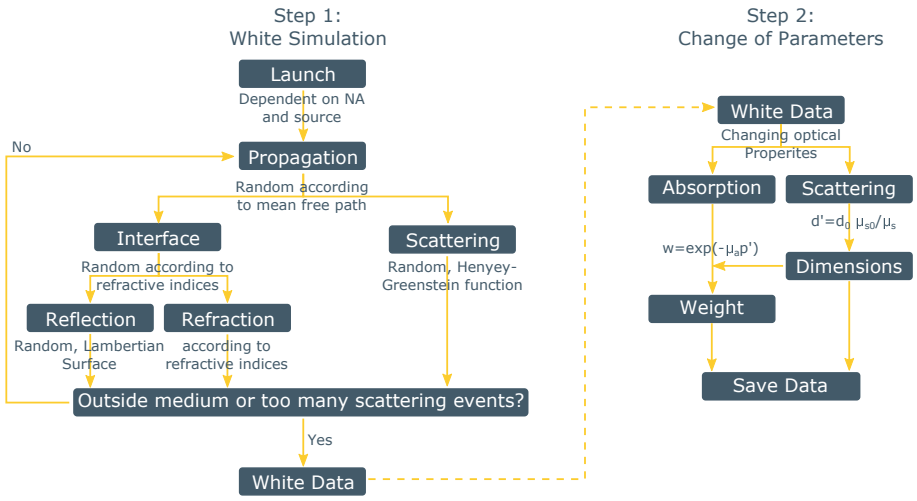


Figure 5.5: Structure of the White Monte Carlo code.

approximation and a skew optics calculation are implemented. The first one is used for small NA of the system and the second one when a higher NA of the system is tested.

### Paraxial and thin Lens Approximation

Lenses are approximated by thin lenses and angles are assumed to be small resulting in the cosine of the angle towards the optical axis to be 1 ($\cos(\gamma) \approx 1$) and the sine and tangent are approximated by the angle itself ($\sin(\gamma) \approx \gamma$ and $\tan(\gamma) \approx \gamma$), according to the paraxial approximation. The paraxial approximation is valid when the system with small NA of 0.08 is simulated. For example the error $e = \frac{\alpha - \sin(\alpha)}{\sin(\alpha)}$ is 0.11 % for the angle $\alpha = 0.08\,\text{rad} = 4.6\,\text{deg}$ equal to the NA of 0.08. The formulae for geometrical optics in the 3-dimensional case are described in [211]. For the 3-dimensional case the components $x$ and $y$ perpendicular to the optical axis $z$ can be calculated independently and the output position $x'$ and output angle $\alpha'$ are given by

$$\begin{pmatrix} x' \\ \cos(\alpha') \end{pmatrix} = M \cdot \begin{pmatrix} x \\ \cos(\alpha) \end{pmatrix} \tag{5.11}$$

where $x$ and $\alpha$ are input parameters, and $M$ is the propagation or refraction matrix. For the y-components $x$ is replaced by $y$ and $\alpha$ by the angle in y-plane $\beta$. The $z$-dimension is not calculated as $\cos(\gamma)$ is assumed to be 1. The propagation matrix for a free air space is

$$M_{\text{Air}} = \begin{pmatrix} 1 & d \\ 0 & 1 \end{pmatrix} \tag{5.12}$$

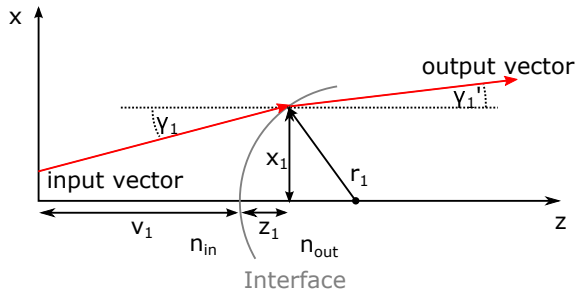


Figure 5.6: Geometry used for skew ray propagation, only two dimensions are shown.

with propagation distance $d$, and the matrix for refraction at a thin lens is

$$M_{\text{Lens}} = \begin{pmatrix} 1 & 0 \\ -1/f & 1 \end{pmatrix} \tag{5.13}$$

with the focal length $f$.

### Skew Ray Optics

The paraxial approximation is not true for photons with high angles towards the optical axis. This is the case when simulating optical systems with higher NA. Thus, a second code is implemented to propagate the photons through the optical system without using approximations. The formulae for non-paraxial and non-meridional or skew rays are given in [212]. Instead of the thin lens approximation, the real lens definitions are used here, given by the surface curvatures, thickness, and refractive index of the materials. Hence, the propagation through a singlet lens is composed of three actions, refraction at the first surface, transmission through the lens to the second surface, and refraction at the second surface. The new coordinates ($x'$ and $y'$) and angles ($\alpha'$ and $\beta'$) are calculated as done previously according to Equation (5.11) and the calculation of the third dimension $z'$ and angle $\gamma'$ changes to

$$\begin{pmatrix} z' \\ \cos(\gamma') - K/(c \cdot n_{\text{out}}) \end{pmatrix} = M_{\text{refraction}} \cdot \begin{pmatrix} z \\ \cos(\gamma) \end{pmatrix} \tag{5.14}$$

for refraction and

$$\begin{pmatrix} z' + v \\ \cos(\gamma') \end{pmatrix} = M_{\text{transformation}} \cdot \begin{pmatrix} z \\ \cos(\gamma) \end{pmatrix} \tag{5.15}$$

for transformation.

The propagation and refraction matrices are defined differently. Figure 5.6 shows a sketch of the geometry of an optical system showing only two dimensions for simplicity. The matrix for

propagation in a medium is given by

$$M_{\text{transformation}} = \begin{pmatrix} 1 & T \\ 0 & 1 \end{pmatrix} \tag{5.16}$$

$$T = \frac{F}{-E + \sqrt{E^2 - cF}} \tag{5.17}$$

$$E = c \cdot [d\cos(\gamma) + x\cos(\alpha) + y\cos(\beta)] - \cos(\gamma) \tag{5.18}$$

$$F = c \cdot (d^2 + x^2 + y^2) - 2d \tag{5.19}$$

$$c = \frac{1}{r} \tag{5.20}$$

$$d = z - v \tag{5.21}$$

with the surface radius $r$ of the lens with curvature $c$, $v$ the distance on the optical axis from start position to intersection of the next interface with the optical axis, and $E$ and $F$ are dummy variables to simplify the formula. $z$ is the distance from the intersection of the interface at the optical axis to the z-position where the ray hits the interface.

The matrix for refraction at a medium interface is given by

$$M_{\text{refraction}} = \begin{pmatrix} 1 & 0 \\ -K/(SQn_{\text{out}}) & n_{\text{in}}/n_{\text{out}} \end{pmatrix} \tag{5.22}$$

$$K = c \cdot \left[ n_{\text{out}} \sqrt{1 - \left(\frac{n_{\text{in}}}{n_{\text{out}}}\right)^2 (1 - \cos(\phi)^2)} - n_{\text{in}} \cdot \cos(\phi) \right] \tag{5.23}$$

$$\cos(\phi) = \frac{\cos(\gamma)(1 - cz) - \cos(\alpha)xc - \cos(\beta)yc}{SQ} \tag{5.24}$$

$$SQ = \sqrt{(x^2 + y^2)c^2 + (1 - cz)^2} \tag{5.25}$$

### 5.3.4 Test of the Code

The code is tested and compared to codes presented in literature in order to ensure correct implementation.

#### Monte Carlo Code

The standard and white Monte Carlo code are tested on and compared to the results of the tests geometries described in [204], Chapter 6.1, 6.2, and 6.6.

The first geometry (6.1a) is a single slab with refractive index of 1, scattering coefficient of $9\,\text{mm}^{-1}$, absorption coefficient of $1\,\text{mm}^{-1}$, anisotropy factor of 0.75, and a thickness of 0.2 mm. 50,000 photons are simulated and total transmittance and reflectance recorded. Results of the normal and white Monte Carlo code implemented here and the reference code are given in Table 5.1. Second, the total reflectance of a semi-infinite half space with refractive index of 1.5, scattering

Table 5.1: Results of test geometry [204] 6.1a). The average and standard deviation of 5 independent simulations is given for the tested code.

| Source | Reflection | Transmission |
|---|---|---|
| [204] | 0.0973 ± 0.0004 | 0.6610 ± 0.0002 |
| standard Code | 0.0973 ± 0.0005 | 0.6611 ± 0.0013 |
| white Code | 0.0978 ± 0.0010 | 0.6605 ± 0.0010 |

Table 5.2: Results of test geometry [204] 6.1b). The average and standard deviation of 5 independent simulations is given.

| Source | Total Reflection |
|---|---|
| [204] | 0.2591 ± 0.0017 |
| standard Code | 0.2590 ± 0.0009 |
| white Code | 0.2595 ± 0.0007 |

coefficient of $9\,\mathrm{mm}^{-1}$, absorption coefficient of $1\,\mathrm{mm}^{-1}$, and anisotropy factor of 0 is simulated using 50,000 photons and the results is presented in Table 5.2.

The angular resolved reflectance and transmission of a slab is tested in 6.2. The optical properties are the same as in 6.1a and 100,000 photons are used this time. Figure 5.7 compares the angle of the exiting photons of both simulations.

Finally, a multi layered tissue is simulated. Transmission through three layers and the reflection are recorded and resolved by distance of exit position to incident position. The optical properties of all three layer are reported in [204], 100,000 photons are simulated, and total transmittance and reflectance reported in Table 5.3 and the radial resolved transmittance and reflectance in Figure 5.8. It has to be noted that the radial position in the multi-layer geometry (6.6) is scaled by the area (circumference and radial step size) thus the units of $\mathrm{mm}^{-2}$. Further, no reflection at the first surface is considered in this simulation.

The presented tests involve single and multiple layered tissues, transmission, reflection, radial,

Table 5.3: Results of test geometry [204] 6.6. The average and standard deviation of 5 independent simulations is given.

| Source | Diffuse Reflection | Transmission |
|---|---|---|
| [204] | 0.2375 | 0.0965 |
| standard Code | 0.2390 ± 0.0021 | 0.0959 ± 0.0010 |
| white Code | 0.2392 ± 0.0027 | 0.0963 ± 0.0011 |

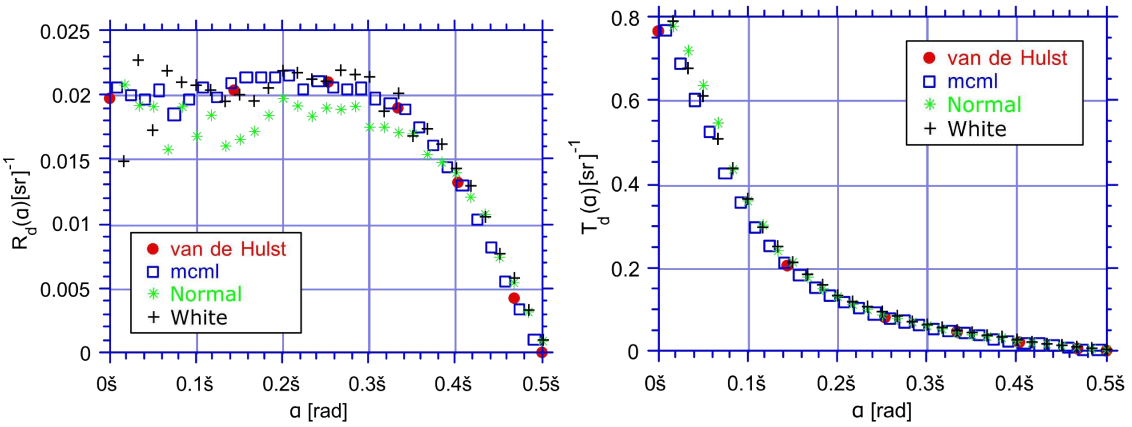


(a) Reflection (b) Transmission

Figure 5.7: Test (Normal and White) and original (van de Hulst and mcml [204]) results of scenario [204] 6.2. Simulated without reflection at the first surface.

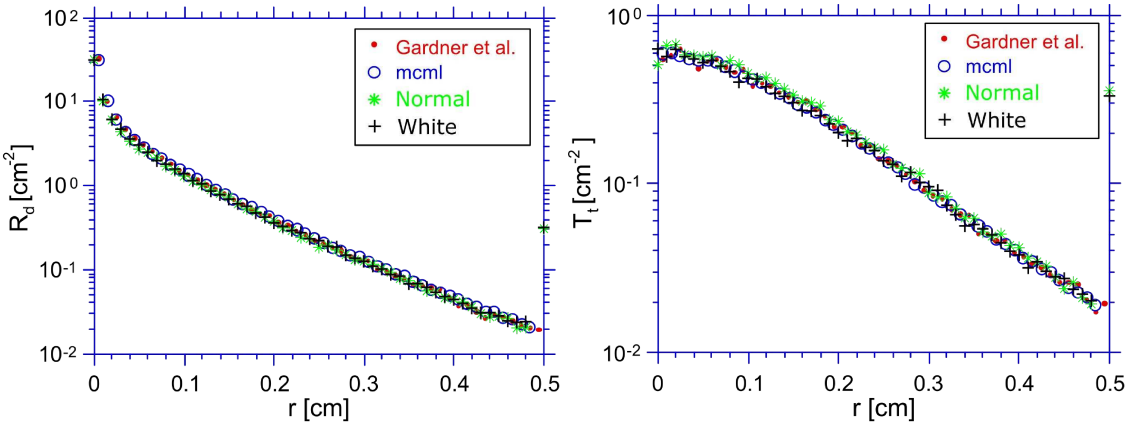


(a) Reflection (b) Transmission

Figure 5.8: Test (Normal and White) and original (Gardner and mcml [204]) results of scenario [204] 6.6. Simulated without reflection at first surface, all other reflections are specular. Changes of the normal MC code as suggested not implemented.

Table 5.4: Test of different implementations of the white Monte Carlo code using normal code and white code implementing scaling of absorption and scattering coefficient. White base simulation for test of scaling of the scattering coefficient was done with $\mu_{s,0} = 20\,\mathrm{mm}^{-1}$. $10^6$ photons were simulated for each run. The average and standard deviation of five simulations are given here. "white $N$" means the weight was calculated by the number of scattering events, "white $p$" means the weight was calculated by the path length.

| **coefficients** [$\mathbf{mm}^{-1}$] | | **Reflection** [%] | | | | |
|---|---|---|---|---|---|---|
| | | | **scaling of $\mu_a$** | | **scaling of $\mu_a$ and $\mu_s$** | |
| $\mu_s$ | $\mu_a$ | **normal** | **white $N$** | **white $p$** | **white $N$** | **white $p$** |
| 10 | 10 | $0.108 \pm 0.004$ | $0.070 \pm 0.002$ | $0.225 \pm 0.005$ | $0.071 \pm 0.003$ | $0.232 \pm 0.011$ |
| 10 | 1 | $3.144 \pm 0.034$ | $3.129 \pm 0.036$ | $3.515 \pm 0.048$ | $3.157 \pm 0.050$ | $3.548 \pm 0.060$ |
| 10 | 0.1 | $25.871 \pm 0.095$ | $25.870 \pm 0.096$ | $26.050 \pm 0.102$ | $26.107 \pm 0.071$ | $26.256 \pm 0.069$ |

and angular distribution of the signal. The results of both codes are similar (within variability due to the random nature of MC simulation) to the reference, indicating a correct implementation of the code used here.

None of these tests checks for correct implementation of the scaling of the scattering coefficient in white simulations. Hence, a custom test geometry is set up and simulations performed to test scaling of the scattering coefficient in the white Monte Carlo Code. Results from the normal, white code with actual simulated scattering coefficient, and white code with scaled scattering coefficient are compared. The geometry is a semi-infinite slab and the reflection signal is registered. Optical parameters and total reflection values are given in Table 5.4 and Figure 5.4 shows the radial distribution indicating correct scaling of dimensions (scaling by scattering events, not path length). 100,000 photons are used for simulation, five simulations were conducted with the average and standard deviation shown in the table, and reflection at the surface is neglected.

An error between the different implementations is visible for high absorption coefficient but falls within the error due to the random nature of the Monte Carlo simulation for small absorption coefficients, that are typical for tissues. Scaling by scattering event produces more accurate results and is implemented here.

### Geometrical Optics

The code for geometrical optics was compared with the results of the design software for optical systems "WinLens3D" (Qioptiq, Paris, France). A single lens system is simulated, using the thin lens approximation for paraxial optics and a completely defined lens for skew optics. The tested

geometry is shown as sketch in Figure 5.9 on the top. The lens has a focal length of 30 mm (AC254-030-B, Thorlabs, Newton, New Jersey, USA) and is an achromatic doublet. The distance from the object to the first lens surface is set to 40 mm, and the distance to the image is 120 mm for the thin lens approximation and 115.08 mm for the complete defined skew ray test.

Several rays are tested, as shown in Figure 5.9 in subfigures 1 to 5. In the first one, only one plane is used. The ray starts at distance $x = o$ off axis at the object (indicated by the red dot) and propagates to the optical axis at the lens surface (indicated by the tip of the arrow). In the second test only one plane is used again, but the propagation angle is changed, the start position is the same but the ray propagates parallel to the optical axis. In the other tests the geometry is expanded to 3 dimensions. In (3) the start position is the same, but the ray moves in an angle of 45 deg and reaches the lens at $x = 0$ and $y = o$. In (4) the y-coordinate is included into the start position ($x = y = o/\sqrt{2}$) and the ray reaches the lens on the optical axis. And finally, in (5) the ray propagates in a way that the optical axis is not passed.

To change the rays in WinLens3D, one must open the table "Single Ray" and change the input "Field X/Y" and "Apt. X/Y". Both field are values between $-1$ and 1, where 1 for the field means the ray starts at the maximum diameter of the object $o$, and $-1$ results in $-o$. The value for "Apt." gives the position where the ray passes the aperture, and a value of 1 again means maximum aperture. The image position is given by "X" and "Y" of the last plane called "Img" and the cosine of the angle to the optical axis is given by the field "N".

The calculated position at the image plane and the angle between the ray and the optical axis are compared for WinLens3D and the implemented MATLAB code and results shown in Table 5.5. The results fit well, showing that the code is correct. The variation in the position calculated with skew optics and the thick lens compared to the paraxial approximation result from aberrations of the lens that are not calculated by the approximations and are the same for the WinLens3D reference and for the implemented code.

## 5.4 Simulation of the Anti-Confocal System

After the anti-confocal system and simulation code have been explained, the simulated geometries and the simulation results will be presented in this section.

### 5.4.1 Simulated Geometry

First, the transmission experiment to characterise the eardrum and eardrum phantoms presented in Section 3.4.4 was simulated in order to determine the optical parameters of the eardrum. Results were presented earlier.

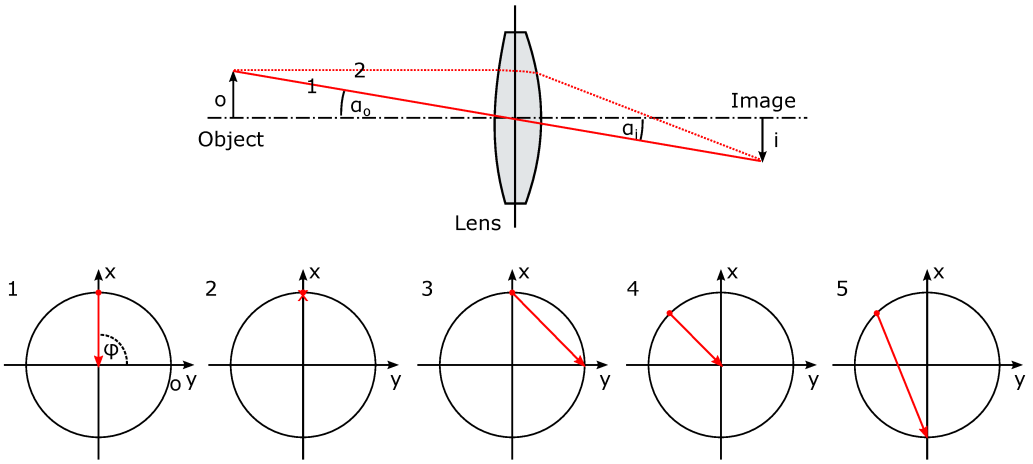


Figure 5.9: Test Geometry for geometrical optics code. The top drawing shows the system composed of a doublet lens, object, and image. The images on the bottom show 5 tested rays, when looking along the optical axis of the system. The red arrow indicates the tested ray, starting at the object at the position marked with the dot and hitting the first lens surface at the end of the arrow. The cases 1 and 2 are shown in the top sketch.

Table 5.5: Comparison of WinLens3D (WL3D) results with the code implemented here

| | | **Inputs/Object** | | | | **Outputs/Image** | | | |
|---|---|---|---|---|---|---|---|---|---|
| | | **Size** $o$ | | **Angle** $\alpha$ | | **Angle** $\alpha'$ | | **Size** $i$ | |
| | **Case** | $x$ | $y$ | $\alpha_o$ | $\varphi$ | **WL3D** | **code** | **WL3D** | **code** |
| **paraxial** | 1 | 0 | 1.397 | 2 | 90 | 2.000 | 2.000 | 4.190 | 4.191 |
| | 2 | 0 | 1.397 | 0 | 90 | 2.666 | 2.666 | 4.191 | 4.191 |
| | 3 | -1.397 | 0 | 2.828 | 45 | 2.108 | 2.109 | 4.191 | 4.191 |
| | 4 | 0.988 | 0.988 | 2 | 45 | 2.000 | 2.001 | 4.190 | 4.191 |
| | 5 | 0.988 | 0.988 | 3.692 | 22.5 | 1.600 | 1.602 | 4.190 | 4.191 |
| **skew** | 1 | 0 | 1.397 | 2 | 90 | 1.948 | 1.948 | 4.198 | 4.198 |
| | 2 | 0 | 1.397 | 0 | 90 | 2.617 | 2.617 | 4.207 | 4.207 |
| | 3 | -1.397 | 0 | 2.828 | 45 | 2.058 | 2.059 | 4.190 | 4.191 |
| | 4 | 0.988 | 0.988 | 2 | 45 | 1.948 | 1.948 | 4.198 | 4.198 |
| | 5 | 0.988 | 0.988 | 3.692 | 22.5 | 1.536 | 1.537 | 4.159 | 4.160 |

Table 5.6: Optical parameters of the simulated middle ear

| Layer | scattering coef., $\mu_s$ [1/mm] | scattering anisotropy, $g$ | absorption coef., $\mu_a$ [1/mm] | refractive index, $n$ | thickness, $t$ [mm] |
|---|---|---|---|---|---|
| Eardrum | 11.00 | 0.990 | 1.800 | 1.43 | 0.1 |
| Middle ear cavity | 0 | 0 | 0 | 1 | 3 |
| Mucosa | 6.25 | 0.897 | 0.035 | 1.40 | inf. |

Next, the complete anti-confocal system is simulated. Two slightly different geometries were simulated, one including the otoscope speculum and one without. The first variation is used to characterise the anti-confocal system and simulate the influence of different parameters on the performance. The latter is used to investigate changes of the NA of the system and in the next chapter simulating spectroscopic measurements. The reason for this is that the optical bench top setup was implemented without the speculum in place and simulations are intended to be as close to the optical setup as possible.

The simulated sample consists of 4 layers, layer 1 includes the optical system and the medium is air. The middle ear is composed of eardrum, air-filled middle ear cavity, and mucosa with infinite expanse. The properties of these three layers are summarised in Table 5.6 and were defined in Section 3. The illumination is simulated by a beam with homogeneous power distribution, focus angle given by the NA, and focused on the eardrum surface. These settings are used as standard parameters in all simulations unless stated otherwise.

Figure 5.10 shows the complete simulated geometry of middle ear and optics used to characterise the anti-confocal system. For simulations presented in this chapter, both lenses are simulated with a focal length of 30 mm and placed $2f = 60$ mm apart. In all simulations using the small NA of 0.08, the lenses are simulated as thin lenses and a paraxial approximation is used for light propagation. In the case simulating higher NA real lens models and skew optics formula are used. The stop is placed in the image plane of the eardrum. The speculum aperture is placed 9.9 mm away from the eardrum (resulting from an average distance of the speculum to eardrum of 13 mm [45] scaled to the focal length of the simulated lens) and has an aperture radius of 1.5 mm.

The aperture is only used when simulating the system with NA of 0.08 and varying the other parameters but not used when simulating different NAs. The radius of the objective lens aperture is $r = D/2$ with the diameter $D$ given by the NA of the system as follows.

$$D = \tan(\arcsin(NA)) \cdot 2f \tag{5.26}$$

The system without speculum was simulated in order to compare simulations with the experimental system. Dimensions were adapted to the experimental system, the objective lens has a

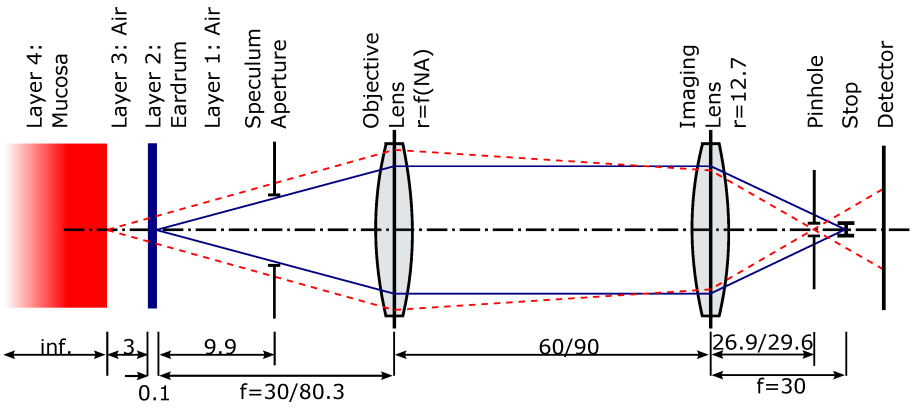


Figure 5.10: Simulated Geometry with both stop and pinhole position shown. Dependent on the simulation parameters either pinhole, stop, or both elements are used.

focal length of 80.3 mm, and the distance between both lenses is 90 mm. The beam splitter is not simulated and the aperture of the speculum removed. The radius for the objective lens aperture of 6 mm is used in the simulations giving an NA of about 0.08. Skew optics are used here instead of the paraxial approximation.

### 5.4.2 Variable Parameters of the System

Several parameters of the optical system as well as the middle ear can change and might have an influence on the measurements. While parameters of the optical system can be changed (within certain limits) the parameters of the middle ear cannot be controlled. During simulations of the anti-confocal system below, simulation of spectroscopic measurements (Section 6), and experiments on the anti-confocal, and spectroscopic system (Section 7) these parameters will be varied and their influence on measurements investigated. Table 5.7 summarises these parameters, their standard value, and variation range during simulations.

The absorption of the middle ear mucosa is influenced by the inflammatory state and blood content and is the value to be measured. It changes during inflammation, is wavelength dependent, and spans the range from 0.037 to 2.74 $\mathrm{mm}^{-1}$. A constant value is used during the investigation of the anti-confocal system and is only varied when investigating spectroscopic measurements of inflamed tissue. The stop radius is to be optimised, finding a trade-off between low detected signal from the eardrum and high signal from the mucosa.

According to previously presented theory the anti-confocal system is best focused on the eardrum, nonetheless, a shift of the focus is investigated. Further, a combination of confocal and anti-confocal filtering is investigated. Last, the NA of the system can be adopted as well. The maximum possible NA of the optics within the otoscope speculum is 0.08. A smaller illumination

Table 5.7: Parameters that can change in the optical system and the middle ear and can have an influence on the anti-confocal measurement of inflammation.

| **Parameter** | **Standard Value** | **Variations** |
|---|---|---|
| **Parameters of the Middle Ear** | | |
| Absorption of the mucosa | dependent on inflammatory state | |
| Scattering of the mucosa | 6.25 | $\pm 5$, 10, 20 % |
| Absorption of the eardrum | 1.8 | $\lambda$ dependent and independent change |
| Scattering of the eardrum | $g = 0.99$; $\mu_s = 11\,\mathrm{mm}^{-1}$ | $g = 0.9$, 0.6; $\mu_s = 22$, 33, $44\,\mathrm{mm}^{-1}$ |
| Distance between eardrum and mucosa | 3 mm | 0.1, 0.5, 2, 4,8 mm |
| Roughness of the surfaces | flat | rough |
| Angle between eardrum and mucosa | 0 ° | 5, 10 ° |
| **Parameters of the Optical System** | | |
| Stop radius | to be determined | |
| Combination of pinhole and stop | stop only | stop & pinhole |
| Focus | on eardrum surface | focus shifted towards eardrum |
| Illumination NA | 0.08 | 0.003 |
| Detection NA | 0.08 | 0.027–0.27 |

NA will reduce the complexity of the optical system as less lenses are required for beam expansion and its influence on the system tested. A maximum possible NA is assumed to be best as more signal can be detected, this is tested by varying the NA over a wider range of 0.027 to 0.27.

While the absorption of the mucosa is the change to be measured other parameters of the sample can influence the measurement and may make detection of the absorption impossible. To investigate their influence each parameter is changed while all other parameters are kept constant. These parameters are listed in Table 5.7 and shortly explained here: The scattering coefficient of the mucosa which will directly influence the back scattered signal but changes might be compensated for my multiple wavelength measurements. The absorption and scattering characteristics of the eardrum will influence the signal level and distribution reaching the mucosa as well as the background signal from the eardrum itself. The distance between eardrum and mucosa will influence the spread of the signal and thus the illuminated area on the mucosa as well as the need for a sharp cut-off between signal and background planes. Finally, the orientation angle and roughness of both eardrum and mucosa will influence the distribution of reflected light and thus influence the signal level detected by the system with NA of 0.08.

The influence of most of these parameters on the anti-confocal is discussed in the results below. Absorption of eardrum and mucosa are wavelength and inflammation dependent and hence, are not discussed here as only the performance of the anti-confocal system is investigated but are included later when discussing spectroscopic measurements. Also, scattering of the mucosa is not investigated here as multi-wavelength measurement might be able to compensate for these changes.

### 5.4.3 Results

In order to analyse the performance of the confocal compared to the anti-confocal system, the signal-to-background (SBR) is proposed analogue to the commonly used signal-to-noise ratio (SNR). The signal $s$ is calculated as the sum of the weight of photons exiting the middle ear that reached the mucosa surface or penetrated the mucosa and thus carry information about the mucosa. Background $b$ on the other hand is defined as the photons that do not reach the mucosa and have been back scattered by the eardrum and have then been detected. The SBR is given as the relation of signal to background photons.

$$SBR = \frac{s}{b} \tag{5.27}$$

While the signal level and SBR of a single measurement are investigated here, multi-wavelength measurements will be investigated in the next chapter.

#### Flux

First, the flux of all simulated photons is shown in Figure 5.11 a). The right part of the figure shows the optical system with positions of speculum aperture, both lenses, and focus of the eardrum marked in white. The left figure shows the middle ear with interfaces between eardrum middle ear cavity, and mucosa marked. The flux is shown in logarithmic scale dependent on the radius and consequently the power at higher radii is higher as a larger area is analysed. The z-axis of both figures is scaled differently while the radius from the optical axis shows the same scale.

Subfigure (a) shows the complete signal and background superposed. The signal propagates far into the mucosa, but the power decreases exponentially, even though this is not obvious due to logarithmic scaling. Photon paths in the optical system are cut off, when passing outside the speculum and objective lens aperture. Subfigure (b) shows only signal reaching the detector, and (c) shows only background reaching the detector.

The background shows a clear focus at the eardrum image plane. The stop is best placed at this position. The signal focus is shifted towards the sample and shows much more scattered and wide spread signal and hence signal is able to pass the stop. The signal near the optical axis inside the mucosa seems to be low and photons to be scattered away from the axis. This is due to the fact

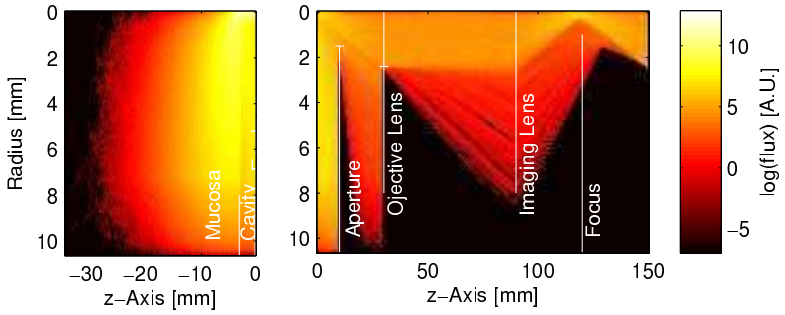


(a) All photons

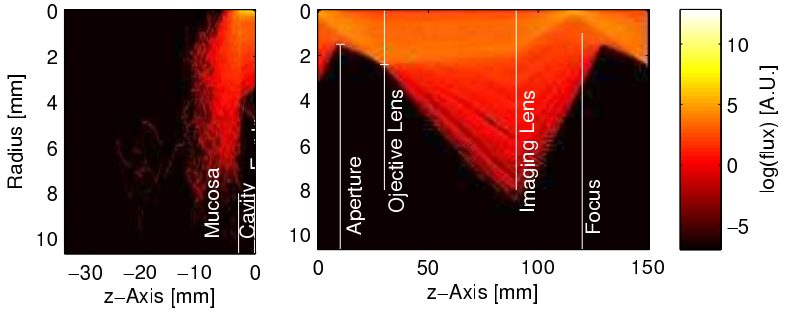


(b) Signal reaching detector (no confocal or anti-confocal filtering)

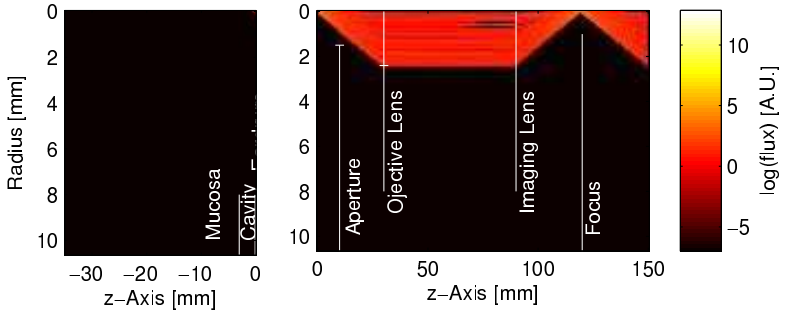


(c) Background reaching detector (no confocal or anti-confocal filtering)

Figure 5.11: Simulated flux of photons in middle ear and optical system. The graphs are split into tissue (left) and optical system (right). The positions of the surfaces are marked in white in the tissue and the position of the speculum aperture, lenses, and focus in the optical system. Further, the maximum aperture of objective lens and speculum are marked by horizontal lines.

that the signal is shown over radius and hence larger volumes are sampled for a higher radius. A scaling by the area would normalise the signal but this is not done as the total power is important.

### Combination with Pinhole and Variation of the Position

First, it is tested whether variation of the theoretical stop position and combination of stop and pinhole can improve the performance of the anti-confocal system. For this the stop and pinhole are moved along the optical axis, the radius of both elements changed, and signal and SBR recorded.

The simulation results (no plots given) show, that neither addition of a pinhole nor changes of the position of either element improves the performance of the anti-confocal system. The speculum and objective lens aperture reject widely scattered and reflected light and act as large apertures. As shown later, when changing the NA of the optical system in simulations, this restricts the detected signal and reduces the SBR.

### Stop Radius

The influence of the radius of the pinhole in the confocal case and the stop in the anti-confocal case on the signal and SBR are investigated here. For this the radius of both elements is varied from 0 to 2.5 mm and the results are shown in Figure 5.12, where the confocal data is shown in blue and the anti-confocal data in red. The left graph shows the signal (in arbitrary units A.U. equal to the weight of detected photons, with $10^7$ simulated photons and initial weight of 1) and the right graph the SBR.

The confocal system has its lowest signal level for the smallest pinhole radius, as expected as a small pinhole rejects most light. The signal level increases with increasing pinhole radius as more light can pass through the pinhole. For small radii the increase is high and then slows down. The SBR behaves inversely, it is highest for a small pinhole radius and then decreases, first quickly and then is almost constant and even increases slightly. The anti-confocal system shows highest signal level for a small stop radius and the signal decreases with increasing stop radius. The SBR is lowest for a small stop and increases continuously, with a high increase for very small radii.

As the pinhole blocks out of focus light it is obvious that the SBR is highest for small pinhole radii as most background is blocked. But at the same time more signal components are blocked, as signal is defined as photons not only from the focus plane but also as photons penetrating the mucosa, a semi-infinite half space. A confocal microscope achieves best performance with respect to SBR and signal level at a pinhole radius of just below 4 optical units $OU = \frac{\lambda}{2\pi NA}$ [196]. Here, this value is $4 \cdot OU = 6.4\,\mu\text{m}$ and a pinhole radius of $5\,\mu\text{m}$ is used for further analysis (chosen as closest value within the sampled grid in the simulations) of the confocal setup and marked in both signal and SBR plot with a black circle. The strong increase in signal at the beginning is due

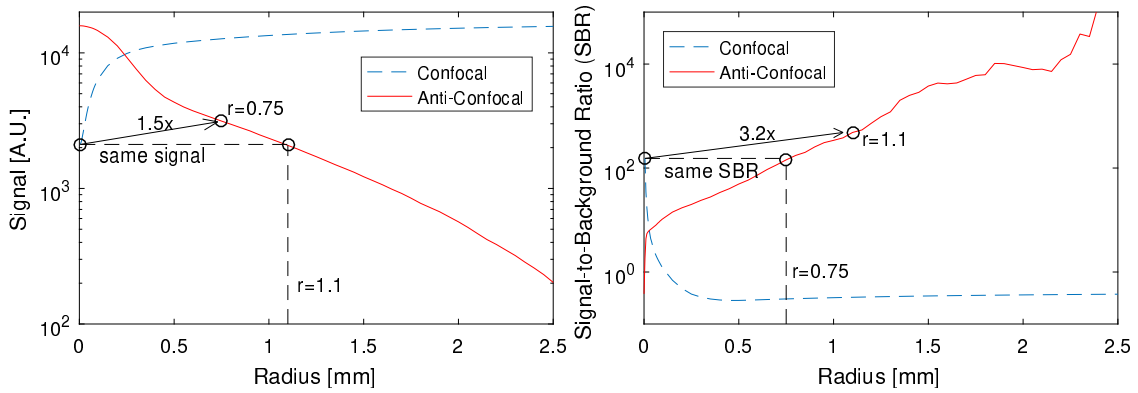


(a) Signal (b) SBR

Figure 5.12: Influence of the stop and pinhole radius on signal and SBR. The confocal system would normally be used with a pinhole radius of around 6 µm [196]. This point is marked in both plots and the same signal level and SBR of the anti-confocal system are marked in the left and right figure, respectively, connected by the dotted line. In the signal plot, the third marker (connected by the arrow) indicates the improved signal level at the radius ($r = 0.75\,\text{mm}$) where the SBR is the same, as shown in the SBR graph. In the SBR plot, the improved SBR at $r = 1.1\,\text{mm}$ is shown where the signal is the same.

to the fact of the exponential light distribution in tissue and hence most signal close the optical axis. Much more signal components are detected close to the optical axis while fewer signal is present further away from the optical axis resulting in a slower increase. The SBR decreases as more background is detected and its level increases more quickly than the signal. At higher radii, the background increases less and the SBR can increase slightly. This is due to the fact, that the background is mostly caused by reflections and the signal caused by scattering. Scattered light is further spread and still present far away from the optical axis. Background on the other hand is only present closer to the optical axis and does not increase further for high stop radii.

The signal in the anti-confocal case is highest for small stop radii as no signal is blocked. A small stop does not block much signal as it is out of focus and hence the signal shows a slow decrease at first. Up to a stop radius of 0.5 mm the signal then decreases more quickly as the blocked area increases and most signal is concentrated close to the optical axis. Over 0.5 mm stop radius the decrease slows down as less signal is scattered this far. The SBR increases quickly for small stop radii as the direct reflection from the eardrum surface is blocked easily by a small stop as the illumination beam is focused on the eardrum surface and the image is small. The increase in SBR then slows down as firstly, the signal decreases as well and secondly, as little more background components are scattered this far and are blocked by the increasing stop radius.

The SBR reaches much higher values for the anti-confocal system than for the confocal system. But the signal level is compromised when reaching a high SBR. For better comparison, the signal of the anti-confocal system is fixed to the level of best performance of the confocal system (pinhole radius of 5 µm) and the SBR compared. The signal level at this radius is about 2100 and the SBR is 150. The anti-confocal system reaches a similar signal level with a stop radius of 1.1 mm. The SBR is with a value 480 about 3.2 times higher. When fixing the SBR of the anti-confocal system to the best value of the confocal system, and comparing the signal level an improvement of factor 1.5 (signal level of 3140) is achieved. The stop radius is 0.75 mm in this case. This shows that the anti-confocal system can reach better performance than the confocal system as expected and explained in the introduction of the anti-confocal system.

#### Random Error of the Simulation

The error in the results due to the random nature of the Monte Carlo methods is investigated here. For this 10 simulations with each $10^6$ photons are performed and the standard deviation is calculated and used to characterise the error of the simulation. When combined, this results in the $10^7$ photons used in the previous section. The maximum error of the signal is 23 % and occurs when high stop radii are used. In these cases the signal level is low and hence the variation due to the random nature of the simulation is higher as the error scales with the square root of the number samples $\sqrt{N}$ [213]. The calculation of the SBR is dependent on the background, which is much lower than the signal using correct filtering. This results in lower samples and thus higher variations. Hence, the variation of the SBR is higher and shows standard deviation values up to 89 %.

But as all 10 simulations are combined in the previous results, the photon number is increased by a factor of 10 while the error is only increased by a factor of $\sqrt{10}$, resulting in a $\frac{1}{\sqrt{10}}$ smaller error. In all future simulations the number of photons is increased to $10^8$ and hence the error reduced by a factor of 10 and can be assumed to be below 3 % for the signal and below 10 % for the SBR.

#### Scattering of the Eardrum

The optical properties of the eardrum used in the simulation were approximated using an animal eardrum model, consequently, the properties might not be accurate. Further, the eardrum changes its properties from human to human and especially during disease where the eardrum might be thickened or biofilms might be attached to the eardrum as discussed in Section 3.4.2. To account for these variation and inaccuracies, the scattering coefficient (11, 22, 33, and 44 $\mathrm{mm}^{-1}$) and anisotropy (0.99, 0.9, and 0.6) are varied and signal and SBR analysed. Results are shown in Figure 5.13, with

the scattering coefficient along the x-axis and different plots for changing scattering anisotropy. A stop radius of 1.1 mm is used in this and all following comparisons. The simulated values are indicated by the markers in the graph and the lines show exponential curves fitted to the simulated values. The exponential curves appear linear due to the logarithmic plotted y-scale.

The signal and SBR in the confocal system decrease with increasing scattering coefficient but are almost unaffected by the anisotropy. The anti-confocal system shows an interesting behaviour, signal level and SBR increase in certain cases even though scattering is increased. The signal for highly forward scattering ($g = 0.99$) increases slightly with increasing scattering coefficient, but decreases for less forward scattering ($g = 0.9$ and 0.6). The SBR decreases for highly forward scattering while it increases for the other cases. The signal decreases with a decreasing scattering anisotropy while the opposite is true for the SBR. The exponential curves fit well with $R^2$ values higher than 0.98 except for two cases. Approximating the SBR of the anti-confocal system with a scattering anisotropy of 0.99 results in $R^2 = 0.81$ and in the case of the anti-confocal SBR with $g = 0.6$ the last value ($\mu_s = 44\,\mathrm{mm}^{-1}$) is ignored to achieve a good fit with $R^2 = 1$. The latter shows that while the SBR can increase with increasing scattering, too high scattering will decrease the SBR again.

As described previously, the confocal system only detects scattered light when the distance between mucosa and eardrum is 3 mm as in this simulation. The number of unscattered photons is dependent on the scattering coefficient. The scattering anisotropy does not influence the number of scattered photons and hence does not influence the signal level significantly. The background mostly caused by reflections is less affected by the scattering characteristics and is relatively constant meaning the SBR decreases with the signal level.

The situation is more complex in the anti-confocal system, since scattered photons are detected here. The signal level depends on the number of photons scattered into the detection annulus defined by the stop radius and NA. The signal does increase when the scattering causes more photons directed into this annulus. This is the case for highly forward scattering and increasing scattering coefficient. For less forward scattering more photons are scattered away from the detection NA and the signal decreases. In the anti-confocal case, the detected background is not only caused by reflections from the eardrum surface but also by scattering inside the eardrum. Consequently, the noise is dependent on the scattering coefficient and anisotropy. For highly forward scattering a higher scattering coefficient causes more background to reach the detector, decreasing the SBR. For less forward scattering on the other hand, the higher scattering coefficient reduces the background and increases the SBR. A decreasing scattering anisotropy causes photons to be scattered with a wider angle and not falling into the detection NA, causing a decrease in the signal level. Nonetheless, the SBR increases as also less noise is detected.

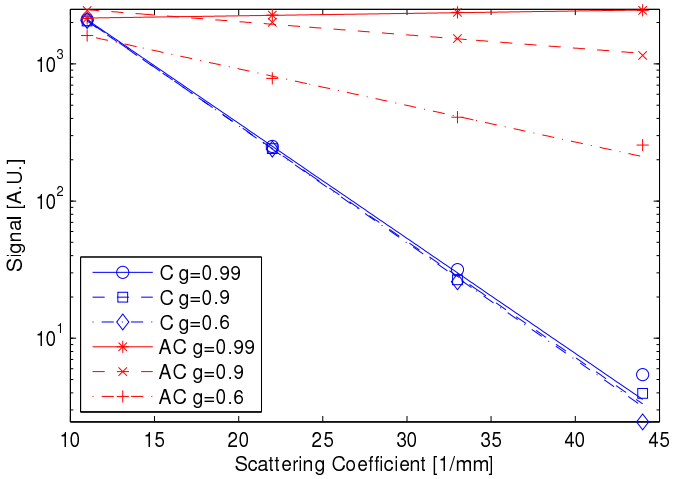


(a) Signal. $R^2_{\mathrm{C},0.99} = 1$, $R^2_{\mathrm{C},0.9} = 1$, $R^2_{\mathrm{C},0.6} = 1$, $R^2_{\mathrm{AC},0.99} = 0.986$, $R^2_{\mathrm{AC},0.9} = 0.993$, $R^2_{\mathrm{AC},0.6} = 0.997$.

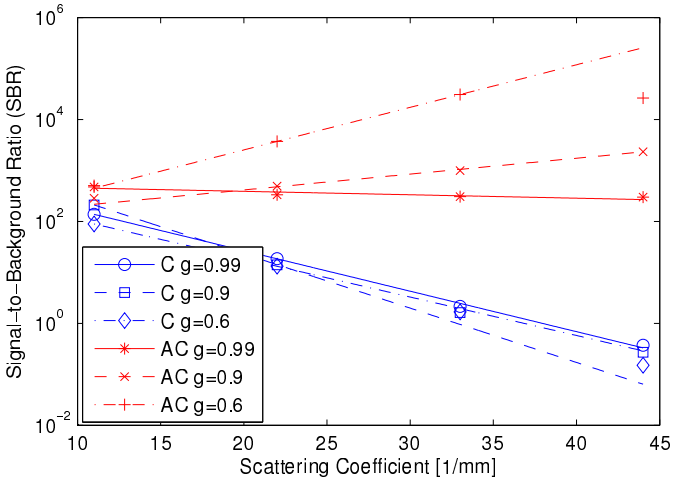


(b) SBR. $R^2_{\mathrm{C},0.99} = 1$, $R^2_{\mathrm{C},0.9} = 1$, $R^2_{\mathrm{C},0.6} = 1$, $R^2_{\mathrm{AC},0.99} = 0.81$, $R^2_{\mathrm{AC},0.9} = 0.997$, $R^2_{\mathrm{AC},0.6} = 1$ (ignoring last point).

Figure 5.13: Influence of scattering of the eardrum on signal and SBR. Markers indicate simulated values and lines indicate exponential fits, with $R^2$ values given for each fit. C – confocal, AC – anti-confocal.

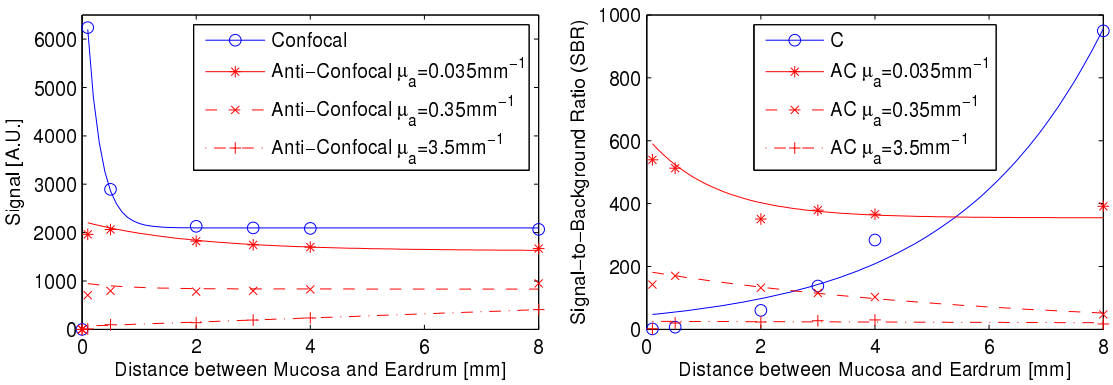


(a) Signal. $R^2_{\mathrm{C}} = 1$, $R^2_{\mathrm{AC},0.035} = 1$, $R^2_{\mathrm{AC},0.35} = 1$, $R^2_{\mathrm{AC},3.5} = 0.996$.

(b) SBR. $R^2_{\mathrm{C}} = 0.983$, $R^2_{\mathrm{AC},0.035} = 0.941$, $R^2_{\mathrm{AC},0.35} = 0.994$, $R^2_{\mathrm{AC},3.5} = 0.084$.

Figure 5.14: Influence of distance between eardrum and mucosa on signal and SBR. Three different graphs are shown for the anti-confocal case, with changed absorption of the mucosa according to the legend. Markers indicate simulated values and lines indicate linear (anti-confocal, $\mu_{\mathrm{a}} = 3.5\,\mathrm{mm}^{-1}$) or exponential (all others) fits, with $R^2$ values given for each fit.

The performance of the confocal system is always decreased for higher scattering coefficient while this is not the case for the anti-confocal system. The performance can even increase in certain cases. This shows that the anti-confocal system is suitable over a wider range of optical parameters of the scattering layer.

### Distance between Eardrum and Mucosa

The distance between eardrum and mucosa can vary from person to person and is dependent on the measurement position as neither eardrum nor mucosa are flat and both surfaces are not aligned in parallel. A distance between 2 to 4 mm is expected [3] and 3 mm is used as standard parameter, but here the distance is varied in a wider range of 0.1 to 8 mm in order to enhance the understanding of the system and results are shown in Figure 5.14. Three different plots are shown for the anti-confocal system, with the absorption coefficient of the mucosa increased by a factor of 10 and 100. This increase is appropriate as the absorption in the green wavelength range is about 10 times higher than in the NIR and the inflammation can increase the blood concentration and thus absorption again by a factor of 10. Markers indicate simulated values and lines indicate exponential or linear fits, with $R^2$ values given for each fit below the figure.

The confocal system shows a highest signal for a small distance between eardrum and mucosa. The signal decreases in exponential form with increasing distance and reaches a minimum limit at a distance of about 2100 A.U. at around 2 to 3 mm distance. The SBR is lowest for a small distance

and increases continuously with distance, also approximated by an exponential function. The anti-confocal system is less influenced by the distance between eardrum and mucosa. The signal decreases slightly for a low absorption coefficient but increases for higher absorption coefficients with increasing distance. The first value ($d = 0.1\,\mathrm{mm}$) is ignored for curve fitting in the anti-confocal case as it does not fit the general trend and an additional effect seems to play a role. The cases of lower absorption are best approximated with an exponential function with offset and the case with highest absorption ($\mu_\mathrm{a} = 3.5\,\mathrm{mm}^{-1}$) with a linear function. The SBR generally follows the signal but shows more fluctuations and bad $R^2$ value for highest absorption.

A confocal system with small pinhole diameter detects mostly unscattered photons. This number is unaffected by the distance between eardrum and mucosa. Hence, a constant signal level is expected as shown by the almost constant value for distance higher than 3 mm. The reason that the signal increases at small distances is the forward scattering nature of the eardrum. In case of a small distance, photons scattered with a small angle between optical axis and propagation direction can still reach the sampled volume as not propagating a long distance. These photons contribute to the signal even though they were scattered. When increasing the distance between scattering event and target, the travelled distance gets bigger and more and more photons fall outside the sampled volume and are not detected any more, decreasing the level of detected signal. The SBR increases as the background rejection ratio of a confocal system increases with distance of scattering and target layer, according to the point spread function presented in Equation (4.1).

Three separate effects are present for the anti-confocal system. Firstly, the optics focused on the eardrum move away from the mucosa when increasing the distance and hence the effective NA decreases. This results in less signal being detected, visible for an absorption coefficient of $0.035\,\mathrm{mm}^{-1}$. The second effect is that the stop moves further away from the image of the mucosa surface and thus blocks less signal photons and increasing the signal. This effect is strongest for small distances ($d = 0.1\,\mathrm{mm}$) and can be seen for all cases, and was ignored during curve fitting. The last effect is that with increasing distance, the signal is further spread on the mucosa due to scattering in the eardrum and the light being focused on the eardrum. This effect is small for low absorbing samples as the light propagates far inside the mucosa, compared to the size of the illuminated area. In case of high absorbing media, the path length inside the mucosa is smaller compared to the illuminated area. A stop rejects more signal, when the illuminated area is small. Hence, the signal is bigger when the absorption is lower (visible in the different plots for the anti-confocal system), and when the distance between focus and mucosa is bigger, causing a wider spread of the signal, visible in the plot for $\mu_\mathrm{a} = 3.5\,\mathrm{mm}^{-1}$. The noise is unaffected by the distance and changes are due only to the random nature of MC simulations. Consequently, the SBR is following the signal. The fluctuations seen in the graph, especially at $0.035\,\mathrm{mm}^{-1}$ with low

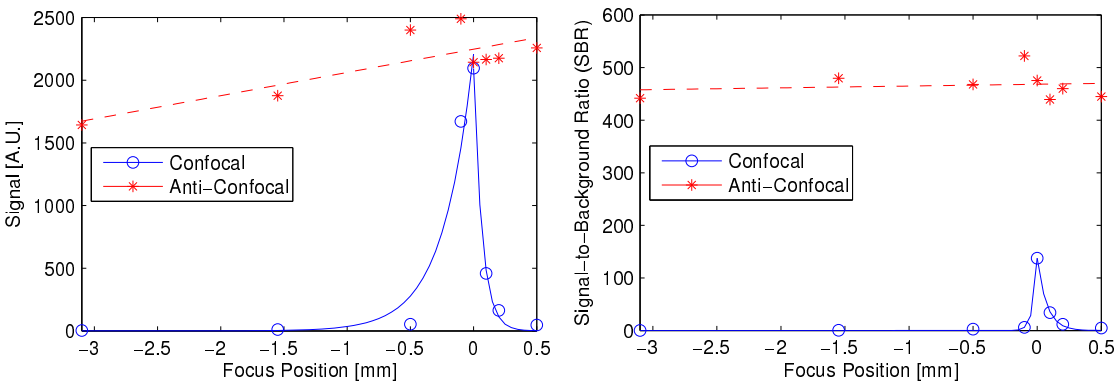


(a) Signal. $R^2_{\mathrm{C}(-3.1-0)} = 0.975$, $R^2_{\mathrm{C}(0-0.5)} = 0.998$, $R^2_{\mathrm{AC}} = 0.664$.

(b) SBR. $R^2_{\mathrm{C}(-3.1-0)} = 1$, $R^2_{\mathrm{C}(0-0.5)} = 0.997$, $R^2_{\mathrm{AC}} = 0.022$.

Figure 5.15: Influence of the focus on signal and SBR. '-3.1' equals to focus on the eardrum surface (anti-confocal configuration), '0' equals to focus on the mucosa surface (confocal configuration), and positive values indicate the focus is placed inside the mucosa. Markers indicate simulated values and lines indicate fits, with $R^2$ values given for each fit. The anti-confocal graphs were linearly fitted while the confocal graphs were exponentially fitted with two independent sections, separated at '0'.

$R^2$ value, are results of the random nature of the simulation and a low number of detected noise photons.

**Focus**

This section investigates the importance of an exact focus of the anti-confocal system on the performance of the system. In previous simulations the confocal system was focused on the mucosa surface and the anti-confocal system on the eardrum surface. This is changed here, the focus for both systems is shifted from the eardrum surface (focus = $-3.1\,\mathrm{mm}$) to the mucosa surface (focus = $0\,\mathrm{mm}$), and into the mucosa (positive focus values). The dependence of signal level and SBR on the focus is shown in Figure 5.15. Markers indicate simulated values and lines indicate fits, with $R^2$ values given for each fit below the figure. The anti-confocal graphs were linearly fitted while the confocal graphs were exponentially fitted with two independent sections, one from -3.1 to 0 and the second from 0 to 0.5.

The signal level of the confocal system is close to zero when focused outside the mucosa, increases exponentially to reach a peak on the mucosa surface, and then decreases exponentially when focused inside the mucosa. The SBR behaves similarly, with all curves well fitted by the exponential functions as shown by the high $R^2$ values. The signal of the anti-confocal system

increases when moving the focus from eardrum to mucosa with some fluctuations near the mucosa surface where more data points are simulated. The SBR is relatively unaffected by the focus and shows similar fluctuations. Both graphs were linear fitted and show low $R^2$ values, caused by the fluctuations of the graphs.

The signal of the confocal system is close to zero when focused outside the mucosa as rejected by the pinhole. The signal is maximal on the mucosa surface as reflections from the surface and scattered light are detected. The reflected light could be labelled as background as well as independent on the scattering and absorption characteristics of the mucosa and only affected by the refractive index and incident angle. This would result in a lower signal level and SBR of the confocal system but less so in the case of the anti-confocal system as the signal is mostly caused by scattering. In this case the superiority of the anti-confocal system would be even more significant. When moving the focus into the mucosa, the signal decreases again, as no reflections are detected and the light reaching the detector is attenuated by the superficial mucosa layers. The background is high when focused on the eardrum but otherwise constantly low and the SBR follows the course of the signal.

The anti-confocal system was designed with a focus on the eardrum surface but this simulation shows that the signal increases slightly when shifting the focus towards the mucosa and adopting the stop position at the same time. This increase in signal can be explained by the increased NA of the optics moving closer to the sample and hence increase in detected signal. The SBR is almost not affected as both signal and background increase with NA and the effect is cancelled. The observed fluctuation in both signal SBR of the anti-confocal system and thus low $R^2$ is assumed to be related to the random nature of the Monte Carlo simulation.

The performance does not decrease with change of the focus for two reasons, firstly the small NA of 0.08 and the relatively high stop radius of 1.1 mm. The small NA results in only a slow increase of the illuminated area on the eardrum ($r \approx NA \cdot d = 0.25\,\text{mm}$ when focused on mucosa surface) and hence the background is not spread much further. This means a stop with the same radius can still block most of the background and hence the SBR does not decrease significantly. A more significant change would be visible when using a smaller stop radius closer to the illuminated area on the eardrum. An increase in the illuminated area would then result in reflections passing the stop and significantly decrease the SBR. In case of a higher absorption coefficient of the mucosa, the focus would have a bigger influence. In this case, the signal level would be affected by the illuminated area on the mucosa as described in the previous section when changing the distance between eardrum and mucosa. A focus closer to the mucosa would cause a smaller signal and also affect the SBR.

Overall, this shows a good performance of the anti-confocal system, even when out of focus, in

contrast to the confocal system that requires an exact focus.

### Illumination NA

So far, the illumination NA was the same as the detection NA, as is the case for confocal systems. In the confocal system both the focused illumination beam and detection pinhole are necessary in order to achieve good background rejection.

In a simulation the illumination beam was restricted to a radius of 0.1 mm (effective NA of 0.003). No significant change in signal or SBR was observed (graphs not shown here) compared to the normal illumination. The illumination NA determines the illuminated area on the mucosa. But this is also affected by the scattering characteristics of the eardrum. Further, light propagates inside the mucosa increasing the illuminated volume even further. Propagation inside the tissue has a bigger effect on sampled volume than the NA in the investigated range, consequently no changes are observed.

In an experimental implementation, this would simplify the set-up as no beam expansion is necessary.

### Detection NA

The detection NA in the middle ear is restricted by the speculum. Nonetheless, the NA is varied in this section to investigate its influence on the anti-confocal system. Figure 5.16 shows the signal and SBR for varied NA. Markers indicate simulated values and lines indicate fits, with $R^2$ values given for each fit below the figure. Exponential fits are used for the anti-confocal graphs while linear functions fit the confocal graphs better.

Both the confocal and anti-confocal system show an increase in signal level and SBR with increasing NA while the increase in the anti-confocal case is much higher and approximates an exponential function compared to linear increase in the confocal case. The increase in the signal of the confocal system results from more photons being detected by the higher NA. But as the signal is mostly caused by reflections (simulated by a lambertian distribution) this increase is relatively small as the power reduces with higher angle. The SBR increases because both the signal and the background rejection ratio increase as given in Equation (4.1), resulting in less background.

The signal of the anti-confocal system increases more significantly as the signal is mostly due to scattered photons, showing a high exit angle and thus much more photons are detected by a higher NA. The SBR increases with the signal even though more background is also detected, as the background is mostly caused by reflections from the eardrum whose power increases less with increasing NA.

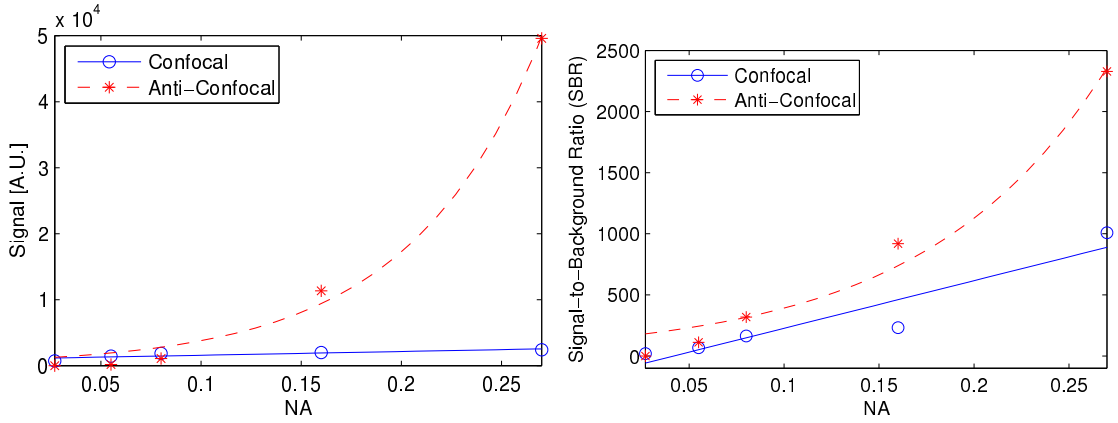


(a) Signal. $R^2_{\mathrm{C}} = 0.756$, $R^2_{\mathrm{AC}} = 0.994$.

(b) SBR. $R^2_{\mathrm{C}} = 0.889$, $R^2_{\mathrm{AC}} = 0.977$.

Figure 5.16: Influence of NA on signal and SBR. Markers indicate simulated values and lines indicate exponential (anti-confocal) or linear (confocal) fits, with $R^2$ values given for each fit.

This shows an even more improved performance of the anti-confocal system over the confocal system where optics with higher NA can be used.

#### Angle and Roughness

The middle ear is simulated with flat surfaces orthogonal to the optical axis although this is not the case in the ear where the eardrum and mucosa are tilted and not flat. The roughness is considered in simulations by the use of Lambertian reflection instead of specular reflections at the surfaces.

A change in orientation of the interfaces will cause a change in direction of the main reflection axis and affect the detected light level. This will influence the background from the eardrum more as mostly composed of reflections, while the signal from the mucosa is less affected as mostly composed of scattering. This will rather improve the SBR unless the eardrum is orthogonal orientated while the mucosa is not.

### 5.4.4 Summary of the Simulations

The simulation of the anti-confocal system showed that it is superior to the confocal system when measuring through an eardrum. Both signal level and SBR are higher. The signal decreases and the SBR increases with stop radius and an optimum must be found so that SBR is maximised with still detectable signal level. This optimum is dependent on the system noise, sample characteristics, and other parameters. This still holds with increased scattering of the eardrum or the surfaces in the sample being tilted. A change in the distance between eardrum and mucosa does not affect the

performance of the system significantly. This shows suitability of the anti-confocal system even if the used model does not match optical properties of real tissue accurately.

The simulations further showed that an inaccurate focus of the system does not affect the performance, increasing the ease of use of the system. Considering other applications where the NA of the system can be varied, a higher NA is advantageous as more scattered signal is detected and the SBR improves.

## 5.5 Physical Stops Compared to Camera Detection

Either a physical stop combined with a simple detector such as a photo diode or a camera combined with virtual filtering could be used to implement the anti-confocal system. In the second case the central pixels of the camera would be neglected during post-processing simulating a stop. The use of a camera has several advantages. Firstly, the alignment is easy as the beam can be observed. Secondly, the distribution of the power can be analysed and the radius of the virtual stop adopted accordingly. Last, the camera can be used for visual feedback and observation of the middle ear when using widefield illumination instead of anti-confocal laser illumination. Disadvantages are the higher costs of the camera and need for a high dynamic range due to a high signal component resulting from the eardrum and the low signal from the mucosa. A camera will be used during design of the system to investigate the signal components closer and determine the most suitable stop radius. Nonetheless, the construction of a physical stop is investigated in Appendix C.

## 5.6 Conclusion

Due to the special geometry of the middle ear, the confocal idea was adopted and the anti-confocal system introduced. After introduction of literature, the principle of the system, and simulation methods, the anti-confocal system was simulated and its performance compared to the conventional confocal system. The performance was rated by detected signal level and signal to background ratio.

Results showed the ability to detect signals from the mucosa when measured through the eardrum with an increased signal level and better background rejection of the anti-confocal system compared to the conventional confocal system. For the standard simulation parameters, the signal is increased by a factor of 1.5 while showing the same SBR in confocal and anti-confocal case. When keeping the signal level constant, the SBR can be increased by a factor of 3.2. The standard optical properties of the simulated system were then changed and the performance rated again. Increased scattering of the eardrum causes the signal level and SBR to decrease in all cases when using a

confocal system. In contrast, the anti-confocal system shows a less decreased performance and in some cases an even improved performance when increasing the scattering of the eardrum. An increasing distance between eardrum and mucosa increases the SBR of the confocal system while the anti-confocal system is less affected in the range expected in the middle ear. An inaccurate focus of the confocal system causes a strong decrease in performance while the anti-confocal system is relatively unaffected by a defocused system. An increased NA of the system increases the performance of both confocal and anti-confocal system while the increase is stronger for the anti-confocal case.

These results show an improved performance of the anti-confocal system over a wide range of variation of the middle ear. Further, the ease of use is improved as no accurate focusing of the anti-confocal system is necessary. Hence, the anti-confocal system will be implemented and experimentally characterised in Section 7. Prior to this, multi wavelength measurements are introduced in Section 6 and the ability of the anti-confocal system not just to pick up a signal but also to pick up changes in the inflammation are investigated.

# Chapter 6

# Spectroscopy

The previous chapter introduced the anti-confocal system and simulation results showed that it is able to reject background signal from the eardrum while still detecting enough signal from the mucosa. This chapter is based on these simulations and investigates whether measurements at multiple wavelengths with the anti-confocal system allow to assess the inflammation. For this the concentration of blood in the mucosa, linked to its metabolism, is to be measured in order to assess the inflammation. First different oxygenation and blood concentration measurements used in literature are presented. Then the theory behind the measurements is derived and simulations conducted. Finally, the wavelengths giving best measurements are determined using data acquired from the simulations.

## 6.1 Literature: Measuring Oxygenation and Blood Concentration

Several different indices measuring blood concentration and oxygenation are defined in literature and have been presented in Section 2.3. The indices vary in the used wavelengths, the number of wavelengths, and calibration factors. The most common and established use is in pulse oximeters where only the oxygenation is measured. Other methods where 2D or 3D images are used to separate background absorption from blood absorption are mostly still in the research phase. Examples presented below focus on the wavelengths used and mathematical calculation of the oxygenation and blood concentration.

Pulse oximeters (previously presented in Section 2.3.3) measure the reflection or transmission signal at two wavelengths, usually red (660 nm) and NIR (940 nm). The absorption is recorded over time in order to measure the constant signal $DC$, resulting from tissue, venous, and partly arterial

blood absorption, and a pulsating signal $AC$, resulting from blood absorption in arteries changing their volume due to pressure changes caused by the pulse. The ratio of $AC$ to $DC$ absorption ($AC$ is about 1 to 5 % of the $DC$ signal) compensates for changes in the light source and allows the measurement of signals with similar level rather than the measurement of input and output signal whose difference is much higher. The ratio of red to NIR signal

$$r = \frac{AC_{660}/DC_{660}}{AC_{940}/DC_{940}} \tag{6.1}$$

reflects the ratio of deoxygenated to oxygenated blood and can be converted to oxygen saturation in blood using experimentally derived calibration curves [75].

Setzer et al. [79] use a commercial pulse oximeter to characterise pulp inflammation. The only change in the system is an amplification factor of 2.5 of the pulse signal in order to compensate for the reduced signal in this measurement. Otherwise the system is unchanged and allows measurement of statistically significant different oxygen saturations in different inflamed tissues. The assessment of the tissue is based on oxygenation, while the total blood content is not measured.

Hardarson et al. [82] measure the blood oxygenation using camera images of the retina recorded with illumination at four different wavelengths. The oxygen saturation of haemoglobin $SO_2$ has an approximately linear relation to the ratio of optical density $OD$ at certain wavelengths (e.g. 586 and 605 nm) [82]. These wavelength were selected as the difference in absorption between oxygenated and de-oxygenated blood is high at 600 nm and 569 nm is an isobestic point. The almost linear relation of OD to oxygen saturation was discovered in experiments [214]. This relation is used to define the oxygenation (in percentage) as

$$SO_2 = a + k \cdot \frac{OD_{586}}{OD_{605}} \tag{6.2}$$

The optical density is defined as the logarithm of the relation of the intensity level inside a blood vessel $I$ and just outside the vessel $I_0$ according to $OD = \log(I_0/I)$. During calibration the constants were determined to be $a = 125$ and $k = -142$.

Su et al. [154] measure the mucosal haemoglobin concentration $IHB$ and oxygen saturation $ISO_2$ endoscopically, using the relative absorbance $Er = \log(\frac{Ir_{\text{standard}}}{Ir_{\text{tissue}}})$ at 569, 577, 586, and 650 nm. $Ir$ is the intensity of diffusely reflected light. Normalisation by a standard is used to compensate for differences in the input signals. The indices are defined as

$$ISO_2 = 0.673 \cdot \frac{\Delta Er_{577-586} - 9/17\Delta Er_{569-586}}{\Delta Er_{569-586}} \tag{6.3}$$

$$IHB = 200 \cdot \Delta Er_{569-650} \tag{6.4}$$

where $\Delta Er$ is the difference in relative absorption of the two wavelengths indicated in the subscript. 569 nm is an isobestic point, hence the reflectance is independent of the oxygenation while the

absorption at 650 nm is relatively low compared to 569 nm and Su et al. approximate it with zero. This choice of wavelengths allows measuring the total haemoglobin content. The index is linear up to a haemoglobin concentration of 150 nmol/g of tissue, above this errors are introduced due to the approximation, but still this index is used in commercial systems. The tissue oxygenation is measured at two isobestic point 586, and 569 nm, and at the peak absorption of oxyhaemoglobin $HbO_2$ at 577 nm giving a high difference between the absorption of oxy- and de-oxygenated blood.

The InSpectra$^{TM}$ StO2 Tissue Oxygenation Monitor, Model 650 (Hutchinson Technology Inc., Hutchinson, MN, USA) is able to measure tissue oxygenation and tissue haemoglobin index. The latter is a measure of the haemoglobin signal strength and used to determine correct positioning of the sensor [215]. Myers et al. [215] investigate the use of tissue haemoglobin index to measure total haemoglobin concentration. The tissue haemoglobin index $THI$ is defined as

$$THI = \frac{M_{\mathrm{SO2}}(2D_{760})}{PSF} \tag{6.5}$$

$$2D_{760} = A_{800} - 2A_{760} + A_{720} \tag{6.6}$$

with a scaling factor $PSF$ accounting for spacing between illumination and probe optical fibre, the linear slope coefficient $M_{\mathrm{SO2}}$, the second derivative attenuation $2D_{760}$, and the tissue attenuation $A = \log(I_{\mathrm{ref}}/I_{\mathrm{sample}})$ measured at the wavelength denoted by the subscript [216]. This is an empirically determined equation and requires the measurement of the tissue oxygenation in order to determine the linear slope coefficient. While the tissue haemoglobin index is insensitive to changes of the oxygenation is does not reliably measure the total haemoglobin concentration showing the need for a better choice of wavelengths for measurements.

Other groups determine the total haemoglobin concentration with measurements at 758, 795, and 833 nm in a time resolved spectroscopy system [217], in the range of 740 to 1040 nm using Photo-Acoustic Spectroscopy [218], or find in simulations that the best wavelengths for measurements are 1040, 1120, 1140 and 1200 nm (investigating the range of 800 to 1600 nm) [219].

A wide variety of wavelength in the range of 560 to 1200 nm and different calculations are used to determine the tissue oxygenation and haemoglobin concentration. The choice of wavelengths is important in order to get a reliable and measurable response as well as to measure the oxygenation independent of the total haemoglobin content and vice versa. Simulations are conducted later in order to find the best wavelengths to measure blood content and oxygenation in this application.

## 6.2 Theory of Absorption Measurements

### 6.2.1 Lambert-Beer Law

For simplicity, absorption models in literature are mostly based on the Lambert-Beer or Modified Lambert-Beer law. According to the Lambert-Beer law the light intensity $I$ in non-scattering tissue is given by

$$I = I_0 \exp(-\mu_\mathrm{a} \cdot d) \tag{6.7}$$

where $I_0$ is the input intensity and $d$ the thickness of the tissue. The attenuation $A$ is given by $A = \log\left(\frac{1}{R}\right)$ in reflection or $A = \log\left(\frac{1}{T}\right)$ in transmission mode. Using the Lambert-Beer law this results in

$$A = \log\left(\frac{I_0}{I}\right) = \mu_\mathrm{a} \cdot d \tag{6.8}$$

The absorption coefficient $\mu_\mathrm{a}$ of tissue is given by the wavelength dependent molar extinction coefficient of the absorber $\epsilon$ and the concentration of the absorber $c$ by

$$\mu_\mathrm{a} = \epsilon(\lambda) \cdot c \tag{6.9}$$

This assumes only one absorber, otherwise the absorption coefficient is the sum of several molar extinction coefficient multiplied by their concentration $\mu_\mathrm{a} = \sum_\mathrm{i} \epsilon_\mathrm{i}(\lambda) \cdot c_\mathrm{i}$. The attenuation can be rewritten as

$$A = \epsilon(\lambda) \cdot c \cdot d \tag{6.10}$$

This relation can be used to calculate the absorber concentration $c$ (in this case haemoglobin) using the measured attenuation $A$, the known molar extinction coefficient, and the thickness of the sample. This model is not correct as the Lambert-Beer law is only valid in non-scattering media. Hence, experimental calibration of the factor $k$ describing the relation of blood concentration and absorption $c = A \cdot k$ is necessary.

### 6.2.2 Modified Lambert-Beer Law

In reality tissue is scattering and the Lambert-Beer law is not valid. An offset $A_\mathrm{s}$ is added to account for scattering resulting in the Modified Lambert-Beer Law

$$A = A_\mathrm{s} + \mu_\mathrm{a} \cdot d \tag{6.11}$$

This model is more accurate but still requires experimental calibration of the system for the given range. This is shown in Figure 6.1 where the simulated attenuation is shown dependent on the absorption coefficient of the tissue. The blue curve shows the simulated data for a scattering coefficient of $24.83\,\mathrm{mm}^{-1}$ and a scattering anisotropy of 0.9 using the Monte Carlo simulation

presented in Section 6.2.3. The green and red curve show linear fits according to the Modified Lambert-Beer law, while the red one approximates the range of $\mu_a = 0.14$ to $0.59\,\mathrm{mm}^{-1}$, the green one approximates the range from 0.70 to $1.14\,\mathrm{mm}^{-1}$.

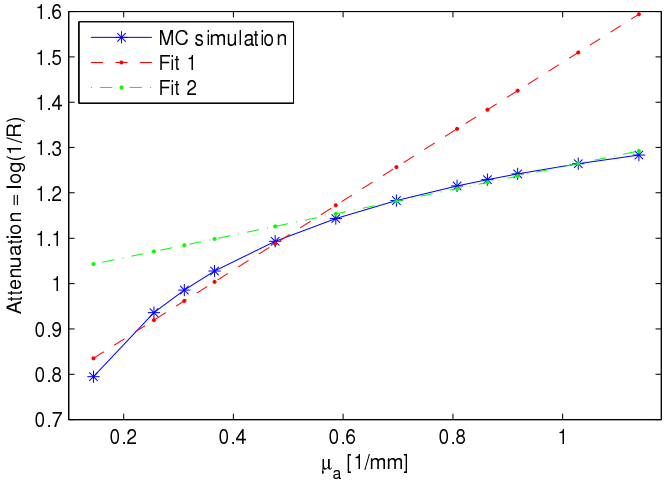


Figure 6.1: Simulated attenuation and approximations by the Modified Lambert-Beer law for different ranges.

It is obvious that the model is only accurate for the approximated range and the error increases rapidly outside the approximated range. Selection of appropriate wavelengths and calibration in the desired range ensure a linear relation.

### 6.2.3 Monte Carlo Simulation of the Reflection

As the above models of the attenuation are only approximations, more accurate values are simulated here using Monte Carlo methods as presented in Section 5.3. The simulations are based on the model for blood absorption and scattering as presented in Section 3.3.3 and given in Equation (3.10) for the absorption and Equation (3.11) for the scattering coefficient.

Simulations are conducted in the wavelength range of 500 to 940 nm as this is the typical range used for the assessment of blood. This range includes the optical window of low absorption and highest penetration depth in tissue as well as absorption peak of blood needed for contrast. The absorption of the mucosa is altered according to the model developed in Section 3.3.3, based on

$$\mu_a(\lambda) = \frac{V_{Hb}\ln(10)c_{Hb}\cdot(\alpha\epsilon_{HbO2}(\lambda)+(1-\alpha)\epsilon_{Hb}(\lambda))}{64500[g/mol]} \tag{6.12}$$

where $\epsilon_{HbO2}$ is the molar extinction of oxyhaemoglobin, $\epsilon_{Hb}$ the molar extinction of haemoglobin, $c_{Hb} = 120\,\mathrm{g/l}$ the concentration of haemoglobin per litre of blood and the molecular weight of haemoglobin of 64500 g/mol. During inflammation the metabolism is increased resulting in an

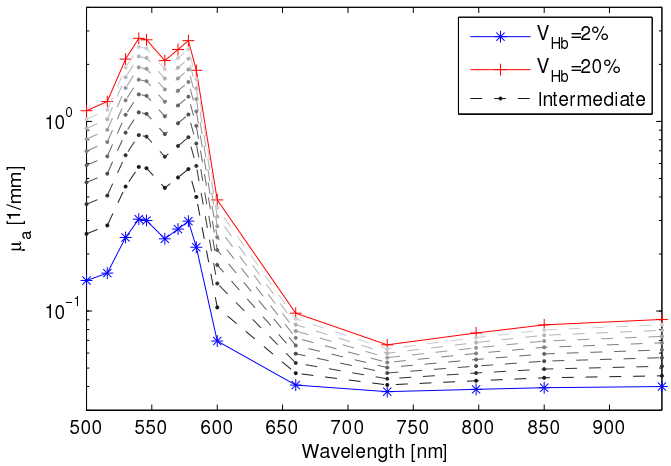


Figure 6.2: Absorption coefficient for different blood volume fractions $V_{\mathrm{Hb}}$. Intermediate plots are given in 2 % steps of blood volume fraction.

increased blood flow in the tissue. Thus, the volume fraction of blood in tissue $V_{\mathrm{Hb}}$ is increased. This results in an increased absorption coefficient $\mu_{\mathrm{a}}$ of the tissue as shown in Figure 6.2 were the absorption coefficient in the visible and NIR range is shown for a blood fraction of 2 % in blue, for 20 % in red, and in black dashed for intermediate concentrations in 2 % steps. The oxygenation $\alpha$ for all curves is fixed to 70 % [139] as literature review showed no consistent change of oxygenation during inflammatory diseases.

As the simulations are time consuming wavelength space was sampled as approximate using points around significant values minima, maxima, and isobestic points of the absorption curves.

The scattering coefficient is assumed to be independent of the inflammatory state (see Section 3.3) and thus Figure 6.3 shows only one curve of the scattering coefficient, used for all inflammatory states.

The simulated reflection signal $R$ is given in percent as a proportion of the summed output photon weight $w_{\mathrm{photons,out}}$ divided by the total input photon weight $w_{\mathrm{photons,in}}$

$$R = \frac{w_{\mathrm{photons,out}}}{w_{\mathrm{photons,in}}} \tag{6.13}$$

The model of the eardrum was presented in Section 3.4. A scattering coefficient of $11\,\mathrm{mm}^{-1}$, absorption of $1.8\,\mathrm{mm}^{-1}$, and scattering anisotropy of 0.99 is used. The thickness of the eardrum is 100 µm. Simulated reflectance signal and attenuation will be presented in this chapter.

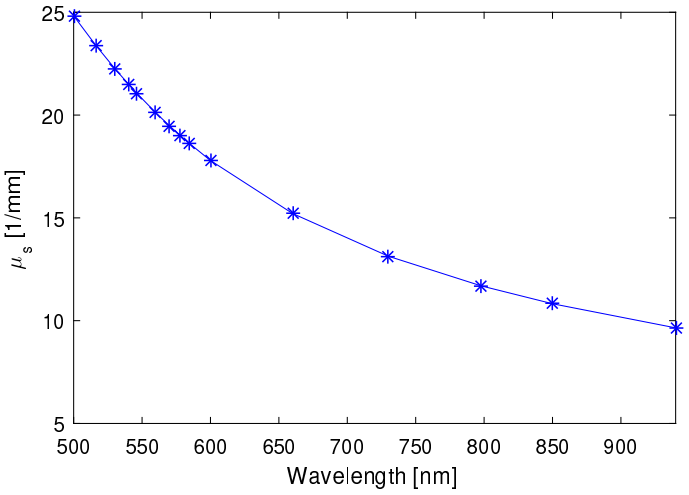


Figure 6.3: Scattering coefficient used in the simulations.

## 6.3 Definition of an Inflammation Index

A measure for the inflammation will be based on the blood concentration in the tissue. Nonetheless, oxygenation is included into the theory later on as it might give some additional information and state of the tissue.

### 6.3.1 Direct Measurements on Mucosa

In case of no eardrum in the light path where direct measurements on the mucosa are possible, the inflammation could be assessed by one wavelength only. The detected signal $S_{\text{total}}$ is given by the input power $I_0$ and the wavelength dependent reflection of the mucosa $R_{\text{M}}$. Only input and reflected power must be known.

$$S_{\text{total}} = I_0 \cdot R_{\text{M}} \tag{6.14}$$

The reflection from the mucosa is dependent on the absorption of the tissue. As blood is the main absorber in tissue, the measured reflectance is a function of the blood concentration and thus inflammation. This means inflammation causing higher metabolism, increased blood content, higher absorption and thus a smaller reflection signal. Using experimental calibration, the relation could be determined. The reflection signal depends on other parameters such as the scattering coefficient as well, although this will be neglected for now it will be considered later.

Figure 6.4 shows the simulated reflectance for a varied blood concentration in tissue. The figure clearly shows a decrease in the reflectance signal when increasing the blood content.

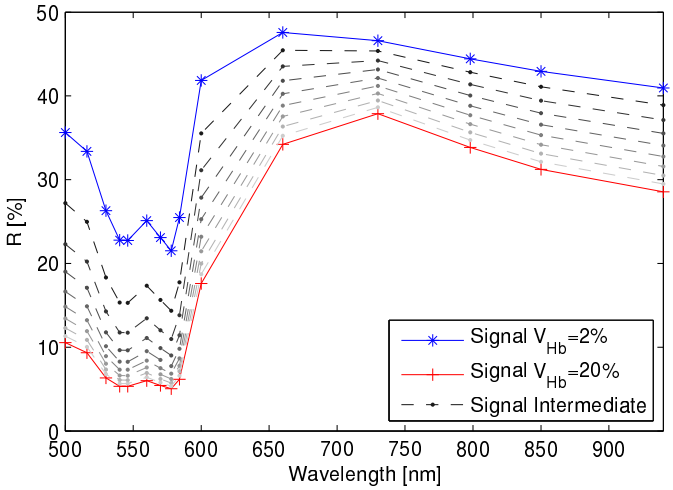


Figure 6.4: Simulated total reflectance of the mucosa. Intermediate plots are given in 2 % steps of blood volume fraction $V_{\mathrm{Hb}}$.

### 6.3.2 Measurements in the Ear

During measurements in the ear, no direct measurements are possible as the eardrum blocks the view on the middle ear mucosa. The detected signal $S_{\mathrm{total}}$ is composed of the reflection from the eardrum $S_{\mathrm{TM}}$ and the reflections from the mucosa $R_{\mathrm{M}}$ attenuated by the eardrum $T_{\mathrm{TM}}$ as schematically shown in Figure 6.5.

All other possibilities such as reflections from ossicles are neglected as these can be avoided during measurements choosing an appropriate sampling area. The best area for measurements is marked in Figure 1.2. This position is close to the Eustachian tube, where the inflammation is most severe. Further, the ossicles are located in the upper part of the tympanic cavity and thus do not obscure the light path in this area. Last, the eardrum is thinnest in this region resulting in the lowest scattering and absorption possible. Reflections from the wall of the external ear canal are blocked by the speculum allowing only light to enter and pass the optical system with small angles towards the optical axis. This negative effect restricting the NA thus filters wide scattered light that could reach parts of the middle ear other than mucosa and eardrum.

The signals are given by

$$S_{\mathrm{total}} = S_{\mathrm{TM}} + S_{\mathrm{M}} \tag{6.15}$$

$$S_{\mathrm{TM}} = I_0 \cdot R_{\mathrm{TM}} \cdot c_{\mathrm{optics}} \tag{6.16}$$

$$S_{\mathrm{M}} = I_0 \cdot R_{\mathrm{M}} T_{\mathrm{TM}}^2 \cdot c_{\mathrm{optics}} \tag{6.17}$$

where $I_0$ is the input power, $R_{\mathrm{TM}}$ is the reflectance of the eardrum, $R_{\mathrm{M}}$ the reflectance of the

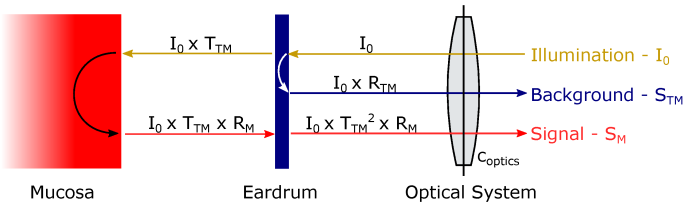


Figure 6.5: Signals in the ear, neglecting scattering and assuming direction independent transmission of the eardrum.

mucosa, $T_{\mathrm{TM}}$ the transmittance of the eardrum, and $c_{\mathrm{optics}}$ a scaling factor of the optics dependent on the aperture and other factors affecting the amount of detected light. These formulae assume the same attenuation of the eardrum in both directions and also neglect the light distribution due to scattering in the eardrum. Simulations considering these factors are explained below but these factors are neglected in the formula for an easier understanding. A similar model was chosen by Takiwaki [220] to describe attenuation in layers of skin.

It is obvious from this formula that the inflammation cannot be assessed with a single measurement as the reflection of the mucosa signal is not only dependent on the blood content but also on the eardrum properties. The detected signal is the desired signal scaled by the transmittance of the eardrum with an added offset resulting from reflections from and scattering within the eardrum.

Hence, measurements at two (or more) wavelengths must be conducted to extract the signal from the mucosa. The methods presented in Section 6.1 use the same approach, measurements at multiple wavelength are used to assess blood volume or oxygenation making use of spectral characteristics of blood absorption [75, 82, 154, 215]. We define the inflammation index $II$ as ratio of the detected signal at two wavelengths as done by [75, 82]

$$II = \frac{S_{\mathrm{total}}(\lambda_1)}{S_{\mathrm{total}}(\lambda_2)} = \frac{[R_{\mathrm{TM}}(\lambda_1) + R_{\mathrm{M}}(\lambda_1)T^2_{\mathrm{TM}}(\lambda_1)] \cdot I_0(\lambda_1) \cdot c_{\mathrm{optics}}}{[R_{\mathrm{TM}}(\lambda_2) + R_{\mathrm{M}}(\lambda_2)T^2_{\mathrm{TM}}(\lambda_2)] \cdot I_0(\lambda_2) \cdot c_{\mathrm{optics}}} \tag{6.18}$$

can extract the signal under certain circumstances as will be derived below. The first advantage of this measurement is already obvious in this formula as the scaling factor of the optics and the input power can be neglected (requiring the same input power for both wavelengths which can be achieved by reference measurements and scaling of the signals).

$R_{\mathrm{TM}}$ adds an offset to the desired signal $R_{\mathrm{M}}$ and is denoted as background from now on. The aim of the anti-confocal system is to increase the signal-to-background ratio (SBR) in order to minimise $R_{\mathrm{TM}}$ with respect to $R_{\mathrm{M}}T^2_{\mathrm{TM}}$. If the SBR is high enough (as will be assured by the choice of a high stop radius rejecting most of the background) then $R_{\mathrm{TM}}$ can be neglected and Equation (6.18) approximated by

$$II \approx \frac{R_{\mathrm{M}}(\lambda_1)T^2_{\mathrm{TM}}(\lambda_1)}{R_{\mathrm{M}}(\lambda_2)T^2_{\mathrm{TM}}(\lambda_2)} \tag{6.19}$$

Figure 6.6 (a) shows the simulated signal when detected with the optical system without applying stop filtering and when filtering the signal with a stop of 0.75 mm radius (the actual used radius on the detector is 0.3 mm but this corresponds to a stop radius of 0.75 mm at the used magnification of the lenses $m = 0.37$) in subfigure (b). The detected signal is split into the background from the eardrum and the signal from the mucosa. Without the stop filtering the background is higher than the signal (SBR of 0.3 to 0.8) and changes in the background will affect the measurement. When using stop filtering the background is reduced to less than the signal (SBR of 16 to 216), showing the approximation made in Equation (6.19), neglecting the background $R_{\mathrm{TM}}$, is valid. But also the detected signal power is reduced by the stop, limiting the maximum possible stop size. The dotted vertical lines in subfigure (b) indicate the wavelengths that were determined to be best for measurements of the blood concentration as will be described later.

The transmission of the eardrum at different wavelengths can be combined into one factor $c_{\mathrm{TM}} = \frac{T^2_{\mathrm{TM}}(\lambda_1)}{T^2_{\mathrm{TM}}(\lambda_2)}$. An equal multiplicative change of the transmission at both wavelengths does not affect the measurement as the eardrum factor $c_{\mathrm{TM}}$ is constant. Only different changes at both wavelengths will affect the measurement. This will be investigated closer in Section 6.5.3, an equal change will be assumed for now. As the transmission is mainly influenced by scattering this assumption can be ensured by selecting both wavelengths to be similar. Hence the inflammation index is given by

$$II \approx \frac{R_{\mathrm{M}}(\lambda_1)}{R_{\mathrm{M}}(\lambda_2)} \cdot c_{\mathrm{TM}} \tag{6.20}$$

where $c_{\mathrm{TM}}$ is constant given the assumptions made above. The relation (scaling and linearity) of $\frac{R_{\mathrm{M}}(\lambda_1)}{R_{\mathrm{M}}(\lambda_2)}$ to the inflammation and the best choice of wavelengths is investigated later in Section 6.4.

### 6.3.3 Alternative Indices

Previously, the inflammation index was defined as the ratio of the detected signal at two wavelengths Equation (6.18). Alternative indices such as a difference of the signals at different wavelengths as done by Su and Myers [154, 215] could be defined:

$$\begin{aligned} II_{\mathrm{Dif.}} &= S_{\mathrm{total}}(\lambda_1) - S_{\mathrm{total}}(\lambda_2) \\ &= [R_{\mathrm{TM}}(\lambda_1) + R_{\mathrm{M}}(\lambda_1)T^2_{\mathrm{TM}}(\lambda_1)] \cdot I_0(\lambda_1)c_{\mathrm{optics}} - [R_{\mathrm{TM}}(\lambda_2) + R_{\mathrm{M}}(\lambda_2)T^2_{\mathrm{TM}}(\lambda_2)] \cdot I_0(\lambda_2)c_{\mathrm{optics}} \end{aligned} \tag{6.21}$$

The input power and scaling factor of the optics cannot be neglected as constituting a scaling factor. But when assuming a high SBR, the reflection from the eardrum can be neglected. Also

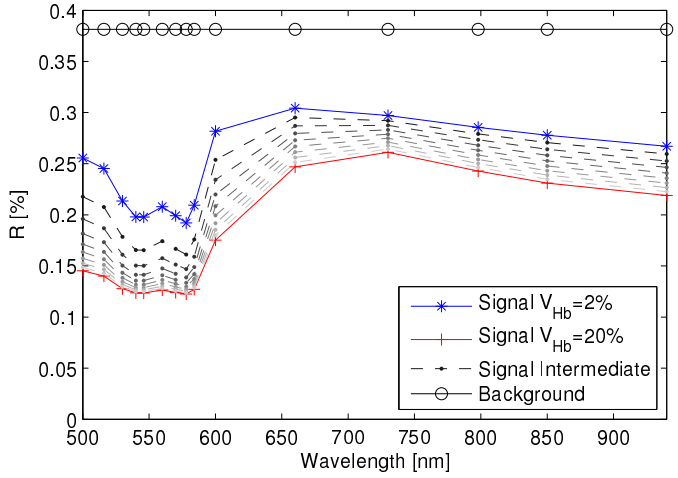


(a) Reflectance at the anti-confocal detector

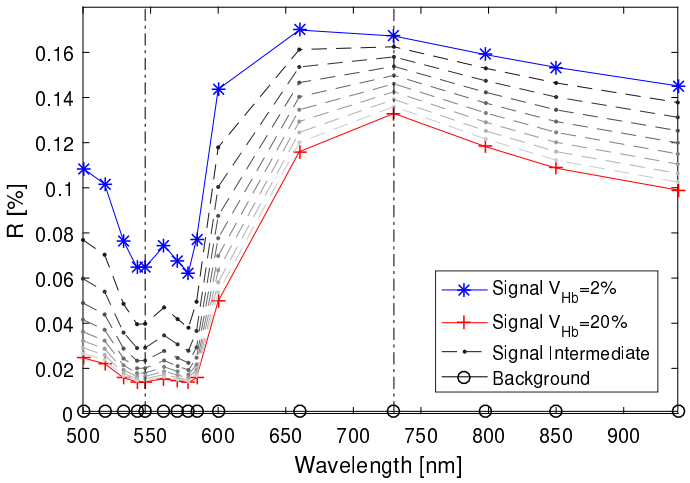


(b) Reflectance using stop with $r = 0.75\,\mathrm{mm}$. Dotted, vertical lines indicate wavelengths that were found to be best to measure blood content.

Figure 6.6: Reflection signal with and without stop filtering. Signal and background are plotted separately; a sum of both would be measured. Intermediate plots are given in 2 % steps of blood volume fraction.

the transmission factor $c_{\mathrm{TM}}$ is included, resulting in

$$\begin{aligned} II_{\mathrm{Dif.}} &\approx R_{\mathrm{M}}(\lambda_1)T_{\mathrm{TM}}^2(\lambda_1)I_0(\lambda_1)c_{\mathrm{optics}} - R_{\mathrm{M}}(\lambda_2)\frac{T_{\mathrm{TM}}^2(\lambda_1)}{c_{\mathrm{TM}}}I_0(\lambda_2)c_{\mathrm{optics}} \\ &= \left(R_{\mathrm{M}}(\lambda_1)I_0(\lambda_1) - \frac{R_{\mathrm{M}}(\lambda_2)I_0(\lambda_2)}{c_{\mathrm{TM}}}\right)T_{\mathrm{TM}}^2(\lambda_1)\cdot c_{\mathrm{optics}} \end{aligned} \tag{6.22}$$

It is obvious, that this index is dependent on the transmission of the eardrum, optics, and input power. Hence, this definition cannot be used. In contrast, the index defined by a normalised difference

$$\begin{aligned} II_{\mathrm{Norm.Dif.}} &= \frac{S_{\mathrm{total}}(\lambda_1) - S_{\mathrm{total}}(\lambda_2)}{S_{\mathrm{total}}(\lambda_1) + S_{\mathrm{total}}(\lambda_2)} \\ &\approx \frac{\left(R_{\mathrm{M}}(\lambda_1) - \frac{(R_{\mathrm{M}}(\lambda_2)}{c_{\mathrm{TM}}}\right)T_{\mathrm{TM}}^2(\lambda_1)}{\left(R_{\mathrm{M}}(\lambda_1) + \frac{(R_{\mathrm{M}}(\lambda_2)}{c_{\mathrm{TM}}}\right)T_{\mathrm{TM}}^2(\lambda_1)} = \frac{R_{\mathrm{M}}(\lambda_1) - \frac{R_{\mathrm{M}}(\lambda_2)}{c_{\mathrm{TM}}}}{R_{\mathrm{M}}(\lambda_1) + \frac{R_{\mathrm{M}}(\lambda_2)}{c_{\mathrm{TM}}}} \end{aligned} \tag{6.23}$$

would be independent on the transmission of the eardrum itself and also not affected by an equal change of the eardrum transmission at both wavelengths as the eardrum factor $c_{\mathrm{TM}}$ is constant. Consequently, this index is suitable.

For simplicity, only indices using two wavelengths are considered. As only the two main derivatives of haemoglobin (oxy and de-oxy) are measured, two wavelengths should be sufficent except for cases of abnormal high concentrations of other blood derivatives which would introduce an error [221]. An option would be the use of more complicated indices based on measurements of three or more wavelengths as for example done by Su et al. [154] using four wavelengths to measure the oxygenation as given in Equation (6.3) and Equation (6.4). Another example are pulse co-oximeters using more than seven wavelengths compared to standard pulse oximeters using only two wavelengths. This allows to determine the concentration of oxy-, carboxy, and methaemoglin as well as total haemoglobin concentration [81]. While this project considers only the measurement of total haemoglobin content and oxygenation and only two wavelengths are considered, the use of additional wavelengths might add more information and increase accuracy.

### 6.3.4 Oxygenation

In order to study the influence of blood oxygenation $\alpha = \frac{HbO_2}{HbO_2+Hb}$ on reflection and inflammation index the simulations were repeated with constant blood volume fraction of 5 % and changed oxygenation from 30 to 90 %. This changes the absorption coefficient according to Equation (3.10) and shown in Figure 6.7. The resulting reflection spectra are shown in Figure 6.8 when detected with the anti-confocal system with stop radius of 0.75 mm. The dotted vertical lines indicate the wavelengths that were determined to be best for measurements of the oxygenation as will be described later.

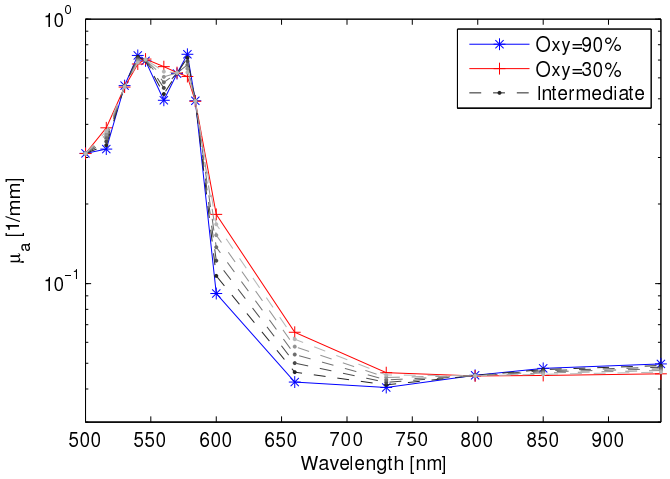


Figure 6.7: Absorption coefficient dependent on oxygenation and wavelength with a constant blood volume fraction of 5 %. Intermediate steps are shown in 10 % steps of oxygenation.

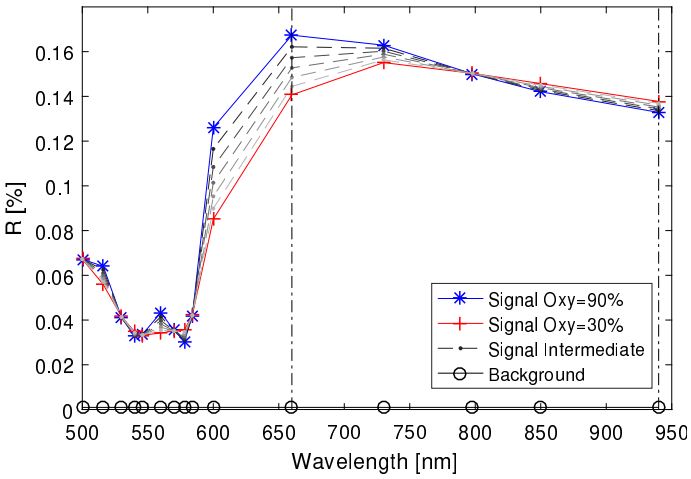


Figure 6.8: Simulated reflectance $R$ for changing oxygenation and a stop with 0.75 mm radius. Intermediate steps are shown in 10 % steps of oxygenation. Dashed-dotted, vertical lines indicate wavelengths that were found to be best to measure blood oxygenation.

The same indices as defined for the blood content will be applied to the oxygenation, resulting in

$$I_{\text{Oxy,frac}} = \frac{S(\lambda_1)}{S(\lambda_2)} \tag{6.24}$$

$$I_{\text{Oxy,rel.dif.}} = \frac{S(\lambda_1) - S(\lambda_2)}{S(\lambda_1) + S(\lambda_2)} \tag{6.25}$$

## 6.4 Finding the best Inflammation Index

An optimum wavelength combination and formula for the inflammation index is to be found. A good index is characterised by:

1. High dependency of the inflammation index of the blood concentration $C_{\text{Hb}}$. This is measured by the sensitivity of the system, measured by the slope $m_{\text{cHb}}$ [222] of a linear interpolation of the inflammation index $II = m_{\text{cHb}} \cdot C_{\text{Hb}} + b_{\text{cHb}}$ or $m_{\text{Oxy}}$ of the oxygenation index $I_{\text{Oxy}} = m_{\text{Oxy}} \cdot Oxy + b_{\text{Oxy}}$.

2. High linearity of the output, expressing how strong the actual curve deviates from a linear curve. This is often measured in percent [222] but here the $r^2$ value of the linear interpolation is used as measure. Further, it is checked whether the course is monotonic. If not, then the index is not considered.

Hence, we propose the measure

$$M_{\text{cHb}} = |m_{\text{cHb}}| r^2_{\text{cHb}} \tag{6.26}$$

used to evaluate the inflammation index. Further, the blood oxygenation $Oxy$ must be considered. The behaviour of the oxygenation during inflammation is not known, thus the inflammation index must be independent of the oxygenation. This is measured by the slope of the index dependent on the blood oxygenation $m_{\text{Oxy}}$. The linearity of this index is not considered. As this part is to be minimised, the final measure is a subtraction of both elements. Both slopes must be scaled by the simulated range, either $\Delta_{\text{Oxy}}$ or $\Delta_{\text{cHb}}$. As the slope of the oxygenation is desired to be lower than the slope of the blood volume fraction a factor of 5 is introduced to ensure $m_{\text{cHb}} > m_{\text{Oxy}}$ in the selected measure. This is an arbitrary chosen value that decides the influence of both slopes on the index and its influence is investigated later in Section 6.4.2. This results in the measure

$$M_{\text{cHb-Oxy}} = |m_{\text{cHb}}| \Delta_{\text{cHb}} \cdot r^2_{\text{cHb}} - 5 \cdot |m_{\text{Oxy}}| \Delta_{\text{Oxy}} \tag{6.27}$$

A high $M_{\text{cHb-Oxy}}$ indicates a high dependence of the index on the blood volume concentration, a good linear fit, and a low dependence on the blood oxygenation.

However, a non-monotonic dependence of the inflammation index on the oxygenation can result in a small slope even though the difference between two single values can be bigger. To account for this the slope of the influence of oxygenation $m_{\text{Oxy}}$ is replaced by the maximum difference $\max(I_{\text{Oxy}}) - \min(I_{\text{Oxy}})$ so that the measure results in

$$M_{\text{cHb-Oxy}} = |m_{\text{cHb}}|\Delta_{\text{cHb}} \cdot r^2_{\text{cHb}} - 5 \cdot |\max(I_{\text{Oxy}}) - \min(I_{\text{Oxy}})| \tag{6.28}$$

In this case scaling by the range $\Delta_{\text{Oxy}}$ is not necessary as considered in the calculation of the slope (the slope of a linear function is calculated by $m = \frac{|\max(I_{\text{Oxy}}) - \min(I_{\text{Oxy}})|}{\Delta Oxy}$). For completeness, the same measure is applied to an oxygenation index and defined as

$$M_{\text{Oxy-cHb}} = |m_{\text{Oxy}}|\Delta_{\text{Oxy}} \cdot r^2_{\text{Oxy}} - 5 \cdot |\max(II) - \min(II)| \tag{6.29}$$

indicating a high dependence on the oxygenation but low dependence on the total blood content. The literature is not clear if there is a connection of oxygenation and inflammation but this measure could give additional information about the state of the middle ear mucosa in case there is a dependence found during trials.

### 6.4.1 Best Indices

The indices defined as the fraction and relative differences introduced earlier are optimised for oxygenation and blood concentration using the simulated data and a stop radius of 0.75 mm

The measure $M_{\text{cHb}}$ introduced earlier is given in Figure 6.9 for both indices, where white means a good measure and black a low one. The relative difference is symmetrical while the fraction is not. The best indices when only considering blood volume concentration are

$$II_{\text{frac.}} = \frac{S_{\text{total}}(730)}{S_{\text{total}}(570)} \tag{6.30}$$

$$II_{\text{rel.dif.}} = \frac{S_{\text{total}}(730) - S_{\text{total}}(500)}{S_{\text{total}}(730) + S_{\text{total}}(500)} \tag{6.31}$$

Both indices are indicated in Figure 6.9, labelled with “Best”.The best indices when considering blood volume concentration and minimising dependency on blood oxygenation $M_{\text{cHb-Oxy}}$ are found to be

$$II_{\text{frac.,cHb-Oxy}} = \frac{S_{\text{total}}(730)}{S_{\text{total}}(546)} \tag{6.32}$$

$$II_{\text{rel.dif.,cHb-Oxy}} = \frac{S_{\text{total}}(798) - S_{\text{total}}(500)}{S_{\text{total}}(798) + S_{\text{total}}(500)} \tag{6.33}$$

and are also marked in Figure 6.9, labelled with “Best incl. Oxy”. Figure 6.10 shows these indices depending on blood volume content and oxygenation in blue and red respectively.

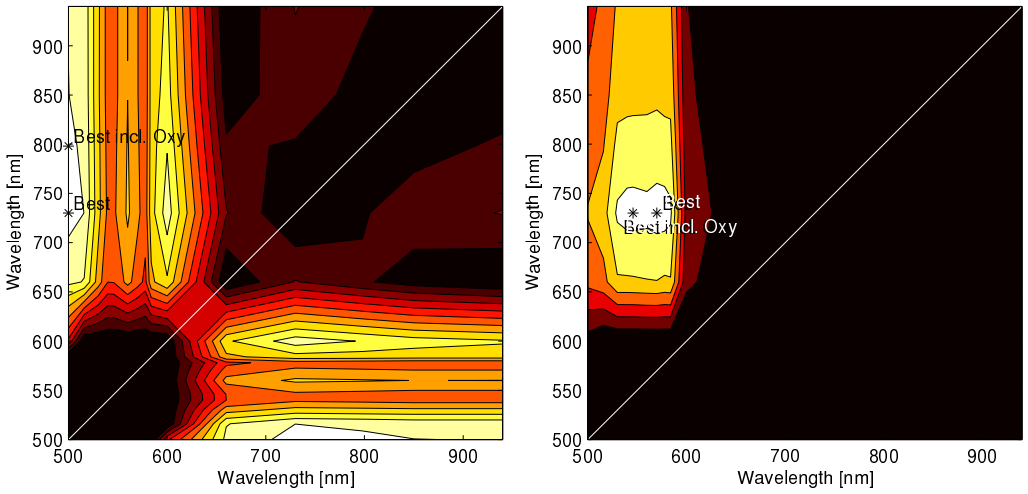


(a) Rel. difference (b) Fraction

Figure 6.9: Inflammation index rating, not considering oxygenation. A brighter value indicates a better index and 'best' marks the best index found for the measure $M_{\text{cHb}}$. 'best incl. Oxy marks the best index found for $M_{\text{cHb-Oxy}}$.

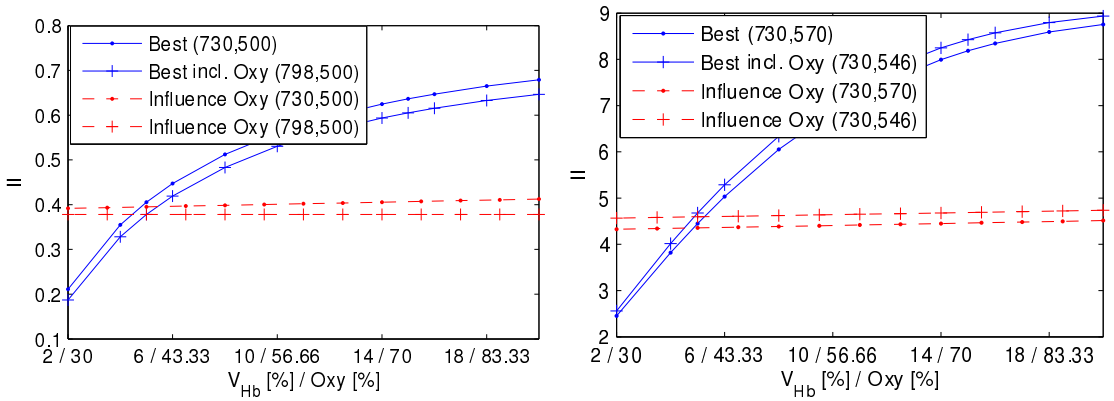


(a) Relative difference (b) Fraction

Figure 6.10: Simulated inflammation index in dependency of blood volume fraction and oxygenation.

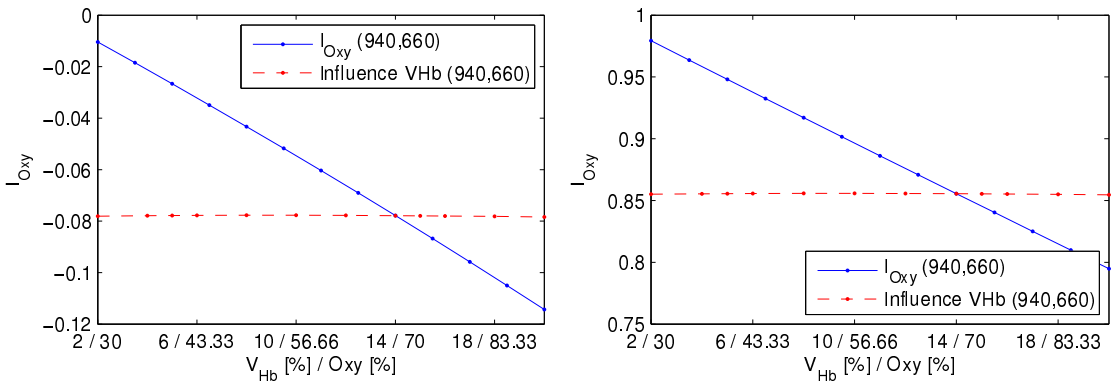


(a) Relative difference

(b) Fraction

Figure 6.11: Simulated oxygenation index dependent on blood oxygenation and blood volume fraction.

Both indices show good dependence of the blood volume fraction and low dependence on the oxygenation, when using the wavelengths found during optimisation. The best index using the relative difference uses wavelengths at the lower end of the simulated range (500 nm). The index is not expected to increase further below this range as the blood absorption first drops down. Another peak is present at lower wavelengths but the scattering is increased in this range and hence a worsened signal expected. All indices flatten out at higher blood concentrations. This means the measurements will be less accurate in this range. The selected wavelengths are in the range of those used in literature but span a wider range than in single measurements. But this wider range is expected to give a higher signal as the contrast in absorption is higher.

The best indices for oxygenation, minimising dependence on blood volume fraction are given by

$$I_{\text{frac,Oxy-cHb}} = \frac{S_{\text{total}}(940)}{S_{\text{total}}(660)} \tag{6.34}$$

$$I_{\text{rel.dif.,Oxy-cHb}} = \frac{S_{\text{total}}(940) - S_{\text{total}}(660)}{S_{\text{total}}(940) + S_{\text{total}}(660)} \tag{6.35}$$

and the relation to oxygenation and blood concentration shown in Figure 6.11. The found wavelengths for the fraction are in accordance with those used in pulse oximetry [75].

### 6.4.2 Influence of the Scaling Factor and Stop Radius

#### Scaling Factor

The factor of 5 was chosen in Equation (6.27) to ensure a small influence of the oxygenation on the inflammation index. The influence of this factor on the selected wavelengths is shown in Table 6.1

Table 6.1: Selected wavelength in dependence of the scaling factor.

| Scaling | Blood Concentration | | Oxygenation | |
|---|---|---|---|---|
| Factor | fraction | rel. dif. | fraction | rel. dif. |
| 0 | 730/570 | 730/500 | 578/600 | 940/600 |
| 1 | 730/570 | 798/500 | 578/560 | 578/560 |
| 3 | 730/546 | 798/500 | 940/660 | 560/530 |
| 5 | 730/546 | 798/500 | 940/660 | 940/660 |
| 10 | 798/584 | 798/500 | 940/660 | 940/660 |
| 20 | 798/584 | 798/500 | 940/660 | 940/660 |

listing the selected wavelengths for different factors.

While the selected wavelengths for measuring the blood concentration as relative difference are independent of the scaling factor (except for factor 0), this is not true for the index defined as fraction. The wavelengths change slightly but in all cases one wavelength in the high absorptive green region and one in the low absorptive NIR region are selected.

For oxygenation measurements the wavelength of 940 and 660 nm are mostly selected, especially for higher scaling factors. The oxygenation index defined by relative fraction shows that the selected wavelengths have a similar rating as the selection switches from 940/660 nm to wavelengths in the green range and back, indicating that small changes in the rating metric cause a change in the selected wavelengths. The scaling factor does not change the selected wavelengths significantly, and a factor of 5 seems to be a good compromise.

### Stop Radius

The influence of the stop radius on the inflammation index and the selected wavelengths is investigated. Table 6.2 shows the selected wavelengths depending on the stop radius. In case of oxygenation measurements it is obvious that the stop radius does not have a big influence. Only for small radii, an influence is observed and the wavelengths do not change above a stop radius of 0.25 mm. In the case of the blood concentration measurements defined by the relative difference no changes are observed while in case of the index defined as the fraction the wavelength change within a small range. But again, as for variation of the scaling factor, one wavelength in the green and the second one in the NIR range are selected. This shows that also the stop radius does not have a significant influence on the selected wavelengths.

In contrast to the wavelengths, the index itself is influenced by the stop radius as shown in Figure 6.12. The inflammation index (defined by fraction) is shown for the respective best

Table 6.2: Selected wavelength in dependence of the stop radius.

| Stop Radius | Blood Concentration | | Oxygenation | |
|---|---|---|---|---|
| [mm] | fraction | rel. dif. | fraction | rel. dif. |
| 0 | 798/500 | 798/500 | 560/584 | 584/560 |
| 0.25 | 798/500 | 798/500 | 940/660 | 940/660 |
| 0.5 | 798/584 | 798/500 | 940/660 | 940/660 |
| 0.75 | 730/546 | 798/500 | 940/660 | 940/660 |
| 1 | 730/546 | 798/500 | 940/660 | 940/660 |
| 1.5 | 798/584 | 798/500 | 940/660 | 940/660 |

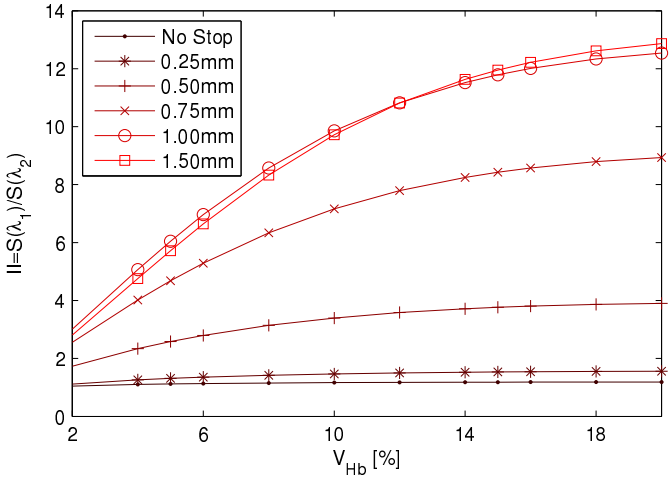


Figure 6.12: Simulated inflammation index for changing stop radius.

wavelength combination for different stop radii. The index increases with stop radius as more background is blocked and thus the dependence of the signal on the absorption in the mucosa increased.

### 6.4.3 Explaining the Index

The inflammation index defined as a fraction will be used further as the measure rating the indices yields higher values and the selected wavelength are closer (730 and 546 nm for the fraction versus 798 and 500 nm for the relative difference). The selected indices are

$$II = \frac{S_{\text{total}}(730)}{S_{\text{total}}(546)} \tag{6.36}$$

$$I_{\text{Oxy}} = \frac{S_{\text{total}}(940)}{S_{\text{total}}(660)} \tag{6.37}$$

These wavelengths were marked in the plots of simulated reflectance Figure 6.6 and Figure 6.8. The physical meaning for these indices is explained below.

**Blood Volume Content**

Inflammation results in a higher metabolism, which in turn results in a higher blood content to meet the higher oxygen demand. Both oxygenated and de-oxygenated blood content are increased and the oxygenation kept constant, in the model used here. Also the scattering is assumed to be unaffected by inflammation (see Section 3.3.2). As blood is the main absorber in tissue this increases the absorption coefficient and reduces the reflection signal. The change in absorption coefficient with blood concentration was previously presented in Figure 6.2 and the change of reflection signal in Figure 6.6.

In the 700 to 940 nm wavelength range the absorption and scattering coefficients are lower than in the range of 500 to 600 nm. An increased absorption coefficient reduces the reflection signal significantly while increased scattering increases the reflection signal but shows a lower dependence. This causes the reflection to be higher at 700 to 940 nm than 500 to 600 nm, due to the stronger influence of absorption compared to scattering. The change of blood concentration has the same multiplicative effect on the absorption coefficient at all wavelengths (apart from a small offset in the model due to tissue background absorption) but not on the reflection due to a non-linear relation (the linear Lambert-Beer relation is only an approximation) and influence of the scattering coefficient.

This is shown in Figure 6.13 where the reflection signal at four wavelengths (changing the scattering coefficient) is shown dependent on the absorption coefficient in (a) and the blood concentration in (b). The thin lines in subfigure (a) show the full range of absorption coefficient, while the thick lines indicate the range spanned when varying the blood concentration from 2 to 20 %. The x-axis is shown in logarithmic scale for better visibility at small values of the absorption coefficient. The curves show a non-linear behaviour as mentioned earlier. When varying the blood concentration different sections of these curves are reached. Subfigure (b) shows these sections of the reflectance signal indicated as thick lines in dependence of the blood concentration instead of the absorption coefficient.

This shows clearly how the change in reflectance depends on the wavelength. For example, at 730 nm the reflection value decreases by 0.034 % (factor of 0.20 of start value) while the decrease at 546 nm is higher with a change of 0.051 % (factor of 0.77). While both reflection values are decreasing, the decrease is more significant at 546 nm. The inflammation index defined as the reflection at 730 nm divided by the reflection at 546 nm is thus increasing with increasing blood concentration as the denominator is decreasing faster.

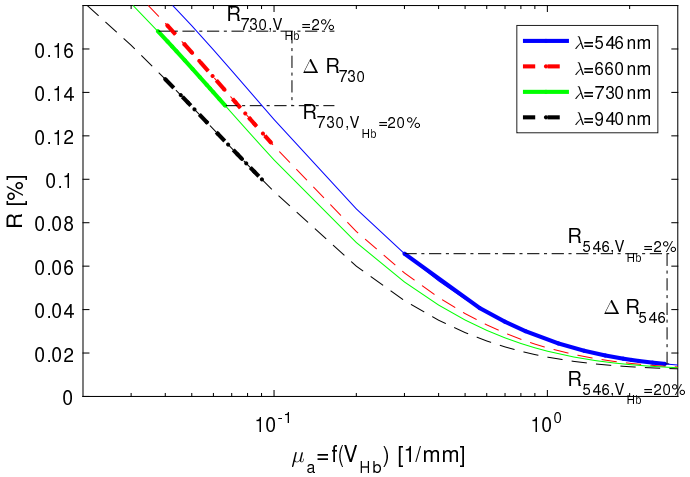


(a) Reflectance dependent on absorption coefficient changing with blood concentration

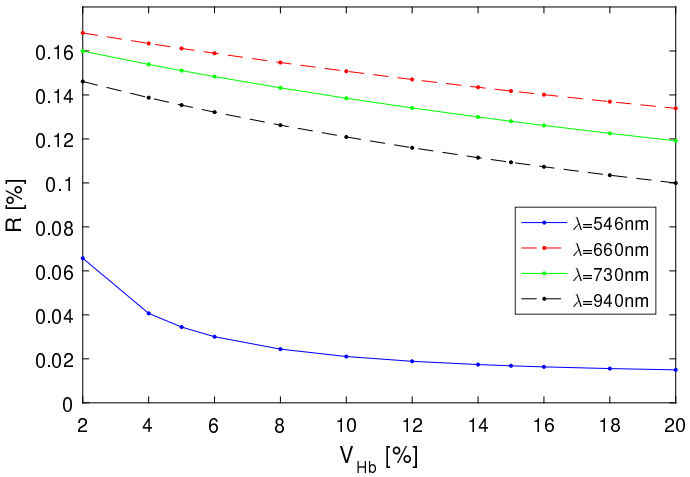


(b) Reflectance dependent on blood concentration.

Figure 6.13: Simulated reflectance. The thick lines in subfigure (a) indicate the range achieved when varying the blood concentration from 2 to 20 % while the thin lines show the full range. Subfigure (b) shows the reflectance dependent on the blood concentration. $R(730)/R(546)$ gives a good index while $R(940)/R(660)$ does not.

In contrast the two other wavelengths shown in the graph show a similar change of reflection with changing blood concentration and the relation of both reflection values is almost independent of the blood concentration. This shows that a good choice of wavelengths is necessary in order to allow measurements of the inflammation and best measurements are achieved using one wavelength where the absorption of blood is high (e.g. 546 nm) and one where it is low (e.g. 730 nm).

The whole chain of effects is summarised in Figure 6.15.

**Oxygenation**

Literature is inconsistent about the relation of metabolism and oxygenation, both an increase due to increased blood supply and decrease due to higher oxygen demand are reported (see Section 3.3.2). An increase in oxygenation is assumed here in order to explain the further chain of causes.

Oxygenation measurements are based on the different specific extinction coefficients of oxygenated haemoglobin $\epsilon_{\mathrm{HbO2}}$ and deoxy-haemoglobin $\epsilon_{\mathrm{Hb}}$ causing the total absorption spectrum to change as shown in Figure 6.7. The extinction coefficient of oxy-haemoglobin $\epsilon_{\mathrm{HbO2}}$ at 940 nm is higher than the extinction coefficient of deoxy-haemoglobin $\epsilon_{\mathrm{Hb}}$, the reverse is true at 660 nm. Consequently, the absorption coefficient is increasing at 940 nm and decreasing at 660 nm with increasing oxygenation. This causes the reflection signal to increase at 660 nm and decrease at 940 nm as shown in Figure 6.8.

As done previously for the blood concentration, the reflection is first shown in Figure 6.14 (a) in dependence of the absorption coefficient, with the thin lines indicating the full range and the thick lines showing the range spanned when changing the oxygenation of blood. It has to be noted that the absorption at 660 nm is highest for high oxygenation and decreases with decreasing oxygenation, while the opposite is true for the other shown wavelengths. Figure 6.14 (b) shows the reflection signal in dependence of the oxygenation and the increase at 660 nm and decrease at 940 nm of the reflection signal with oxygenation is more obvious.

The index defined as the reflection at 660 nm divided by the reflection at 940 nm increases with increasing oxygenation. Again a good choice of wavelengths is necessary as indicated by the other two wavelengths in the graphs, both showing a small change with oxygenation and thus a relation that is almost independent of the oxygenation. The whole chain of effects is summarised in Figure 6.15.

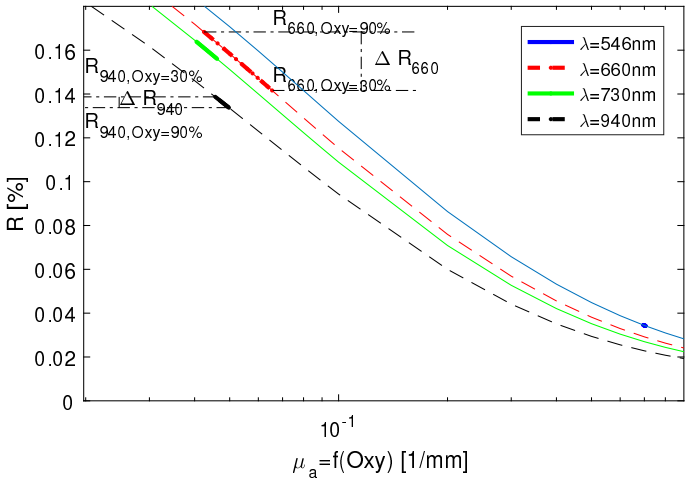


(a) Reflectance dependent on absorption coefficient changing with blood oxygenation

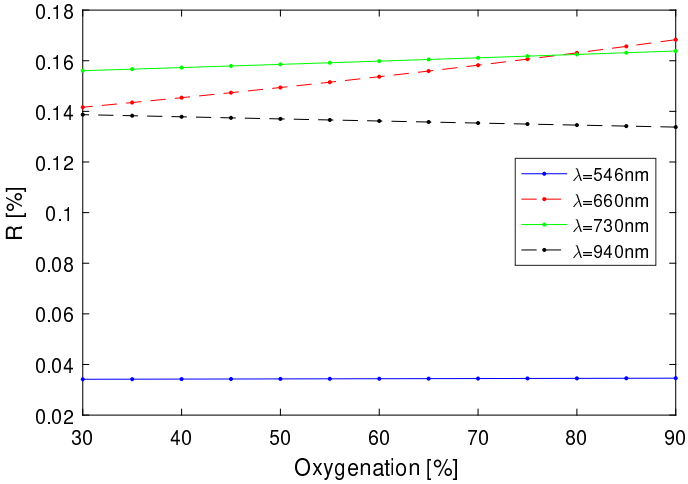


(b) Reflectance dependent on the blood oxygenation

Figure 6.14: Simulated reflectance dependent on blood oxygenation. The thick lines in (a) indicate the range achieved when varying the oxygenation from 30 to 90 % and thin lines show the full range. Subfigure (b) shows the reflectance dependent on the blood oxygenation. $R(940)/R(660)$ gives a good index for oxygenation while $R(730)/R(546)$ does not.

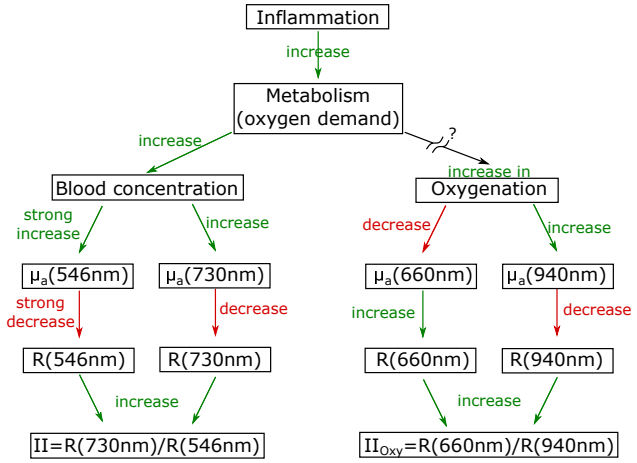


Figure 6.15: Causal relations in formation of the inflammation and oxygen index. Literature is inconsistent about the relation of metabolism and oxygenation, both an increase due to increased blood supply and decrease due to higher oxygen demand are reported (see Section 3.3.2). An increase in oxygenation is assumed here in order to explain the further chain of causes.

## 6.5 Influence of Other Parameters on the Inflammation Index

Changes of optical properties of the middle ear and optical parameters of the anti-confocal system (listed in Table 5.7) have been simulated and their influence on single measurements presented in Section 5.4.3. Here, the influence of these parameters on measurements of the inflammation index is investigated. Some of these effects are expected to have no influence on the inflammation index as acting similarly on both wavelengths while others will have an influence. The properties of the middle ear (distance between eardrum and mucosa, scattering coefficient of the mucosa, transmission characteristics of the eardrum, and surface orientation and roughness) are altered and their influence investigated while the optical system (focus, both illumination and detection NA, and stop radius) are kept constant according to the previous results. The wavelength and blood content dependent absorption coefficient of the mucosa is the input parameter to be measured, while all other parameters of the mucosa interfere with the assessment of the inflammation.

### 6.5.1 Distance from Eardrum to Mucosa

The distance between eardrum and mucosa is changed from 3 mm to 2 and 4 mm in simulations of the inflammation index and results shown in Figure 6.16.

A change in inflammation index is obvious and results from the different influences of the

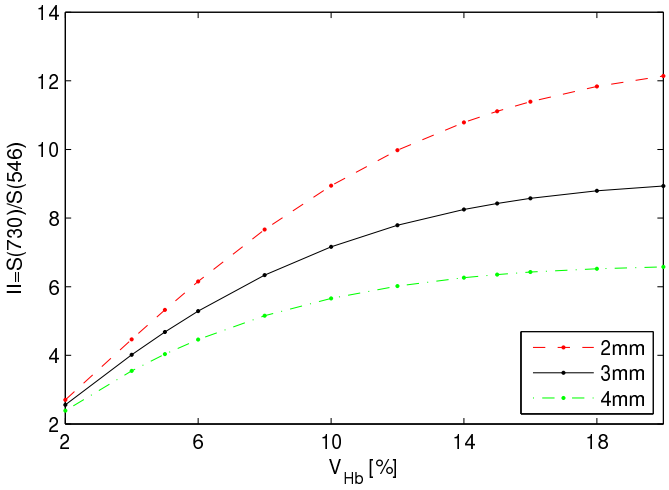


Figure 6.16: Influence of distance from eardrum to mucosa on the inflammation index.

distance on the detected reflection of the mucosa for different absorption coefficients observed in Section 5.4.3. While the distance does not have a significant influence on the detected signal in case of a low absorption of the mucosa, a large dependence is present for higher absorption. This causes the green signal to change with changing distance while the NIR signal is relatively unaffected and this in turn affects the inflammation index.

### 6.5.2 Scattering of the Mucosa

The scattering coefficient of the mucosa was assumed to be constant for different inflammatory stages. This assumption is based on literature research presented in Section 3.3.2. But the scattering coefficient of tissue can change from person to person and variations of the scattering coefficient are simulated here and its influence on the inflammation index investigated.

The scattering coefficient of the mucosa is changed by ±20, ±10, and ±5 % (corresponding to scaling by the factors 0.8, 0.9, 0.95, 1.05, 1.1, and 1,2), the reflectance simulated, and the inflammation index calculated. Figure 6.17 shows the used scattering coefficients over the whole wavelength range.

The inflammation index is shown in Figure 6.18 a) with the original simulation as black, solid line and the resulting index with changed scattering as dashed lines. The error in the index is smaller than the variation of the scattering coefficient as obvious from Figure 6.18 b) showing the error in percent of the original value $E = \frac{|II_{\text{changed}} - II_{\text{original}}|}{II_{\text{original}}}$. The maximum error is 3.7 % for a 20 % change in the scattering coefficient, 1.5 % for a 10 % change, and 0.7 % for a 5 % change. This shows that the inflammation index is relatively robust to variations of changes in the scattering of

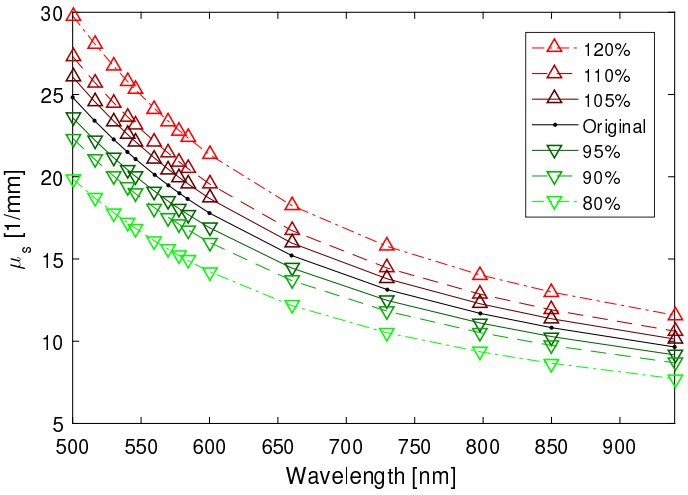


Figure 6.17: Values for the changed scattering coefficient of the mucosa.

the middle ear mucosa.

### 6.5.3 Properties of the Eardrum

A change in the transmission of light through the eardrum with the same factor at both used wavelength ($k \neq f(\lambda)$) will not affect the measurement of the inflammation index in the simplified equations presented above as the transmission factor $c_{\mathrm{TM}} = \frac{k^2 \cdot T_{\mathrm{TM}}^2(\lambda_1)}{k^2 \cdot T_{\mathrm{TM}}^2(\lambda_2)}$ is constant. But if the transmission of the eardrum is affected by absorption of blood or other absorbers and scattering elements within the tissue with wavelength dependent relation, then the measurement of the inflammation index will be affected $c_{\mathrm{TM}} = \frac{k^2(\lambda_1) \cdot T_{\mathrm{TM}}^2(\lambda_1)}{k^2(\lambda_2) \cdot T_{\mathrm{TM}}^2(\lambda_2)}$.

A possibility to account for this change is to use the reflected light from the eardrum $R_{\mathrm{TM}}$ collected inside the stop radius and use its information to make conclusions about the transmission. In effect, this would be confocal detection of the properties of the eardrum at the same time as performing anti-confocal detection of the mucosa. Only the small illuminated area would be probed and the eardrum characteristics of a small area determined. This area affects the transmission of the illumination. The characterisation of a wider area of the eardrum would be necessary to also characterise the transmission of backscattered light. Further, the axial resolution of the confocal system with NA of 0.08 would be $r_{\mathrm{axial}} = 1.5n\frac{\lambda}{NA^2} = 189\,\mu\mathrm{m}$ for 808 nm [195]. This is more than the thickness of the eardrum. Hence, reflections from the surface cannot be rejected and will influence the measurements.

Increased absorption inside the eardrum would result in a smaller reflection signal $R_{\mathrm{TM}}$ and lower transmission. Hence, it should be possible to account for a changed absorption coefficient in the eardrum. An increased scattering coefficient will decrease the transmitted signal but increase

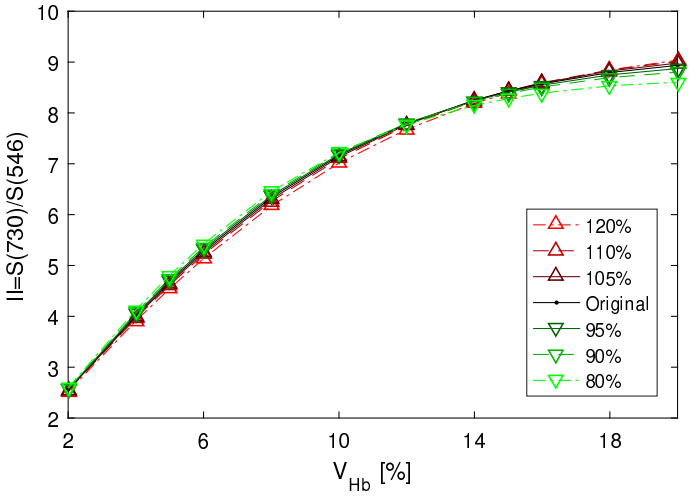


(a) Inflammation index

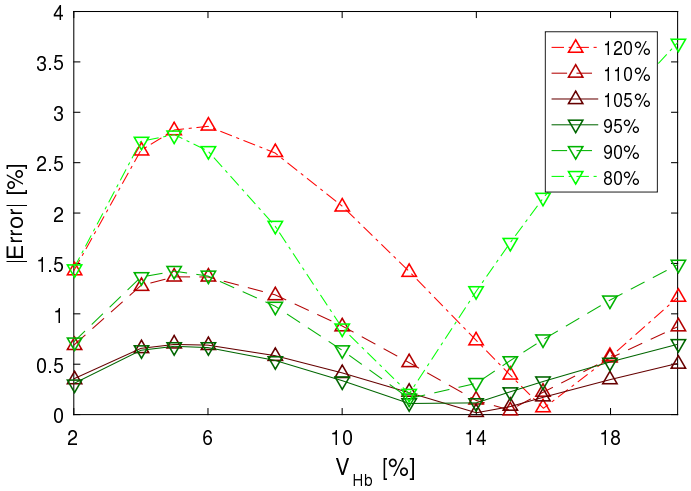


(b) Error

Figure 6.18: Influence of scattering of the mucosa on the inflammation index.

the reflected background (as presented in Section 5.4.3 describing the influence of scattering in the eardrum on signal and background). These assumptions will be tested on simulations varying the eardrum parameters presented below.

### Absorption of the Eardrum

The absorption of the eardrum is changed in simulations in order to investigate the influence on the inflammation index. Two wavelength independent cases were investigated, in one the absorption at both wavelengths is either doubled or halved. Further, the absorption is changed differently at both wavelength by a factor $k$ of 2.2 (multiplication by 4.33 and 2 for 546 nm and 730 nm, respectively) and 1.7 (multiplication by 2.5 and 1.45). Figure 6.19 shows the wavelength independent cases in red and the wavelength dependent cases in green. Subfigure a) shows the original data while subfigure b) shows the data scaled by the square of the relation $k^2$ at 730 and 546 nm.

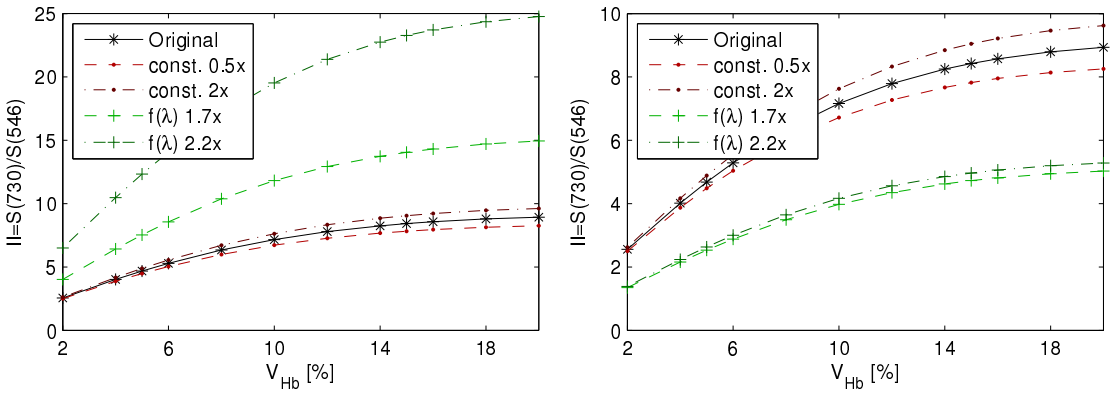


(a) Original Data

(b) Data scaled by $k^2$

Figure 6.19: Influence of absorption of the eardrum on the inflammation index.

The wavelength independent change of absorption introduces an error (maximum of 7.6 % and 7.7 % for scaling of 0.5 and 2 respectively) due to non-linear effects due to scattering that were neglected in the simplified derivations and definition of eardrum factor $c_{\mathrm{TM}}$. A wavelength dependent change has a much higher effect on the inflammation index as observed in Figure 6.19 (a). This influence is due to the fact that the light at 546 nm is more strongly attenuated than at 730 nm and thus the relation reduced. As the light passes the eardrum twice, the index is correct by the square of the scaling factor $k^2$; the results are shown in subfigure (b). The error is still higher than for the cases of equal change showing that correction of the inflammation index using the absorption of the eardrum is not trivial.

Next the confocal detected signal of the eardrum $S_{\mathrm{conf}}$ is measured and the relation $r_{\mathrm{conf}}$ of

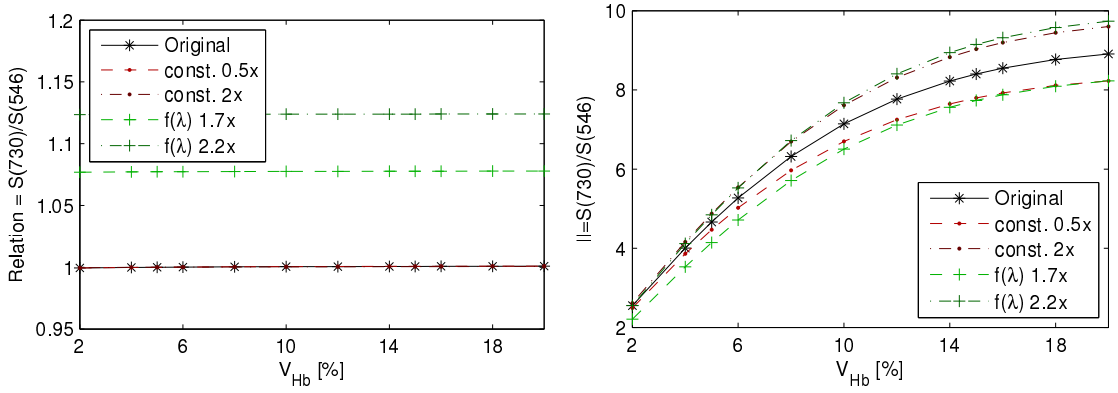


(a) Relation $r_{\text{conf}}$

(b) Data scaled by $r_{\text{conf}}^8$

Figure 6.20: Relation $r_{\text{conf}}$ of confocal signal (0.04 mm pinhole radius) from eardrum at 730 and 546 nm used to correct inflammation index for changing absorption.

the signal at 730 and 546 nm shown in Figure 6.20 (a). The relation of detected signal is almost independent on the blood concentration and only determined by the absorption of the eardrum as the confocal pinhole rejects all light from the mucosa. Subfigure (b) again shows the inflammation index, this time corrected by the confocal signal according to $1/r_{\text{conf}}^8$.

$$r_{\text{conf}} = \frac{S_{\text{conf}}(730)}{S_{\text{conf}}(546)} \tag{6.38}$$

This correction factor is chosen to minimise the change in inflammation index and achieves good results. A correction factor will have to be determined in experiments and will most likely differ from this factor found in simulations.

### Scattering Coefficient of the Eardrum

The influence of the scattering on the signal and SBR of the anti-confocal system was investigated in Section 5.4.3. An increase of the scattering coefficient reduces the signal but increases the SBR in most cases. For strongly forward scattering, the opposite can be true. The effect of scattering on the inflammation index is investigated here.

Wavelength independent and wavelength dependent changes of the scattering coefficient are investigated. Figure 6.21 (a) shows wavelength independent changes (factor of 2, 1.5, and 0.84) in red and wavelength dependent changes ("2x" indicates the signal at 730 nm is multiplied by 2 and "0.5" that the signal at 546 nm is multiplied by 2) in green.

Both, the wavelength independent and dependent cases change the inflammation index significantly in contrast to the simplified signal model presented earlier. This is a result of the scattering coefficient changing the spatial distribution of transmitted light and different distributions of the

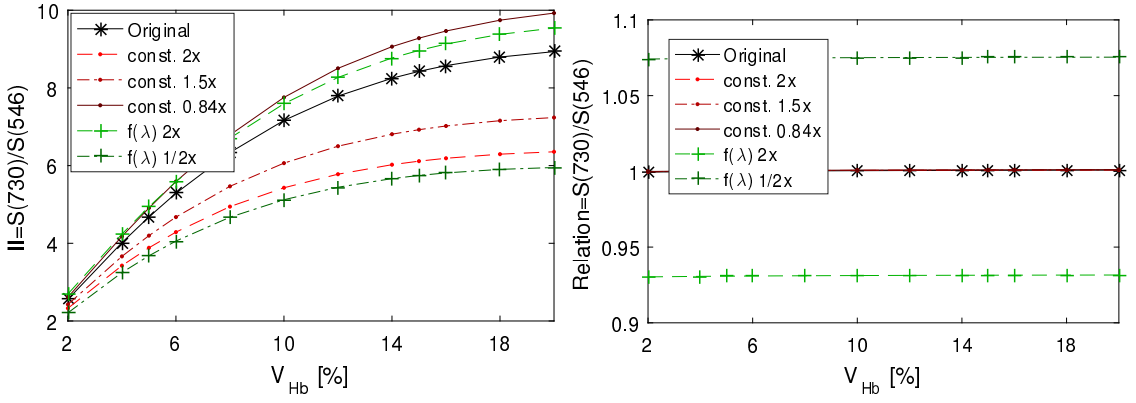


(a) Inflammation Index

(b) Relation $r_{\text{conf}}$ of confocal signal (0.04 mm pinhole radius) from eardrum at 730 and 546 nm

Figure 6.21: Influence of scattering of the eardrum on the inflammation index and confocal signal from the eardrum.

signal on the detector. A wavelength independent increase in scattering reduces the inflammation index, while the opposite is true for a decrease in scattering. An increase in scattering at 730 nm ("2x") increases the index. This is unexpected as an increase in scattering is expected to reduce the signal at 730 nm and thus decrease the index. But the opposite is true as the signal is further spread due to higher scattering and thus more signal detected using a stop. In the same way, an increase of scattering at 546 nm ("0.5x") increases the detected signal in the green range due to more signal being scattered into the detection aperture and the inflammation index is decreased.

Figure 6.21 (b) shows the confocal detected signal from the eardrum which is again independent of the blood content. The wavelength independent cases do not show a change in confocal signal relation even though the anti-confocal signal changed. Further, a decreased anti-confocal signal relation (dark green) is associated with an increased confocal signal while the opposite is true for changes in the absorption coefficient.

### Conclusion

The simulations showed that both the absorption as well as the scattering coefficient of the eardrum influence the inflammation index even when a change is independent of the wavelength. This shows that the simplified calculations made above are not valid (still they visualise the basic concept of the measurements). Also, the correction of the inflammation index by the confocal detected signal of the eardrum is not trivial as scattering and absorption show opposite effects. The influence of the scattering anisotropy has not been simulated and would complicate the signal processing even more.

### 6.5.4 Roughness, Rotation, and Noise

Other factors such as the rotation of the sample surface towards the beam affect the measured power as well. An increased angle results in the main direction of reflection directed away from the detector and a factor $c_{\text{rot}}$ must be included in the calculation of the signal Equation (6.15). Second, the surface roughness will affect the measurement as well accounted for by the factor $c_{\text{rough}}$. The use of a factor for the roughness is an approximation, as the roughness influences the distribution of the reflected signal. But in combination with the optics this results in a change in the detected signal, and the approximation is valid. Finally, some noise offset is added to the signal due to internal reflections on optical elements $n_{\text{refl.}}$ and camera noise $n_{\text{camera}}$. The signal can be expressed as

$$\begin{aligned} S_{\text{total}}(\lambda) = {} & I_0 \cdot R_{\text{M}}(\lambda) T_{\text{TM}}^2(\lambda) c_{\text{rot,M}}(\lambda) c_{\text{rough,M}}(\lambda) \cdot c_{\text{optics}} \\ & + I_0 \cdot R_{\text{TM}}(\lambda) c_{\text{rot,TM}}(\lambda) c_{\text{rough,TM}}(\lambda) \cdot c_{\text{optics}} \\ & + n_{\text{camera}} + n_{\text{refl.}} \end{aligned} \tag{6.39}$$

As explained previously, the background reflection by the eardrum is avoided by use of the anti-confocal system with high SBR. Noise subtraction (by use of an image recorded with the laser switched on and beam reflected from the sample directed away from the detector) both noise components can be minimised. The total signal simplifies to

$$S_{\text{total}}(\lambda) \approx I_0 \cdot R_{\text{M}}(\lambda) T_{\text{TM}}^2(\lambda) c_{\text{rot,M}}(\lambda) c_{\text{rough,M}}(\lambda) \cdot c_{\text{optics}} \tag{6.40}$$

Use of the inflammation index as measure will get rid of the roughness and rotation constants if both factors are independent on the wavelengths. This is assumed to be the case as it is intended to use wavelengths that are relatively close to each other and the same surface is sampled due to alignment of the lasers. The optics scaling factor and input power can also be neglected as explained previously. Hence, the inflammation index can be expressed as given in Equation (6.20) and will not be affected by the above factors.

## 6.6 Conclusion

Best wavelength for the measurement of the inflammation (blood concentration in tissue) and oxygenation have been found in simulations and match with wavelengths used in literature. The index is relatively unaffected by changes in scattering of the mucosa, roughness, angle of the surface, and wavelength independent changes of the absorption of the eardrum. In contrast, the distance between eardrum and mucosa, the scattering and wavelength dependent changes of the absorption of the eardrum affect the measurement. While the confocal detected signal of the eardrum might

give information about its properties signal processing is not trivial as scattering and absorption have opposite influences on the inflammation index and the confocal eardrum signal. The use of wavelengths closer to each other would reduce the influence of changes in scattering on the eardrum, but reduce the sensitivity of inflammation index to changes in the blood content.

While the influence of the eardrum on the measurements can be reduced using these two approaches, they cannot completely compensate for it. This means, if the absorption and scattering of the eardrum vary significantly between different patients or within one person over time, then the inflammation index cannot be reliably measured as the eardrum properties affect the measurement and calibration can only be performed on an average set of optical properties.

# Chapter 7

# Experimental Validation

During simulations the wavelengths 730 and 546 nm were found to be most suitable for measurements of the inflammation giving highest sensitivity. But no lasers are available at 546 nm or in the green range above. Hence, a laser with 532 nm wavelength is used instead. An NIR laser with 808 nm wavelength was available and used instead of a 730 nm laser as suggested by simulations. This will decrease the sensitivity of the inflammation index as shown in Figure 7.1, where the inflammation index and dependence of the measurement on oxygenation of the simulated and for experiments selected wavelengths is shown. The dependence on the oxygenation is low for both wavelength combinations while the dependence on blood concentration is lower for the wavelengths used in experiments. The measure for the sensitivity of the inflammation index $M_{\text{cHb-Oxy}}$ defined according to Equation (6.28) is decreased by a factor of 0.82.

## 7.1 Optical Setup

The anti-confocal system was set up on an optical bench for characterisation. A sketch of the system is shown in Figure 7.2. The used lasers are either a red laser with 650 nm wavelength or a green laser with 532 nm (BWN-532-30, B&W Tek, Newark, DE, USA) and a NIR laser with wavelength of 808 nm (L808P010, Thorlabs, Newton, New Jersey, USA, controlled by the power and temperature controller kit LTC100-B LD, Thorlabs, Newton, New Jersey, USA). The red laser is used for characterisation of the anti-confocal system and later replaced by the green laser for spectral measurements. The red laser was used to characterise the anti-confocal system and replaced by the green laser after according to spectral simulations presented in the previous chapter. The beams are expanded to achieve a diameter larger than 12 mm, aligned using a mirror pair, and attenuated to the same power level so avoiding saturation of the camera during recordings

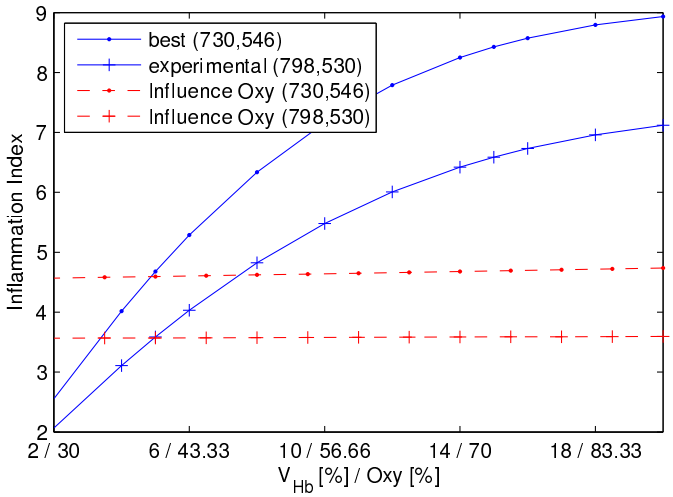


Figure 7.1: Simulated inflammation index for best wavelengths (730 and 645 nm) and experimentally used wavelengths (798 and 530 nm). Actually, 808 and 532 nm were used in experiments but were not simulated and hence the closest simulated wavelengths are used as approximations.

and allowing to use the same exposure time for measurements with both lasers. The second mirror in beam path of laser 1 is a cold mirror (M254C45, Thorlabs, Newton, New Jersey, USA) transmitting wavelengths higher than 700 nm and reflecting wavelengths lower than 700 nm used to combine both laser beams without significant loss of power.

An adjustable iris diaphragm with a maximum beam diameter of 12 mm (SM1D12C, Thorlabs, Newton, New Jersey, USA) restricts the beam diameter before directing the beam on the pellicle beamsplitter (CM1-BP145B2, Thorlabs, Newton, New Jersey, USA) with a split ratio of 45:55 (R:T) in the 700 to 900 nm wavelength range. The use of a pellicle beamsplitter is important because cube or plate beamsplitters result in ghost images with intensities higher than the signal reflected from diffuse samples. The reflected beam in the unused path is eliminated in a beam dump to avoid reflections to influence the measurements. A second iris diaphragm placed between objective lens and beam splitter is used to restrict the detection aperture. The aperture of both irises is adjustable to allow a change of the NA of the system for characterisation. The first one is necessary to reduce the beam diameter before the beamsplitter to avoid reflections from the backside of the second iris that can reach the detector and add background noise.

Two achromatic doublet lenses are used as imaging and objective lens respectively. The focal lengths are 80.3 mm (AC254-080-B, Thorlabs, Newton, New Jersey, USA) for the objective and 40 mm for the imaging lens when using the red laser. The lenses are coated for low reflections in the 650 to 1050 nm range. In case of the green laser, the focal lengths are 90 mm for the objective

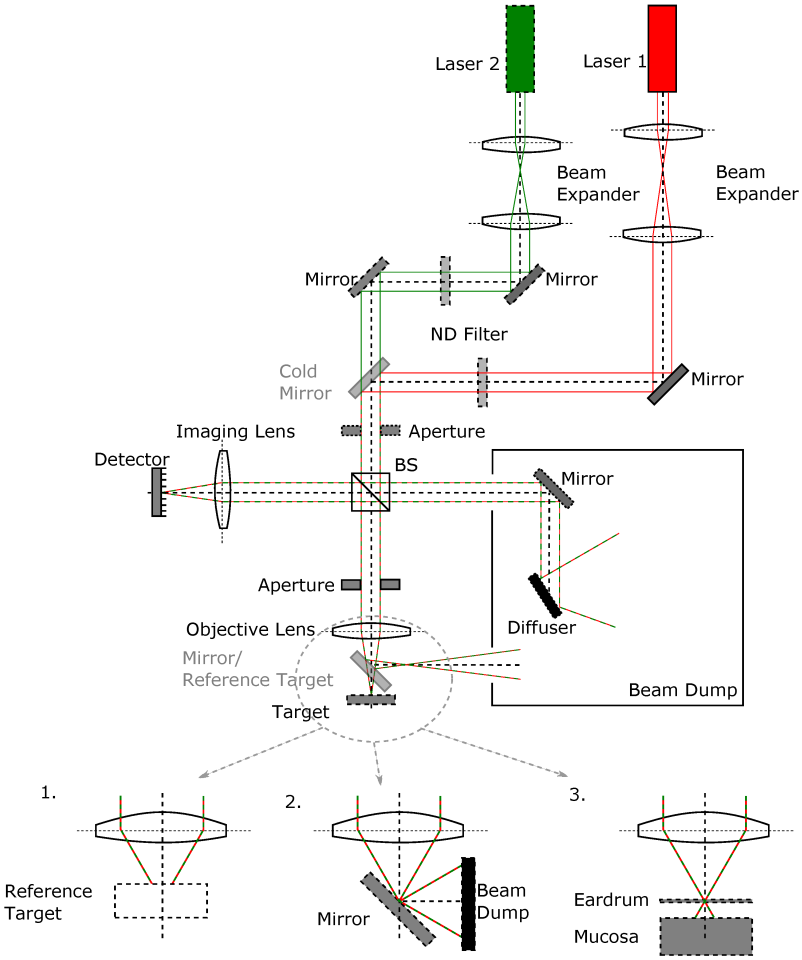


Figure 7.2: Optical bench top setup of the anti-confocal system. The magnified images of the sample show setups for recording a reference image (1), a background image (2), and a sample signal image (3).

and 80.3 mm (AC254-080-B, Thorlabs, Newton, New Jersey, USA) for the imaging lens. The lenses are again coated for low reflections but this time in a wider wavelength range down to green. The middle ear phantom is placed on the sample holder presented in Section 3.5.4 with the eardrum phantom in focus. The camera iXon$^{EM}$+ (Andor, Belfast, Northern Ireland) is placed in the image of the eardrum and acts as stop and detector. Spatial filtering is done in post-processing using MATLAB, by rejecting pixels within the stop radius. The camera has a monochrome CCD sensor with 1002x1004 resolution, pixel dimension of 8 µm square, and 14 Bit depth. A high dynamic range is necessary to allow detection of scattered light with low intensity while not saturating central pixel recording the high power reflected and focused signal from the eardrum. $2 \times 2$ pixel binning mode is used as the full 14 bit depth is not achieved without pixel binning. This results in $501 \times 502$ resolution with 16 µm pixel size.

An angled mirror and a reference target (WS-1-SS, Ocean Optics, Dunedin, Florida, USA) can be placed between sample and objective lens for either noise or reference measurements. The mirror directs all light to a beam dump so that all noise within the system (sensor noise, reflections within the optical system, ambient light) is recorded. The reflection standard is used to normalise the power of both lasers. The whole optical system is placed in a box blocking most ambient light in order to reduce the background noise in the system.

The alternative to the use of a camera would be to use a physical stop and a photo diode. This would increase the ability to detect small signals as high background reflections from the eardrum are directly rejected by the stop and the power could be increased to levels where central camera pixel would saturate and cause blooming effects. On the other hand, alignment would be more difficult, the stop radius would be fixed and the spatial distribution of the signal would be unknown. With the camera as detector, the stop radius can easily be changed in software and the whole detector area investigated to find the highest signal and lowest background components. Additionally, the central pixel of the CCD detector can also be used to confocally assess the eardrum as explained in Section 7.3.3.

### 7.1.1 Noise Reduction and Normalisation

Dark noise and reflections within the optical system add an offset to the recorded images. Hence, noise images are subtracted from the recordings in order to minimise the background. These are recorded as shown in Figure 7.2 option 2; a mirror directs the sampling beam to a beam dump resulting in no signal reaching the detector. Further, the power of each laser is normalised using the measurement of reflections from a reflection standard with refection bigger than 98 % for 250 to 1500 nm [223].

The recorded power changes over time as shown by the example recording in Figure 7.3. The NIR laser and camera are switched on for at least 15 minutes to allow the temperatures and laser output to stabilise. Noise images are then recorded over a time course of 27 minutes and subtracted from a signal image recorded at $t = 15$ min, resulting in a longer break in the recording of the noise images and exposure of the sensor to laser radiation, indicated by the dashed section in the graph. The sum of all pixels normalised by the average of all measurements $\frac{\sum s-n(t)}{\text{mean}(\sum s-n(t))}$ is shown here and variations are up to 5 % are visible. This is assumed to be a result of temperature changes of the detector even though the camera is temperature controlled. These small temperature changes change the background level and thus the final signal. The influence is relatively high here as the signal is very low. The highest change when recording the signal image can be explained by the longer interval between the noise recordings and exposure of the camera to laser radiation and hence warming of the detector.

As a result, the background and normalisation images have to be recorded as close as possible to the recording of signal images in order to minimise variations in the background noise. This results in the experimental protocol as follows:

1. The reflection from a white reflection standard is measured to determine the laser power.
2. The background noise is measured with a mirror directing the sampling beam away from the detector.
3. The reflection from the sample is measured.

This process is repeated for every sample and each wavelength. The final signal $s$ is then calculated as the sum over the pixel values of the selected area of the signal image $P_{\text{img}}$ with background noise $P_{\text{background}}$ subtracted and scaled by the input power given by the reference power $P_{\text{ref}}$ minus background image

$$s = \sum_{\text{sel. area}} \frac{P_{\text{img}} - P_{\text{background}}}{P_{\text{ref}} - P_{\text{background}}} \tag{7.1}$$

The short term variation from one time point to the next is smaller than the long term variation over the whole timespan. Hence, the signal will be improved by repeated updates of the background image.

32 frames were averaged for each measurement and the exposure time was 20 ms. Experiments showed that the contrast between the phantoms cannot be reliably detected when using only 4 or less frames or reducing the bit depth to 10 bit or lower. This again shows how critical good noise reduction is. It also shows the requirements of high dynamic range of detectors for anti-confocal measurements.

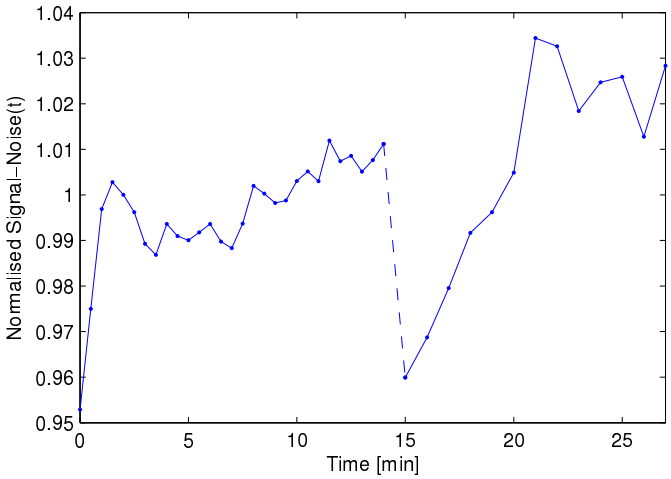


Figure 7.3: Influence of varying background on the measured signal over time. The shown example is recorded using the NIR laser. In the beginning an image was recorded every 30 s and after a short break (dashed section) the interval was set to 60 s.

### 7.1.2 Beam Width at Sample

In order to characterise the focus of illumination at the sample, the beam width at the focal region is measured. This is necessary to ensure a good focus to allow comparison of confocal and anti-confocal detection later. The beam width is measured by the knife edge measurement according to [224]. For this the detected power is recorded on the transition of a non-reflecting to reflecting straight edge. This is achieved here by moving a test resolution target orthogonal to the optical axis (x-direction) and an example result shown in Figure 7.4 (a).

When the beam is incident on the reflective area, the highest power is recorded. As soon as part of the beam hits the non-reflective area, the reflected power is reduced and reaches a minimum when the whole beam is falling on the non-reflective area. The width of the transition is used to determine the beam width. The distance $d_{90/10}$ between the point showing 90 % of the power to the point showing 10 % of the power is used as a measure as the edges of the transition are not easy to identify. The 90/10 distance of a Gaussian beam is related to the full width at half maximum (FWHM) and $1/e^2$ radius of the PSF by [224]

$$d_{90/10} = 1.09 \cdot FWHM = 1.28 \cdot r_{1/e^2} \tag{7.2}$$

The $1/e^2$ radius is the measurable diameter of the beam where the power is reduced to $1/e^2$ of the maximum power, containing 86.5 % of the beam power [225]. Figure 7.4 (b) shows this radius is dependent on the position of the target on the optical axis. Several measurements were taken for the green laser, while only one is shown for the NIR laser. The beam is in focus at $z = 0$.

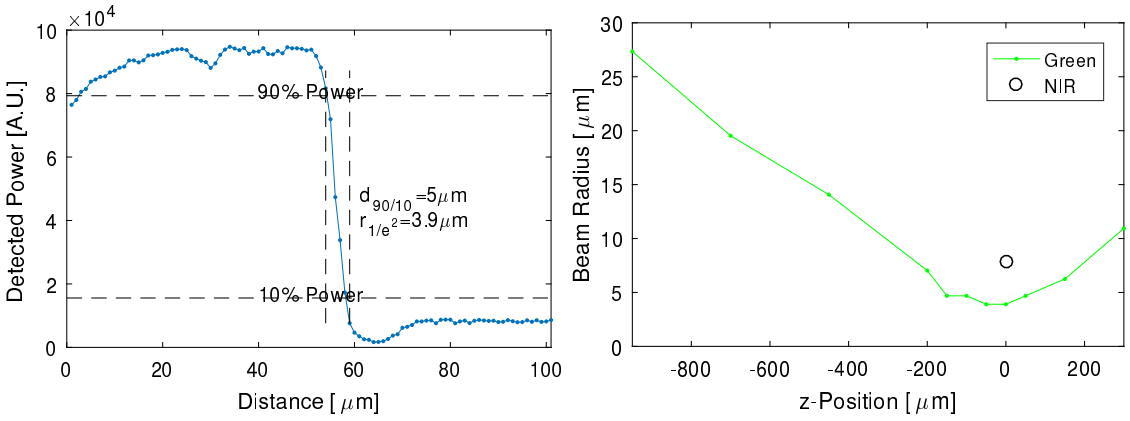


(a) x-scan at $z = 0$

(b) $r_{1/e^2}$ beam width dependent on z-position

Figure 7.4: Measurement of the beam width using the knife edge measurement.

This theory is only valid for Gaussian beams. The beams used here are not Gaussian as they are restricted by the apertures and the beam profiles at the sample are shown in Figure 7.5 (a). The beam is recorded by a RGB camera (DCC1645C, Thorlabs, Newton, New Jersey, USA) placed at the sample position, slightly out of focus. The green beam shows a Gaussian shape but is cut off while the NIR beam shows a relative constant power distribution. The blue dashed line shows an ideal Gaussian distribution with 530 pixel radius.

As both beams show a clear cut-off, the transition from constant maximum and minimum power to transition region is more distinct than for Gaussian beams and the distance between maximum and minimum detected power $d_{100/0}$ is used to measure the beam width. This measurement is shown in Figure 7.5 (b) in green and the previously measured beam width is shown in blue. A scaling of the beam radius measured by the 90/10 distance by a factor of 2.3 approximates the 100/0 distance for the green laser. Another scaling factor is necessary for the NIR beam due to a different beam profile. The measurement fits well with the theory, shown in black dashed, except for a less ideal focus with minimum beam diameter of around 8 instead of 4 µm, caused by aberrations. The theoretical beam width is calculated by

$$w(z) = w_0 \sqrt{1 + \frac{\phi \cdot z}{w_0}^2} \tag{7.3}$$

where $w_0$ is the minimum beam diameter given by the Airy disc $w_0 = 2 \cdot r_{\text{airy}} = 2 \cdot 0.61 \cdot \frac{\lambda}{NA}$, and $\phi$ is the beam divergence given by the NA [224].

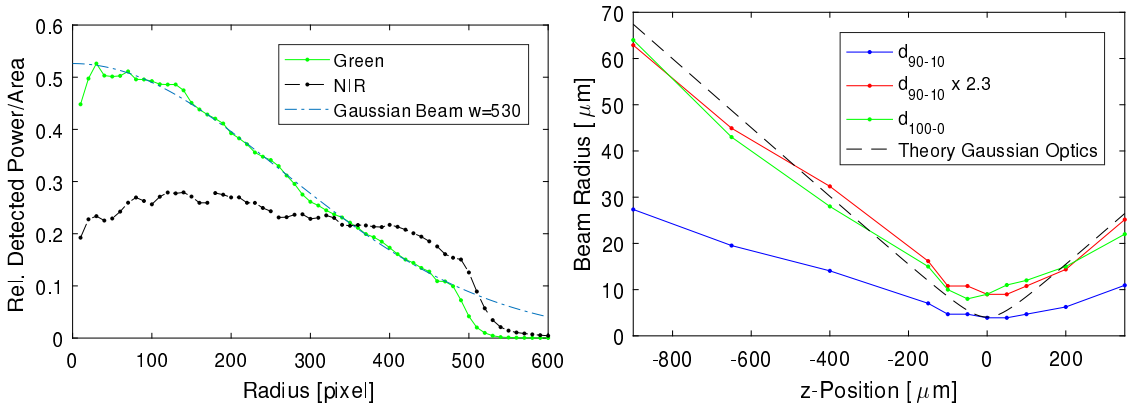


(a) Relative power per area dependent on radius

(b) Beam width dependent on z-position

Figure 7.5: Modified knife edge measurement

## 7.2 Anti-Confocal System

In this section the optical setup with red and NIR laser is used and measurements are made on the one wavelength phantoms. Spectroscopic measurement, presented in the next section, will be conducted on the 2 wavelength phantoms and using the setup with the green instead of the red laser.

### 7.2.1 Axial Resolution

The focal plane is scanned through the sample along the optical axis (z-axis). In case of the confocal system (pinhole filtering) a maximum signal is expected when the sample is in focus, while a minimum is expected for the anti-confocal system. First, a mirror is used as sample and the recorded power dependent on the focus position for different pinhole or stop radii shown in Figure 7.6 (a) and (b), respectively. At $z = 0\,\text{mm}$ the sample is placed closest to the objective lens and is moved further away with increasing $z$.

From subfigure (a) it is obvious that the mirror is in focus, at $z \approx 13.5\,\text{mm}$ as a maximum signal is shown. Further, it can be seen that more power is detected for a higher pinhole radius and also the peak is wider indicating an increased detection depth and decreased depth resolution. The opposite is true for the stop as the stop is the inverse of the pinhole filtering.

The dashed lines in subfigure (a) and (b) show the theoretical signals calculated by geometrical optics. The detected power is calculated using the thin lens and paraxial approximation and optical system as used in the experiment. A homogeneous beam is assumed and the detected power calculated by the transmissive area of the filter divided by the beam diameter at the filter

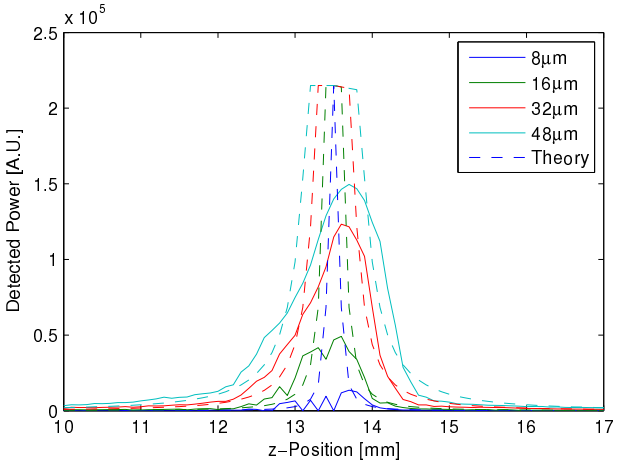


(a) Mirror as sample, pinhole radius according to legend

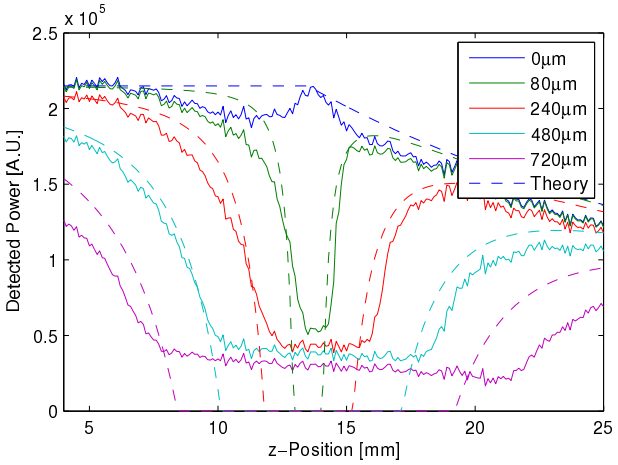


(b) Mirror as sample, stop radius according to legend

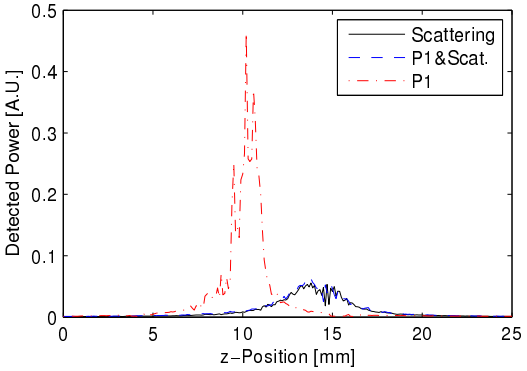


(c) Pinhole with 48 µm radius, sample according to legend

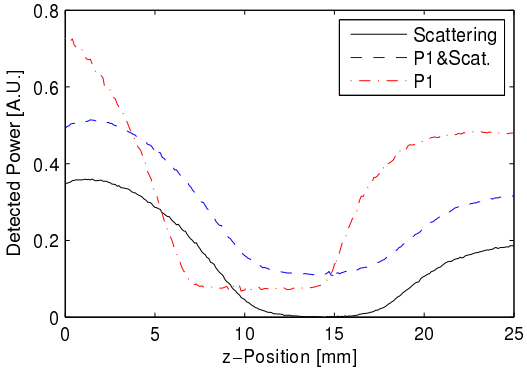


(d) Stop with 480 µm radius, sample according to legend

Figure 7.6: Z-scan through a sample using confocal and anti-confocal filtering. At $z = 0$ the sample is placed closest to the optics.

position.

$$P_{\text{Pinhole}} = \frac{\pi r_{\text{Pinhole}}^2}{\pi r_{\text{Beam}}^2} \tag{7.4}$$

$$P_{\text{Stop}} = 1 - P_{\text{Pinhole}} \tag{7.5}$$

where the beam radius $r_{\text{Beam}}$ is easily calculated using geometrical optics. The theoretical values only account for signal loss at the spatial filter and need to be scaled to match the measured power. The scaling used here is chosen to match the total power when no stop or pinhole filtering is applied. Another effect is visible in the total signal (stop of 0 mm diameter), where the power decreases when the mirror passes the focus. This is due to the fact that the reflected beam is cut off by the lens aperture and thus less light is detected. This effect is shown in measurements and theory. The maths used here is different from the normal confocal theory in that the pinhole radius is increased to a level where diffraction effects are negligible and geometrical optics can be used.

The theory fits well in the anti-confocal case, except that the signal does not go to zero. This is assumed to be due to the offset caused by the background level that cannot be removed due to the long time difference between recording of the background and signal image. The theory and measurement differ more in the confocal case. The peaks are less distinct and wider in the measurement. This is due to aberrations in the system causing a wider and not perfectly focused beam. Hence, a large pinhole must be used, degrading the axial resolution. But as the sample investigated here is characterised by a distance of 3 mm between mucosa and eardrum, the reduced resolution is not a problem. However as the pixel size is $16 \times 16\,\mu\text{m}$ a pinhole with radius similar to the pixel dimension is only able to be approximated with a low resolution.

Figure 7.6 (c) and (d) show the same scan over a wider z-range for different samples, the diffuser as scattering layer, a mucosa phantom, and the complete middle ear phantom composed of mucosa and eardrum. When using the mucosa phantoms only, a clear peak is visible in the confocal case indicating the z-position of the surface. The cases of a scattering layer show a smaller peak at the position of the scattering layer surface. The peak is lower as the signal is smaller for the scattering layer. The case of eardrum only and complete middle ear phantom are not distinguishable and no peak is seen for the phantom surface as only few unscattered photons pass the eardrum phantom twice and very low signal is detected.

The anti-confocal filtering shows a clear minimum for the mucosa phantom only, while the minimum is less clear for the case of middle ear phantom. The case of eardrum phantom only is clearly separated from the case of middle ear phantom.

### 7.2.2 Radial Resolution

The radial resolution of the system is characterised for measurements through the eardrum. The same setup as the beam width measurement explained in Section 7.1.2 is used with the difference that measurements are conducted with an eardrum sample in the beam path. In case of the confocal measurement, the surface of the mirror is placed in focus and the eardrum sample 3 mm in front of it. In case of the anti-confocal measurement the eardrum is placed in focus and the mirror is placed with a distance of 3 mm behind it. The detected signal is measured when moving a reflective edge through the beam. The test resolution target used earlier is replaced by the edge of a mirror because a large homogeneous area is necessary to measure the resolution of the wide spread scattered signal. Resolution for both confocal and anti-confocal systems are measured, with the mirror alone and with the diffuser as eardrum phantom placed in front of the mirror. The green laser is used for sampling.

Figure 7.7 shows the result of the experiment with each measurement normalised to its maximum value resulting in a scale of 0 to 1 of the detected power. The confocal signal measured on the mirror shows a sharp transition with a width of about 25 µm. The approximate transition width is marked by the vertical dotted lines. When placing the diffuser in front the mirror the width of the transition gets wider (about 200 µm) and the contrast is decreased. The latter is the case because the signal is reduced due to scattering and background is added due to a use of a pinhole of 48 µm radius.

The transition area is about 670 µm wide for the anti-confocal system (stop radius of 480 µm) without the diffuser in place. This increase is a result of the beam being focused 4 mm in front of the mirror (at the position where the diffuser would be in focus) resulting in a beam radius of 300 µm at the mirror. This transition area is further increased to about 1050 µm when placing the diffuser in the beam path as the light is spread further due to scattering. But at the same time the contrast is increased compared to the confocal system.

The detected confocal power is about 50 times lower than the anti-confocal signal. This shows the better resolution but lower signal level of the confocal system. As the resolution is not relevant in this application whilst the signal level is, the anti-confocal system is advantageous.

### 7.2.3 Radial Power Distribution

In this section in the CCD camera images are analysed to allow further signal processing. In this and in all following experiments (unless stated otherwise) with the anti-confocal setup the optical system is focused on the surface of the eardrum. If no eardrum phantom is used during the experiments, the focus is not changed and is where the surface of the eardrum would be if placed.

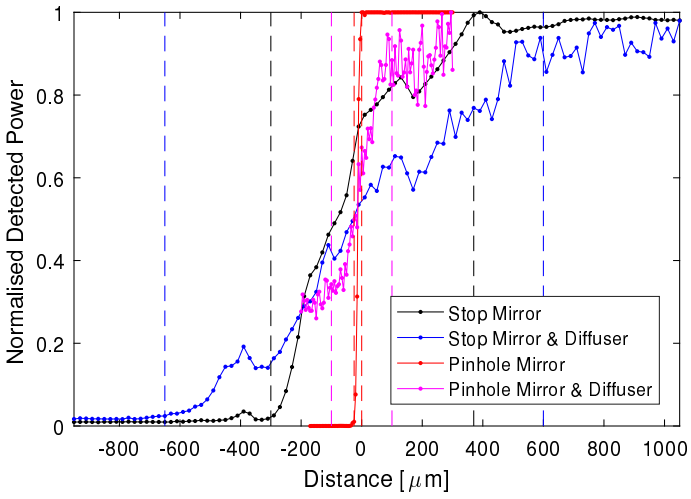


Figure 7.7: X-scan through a sample using confocal and anti-confocal filtering. Pinhole radius = 48 µm, stop radius = 480 µm, and sample and filtering according to legend.

The mucosa phantoms are placed 3 mm behind the eardrum or its theoretical position and out of focus.

Recorded images of the anti-confocal detector are shown in Figure 7.8 using a logarithmic scale. The left image shows the power distribution when only a mucosa phantom is used as target, in the middle image only the eardrum phantom is used as target, and on the right the detected power is shown when both mucosa and eardrum phantom are used as target. All three images show the same scale of pixel readings of the camera. In case of the mucosa phantom, the signal is distributed over a wider range as the beam is defocussed and light scattered inside the phantom. The illumination is focused on the eardrum and thus a higher maximum intensity is seen and the power is more concentrated in the middle graph in Figure 7.8. For the complete middle ear phantom both images are superimposed, with the signal from the mucosa attenuated.

Smearing of the signal below the centre is observed in all images even though images are not saturated. The used camera is a frame transfer CCD and the pixels are still exposed to light during the frame transfer [226]. This causes the observed smearing, which is more obvious for smaller exposure times (20 ms are used here). To avoid this effect, the lower half of the images is ignored.

To analyse the power distribution in more detail, the power dependent on the radial distance $r$ from the centre of the beam is shown in Figure 7.9. MATLAB was used to find the centre of the beam, defined as centroid of the area where the intensity is higher than $\frac{1}{e}$ maximum intensity, and calculation of the power. The radius is analysed in steps of 2 pixel equal to 32 µm or about four times the diameter of the point spread function at the focus. The power in each radial area is shown dependent on the radius on the x-axis and is different from the intensity (power per area)

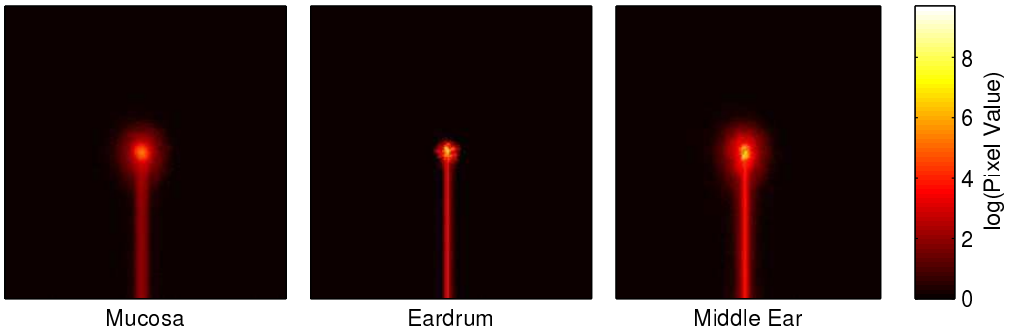


Figure 7.8: Examples of recorded images for anti-confocal detection from different phantoms. Smearing is visible in all images as bright lines below the central signal spot. The camera area is $8 \times 8\,\mathrm{mm}^2$.

as the area for each radial section changes with $r^2$. Hence, the intensity falls off more quickly than the shown power per angle. This current way of plotting is selected as it directly shows the power that will be selected by anti-confocal stop filtering with a certain radius.

The coloured solid lines show the power distribution of the mucosa phantom only, each colour indicates a different phantom. The dashed lines show the power distribution for the middle ear phantom with the same colour coding used for the different mucosa phantoms. The black dash-dotted line shows the recorded power for the eardrum phantom.

It is obvious that the signal from the eardrum phantom is spread over a smaller area and shows a higher maximum value than the mucosa phantoms only. The mucosa phantoms show a main lobe with about 320 µm radius and then a flatter decay for a higher radius (transition indicated by the vertical black dotted line). This main lobe is a result of direct reflections from the phantom surface. The theoretical width of the illumination beam diameter at phantom surface $w$ is given by

$$w = \frac{r}{f} \cdot d \approx NA \cdot d = 0.08 \cdot 4\,\mathrm{mm} = 0.3\,\mathrm{mm} \tag{7.6}$$

where $r$ is the aperture radius, $f$ the focal length of the lens, and $d$ the distance from scattering surface to mucosa surface. This fits well with the measurement and is also visible in experiments shown later where the distance and NA are varied.

The maximum of the power at around 150 µm observed here is a result of decreasing intensity with increasing radius but at the same time increasing area. Intensity plots do not show this behaviour but show a maximum in the center instead.

Further, it can be seen that the power is higher for the phantoms with lower absorption coefficient (lower number) when measuring the reflectance of the mucosa phantom only (factor of about

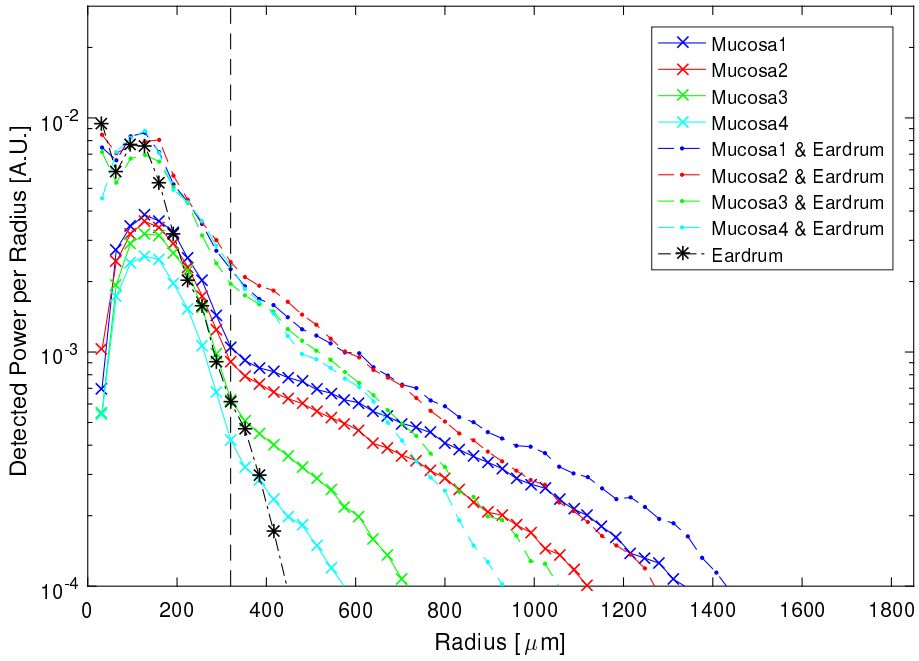


Figure 7.9: Radial distribution of power in the images.

1.1, 1.2, and 1.5 in the main lobe or 1.3, 3, and 5.1 in total of phantom 1 compared to the others). At high radii (bigger than around 600 µm) the same is true for the complete middle ear phantom. At lower radii this is not true as in the centre the power is more determined by reflections from the eardrum rather than the mucosa phantom.

### 7.2.4 Filtering of the Signal using the Anti-Confocal Stop

As seen in Figure 7.9, the detected signal from the middle ear phantoms can be distinguished at radii higher than around 600 µm while this is not the case for smaller radii. Hence, the anti-confocal stop is used to reject the central portion and only recover the absorption dependent signal. Figure 7.10 shows the detected signal for the four mucosa phantoms when using stops with different radii ranging from 160 to 640 µm. The detected power is shown dependent on the absorption coefficient of the phantoms at 808 nm wavelength along the x-axis. The total detected power without stop filtering is shown as a solid line while the power when using stop filtering are shown as dashed lines. The red line indicates the measurement where the sample used is the mucosa phantom without the eardrum phantom in place. This is the ideal signal that could be achieved when the signal path is not blocked and is used as a reference. The power is normalised to the power of Phantom 1 (lowest absorption) for each series to allow easy comparison of the contrast between the phantoms. Five positions (1 mm apart) were measured, the mean values are

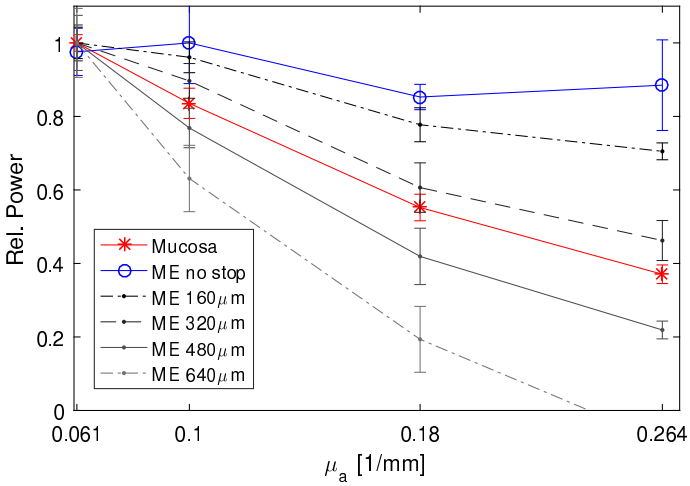


Figure 7.10: Contrast between phantoms for different stop radii. The absorption coefficient for each phantom is given on the x-axis ($\mu_{\mathrm{a,Phantom1}} = 0.061\,\mathrm{mm}^{-1}$, $\mu_{\mathrm{a,Phantom2}} = 0.1\,\mathrm{mm}^{-1}$, $\mu_{\mathrm{a,Phantom3}} = 0.18\,\mathrm{mm}^{-1}$, $\mu_{\mathrm{a,Phantom4}} = 0.264\,\mathrm{mm}^{-1}$). ME – middle ear phantom composed of mucosa and eardrum.

shown here with the standard deviations shown by the errorbars. Additionally to the stop, a large pinhole with radius of 1.92 mm was applied to reduce the influence of background variations far away from the centre of the beam.

The reference measure of the total detected power of the mucosa phantoms shows a contrast between the phantoms with small errorbars indicating homogeneity of the phantoms. This contrast is not visible without stop filtering when the eardrum phantom is placed in front of the mucosa as the mucosa signal is attenuated and superimposed by the reflections from the eardrum. The large errorbars of the total signal stem from inhomogeneities of the diffuser used as the eardrum phantom and the small sampled area as the beam is focused on the eardrum.

When applying a stop, the contrast is improved and the errorbars reduced as the reflections from the eardrum are rejected while signal from the mucosa is still detected. When using a stop, the contrast also improves for the mucosa phantom only (not shown) as direct surface reflections are rejected leaving only scattered light. For the full middle ear phantom including the eardrum, the contrast increases further as more and more scattered light from the eardrum is rejected. Values below zero are reached when the influence of the varying background noise causes negative pixel readings after noise subtraction. But the standard deviation increases again for higher radii because the signal power decreases with increasing stop radius, increasing the influence of the background.

Figure 7.11 (a) shows the absolute power of mucosa phantom 1 alone, eardrum phantom alone,

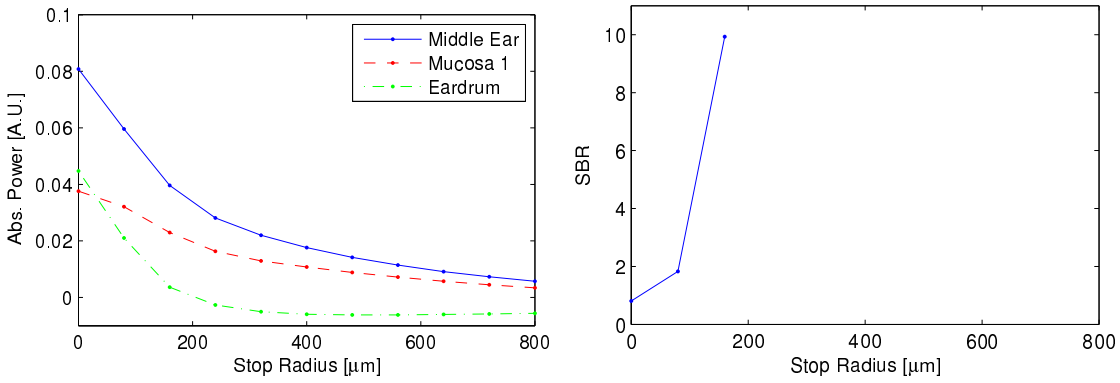


(a) Absolute Power (b) SBR

Figure 7.11: Absolute power and SBR for different stop radii. Inaccurate background noise subtraction causes negative pixel readings for the eardrum phantom and hence the SBR can not be calculated.

and complete middle ear phantom in dependence of the stop radius. The power of the mucosa phantom decreases slower than the power detected from middle ear and eardrum phantom. This shows that the stop is effective at rejecting more power from the eardrum than from the mucosa. The power of the eardrum reaches negative values due to the variation of the background level observed in Figure 7.3 resulting in inaccurate noise subtraction. In case of the eardrum as lone phantom only signals are expected in the center of the camera area. Thus at larger radii, no signal is present ans small error in noise subtraction cause the observed negative values. Similar result were observed in other measurements, an increase in background level results in negative values while a decrease in background causes a positive offset.

The background and combined signal of background and signal are directly available from the measurements, the first measured by the reflection signal from eardrum alone $P_{\text{eardrum}}$ and the latter measured by the complete middle ear phantom $P_{\text{middle ear}}$. The signal is not directly available and must be derived by subtracting the background from the combined signal. The SBR in the measurements is calculated according to

$$SBR = \frac{P_{\text{middle ear}} - P_{\text{eardrum}}}{P_{\text{eardrum}}} \tag{7.7}$$

In accordance with simulations, the resulting SBR shown in Figure 7.11 (b) first increases with stop radius, but no values are shown above 160 µm as the background measurement reaches negative values and the calculation of the SBR is not valid any more. In theory the SBR should increase further as the background decreases faster than the signal and reaches almost zero. The SBR is a derived measure dependent on different measurements and strongly affected by the changing

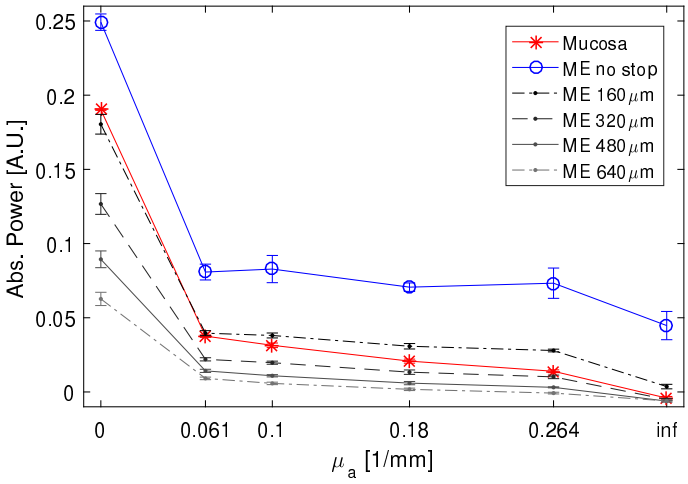


Figure 7.12: Detected Power for different mucosa phantoms with $\mu_a$ for each phantom on the x-axis.

background level, and hence not very accurate. Instead of the signal level and SBR as used in the simulations, the ability of the anti-confocal system to detect a difference in the signal from different mucosa phantoms is used as a measure.

Figure 7.12 shows the absolute power when applying stops similar to Figure 7.10 where the relative power was shown. Additionally to the previous mucosa samples, a white ($\mu_a = 0\,\mathrm{mm}^{-1}$) and completely absorbing ($\mu_a = \mathrm{inf}\,\mathrm{mm}^{-1}$) sample are included. The white sample is the reflections standard and the total absorbing signal is measured when using a mirror to direct all signal away, simulating total absorption. This graph illustrates the contrast of the four mucosa phantoms ($\mu_a = 0.061,\ 0.1,\ 0.18,\ 0.264\,\mathrm{mm}^{-1}$) at a scale ranging from 100 % reflection from the mucosa (reflections standard) to no reflection (mirror). The phantoms span only a small range of the total contrast, but still can be distinguished as shown earlier. The figure further shows the decreasing detected power when using larger stops.

### 7.2.5 Influence of Other Parameters on the Measurement

During simulations the influence of optical parameters other than the absorption of the mucosa on the measurements were investigated. These parameters were listed in Table 5.7 and can be split into parameters of the optical system and properties of the middle ear. The subsequent sections will investigate their influence on anti-confocal measurements experimentally. The combination of pinhole and stop is not investigated as simulations showed no advantage and because it would complicate the optical setup. Further, scattering of the mucosa is not varied as this would require the production of additional phantoms and simulations shows only small influences on measurements

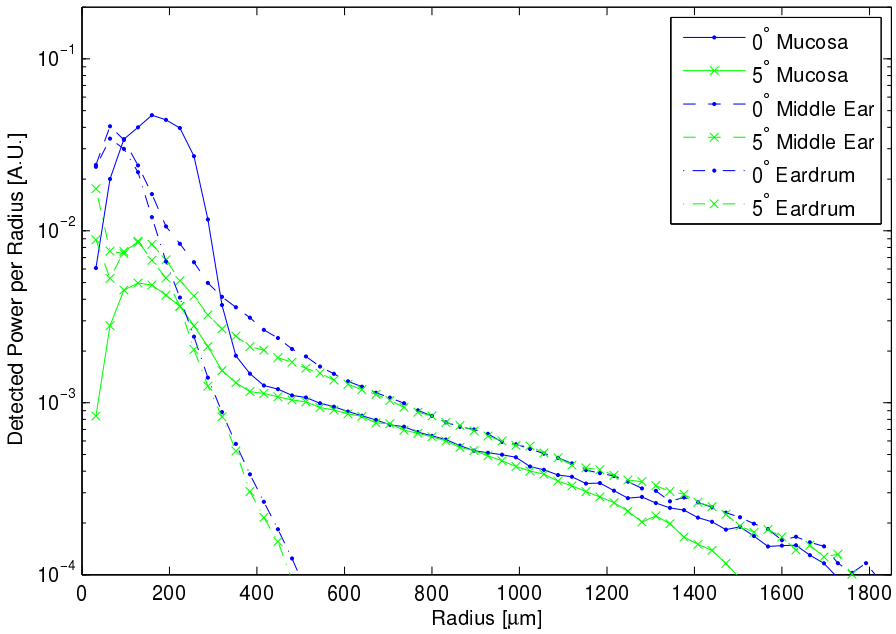


Figure 7.13: Radial distribution of power dependent on the surface orientation.

of the inflammation index. All other parameters will be varied.

### Influence of the Surface

In this section the influence of the surface of the phantom and the angle of the surface towards the optical axis is investigated. For this the above measurement is repeated for two angles (0 and 5 °) of the middle ear phantom and two different surfaces of the mucosa phantom. One surface is rough due to machining of the samples and the second one is polished, showing partly specular reflections.

The influence of the angle on the measurements is shown for the polished side as the effect is more distinct. Figure 7.13 shows the radial distribution for mucosa phantom 1, compared for both angles, where green lines are used for 0 ° and blue lines for 5 ° orientation. Solid lines show the mucosa, dashed lines the middle ear, and dashed-dotted lines the eardrum phantom.

Comparing the signal from the mucosa phantom a higher main lobe for 0 ° is visible. This is due to the fact that specular surface reflections are directly reflected back and reach the detector while this is not the case when angled as specular surface reflections are directed away from the collection optics. The signal from the eardrum phantom is similar but higher for 0 ° as the main scattering direction is towards the detection aperture while it is away from the detection aperture for the angled case. The same effects are visible for the full middle ear phantom, where the main

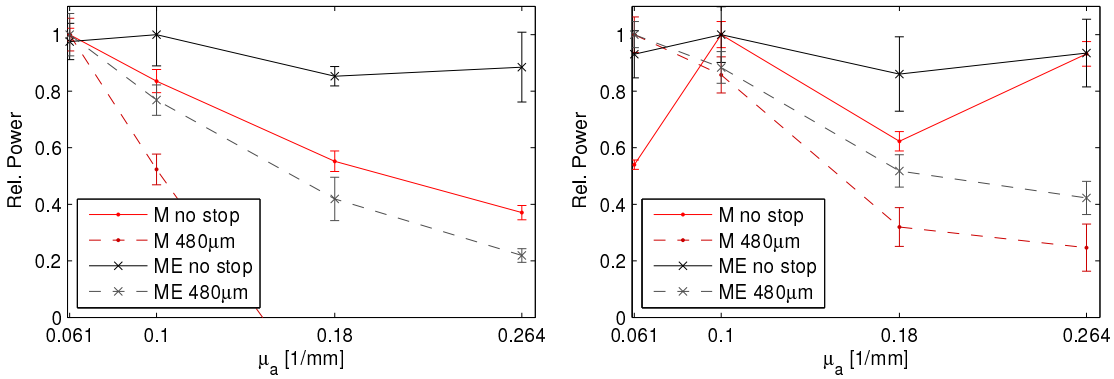


(a) 5 ° orientation

(b) 0 ° orientation

Figure 7.14: Influence of surface orientation on the contrast at stop radius of 0.48 mm. M – mucosa phantom, ME – middle ear phantom.

lobe is more pronounced for 0 °. The falloff of the 5 ° mucosa signal at high radii is a result of a changing background level during the measurement.

Figure 7.14 compares the contrast for both cases at a stop radius of $r = 0.48$ mm. Subfigure (a) was shown previously while subfigure (b) shows the contrast for 0 ° orientation. While the contrast is visible for the mucosa phantom only at 5 ° measurements, this is not the case for 0 °. This is due to direct surface reflections. The phantoms are not polished in exactly the same way and flatter ones show higher specular reflection and higher signal, but stop filtering is able to eliminate this portion and in both cases, the contrast can be reconstructed using the stop but is higher for the 5 ° measurement.

The results for the diffuse side are not shown. Observations are similar, but the influence of the angle is lower as the influence by specular reflections is also lower. But in all cases the contrast can be reconstructed.

### Wavelength

All results shown earlier were recorded using the NIR laser. This section compares the results of the red to the results of the NIR laser. The scattering coefficient of the mucosa samples is higher and the absorption coefficient is lower in the red range compared to the NIR range. This results in a higher reflection signal compared to NIR. This means the reflected power will be higher for red than for NIR and this is shown in Figure 7.15 (a) where the measured reflected signal is shown for red and NIR at a stop radius of 0.72 mm. The x-axis shows the absorption coefficient for each mucosa phantom at the respective wavelength. The NIR signal shows lower power and also reduced

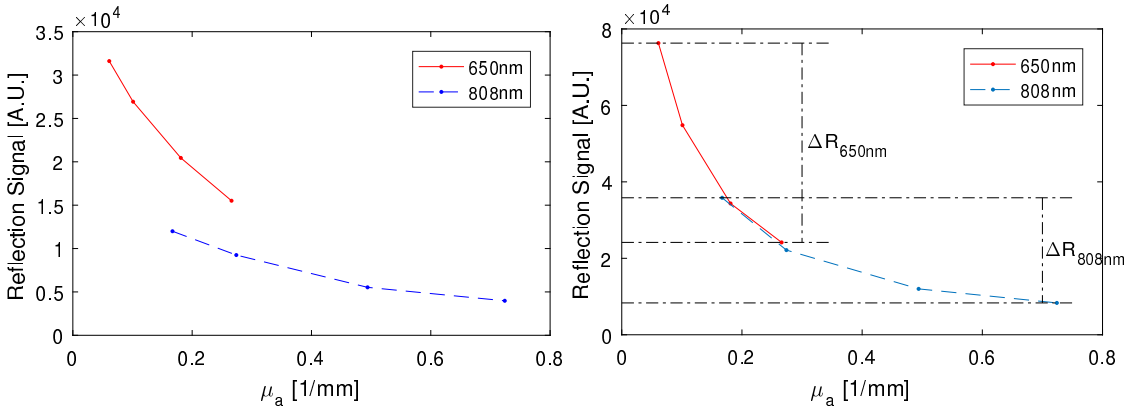


(a) Measurement, 0.72 mm radius

(b) Simulation, 0.75 mm radius

Figure 7.15: Simulated and measured reflectance of the full middle ear phantoms at two wavelengths.

contrast between the phantoms.

Subfigure (b) shows the simulated reflection signal using a stop of 0.75 mm. The measurements show a similar course to the simulation, confirming the simulation results presented earlier.

### Focus

The influence of the focus of the anti-confocal system is tested. For this, one measurement with the eardrum in focus is compared to a defocused case (focus is moved 1 mm away from the middle ear). The NIR laser is used in this case and the polished side with 0 ° orientation is measured. Figure 7.16 shows the contrast for both cases when using a stop of 0.48 mm radius. The signals are very similar but show a lower standard deviation when out of focus. This is due to the fact that the beam is defocused and thus illuminates a bigger area of the eardrum and so an average rather than the reflection from a small area is measured. This effect is bigger for the eardrum as the focus spot is smaller.

The filtered contrast is also slightly better for the defocused case as a wider area is sampled and local inhomogeneities and surface characteristics play a smaller role. This shows that an accurate focus of the anti-confocal system is not of importance and a defocus may even improve the system characteristics. This will improve the ease of use of the whole system and confirms simulations predicting no deterioration of the signal when out of focus.

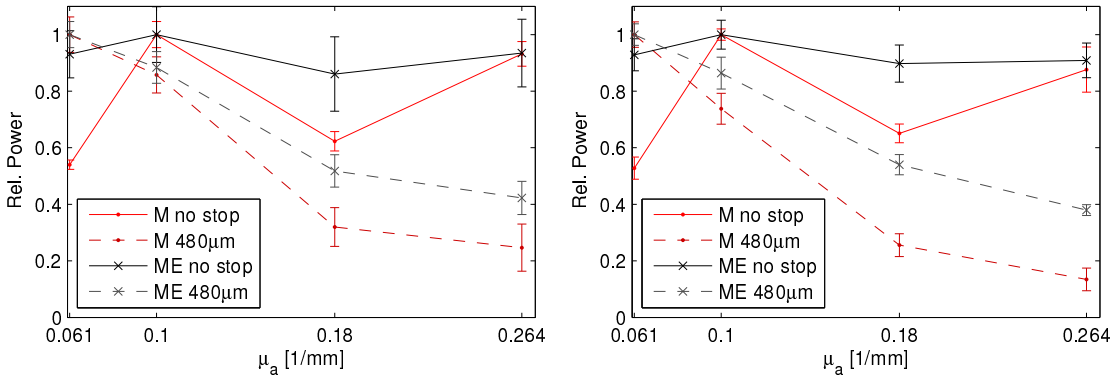


(a) In focus

(b) 1 mm out of focus

Figure 7.16: Contrast at stop radius of 0.48 mm with the system 1 mm out of focus. M – mucosa phantom, ME – middle ear phantom.

### Distance between Eardrum and Mucosa

As the middle ear differs from person to person the distance from eardrum to mucosa may change. Hence, the influence is tested by changing the distance of mucosa and eardrum phantom from 2 to 6 mm spanning the range expected the in humans, while keeping the optics focused on the eardrum and all settings of the optics unchanged. As described earlier the main lobe of the radial power distribution of the mucosa phantom is dependent on the distance between eardrum and mucosa according to Equation (7.6) and an increasing width of the main lobe observed in the measurements (graphs not shown). Also the signal of the middle ear phantom is further spread with increasing distance and the contrast reduced.

### Scattering Layer

The eardrum phantom was changed in order to investigate the performance of the anti-confocal system for changed scattering characteristics. Instead of the diffuser, greaseproof paper and a sandpaper 'treated' glass slide of 1.1 mm thickness (P240 grid, treated in same direction on each side) are used as the eardrum phantom. In the case of the highly scattering greaseproof paper the system is not able to reconstruct the contrast as the attenuation is too high and no signal components are detected. In case of the sanded glass the contrast can be reconstructed.

It has to be mentioned that the direct reflections from the sanded glass are higher than for the diffuser used previously and the illumination power has to be reduced so as not to saturate the camera and no mucosa signal could be reconstructed in the first measurement. In a second step, the phantom was defocussed or was tilted, both reducing the power of the central direct

reflection. This allowed an increase of the illumination power without saturating the camera image and enabled detection of signal from the mucosa.

This shows limitations of the use of a camera instead of a physical stop. A physical stop would reject the central high intensity and avoid saturation of the detector and the need for a high dynamic range of the detector in order to pick up small mucosa signals. However, this also shows another positive effect of a defocussed system, apart from the reduced variation of the signal. It allows an increase of the input power without saturating the detector and thus an increase of the detected signal.

#### Small illumination diameter

The use of a small illumination diameter was proposed in order to simplify the optical setup as no beam expansion would be necessary. The simulations suggested that this will not affect the performance of the anti-confocal system. This is tested by reducing the illumination diameter from 12 to 1 mm in experiments. This causes all power of the input beam to be centred close to the optical axis where the lens surface is almost orthogonal to the optical axis. This results in more power being reflected from the lenses back along the optical axis and increases reflections and background noise on the camera. This introduces noise masking the small mucosa signal and hence no contrast can be recovered. This result could not be predicted in simulations as no reflections on optical elements or noise was simulated.

#### NA

The influence of the NA on the anti-confocal system is investigated by changing the NA from 0.027 to 0.196. One iris is used to restrict the input beam diameter $D$ and a second one to restrict the detection aperture. The NA is changed according to $NA = \frac{D}{f}$. The maximum beam diameter is 12 mm and hence the maximum achievable NA with the current lens with 80.3 mm focal length is about 0.08. To achieve a high NA this lens is replaced by a lens with 30 mm focal length achieving a maximum NA of 0.196. But this changes the magnification of the lens system ($40 : 80.3 = 0.5$ versus $40 : 30 = 1.33$) and the stop dimension on the camera need to be adopted by the change in magnification 2.68.

The results for these experiments are shown in Figure 7.17 where the radial power distribution for each NA is plotted in subfigures (a) to (c). Subfigure (a) shows the power distribution for the mucosa phantom, (b) for the eardrum phantom, and (c) for the middle ear phantom consisting of both. Subfigure (d) shows the total power at the detector for all cases, dependent on the NA. As the incident power is scaled with the input aperture, the data shown here is normalised to the input power and only the effect of the detection aperture is shown.

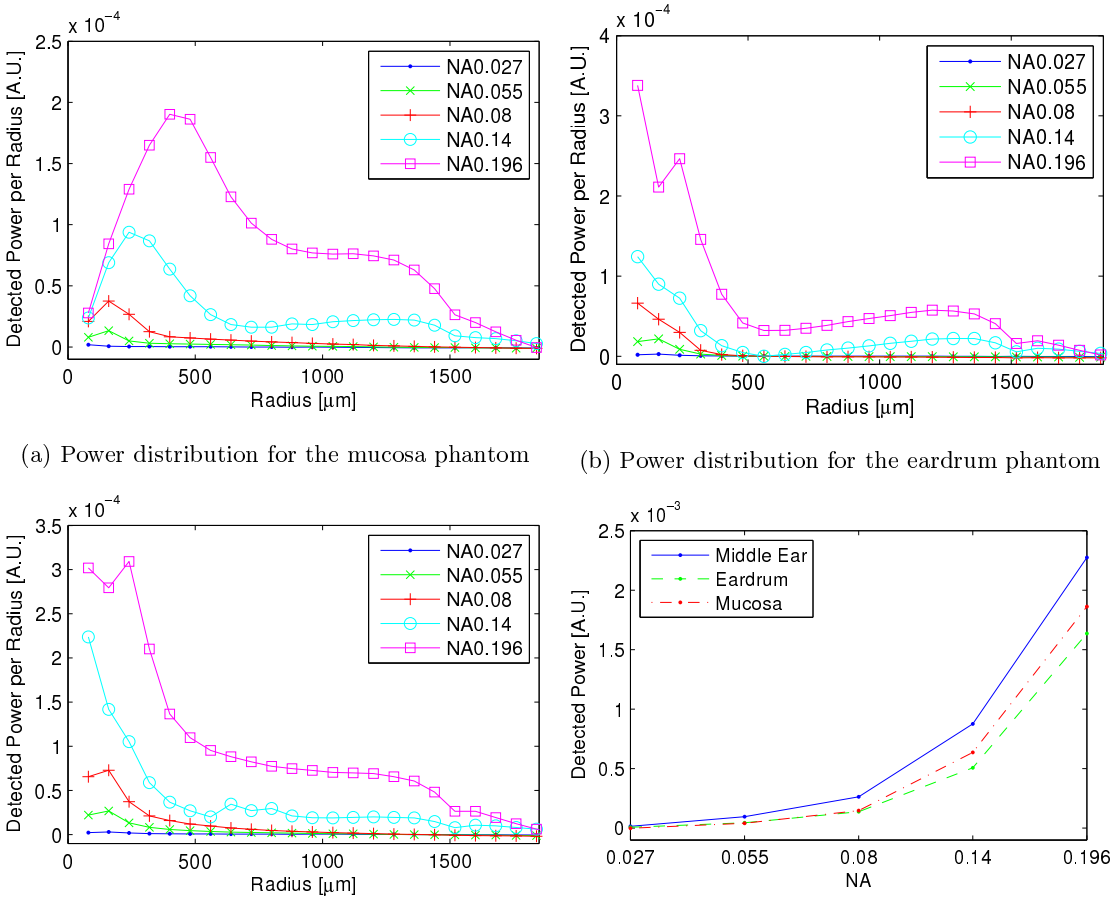


(a) Power distribution for the mucosa phantom

(b) Power distribution for the eardrum phantom

(c) Power distribution for the middle ear phantom

(d) Total Power dependent on NA

Figure 7.17: Radial power distribution for different NA

It is obvious that the detected power increases with increasing NA as more widely scattered photons are detected. In case of the mucosa phantom alone, shown in subfigure (a), the signal is further spread as a bigger area of the mucosa is illuminated according to Equation (7.6). While the mucosa is out of focus and the illuminated area increases with NA, the eardrum is in focus and the illuminated area and signal distribution on the detector should be unchanged, except for a higher signal level. But as Figure 7.17 (b) shows, the signal is also more widely spread in cases of a high NA. This effect is caused by spherical aberrations of the optical system. Two achromatic doublet lenses with 30 and 40 mm focal length, respectively, are used for imaging, resulting in maximum traverse spherical aberrations of 0.3, 2.6, 8, 40, and 100 µm for the NA of 0.027, 0.055, 0.08, 0.14, and 0.196, respectively (calculated using "WinLens3D", Qioptiq, Paris, France and the lens specifications for 'AC254-030-B' and 'AC254-040-B', Thorlabs, Newton, New Jersey, USA). This considers spherical aberrations only and assumes perfect alignment, hence the total aberrations are

expected to be higher. This shows that aberrations are not a problem for small NA but will result in a bad focus of the system using higher NA. This defocus is observed in subfigure (b) and (c). When a stop with small radius is used, background will be able to pass the stop due to aberrations and the performance of the system decreased. But a radius of 0.48 mm of the stop is selected later and hence the aberrations do not pose a problem in the current system.

The contrast does not improve significantly with increasing NA in contrast to results in the simulations. Different scattering and reflection characteristics of the eardrum phantoms between simulation and measurements are the reason. In the simulation it was expected that the background (reflections and scattering from the eardrum) increases much less than the signal (reflections and scattering from the mucosa) with increasing NA. But as shown in Figure 7.17 (d) this is not the case in the measurements, both components increase similarly and the difference is not as big as expected. Nonetheless, the signal level increases making a high NA favourable.

**Summary**

The influence of the surface, wavelength, focus, distance between eardrum and mucosa, scattering of the eardrum, and NA on the anti-confocal measurements have been investigated. The contrast between the reflection signal of the different mucosa phantoms was used to compare the influence of the parameters and the results are summarised below.

The surface roughness and orientation can have a high influence on the measurement due to direct reflections from the surface but in all investigated cases anti-confocal stop filter is able to detect the contrast and minimise the effects. The absorption and scattering of the mucosa phantoms are a function of the wavelength and hence, the detected signal is wavelength dependent and fits well with simulations. A change of the focus position does not have an influence on the contrast itself but decreases the deviation between measurements as higher signals are possible and a larger area of the eardrum is sampled, reducing the influence of surface variations. An increase in the distance between eardrum and mucosa slightly decreases the measured contrast as the distribution of the signal is changed. The eardrum phantom has a strong influence on the measured contrast, at very high scattering no contrast can be recovered and also high direct reflections of the eardrum phantom can cause the need for lower input power and thus no contrast can be detected. While these are extreme cases, the contrast can be recovered when the properties of the eardrum phantom are changed within expected limits. In contrast to simulations, a small illumination diameter cannot be implemented as surface reflections on optical elements mask the signal. The detected signal increases with NA but the contrast does not increase as anticipated as the background changes similarly with increasing NA.

While some of these effects are wavelength dependent, others are not. Thus, the total effect

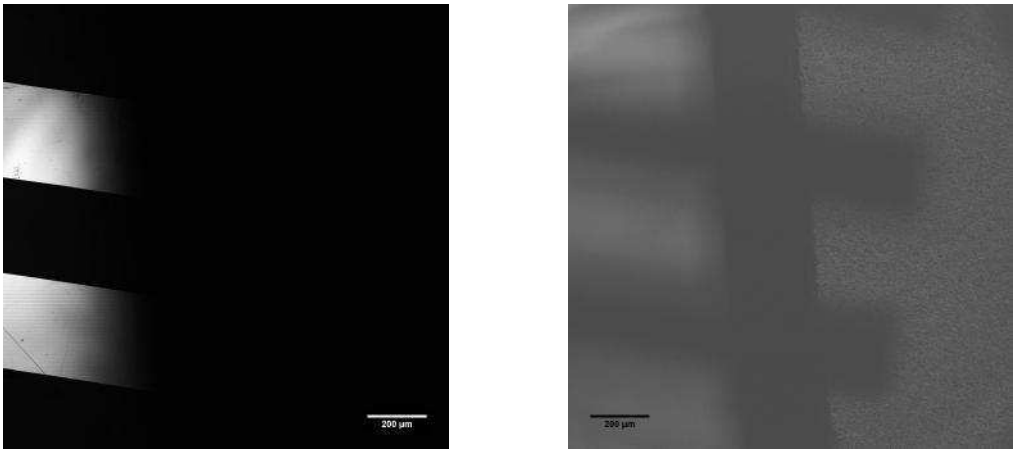


(a) Confocal reflection image at 488 nm, focused on the target

(b) Wide-field transmission image, focused on the diffuser

Figure 7.18: Confocal imaging through the diffuser. The target is directly visible on the left side of the images while it is covered by the diffuser on the right. The confocal image shows the reflective bars as bright areas but these are only visible when directly visible. In the transmission image, the reflective bars are visible as dark area, even when placed behind the diffuser. The vertical dark line in the transmission image is caused by the edge of the diffuser, block light transmission. Its rough surface indicated by the grainy area on the right side of the image.

on the inflammation index can be different as formed by the relation of two measurements at different wavelengths. Consequently, the influence of these parameters on inflammation index are investigated later in Section 7.3.2.

### 7.2.6 Comparison with Confocal

In order to compare the confocal to the anti-confocal system, the optics were rearranged for confocal measurements. For this, the mucosa phantom is placed in focus, pinhole instead of stop filtering is applied, and the previous experiments repeated. The contrast between the four mucosa phantoms could not be recovered and no results are shown.

To confirm these results, comparative tests were conducted on a commercial confocal microscope. The same configuration as previously presented in Section 4 was used and the eardrum is replaced by the 1500 grid ground glass diffuser. The test resolution target provided a high contrast compared to the mucosa phantoms used in the previous experiment.

Figure 7.18 (a) shows the confocal image of the test target half covered by the diffuser, recorded by the commercial confocal system. The target is directly visible on the left side, and the reflective

bars are clearly visible. On the right side, where the diffuser is in the light path, no signal is visible. The transmission image focussed on the diffuser shown in subfigure (b) shows the reflective bars behind the diffuser.

The pinhole diameter was varied from 60 to 600 µm, and the gain set to a maximum until the image saturated. In none of the cases did the bars become visible behind the diffuser in the confocal image. This means the confocal system cannot pick up a signal of the test target when placed behind a diffuser even though the contrast is higher than for the mucosa tissue phantoms. This shows superiority of the anti-confocal system in distinguishing the mucosa phantoms and hence detecting inflammation in the investigated case.

### 7.2.7 Conclusion

The phantoms can be distinguished for most of the presented cases except when the scattering is too high as when the eardrum is simulated by a greaseproof paper. This is not the case for confocal imaging where no signal can be recovered, showing an improved performance of the anti-confocal versus confocal system. Simulation results are mostly confirmed except for the predicted improved SBR with increasing NA due to different characteristics of the eardrum phantom.

## 7.3 Spectroscopy

The anti-confocal system has been tested and been shown to be able to detect signal from different mucosa phantoms. In this section two wavelength spectroscopic measurements will be conducted in order to determine the ability to measure blood content in tissue.

The setup with green and NIR laser is used in this section and measurements are performed on the mucosa phantoms matching the tissue properties at two wavelengths. As previously in Section 7.2, the mucosa phantoms are placed behind an eardrum phantom (standard diffuser) and the reflection detected at two wavelengths to allow measurement of the inflammation index $II$ defined as ratio of reflection in the NIR to reflection in the green.

The contrast for stop filtering is shown in Figure 7.19 (a) for the green, and (b) for the NIR laser. Each of the graphs shows the total detected signal as a solid line and the signal when using a stop for filtering as dashed line, each plot is normalised to its maximum value. Both graphs show the dependence upon the absorption coefficient of the phantom at 532 nm.

The green signal shows the expected course, a decreasing signal with increasing absorption coefficient. The NIR signal is expected to be constant as the phantom is designed to have constant absorption at 808 nm. The reason for the increase is a decreasing absorption coefficient which is due to an error in the characterisation of the dyes. Figure 3.24 shows the spectra of the used dyes

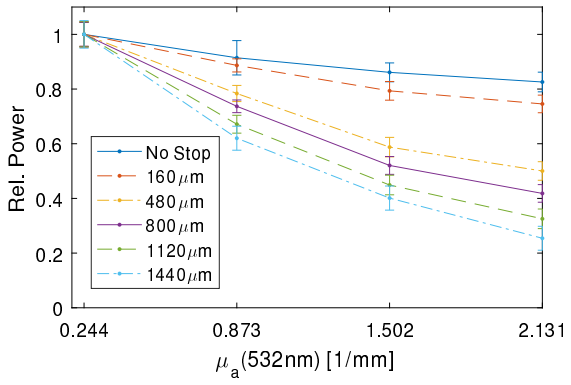


(a) Detected signal green

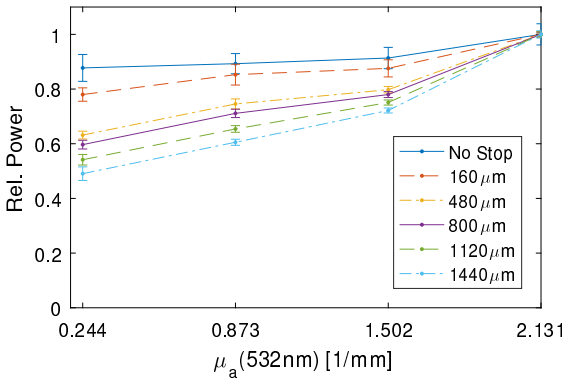


(b) Detected signal NIR

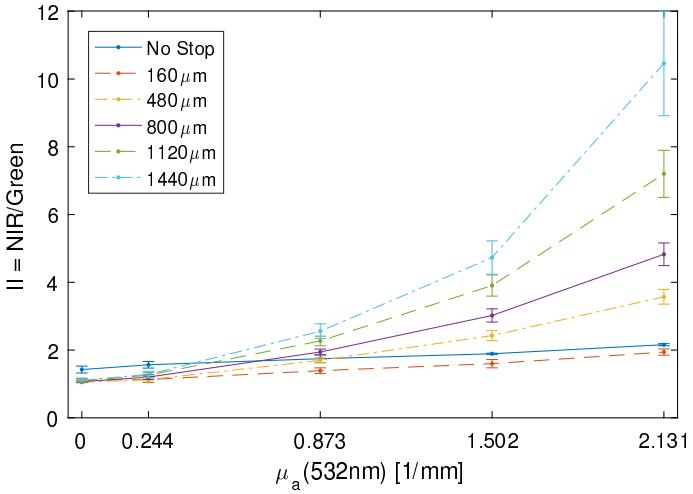


(c) Inflammation index

Figure 7.19: Detected signal and inflammation index dependent on the stop radius.

as well as the data given by Firbank [184] and differences in the spectrum are apparent. At 808 nm the absorption coefficient of [184] is higher than the one measured here. This error is assumed to be caused by the spectrometer. This means the actual absorption is higher than the one assumed in the recipe and results in higher absorption in phantom 1 and lower absorption in phantom 4, explaining the observed increase in reflection signal. Although the phantom was not correctly characterised, new phantoms were not produced as the inflammation index can be measured and the model of absorption was validated on living tissue as described in Appendix F.

Figure 7.19 (c) finally shows the inflammation index $II = \frac{NIR}{Green}$ dependent on the absorption coefficient at 532 nm for different stop radii. For all radii, the inflammation index increases with increased absorption, equivalent to a higher blood concentration and inflammation. A higher stop radius results in a steeper curve due to an increased contrast in the reflectance measurements. Additionally for the four phantoms shown before ($\mu_a(532) = 0.244$, 0.873, 1.502, and 2.131 $\mathrm{mm}^{-1}$) the index for a phantom without absorption ($\mu_a(532) = 0\,\mathrm{mm}^{-1}$) is shown. This phantom shows only scattering and is used as reference. The $II$ for this phantom is expected to be close to 1 as the signal is only affected by the reduced scattering coefficient which is about 11 $\mathrm{mm}^{-1}$ for 532 nm (interpolated from 808 nm using the course given in [185]) and 6 $\mathrm{mm}^{-1}$ for 808 nm.

This shows that changes in the blood concentration can be measured and it should be possible to measure blood concentration after calibration of the system. In the next step different parameters (angle of the surface towards the incident light, distance between scattering layer and mucosa, and scattering as well as absorption characteristics of the eardrum phantom) are altered in order to investigate the robustness of the index to changes of the phantom.

### 7.3.1 Best Stop Radius

The inflammation index increases with stop radius, but the standard deviation increases at the same time. A high linearity with high dependency of the measured index and blood concentration/absorption (sensitivity) and a low variation of the signal is desired (high precision) [222]. Hence, a measure $M$ for a good index is proposed as

$$M = \frac{m \cdot r^2}{\sigma} \tag{7.8}$$

where $m$ is the slope of a linear interpolation of the index $II = m\mu_a + b$, $r^2$ is the coefficient of determination indicating the goodness of the linear fit, and $\sigma$ is the standard deviation of the 5 measurements, shown in Figure 7.19 (c) as errorbars. In the example shown this results in a best inflammation index when using a stop radius of 640 µm. Averaging the best stop radius over all measurements done for different variations of the phantom as presented below results in a value of 480 µm. This stop radius will be used for all further graphs. The variation of the best stop radius

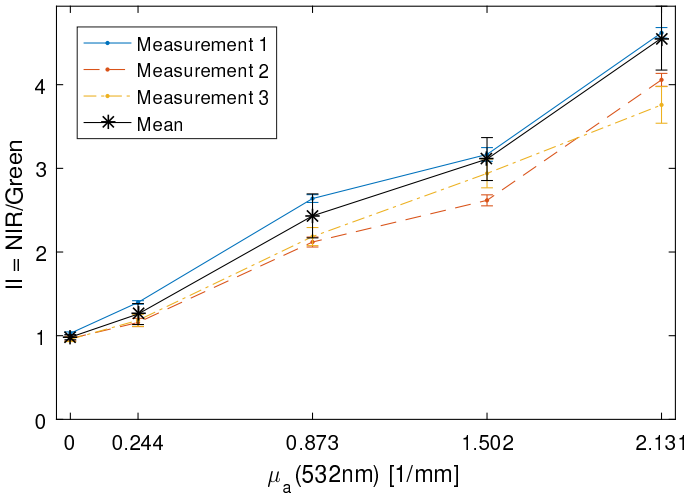


Figure 7.20: Variation of the inflammation index of the same sample during three independent measurements.

is high, ranging over the whole tested range with a standard deviation of ±342 µm. These values are true for the current optical setup and depend on factors such as focal length of the lenses, lens apertures, and distances between the lenses.

### 7.3.2 Parameters affecting the Measurement

When characterising the anti-confocal system the influence of different parameters on the measurements were presented in Section 7.2.5. Now, the influence of these parameters on measurements of the inflammation index is investigated. This could be different from the previous results as the relation of measurements at two wavelengths is taken and changes might cancel each other or amplify.

But before changing any parameters of the sample, the standard measurement is repeated three times to determine the variation from measurement to measurement. Figure 7.20 shows the three independent measurement series in grey with errorbars indicating variation between different measurement points. The mean of all measurements is shown in black with errorbars indicating the standard deviation between the mean of each of the three series. This average is shown in all other graphs as a reference. The standard deviation between measurement positions of a single series is smaller than the deviation between the three series. This shows that the variation of the background noise level still has an influence.

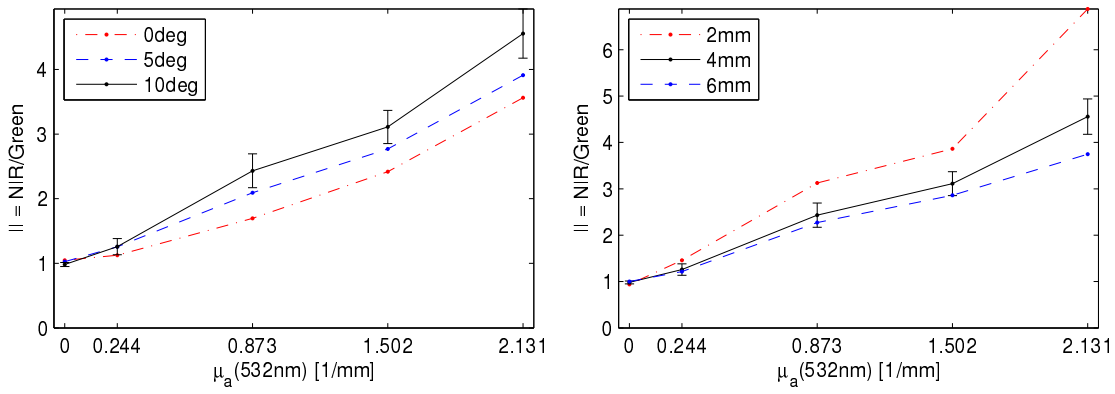


(a) Angle between optical axis and phantom

(b) Distance between eardrum and mucosa

Figure 7.21: Influence of the geometry on the inflammation index.

### Angle between Optical Axis and Phantom Surface

Figure 7.21 (a) shows the dependence of the inflammation index on the angle of the optical axis towards the surface of the sample. The standard shown before is measured with an 10 ° angle and two variations, 5 and 0 ° orientation are shown. A higher angle causes an increased index.

During the investigation of the anti-confocal system it was observed that the detected power is increased with smaller angle due to direct reflections towards the optics. These direct reflections are background components and are not dependent on the absorption of the sample, but only on the surface and refractive index. When angled, these reflections are directed away from the optics and are not detected, decreasing the constant offset in the reflection signals, increasing the contrast between phantoms, and thus increasing the measured inflammation index.

### Distance between Eardrum and Mucosa

The distance between eardrum and mucosa also influences the inflammation index as shown in Figure 7.21 (b). The index decreases with increasing distance (within the tested range). This is in accordance with the simulations and a result of the changed illuminated area on the mucosa. A larger distance results in a larger illuminated area as the illumination beam is focused on the eardrum as observed during characterisation of the anti-confocal system in the previous section. This in turn increases the sampled area and increases the signal detected further away from the optical axis. In the green range this effect is larger as the absorption in the mucosa is higher and path lengths are smaller. The sampled volume increased more compared to the NIR signal causing the inflammation index to decrease.

Table 7.1: Total transmission through different eardrum samples. The 'CFG' samples are made of fibre glass mats cast in resin with absorbing dye added to adopt the absorption.

| | **Total Transmission** | | **Relation** |
|---|---|---|---|
| **Sample** | **532 nm** | **808 nm** | **808/532** |
| Diffuser | 0.21 | 0.39 | 1.88 |
| CFG NIR2 | 0.35 | 0.41 | 1.15 |
| CFG NIR1 | 0.41 | 0.48 | 1.17 |
| CFG white | 0.48 | 0.57 | 1.20 |
| CFG red1 | 0.33 | 0.48 | 1.47 |
| CFG red2 | 0.23 | 0.39 | 1.73 |
| CFG red3 | 0.20 | 0.42 | 2.08 |
| CFG red4 | 0.18 | 0.48 | 2.67 |

### Absorption of the Eardrum

The absorption of the eardrum obviously affects the measured inflammation index. When attenuating one wavelength more than the other, the relation between both, and thus the inflammation index, is changed. Figure 7.22 (a) shows the measured index for different eardrum samples. All samples are fibre glass mats cast in resin. No dye is added to the resin of the "white" sample, while either red or NIR dye is added to the other phantoms. The concentration of each dye increases with number as listed in Table 3.7. The measured total transmission values measuring the absorption of each sample are given in Table 7.1.

As expected, the inflammation index increases with increasing absorption in the green region compared to the NIR absorption (going from sample "NIR1" to "red4"). The only exception is the index measured for "NIR2". This is assumed to be an error introduced by scattering that also influences the inflammation index as shown later. The fibre glass samples show relative inhomogeneous scattering characteristics. This can mask the small change in absorption between the white and two NIR eardrum samples.

All in all, the observations are in accordance with the simulations, showing a strong influence of wavelength dependent absorption on the measured inflammation index. A wavelength independent change in absorption as simulated is not tested, but only a small change of the inflammation index is expected.

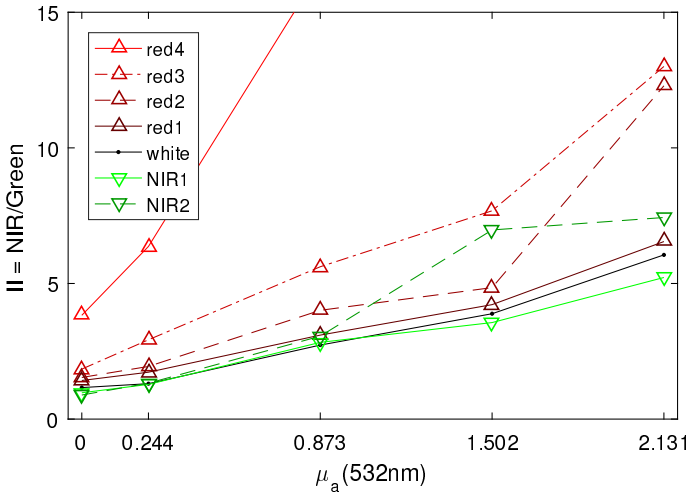


(a) Absorption

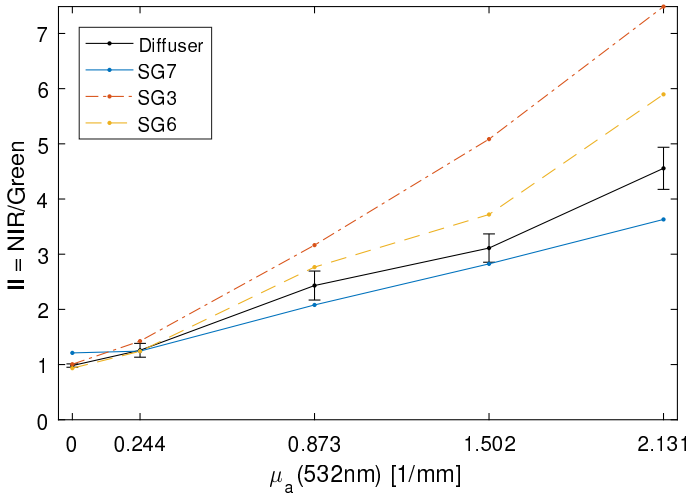


(b) Scattering

Figure 7.22: Influence of eardrum properties on the inflammation index.

Table 7.2: Central transmission through different scattering eardrum samples made using sandpaper 'treated' microscope slides "SG".

| | **Central Transmission** | | **Relation** |
|---|---|---|---|
| **Sample** | **532 nm** | **808 nm** | **808/532** |
| Diffuser | 0.001 | 0.032 | 23.53 |
| SG 3 | 0.061 | 0.174 | 2.83 |
| SG 6 | 0.014 | 0.108 | 7.93 |
| SG 7 | 0.000 | 0.002 | 6.98 |

**Scattering of the Eardrum**

The scattering characteristics also influence the measured inflammation index. This is shown in Figure 7.22 (b) that illustrates the index for the standard sample and three differently sandpaper 'treated' microscope slides. The first sample "SG3" was treated with P240 grid sandpaper at both sides, with orthogonal scratch directions. The other two samples were treated with rougher P40 grid sandpaper, "SG6" at one and "SG7" at both sides. The measured central transmission and so scattering of the phantom at 532 and 808 nm as well as the relation between both transmission values are given in Table 7.2.

The relation between scattering and measured inflammation index is more complex than for absorption. According to simulations, even a wavelength independent change in scattering changes the inflammation index. This is obvious when comparing the results of "SG6" and "SG7". Both have a similar ratio of transmitted light at 532 and 808 nm (7.93 vs. 6.98) but different total transmission (10.8 % vs 0.2 % at 808 nm). This causes one inflammation index measurement to be increased and the other one to decrease even though the relation of transmitted light at both wavelengths is similar. The two effects to be considered are a decrease in total signal due to higher attenuation but at the same time a higher portion of this signal can be detected due to a changed distribution of the signal. This results in a relation of scattering to change in inflammation index that is not easily predicted.

### 7.3.3 Correcting the Inflammation Index

The influence of scattering could be decreased using closer wavelengths and thus reducing the difference in scattering coefficients. But this would decrease the sensitivity of the inflammation index itself and cannot minimise the influence of absorption and geometry on the measured index.

Another idea to correct the inflammation index is to use confocal detection of the eardrum in order to determine its optical properties. Detection is easily done with the camera focused on the

eardrum and pinhole filtering using the central pixel at the same time as performing anti-confocal filtering using peripheral pixel. The confocal signal can then be used to determine the optical properties of the eardrum and reconstruct the original inflammation index. While determination of scattering characteristics is challenging, the influence of absorption can be determined easily. An increase in absorption decreases the confocal as well as the anti-confocal signal and after determining the relation of both effects, the confocal signal can be used to correct the inflammation index.

This is tested on the coloured fibre resin eardrum phantoms used to alter the absorption of the eardrum. Figure 7.23 (a) shows the relation of NIR to green confocal detected signal $r_{\text{conofcal}}$ for the seven different eardrum samples. The confocal signal is measured for six different phantoms (five different mucosa phantoms and one measurement on the eardrum only), the average of these six measurements is shown here, and the standard deviation is indicated by the errorbars.

The red and uncoloured phantoms show the expected relation, the NIR compared to the green signal decreases with decreasing dye concentration. This means a higher absorption in the green range of the eardrum phantom decreases the confocal detected green signal as well as the anti-confocal detected signal of the mucosa. This relation is not observed for the NIR dye samples. Due to the fact that they show a much lower change in absorption and because surface and scattering characteristics of the samples influence the measurement. The axial resolution of the confocal detection system is $r_{\text{axial}} = 1.5n\frac{\lambda}{NA^2} = 189\,\mu\text{m}$ at 808 nm wavelength and the reflections from the surface cannot be rejected. Further, an inaccurate focus of the system also changes the confocal detected signal. This makes the confocal detection of the absorption of the eardrum difficult.

Nonetheless, the detected properties of the eardrum can be used to correct the inflammation index. The ideal correction factor is the inverse of the slope $c = \frac{1}{m_{\text{II}}}$ of the linearly interpolated inflammation index

$$II = m_{\text{II}} \cdot \mu_{\text{a}}(532) + b_{\text{II}} \tag{7.9}$$

But this slope is not available for later measurements. Hence, the relation of the confocal detected signal $r_{\text{confocal}} = \frac{R_{\text{NIR,confocal}}}{R_{\text{green,confocal}}}$ is used to interpolate the slope. This relation is again linearly interpolated

$$c = \frac{1}{m_{\text{II}}} = m \cdot r_{\text{confocal}} + b \tag{7.10}$$

And then the correction factor as a function of the confocal relation $c = f(r_{\text{confocal}})$ used to adopt the inflammation index. Results are shown in Figure 7.23 (b). While the inflammation index measure at the red phantoms show less variation, the signal for the green phantoms is worse compared to the original measured index shown in Figure 7.22 (a).

The calibration and test data set are the same in the experiments shown here. This explains

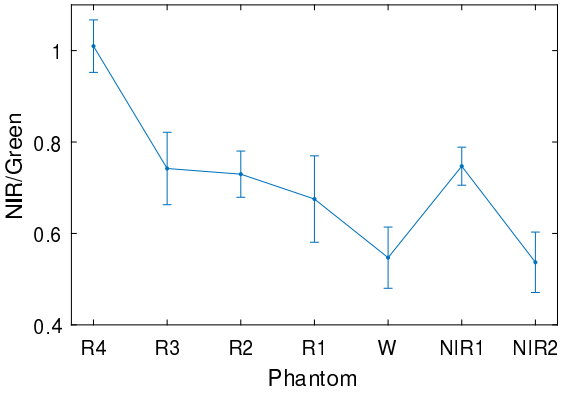


(a) Confocal detection of the eardrum

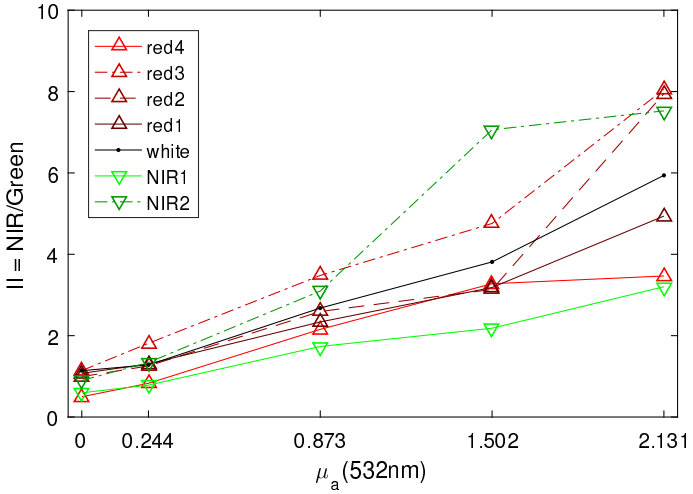


(b) Corrected inflammation index

Figure 7.23: Using confocal detected signal from the eardrum to correct the inflammation index.

party why the inflammation index improved more for the red samples than for the green ones. Another reason for no improvement of the green samples is the influence of surface roughness and focus on the correction algorithm. An inaccurate focus of the confocal detection as well as an more diffuse surface decrease the confocal detected signal $R_{\text{confocal}}$ and thus influence the correction factor $c = f(R_{\text{NIR,confocal}}, R_{\text{green,confocal}})$. Still, the results show that it is possible to use the confocal signal from the eardrum to correct the inflammation index for changes in absorption of the eardrum if correct calibration is used. The remaining challenges are to correct the inflammation index for changes in scattering as well as the absorption and improved calibration of the correction factor $c$ valid for human eardrums.

### 7.3.4 Conclusion

This section showed that measurement of the simulated blood content of the mucosa phantoms through different eardrum phantoms is possible. All measurements show an increase of the inflammation index with blood concentration, but the slope is influenced by the orientation of the sample towards the optical axis, distance between eardrum and mucosa, and properties of the eardrum. While correction of the index is possible using the confocal detected signal of the eardrum, this processing is not trivial due to different influences of the absorption and scattering on the different signals.

# Chapter 8

# Conclusion and Future Work

## 8.1 Summary

The aim of this project is to develop a device to assess the inflammatory state of the middle ear mucosa in children after grommet insertion used to treat OME. It is hypothesised that the inflammation is linked to recurrence of otitis media with effusion and a diagnostic device could be used to predict the course of OME. None of the clinically available diagnostic devices are able to assess the inflammation directly, with only symptoms detected. While several groups are working on improved imaging of the eardrum and diagnosis of different cases of middle ear inflammation, none of these groups addresses the inflammatory state of the mucosa directly. In this report an optical device was developed to do so.

As a first step for this work a stable middle ear phantom was developed, it consists of eardrum and mucosa. All other parts of the ear do not influence the measurements when choosing an appropriate measurement position and method. Hence, no other structures of the middle ear needed to be included in the model. The mucosa phantom is based on the recipe presented in [184,185] where an epoxy resin is used as base material and scattering and absorbing particles are added to set the optical properties. A new dye was characterised and included into the recipe to allow matching the optical properties of tissues in the green and NIR wavelength range. A model for the absorption of the mucosa dependent on the blood content and thus inflammation level was adopted from literature. This model was used to determine the optical properties of the mucosa phantoms and used in simulations. For the first time to the author's knowledge, light transmission and scattering characteristics of the eardrum were measured and a simulation model fitted. Guinea pig eardrums were used as the animal model as no human eardrums were available. As the guinea pig eardrum is thinner than the human one and possesses only one

collagen fibre layer in contrast to two layers in the human eardrum, two guinea pig eardrums orthogonally aligned on top of each other were used as a model. Light is mostly scattered from the collagen fibres in the eardrum, resulting in a main direction of scattering orthogonal to the fibre orientation. As two orthogonal fibre layers are present in the animal eardrum model, two main scattering directions were observed. The collagen fibres have a large diameter (12-22 µm [170]) compared to the wavelengths used, causing the scattering to be very forward directed and resulting an anisotropy factor of 0.99 of the simulation model. A scattering coefficient of $11\,\mathrm{mm}^{-1}$ and absorption coefficient of $1.8\,\mathrm{mm}^{-1}$ approximate the scattering of the eardrum model best. The simulation model ignores the azimuthal direction (rotation around the optical axis) of scattering as the optical system is circularly symmetric. The absorption coefficient of the simulation model is relatively high as the transmitted light was characterised within a small scattering angle only, due to the small detector area. Widely scattered light is not detected as it falls outside the detector area; this decreases the detected power, reduces the measured transmission, and increases the measured absorption of the eardrum. Different phantoms were developed to mimic the eardrum, with the most realistic phantoms being fibre glass mats cast in resin to set the scattering with dye added to determine the absorption of the phantom. A custom built holder allows variation of the distance between eardrum and mucosa phantom as well as measurements with variable but repeatable focus, position, and orientation of the middle ear phantom.

During the literature review photo-acoustic tomography (PAT), spectroscopic optical coherence tomography (SOCT), and confocal microscopy were determined to be the most suitable methods to diagnose the middle ear inflammation as all three methods are able to spectroscopically assess the inflammation and spatially separate signals from eardrum and mucosa. Experiments with the developed eardrum model on a commercial confocal system showed that it is possible to image a target through the eardrum and confocal imaging is selected because it has a simpler setup than the two other options. This is necessary because a cheap and simple system is required with regard to the future clinical use. Inflammation is normally measured spectroscopically at two or more wavelengths and hence, two wavelengths were included into the confocal system.

The confocal system was adopted for the special geometry in the ear, resulting in the "anti-confocal" system. The anti-confocal system uses a central stop rather than a pinhole to reject light inside instead of outside its radius. This allows cancellation of light reflected from the eardrum with only signals from the mucosa detected when performing measurements on the middle ear. The optical resolution is greatly reduced by this change but this is not a disadvantage in the current task as a relatively large area needs to be sampled in order to measure representable properties of the mucosa. MATLAB code was implemented in order to simulate the anti-confocal system. The code utilises Monte-Carlo methods to simulate light propagation inside the tissue and geometrical optics

to simulate the optical system. Simulations show a superiority of the anti-confocal versus confocal system regarding detected signal level and background rejection in the investigated application. This holds for changed parameters of the optical system and tissue model. The NA is restricted to 0.08 in the ear canal when using standard otoscope specula but an increase in NA would increase the detected signal in the anti-confocal system and thus improve its performance although a more complicated optical arrangement would be necessary to achieve this. Increased scattering of the eardrum can even increase the signal in the anti-confocal system while this is not the case in the confocal case. This shows that the simulated results are reliable even for inaccurate optical properties of the middle ear model.

Further, the wavelength dependent reflection signal of the middle ear was simulated in order to determine the best wavelengths to measure inflammation. Results show that a highest dependence on the blood content is achieved when measuring the inflammation as the ratio of detected light in the NIR divided by the reflection in the green according to $II = \frac{R(730)}{R(546)}$. A more severe inflammation increases the blood content in tissue which strongly reduces the detected power at 546 nm due to the high specific absorption coefficient of blood in this region. The reflected signal at 730 nm is less influenced by the blood concentration due to a low absorption coefficient in this range, causing the index $II$ to increase with increasing severity of the inflammation. This measure is independent of the oxygenation of the blood as shown in simulations. Additional wavelengths could be included into the measurement to measure oxygenation as well. A good choice of wavelengths for this would be 940 and 660 nm.

The anti-confocal system was set up as a bench top system using off the shelf optical components. The originally proposed wavelengths (730 and 546 nm) were changed to 808 and 532 nm due to the sources available. This reduces the measurable range of the inflammation index by factor of 0.82 (measured by $M_{\text{cHb-Oxy}}$ defined according to Equation (6.28)) and the system could be improved by using the proposed 730 nm instead of 808 nm but no lasers are available at 546 nm. A CCD camera is used as the detector allowing confocal and anti-confocal filtering with variable stop and pinhole radii during post-processing. Experiments on the optical middle ear phantom confirmed the results of the simulations. The anti-confocal system is able to distinguish between different states of the mucosa (simulated by phantoms with different absorption characteristics according to the blood content) while the confocal system in not able to do so. An optimum stop radius of 0.48 mm has been determined for the current tissue model. Different properties of the eardrum affect the measured inflammation index, while the different phantoms are always distinguishable within one series. In simulations and experiments, the properties of the middle ear phantoms differ and an exact comparison is not possible, but the reported trends and overall results agree.

Confocal detection of the eardrum parameters were performed in order to determine its optical properties to correct the inflammation index changed by transmission characteristics of the eardrum. A change in the measured inflammation index due to absorption can be partly corrected. Improved signal processing algorithms are necessary to improve the correction and also include scattering into the model. Further, the addition of more wavelengths for measurements might provide more information and improve the system. For example, the oxygenation of the tissue could be assessed by addition of measurements at 940 and 660 nm. An example for the use of additional wavelengths is the pulse-co oximeter [80] using seven instead of two wavelength for measurements as compared to the conventional pulse oximeter. This allows measuring the total blood concentration and concentration of blood derivatives additionally to the oxygenation.

The system was also tested on human volunteers (see Appendix F). For this, the system was shown to be safe for tests on humans, a first step of the system towards clinics. e blood flow in a hand was altered by exposure to cold water and used as a model. The anti-confocal system was able to detect changes in the blood level with measurements conducted through an eardrum phantom.

The developed spectroscopic anti-confocal system is able to measure blood content tissues through an eardrum simulating scattering layer. This is true for a variety of different scattering layers while no measurements are possible for very high scattering. The scattering layer influences the measurement of the blood content; while changes in absorption can be corrected by confocal detection of the eardrum, no correction was found for changes in scattering. This means large changes in characteristics of the eardrum will make reliable measurements of the inflammation difficult. Future work includes the minimisation of the system for clinical use and the conduction of trials on improved inflammation models and in clinics, as will be presented in the next section in more detail. The specifications of the anti-confocal system are listed below.

### 8.1.1 Reflecting on Requirements

Section 1.5 stated the requirements of the optical diagnostic device under development. These requirements are that the system must be able to show the inflammation, have an imaging depth high enough to probe the mucosa through the eardrum and middle ear cavity while no requirements were posed to the resolution except for being able to distinguish between eardrum and middle ear mucosa, allow non-invasive and quick diagnosis, be cheap device to enable a wide use, be hand-held for easy use, and finally to be safe on humans. It is discussed below whether these requirements are met.

**Show the inflammation** Experiments showed that the developed system is able to assess the

blood level in the middle ear mucosa phantoms and thus will be able to assess the inflammation. But improved signal processing is necessary to allow repeatable experiments in cases where changing eardrum properties affect the measurement.

**Imaging depth** The system is able to pick up signals from the middle ear mucosa hidden behind the eardrum and middle ear cavity. A depth of up to 4 mm was tested in experiments and up to 8 mm in simulations, while a maxim distance of 4 mm is expected.

**Imaging resolution** A single measurement is performed assessing the inflammation, and background from the eardrum rejected.

**Non-invasive and quick** The measurement is done through the ear canal and data acquisition takes less than a few seconds after the operator aligned the system manually.

**Cheap** The current optical system is not cheap as an expensive and cooled CCD camera (iXonEM+, Andor, Belfast, Northern Ireland) is used as detector at the moment. An improved design of the detection system is necessary to allow the use of a cheaper detector while still solving the noise problem posed by the low signal components spread over a large area.

**Hand-held** The current optical system is not hand held but is a large set-up on an optical bench. But a partly hand-held system is proposed in Section 8.2.2 that will meet this requirement once implemented.

**Safe** The optical system was designed so that the mechanical part in contact with the patient (i.e. the speculum) of standard otoscopes can be used. This ensures safe use if assessment is performed by a trained operator and that the eardrum can not be ruptured during diagnosis. Further, the optical system was shown to be safe for use on humans and laser safety limits are not exceeded.

Most of the requirements are met, while further development is necessary to design a cheap optical system and to allow repeatable results when the optical properties of the eardrum change.

### 8.1.2 Specifications of the Anti-Confocal System

Most of the specifications of the system depend on the optical properties of the sample as described below.

**Sampled area:** The sampled area is dependent on the absorption and scattering characteristics of the mucosa determining the mean free path. It is further influenced by the illuminated area on the mucosa, determined by the scattering characteristics of the eardrum and the distance

of the focus from the mucosa surface as well as the NA of the system. As an example, the sampled volume is derived from simulations based on the standard parameters of the system. The sampled volume is defined as the volume where the light flux is higher than $\frac{1}{e^2}$ of the maximum flux at the mucosa surface. The depth and radius are $0.29 \times 0.4\,\mathrm{mm}^2$ at 532 nm and 20 % blood concentration ($\mu_\mathrm{a} = 2.13\,\mathrm{mm}^{-1}$, $\mu_\mathrm{s} = 22.3\,\mathrm{mm}^{-1}$) and $0.6 \times 1.19\,\mathrm{mm}^2$ for 808 nm and 2 % blood concentration ($\mu_\mathrm{a} = 0.04\,\mathrm{mm}^{-1}$, $\mu_\mathrm{s} = 11.7\,\mathrm{mm}^{-1}$). These values will change when changing properties of the eardrum, the position of the focus, or the NA. The used definition results in a higher axial penetration depth than radial spread of the signal as incident photons propagate forward in axial direction before being scattered and thus increases the penetration depth in axial direction.

**Stop radius:** A radius of 480 µm was identified to show best performance in the investigated phantoms.

**SBR:** The signal-to-background ratio (SBR) defined as ratio of detected signal from the mucosa to background from the eardrum increases with stop radius according to simulations. In measurements, this is not true as noise of the system and dynamic range of the camera restricts the minimum detectable signal level. A balance between signal strength and SBR needs to be found, resulting in the above stop radius.

**Camera:** A camera with at least 10 bit dynamic range is required. When reducing the bit depth below this value in the measurements, results become unreliable. This is due to the fact, that the signal from the mucosa is spread over a large area and the intensity on a single pixel is too low to be detected when using less than 10 bits. While an increase in optical input power is not an option as the camera would saturate due to high background components from the eardrum and possibly damage the tissue. This could be improved by not focusing the optics directly on the eardrum resulting in a larger illuminated area and lower power density, allowing higher power without saturating the detector and thus giving a higher signal. Also cooling of the camera is of advantage in order to minimise offset drifts masking the low signal. For example, using an uncooled 12 bit camera (PL-B955U, PixeLink, Ottawa, Ontario, Canada) instead of the 14 bit camera with cooled sensor presented previously, does not result in reproducible measurements.

**Focus:** An exact focus of the anti-confocal is not necessary. A slight defocus can even improve measurements as the signal level can be increased without saturating the camera. But confocal detection of eardrum parameters will not be possible with a defocused system.

## 8.2 Future Work

Future work involves the improvement of signal processing algorithms to accound for changes in the eardrum and the construction of a hand-held system to allow test on the ear and clinical trials to calibrate the system and test the hypothesis that a recurrence of OME is connected to a remaining inflammation of the middle ear mucosa. Further, some additions to the proposed system are presented that are easily included and have the possibility to add more information and improve diagnostic accuracy.

### 8.2.1 Possible Improvements and Additions to the System

As shown by [34–36] the acquisition of auto-fluorescence spectra can add information about bacteria (assumed to be a cause for OME [7]) in the ear or some pathological cases of the middle ear. This could be easily added to the proposed system by adding filters in the detection path to reject reflections at the illumination wavelength and addition of an appropriate excitation wavelength as done in [36] in case of a standard otoscope.

Additional wavelengths could be included into the system to, for example, measure the oxygenation of tissue and other blood derivatives. While general literature about inflammatory diseases (not specific to middle ear inflammation) showed no correlation of blood oxygenation and inflammation, a connection could be present in middle ear inflammation and an investigation could be of value.

### 8.2.2 Hand-held System

The proposed system is composed of a table top setup including the lasers, electronics, and PC for signal processing as well as data visualisation and the hand-held head including the anti-confocal system as shown in Figure 8.1. In the bench top system the lasers will be aligned, shutters used to quickly select the measurement wavelength, and the light coupled into an optical fibre. More than two lasers can be easily included into this setup. The optical fibre is connected to the hand-held head to provide the illumination.

In the optical head, the beam will be first expanded to use the full aperture available in the ear and then collimated. A beam splitter directs the light towards the ear, while the light in the unused path needs to be directed to a beam dump to avoid reflections. An objective lens with about 80 mm focal length is necessary to focus the illumination light on the eardrum. This lens needs to be movable in order to manually adopt the focus of the system as the position of the eardrum varies in patients. Imaging of the eardrum as visual feedback is necessary in order to allow manual focusing. The NA is restricted to 0.08 by the clinically used speculum providing contact

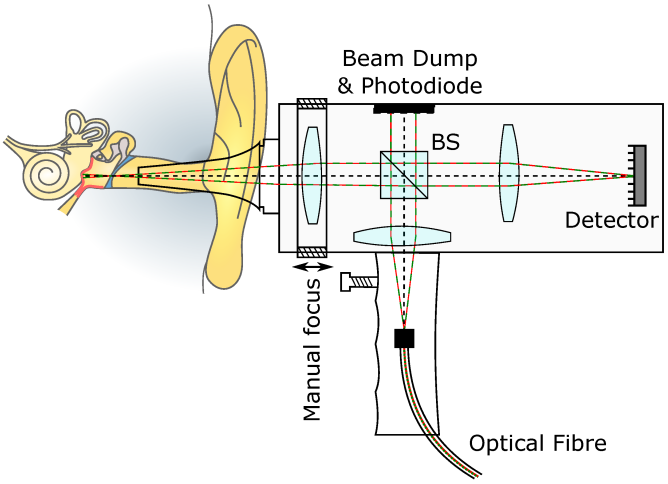


(a) Optical sketch of the hand-held head

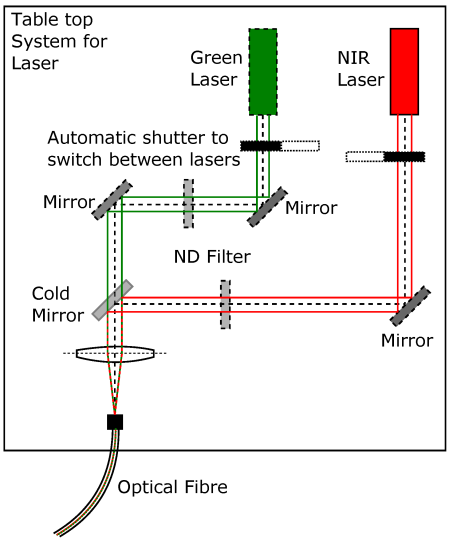


(b) Optical sketch of the table-top subsystem

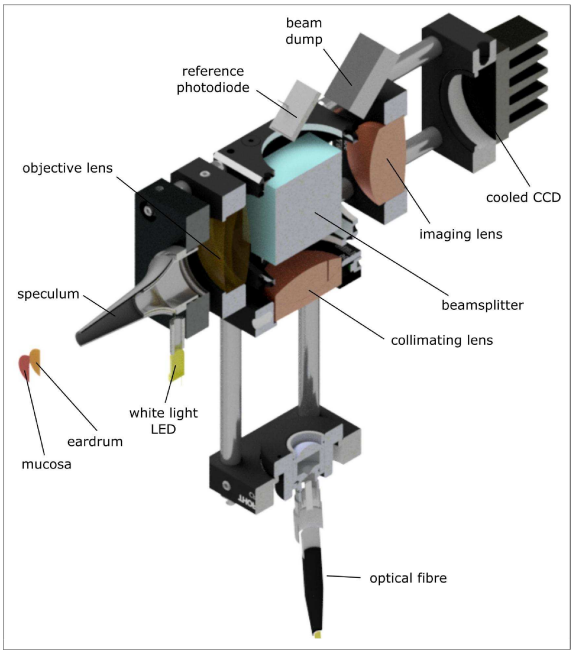


(c) 3D CAD section view of the hand-held head

Figure 8.1: Proposed layout of the optical system.

and alignment of optical head and ear canal. The reflected light is focused on a detector via the objective and an imaging lens. We propose the use of a camera as detector as this allows visual inspection of the eardrum as well as anti-confocal and confocal filtering during image processing. For visual inspection of the ear, the laser sources must be switched off and a wide field illumination similar to normal otoscopes is provided through the speculum. The eardrum can then be observed on a screen connected to the camera. An alternative would be the use of a physical stop and single sensor instead of using a camera. This would reduce the costs of the system but a second light path would need to be included for visual inspection and recording of pictures of the eardrum would not be possible.

The dimensions of the hand-held system depend on the used camera and could be minimised using a sensor with custom electronics partly placed in the table top setup. The CAD view of the head in Figure 8.1 (c) shows a CCD sensor and cooling rib as heat sink instead of a complete camera system. This visualises possible dimensions of a miniaturised CCD set-up with electronics placed in the table top set-up. The dimension of the system shown here are about $40 \times 130 \times 180\,\mathrm{mm}^3$ (width×height×length), including the speculum.

A measurement sequence includes manual alignment of the system including focussing on the eardrum and selection of an appropriate sampling area. The white light source will then be switched off and anti-confocal measurements taken. Reference and noise measurements have to be recorded to reduce background noise and determine the illumination power. The input power can be easily measured by a photo diode in the unused beamsplitter path while an extra measurement is necessary for the background subtraction. During this measurement no signal may be reflected from the sampling path and ambient light needs to be rejected.

### 8.2.3 Improved Signal Processing

The biggest remaining challenge of the system is that measurements of the inflammation index are affected by the optical properties of the eardrum. While a method was presented to allow correction of the inflammation index for changes in absorption of the eardrum, changes of scattering are not considered in the current system. The proposed approach is to determine the optical properties of the eardrum using confocal measurement at the same time as anti-confocally assessing the middle ear mucosa. Improved signal processing and further investigation is necessary in order to develop correction algorithms that account for changes of scattering in addition to absorption. Only when this problem is solved and the optical system minimised clinical trials can be considered.

# Appendix A

# Histological Images of the Guinea Pig Middle Ear

Guinea pig middle ear samples were fixed in formaldehyde for storage. The samples were removed from the formaldehyde solution, dehydrated, and then placed in a paraffin wax mould. A microtome was used to cut sample slices with a thickness of 8 µm. These slices were then placed on a microscope slide, stained with Masson's Technique, and finally mounted using a cover slip and DPX (Mounting medium with refractive index similar to glass). Masson's Technique is suitable for collagen staining [227] and nuclei are stained blue-black; Muscle, red blood cells, and fibrin are stained red; and connective tissue are stained blue or green dependent on the counterstain used.

Figure A.1 shows a 10× magnification sample of the complete guinea pig middle ear on the left and four 50× samples of sections of the eardrum on the right. The full middle ear sample shows the thin eardrum on the right in red and the middle ear mucosa in underlying tissue in turquoise and red. The annulus and attachment of the eardrum to the middle ear can be seen on top and bottom of the eardrum. The eardrum has been fractured during processing but most of it is still in place. The distance from eardrum to mucosa in the middle ear is between 180 to 340 µm with an average of 260 µm.

Four images of the eardrum are shown on the right with higher magnification, each showing another section of the eardrum and different fibre orientation. The top image is located near the attachment of the eardrum to the annulus. A radial fibre is visible, cut along its length but also the cross sections of circular fibres are visible. The second image shows cross-sectional cuts of radial fibres. In the third image, the radial fibres are cut orthogonal to their length and fallen over so that short cylinder segments are visible. These are visible as squares placed next to each other. This image shows that the fibres have different diameter reaching from 2.1 to 7.2 µm and

an average of 4.4 µm. In the last image two fibres are visible. One fibre (lower half of the image) is cut and the next fibre gets visible below (upper half of the image). The thickness of the eardrum varies from 11 to 20 µm with an average of 14 µm.

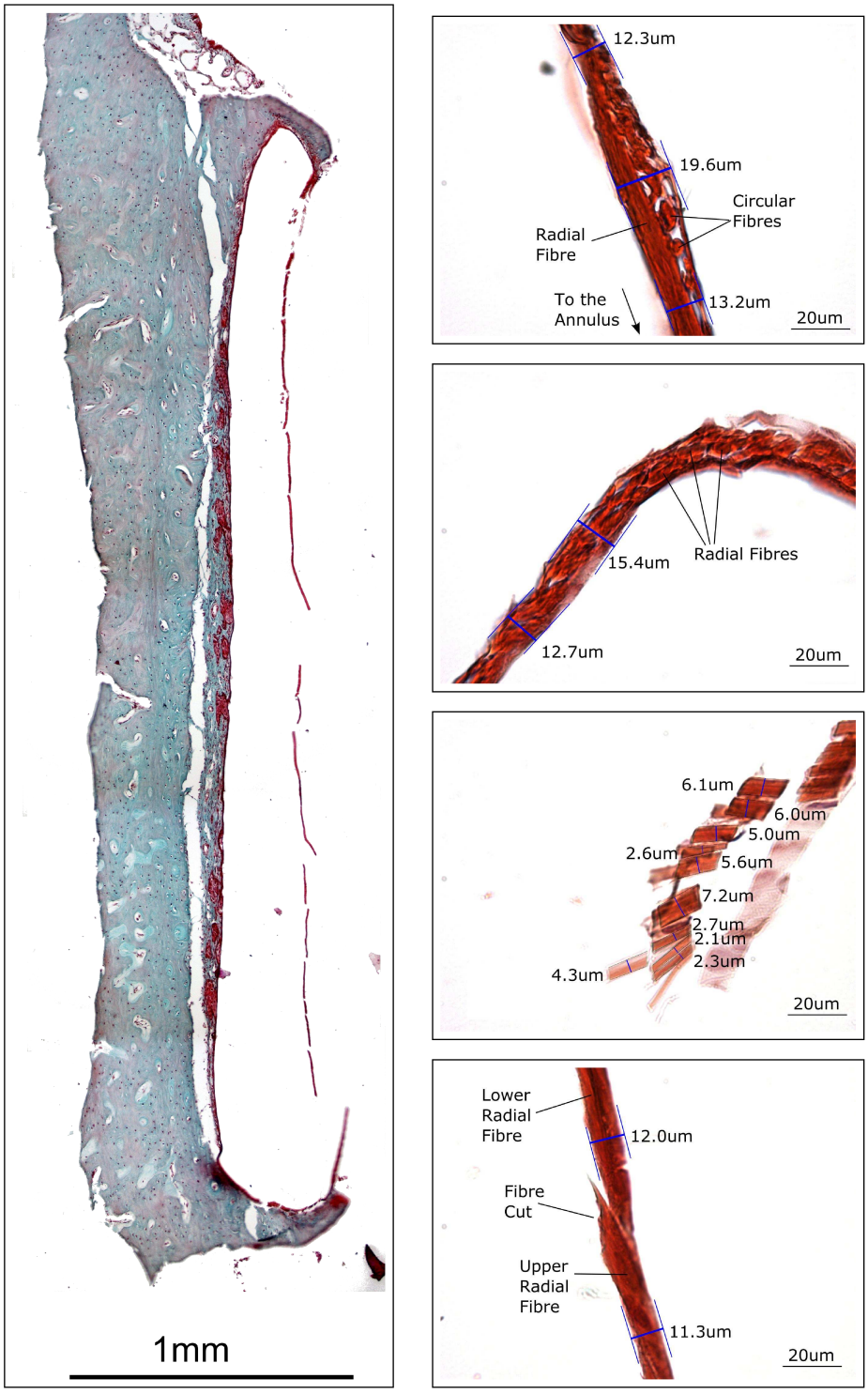


Figure A.1: Masson stained sample of the guinea pig middle ear. See text for description.

# Appendix B

# Additions to the Monte Carlo Software

## B.1 Cosine Distribution for Lambertian Reflection

The deflection angle $\varphi$ of Lambertian reflection is given by a cosine distribution between the angle $-\pi/2$ to $\pi/2$ and the probability density function (PDF) is given by

$$PDF_{\text{cosine}} = I(\varphi) = I_{\max} \cdot \cos(\varphi) \tag{B.1}$$

The cumulative distribution function (CDF) is the integral as the PDF

$$CDF_{\text{cosine}} = \int PDF d\varphi = \int I_{\max} \cdot \cos(\varphi) = \sin(\varphi) \tag{B.2}$$

The inverse of the CDF is then used to generate the random distribution using the uniform random variable $\xi$ between 0 and 1, given in MATLAB by the function"`rand()`".

$$\varphi = CDF^{-1} = \arcsin(\xi) \tag{B.3}$$

The azimuthal angle $\psi$ is given by a normal distribution in the range 0 to $2\pi$ and the random variable generated by

$$\psi = \xi \cdot 2 \cdot \pi \tag{B.4}$$

## B.2 Angular and Radial Distribution to Simulate the Mucosa

In order to reduce the computation time, the angular and radial distribution of photons exiting the mucosa were approximated. Instead of simulating the photon path inside the mucosa, an incident photon is given a random exit angle and radius according to a previously simulated and interpolated distribution.

The angular distribution (given by the cosine of the angle $vz$) is approximated by a linear function

$$PDF = f(x) = a \cdot x + b \tag{B.5}$$

This results for example in $a = -124.7$ and $b = -3.029$ for the parameters of the mucosa of $\mu_a = 0.35\,\mathrm{mm}^{-1}$, $\mu_s = 6.25\,\mathrm{mm}^{-1}$, and $g = 0.9$. The CDF is given by

$$\begin{aligned} CDF = F(vz) &= \int_{-vz}^{0} a \cdot x + b dx && \text{(B.6)} \\ &= \left[\frac{a}{2}x^2 + bx + c\right]_{-vz}^{0} && \text{(B.7)} \\ &= -\frac{a}{2}(-vz)^2 - b(-vz) = -\frac{a}{2}vz^2 + bvz && \text{(B.8)} \end{aligned}$$

solved for $vz$ using the abc-formula this results in

$$\begin{aligned} 0 &= -\frac{a}{2}vz^2 + bvz - F(vz) && \text{(B.9)} \\ vz = F^{-1}(U) &= \frac{-b \pm \sqrt{b^2 - 4 \cdot -\frac{a}{2} \cdot U}}{2\frac{a}{2}} && \text{(B.10)} \\ &= \frac{-b \pm \sqrt{b^2 + 2 \cdot a \cdot \xi}}{a} && \text{(B.11)} \\ & && \text{(B.12)} \end{aligned}$$

For scaling purposes $a$ is replaced by -1 and $b$ by $\frac{b}{-a}$. Using the reverse of the CDF to calculate the random cosine of the angle $vz$ results in

$$\begin{aligned} f(x) &= x + \frac{b}{-a} && \text{(B.13)} \\ vz &= \frac{b}{-a} \pm \sqrt{\left(\frac{b}{-a}\right)^2 + 2 \cdot \xi} && \text{(B.14)} \\ & && \text{(B.15)} \end{aligned}$$

This results in $vz$ between -1.4 and -0.05 while the real distribution results in values between -1 and 0. Hence, the random variable is re-sampled when $vz$ is smaller than -1. The fact that no

samples bigger than 0.05 are created fits well with the distribution shown in Figure B.1 a) and is accepted.

The radial $r$ distribution is interpolated by an exponential function $f(x) = a \cdot \exp(-b \cdot x)$. The exponential function is scaled by the factor $b$ as done in [125] and other calculations are done as previously.

$$PDF = f(x) = a \cdot b \cdot \exp(-b \cdot x) \tag{B.16}$$

$$CDF = F(r) = \int_0^r a \cdot b \cdot \exp(-b \cdot x)dx \tag{B.17}$$

$$= [-a \cdot \exp(-b \cdot x)]_0^r \tag{B.18}$$

$$= -a \cdot \exp(-b \cdot r) + a \tag{B.19}$$

Again, scaling must be done and $a$ is set to 1, while $b$ is not scaled. The random sampling variable is then calculated by

$$r = F^{-1}(U) = \frac{\log(1-U)}{b} \tag{B.20}$$

$$= \frac{\log(\xi)}{b} \tag{B.21}$$

The constant $b$ is $-0.7926$ for the same optical properties of the mucosa as above. Both random distributions must be scaled by the total reflection of the mucosa ($R = 5.99\,\%$ for the properties used here) in order to match the real distribution. The simulated distributions, interpolations, and sampling model of exit angle and radius are shown in Figure B.1.

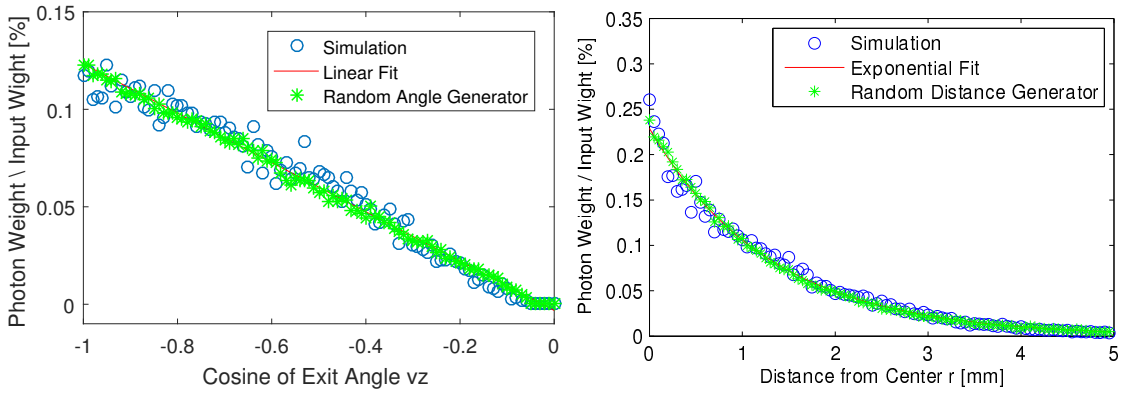


(a) Cosine of exit angle

(b) Exit radius

Figure B.1: Simulation, fitting, and sampling test for the position and angle of photons exiting the mucosa with $\mu_a = 0.35\,\mathrm{mm}^{-1}$, $\mu_s = 6.25\,\mathrm{mm}^{-1}$, and $g = 0.9$.

# Appendix C

# Stop Construction

A possibility to construct an anti-confocal stop is sputtering of a reflective or absorptive stop on a glass slide. Several materials are available for sputtering, such as gold, silver, chrome, indium tin oxide (ITO). Chrome is used as coating material for reflective resolution targets (such as the 1951 USAF Resolution Targets) and results an optical density of bigger than 3 (at 430 nm) for a chrome layer thickness of 0.12 µm [228].

A metal sheet is used as mask and placed on the glass slide. A hole is drilled and the edges bevelled as shown in Figure C.1 (a) to allow the chrome to access the whole area more easily without being blocked by the edges of the mask. Figure C.1 (b) shows a microscope image of a sputtered stop. The diameter is about 0.86 mm. As seen by the brighter edges of the stop it is obvious that less chrome reached the edges of the radius as blocked by the mask. A thinner mask must be used to avoid this problem. But this process is quick and easy and allows adopting the beam diameter.

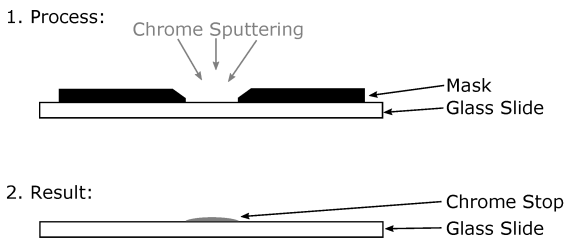


(a) Process

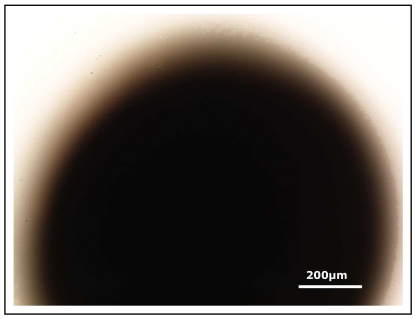


(b) Image of a sputtered stop with about 1 mm diameter.

Figure C.1: Sputtering of the chrome stop on a glass slide.

# Appendix D

# Safety Documentation

The standard operating procedure (SOP) and safety documentation for the optical table top system and experimental procedure for experiments on human volunteers are attached here. These documents are necessary in order to show the safety of the system for experiments on humans and to acquire ethics permission to conduct the experiments.

Permission for the experiments has been granted by the Faculty Research Ethics Committee. on the $4^{\text{th}}$ of March 2016.

# COSHH PROCEDURE ASSESSMENT FORM
# SCHOOL OF BIOLOGY

The University of Nottingham

| Laboratory/Room: A16, Life Sciences Building | UP ☒ QMC ☐ |
|---|---|

| Title of procedure: Operation of class 1 Laser System for Skin Reflectance Measurements |
|---|
| Brief description of procedure: This risk assessment covers the turning on, safety check, use, and shutting down of the laser system. It does not cover changes of the system itself.<br>This risk assessment requires class 3B laser risk assessments to be in place. Safety check of the system requires the user to have 3B laser training and is subject to the Ibios class 3B laser protocols. Normal operation of the system does not require any laser training, but is subject to the attached safety report. |

**Risk severity calculation** – see attached notes (page 3)

| Identified hazard | Severity (S) | Probability (P) | Impact (I) | Score (SxPxI) |
|---|---|---|---|---|
| Electrical supply | 1 | 1 | 1 | 1 |
| Sharps | 1 | 1 | 1 | 1 |
| Biological agents | 1 | 1 | 1 | 1 |
| Class 3B lasers | 3 | 1 | 1 | 3 |

**score = 1-2** – no further action required, but follow and maintain safe working practices.
**score = 3-4** – action should be taken to ensure that control measures are in place within 1 month of hazard identification. Identify control/action required below.
**score = 6-8** – work should not be started until control measures are in place. If work is already in progress, action should be taken as quickly as possible. Identify control/action required below.
**score = 9+** – work must not start until control measures are in place to reduce the risk. If this is not possible then work may not begin. If work is already in progress it must be stopped immediately. Identify control/action required below.

| Control measures required (this may include training) | Action required to achieve this | Date action completed |
|---|---|---|
| Laser registration, training and registration of users applies according to the 'IBIOS laser protocol'. | Refer to Laser registration form. | complete |
| The laser user must confirm class 1 of laser system before the start of experiments. This requires 3B laser training. | Follow checklist on attached safety report. This includes measuring of the output power and mechanical locking of the system. | On going (before each experiment) |
| The user must be familiar with the optical system and measurement protocol. | Individual must read and sign attached safety report. | complete |

| Emergency contact person (if known): |
|---|

| Assessed by: | Signed: | Date: |
|---|---|---|
| Approved by: | Signed: | Date: |

**A HARD COPY OF THIS FORM MUST BE KEPT IN THE AREA WHERE THE PROCEDURE IS USED WITH RELEVANT SUBSTANCE RISK ASSESSMENT FORMS ATTACHED**

# Device Safety

David S. Jung

March 8, 2016

## 1 Purpose of the Device

The described device will be used to measure the signal reflected from the skin of the hand of volunteers. First, the setup of the device will be described, then the experimental protocol, and finally its electrical, mechanical, and laser safety discussed.

## 2 Device

A schematic sketch of the device is shown in Figure 1. Two laser beams are expanded and aligned and focused on the sample. The reflected signal is directed on a camera for detection. The whole optical system is placed inside a box to avoid laser light to exit the system (except at the sample position) and to avoid accidentally changes of the system. Two shutters (one for each laser) are used to block the beams when no measurement is conducted to reduce the time of laser exposure on the sample.

During experiments the volunteer will place their hand on the sample holder and it will be exposed to the laser. The following section will describe the procedure in more detail.

## 3 Experimental Protocol

The volunteer will not have access to the equipment without a trained laser user as the room is locked by a keypad. Before the start of the measurement the trained experiment operator will check the system for any alterations affecting the safety of the system. The check includes measurement of the laser power at the sample and visual inspection of the placement of the shutters to ensure that the laser power is kept below the MPE. Further, is must be ensured that the box enclosing the system is mechanically fixed in order to prevent the volunteer to access the optical system and

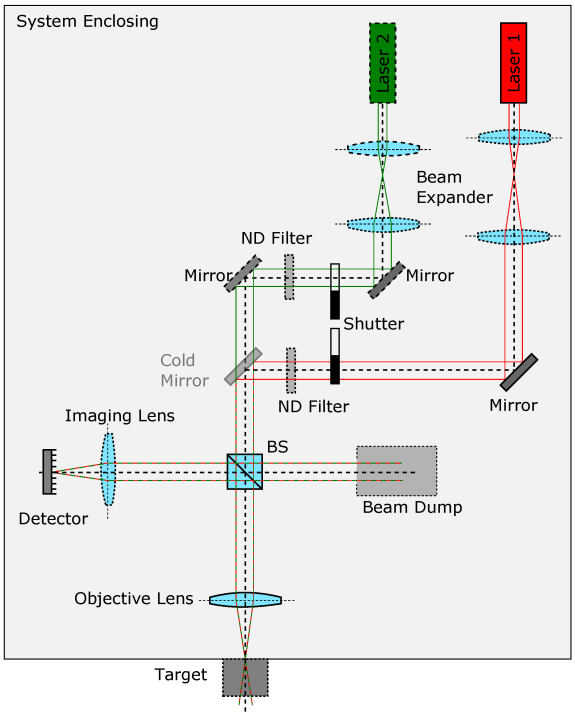


Figure 1: Setup of the system

class 3R laser. A checklist is given in Tab. 4 at the end of this report. The measurement procedure is as follows:

1. Measurement of reference power using reference sample
2. Measurement of noise
3. Placing of the hand on the sample holder
4. Measurement (Started by software). 5 repetitions of the following cycle:
   (a) Opening of laser shutter 1
   (b) Measurement with laser 1
   (c) Closing of shutter 1 and opening of shutter 2
   (d) Measurement with laser 2
   (e) Closing of shutter 2
   (f) Movement interval of 1 mm to new measurement position
5. Removal of the hand from sample stage.

# 4 Hazards

## 4.1 Summary

No hazards have been identified as long as the system is used according to the protocol, as listed in Table 1. A more detailed description of the individual possible hazards follows below.

Table 1: Summary of possible hazards

| **Category** | **Comment** | **Safe** |
|---|---|---|
| Electrical | No electrical elements | Yes |
| Biological and Chemical | Contact with aluminium | Yes |
| Mechanical – Sharps | Flat surfaces | Yes |
| Mechanical – Moving Parts | 4 mm moving distance | Yes |
| Laser | Below MPE (see Tab. 2 for detail) | Yes |
| System | Safe, when used according to intended procedure | Yes |

Table 2: Laser Safety. MPE for skin given for 1 s exposure time (which is 50 times the required camera exposure time allowing for slow switching of the beam shutters).

| **Case** | **MPE [W/m$^2$]** **532 nm / 808 nm** | **actual value [W/m$^2$]** **532 nm / 808 nm** | **Safe** |
|---|---|---|---|
| Skin (normal operation) | 11000 / 18088 | 2.52 / 3.14 | Yes |
| Skin (worst case) | 11000 / 18088 | 7738 / 4193 | Yes |
| Eye (worst case) | 10 / 16.4 | 0.01 / 0.013 | Yes |

## 4.2 Electrical Hazards

The electrical equipment used in the system use either standard power supplies with valid PAT test or their voltage is restricted to 12 V. No electrical equipment is connected to the sample holder. Hence, no electrical hazards have been identified.

## 4.3 Biological and Chemical Hazards

The only contact point of the volunteer and the system is the sample holder, made of aluminium. No other chemical or biological substances are involved in this system and experiment. Hence there are no biological and chemical hazards.

## 4.4 Mechanical Hazards

A hand will be placed on the sample holder for measurements and the holder moved a distance of 4 mm to allow measurements at 5 different positions.

A sketch of the sample holder is shown in Figure 2 and the position of a hand indicated. The sample holder has flat surfaces and is made of aluminium. The movement direction is also marked in the figure. The gaps between the sample holder and the case of the optical system are small and it is not possible to trap a finger. Further, the box is made of plastic that is more elastic than a finger.

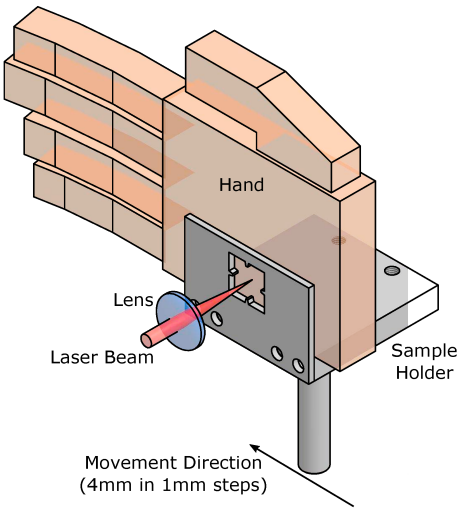


Figure 2: Placement of the hand on the sample holder.

Hence, there are no mechanical safety hazards present in the system.

## 4.5 Laser Hazards

The two lasers used are a NIR laser diode (Uni Ref No. L462; CW, 808 nm, 30 m, WL808P010, Thorlabs, Newton, New Jersey, USA) and a green laser module (Uni Ref No. L396; CW, 532 nm, 50 mW, BWN-532-30, B&W Tek, Newark, DE, USA). ND filters are placed and mechanically fixed just behind the laser output to reduce the power of the lasers to 2.34 and 0.058 mW, respectively. Before reaching the sample stage this power is further reduced by another set of optical filters to 0.5 µW and 0.4 µW for 808 and 532 nm, respectively. The safety limits for skin and eye (accidental viewing into the optics) are derived below.

*Measurements taken on 05/02/2016 with the FieldMaxII power meter with the sensor head OP-2 VIS (Coherent, Santa Clara, USA).*

Table 3: Laser Power in the system. Power in optical system is only accessible when the box is opened. This is mechanically fixed and not possible during experiments.

| | **808 nm** | | **532 nm** | |
|---|---|---|---|---|
| **Location** | **Power** | **Class** | **Power** | **Class** |
| Laser | 30 mW | 3B | 50 mW | 3B |
| Accessible in optical system | 2.34 mW | 3R | 0.058 mW | 1 |
| Accessible at sample | 0.425 µW | 1 | 0.393 µW | 1 |

### 4.5.1 Skin

The hand will be exposed to laser radiation during measurements. The calculations below show that the maximum permissible exposure (MPE) is not exceeded during the experiments. The definition of MPE for laser radiation on skin are defined in the BSI Standard of safety of laser products (BS EN 60825-1:2014) in Table A.5. For exposure times $t = 10^{-7}$ to 10 s the MPE is given by

$$MPE(400-700\,\text{nm}, 10^{-7}-10\,\text{s}) = 1.1\cdot 10^4 \cdot t^{0.25}\,\text{J/m}^{-2} \quad (1)$$

$$MPE(700-1400\,\text{nm}, 10^{-7}-10\,\text{s}) = 1.1\cdot 10^4 \cdot 10^{0.002(\lambda-700)} \cdot t^{0.25}\,\text{J/m}^{-2} \quad (2)$$

and for 10 to $3\cdot 10^4$ s by

$$MPE(400-700\,\text{nm}, 10-3\cdot 10^4\,\text{s}) = 2000\,\text{W/m}^{-2} \quad (3)$$

$$MPE(700-1400\,\text{nm}, 10-3\cdot 10^4\,\text{s}) = 2000\cdot 10^{0.002(\lambda-700)} = 3289\,\text{W/m}^{-2} \quad (4)$$

This can be used to translate the MPE given in energy per area into power according to

$$\textit{max. power exposure}\ [\text{W}] = MPE\ [\text{J/m}^{-2}] \cdot \frac{A_{\text{beam}}}{t} \quad (5)$$

using the area of the beam $A_{\text{beam}} = \pi r_{\text{beam}}^2$ at the sample. Rearranged to calculate the maximum permissible exposure time and replacing the MPE by the measured power at the samples stage results in

$$t_{\max}(532) = \begin{cases} \left(\frac{1.1\cdot 10^4 \cdot A_{\text{beam}}}{P(532)}\right)^{4/3} & \text{if } P(532) > 2000\,\text{W/m}^2 \\ 3\cdot 10^4 & \text{if } P(532) < 2000\,\text{W/m}^2 \end{cases} \quad (6)$$

$$t_{\max}(808) = \begin{cases} \left(\frac{1.1\cdot 10^4 \cdot 10^{0.002(808-700)} \cdot A_{\text{beam}}}{P(808)}\right)^{4/3} & \text{if } P(808) > 3289\,\text{W/m}^2 \\ 3\cdot 10^4 & \text{if } P(808) < 3289\,\text{W/m}^2 \end{cases} \quad (7)$$

where $P(532)$ and $P(808)$ is the power density of the beam given by the measured power of the laser beam divided by the expected beam area $A_{\text{beam}}$.

The permissible exposure time depend on the radius of the beam. Two cases are considered below, first normal operation and second the worst case scenario where all the power is focused into a diffraction limited area.

**Normal Operation:** In normal operation the hand will be placed 3 mm away from the focal spot. The beam radius for the optics with and NA of about 0.08 is 0.225 mm and the beam area is $A_{\text{beam}} = 0.16\,\text{mm}^2$. This results in a power density on the sample of $P(808) = 3.14$ and $P(532) = 2.52\,\text{W/m}^2$. This in turn results in a maximum permissible exposure times of $3 \cdot 10^4\,\text{s}$ for both lasers.

**Worst Case Scenario:** The radius of the diffraction limited spot $r_{\text{airy}}$ is given by

$$r_{\text{airy}} = 0.61 \cdot \frac{\lambda}{NA} \tag{8}$$

giving a radius of 6.16 µm and 4.06 µm for 808 and 532 nm, respectively. The area of the beam is $A_{\text{beam}}(808) = 119$ and $A_{\text{beam}}(532) = 52\,\mu\text{m}^2$. This results in a power per area of $P(808) = 4193$ and $P(532) = 7738\,\text{W/m}^2$ and maximum permissible exposure times of 7.02 and 1.6 s for 808 and 532 nm.

The above measured power is used in current experiments with required exposure time of the camera of 20 ms. This is well below the limits for both worst case scenario and normal operation. The actual exposure time will be controlled by electronic shutters and be less than 1 s.

#### 4.5.2 Eye

For calculation of safety for the eye the program Laser Safe PC Pro 4 (Lasermet Ltd, Bournemouth, UK) was used. Retinal damage worst case is when a collimated beam is incident on the eyes lens. This brings all the laser light into focus on the retina. In this case the MPE is $10\,\text{W/m}^2$ for 532 nm and $16.4\,\text{W/m}^2$ for 808 nm. With 10.4 and $13\,\text{mW/m}^2$ for 532 and 808 nm respectively, the actual power density is about 1000 times smaller than this and so is considered call 1 (inherently safe).

## 5 Safety Check-list

The experiments may only start if all four questions in the following check list have been answered with “Yes” by the trained experiment operator.

Table 4: System Safety Check-list

| No | Check | Yes | No |
|---|---|---|---|
| 1 | Both shutters in place? | ☐ | ☐ |
| 2 | Laser power at sample for 532 nm: ..... $< 0.5\,\mu W$? | ☐ | ☐ |
| 3 | Laser power at sample for 808 nm: ..... $< 0.5\,\mu W$? | ☐ | ☐ |
| 4 | Box closed and fixed? | ☐ | ☐ |

Start experiment only if all checks have been answered with “Yes”.

# Appendix E

# Ethics Approval

The ethics application form for experiments on humans presented in Appendix F including study design, recruitment poster, information sheet for participants, participant consent form, and data collection sheet are printed below. Further, the mail notifying about approval of the application and both reviewer decisions are shown as well.

# Faculty of Engineering
# Process for approval of research study involving human participants

## Introduction

This document describes the process to be followed when planning and obtaining approval for studies involving human participants within the Faculty of Engineering. This process is based on one previously run within the School/Dept M3. The process is administered by the Faculty Research Ethics Committee, and managed by the Chair of the Ethics Committee, Dr. Gary Burnett, and Faculty Research Ethics Officer, Dr. Sarah Sharples. All queries regarding the process should be initially sent to the Faculty Ethics Administrator, Dina Martin.

## What is Ethics Approval?

When conducting any study or observation or collecting data about individuals, it is essential that full consideration is given to ethical issues and that steps are taken to ensure participant well-being throughout the study.

Participants involved in research studies have a right to:
- Know the goals of the study and who is funding the work
- Make an informed decision about whether or not they wish to participate
- Leave the study at any time if they do not wish to continue
- Know what will happen to them during the study and how long it will take
- Know if they may experience any discomfort
- Know what will happen to the findings
- Privacy of personal information
- Be treated courteously

The University of Nottingham and Faculty of Engineering have an ethics procedure that requires all staff and students to submit an application for ethical approval before conducting any research study involving human participants. Members of the Ethics Committee read through study proposals to check that the researcher has demonstrated that they have given full consideration to ethical issues and that they have provided participants with appropriate and sufficient information.

## Who needs Ethics Approval?

ANY member of staff or registered student of the University of Nottingham involved in conducting any study or observation or collecting data about individuals **MUST** adhere to the University Code of Research Conduct and Research Ethics. Those affiliated with the Faculty of Engineering **MUST ALSO** comply with the Faculty ethical approval process before commencing their study.

## Ethics application procedure

The attached document outlines the ethics approval process within the Faculty of Engineering. For all applications required to undergo formal review, applications must be submitted to the **Ethics Administrator**, Faculty of Engineering Research Office, Coates Building. The application will then be reviewed by the ethics committee. We aim to return a decision to applicants within two weeks but the procedure may be delayed if the ethics committee require further information. It is the applicant's responsibility to make sure that applications are submitted in good time.

THE STUDY MAY **NOT** START UNTIL ETHICAL APPROVAL HAS BEEN AWARDED

# Information you should give to ALL participants

The following list describes the information that should be given to all participants. Normally this should be given in a participant information sheet at the beginning of the study, and participants should be required to confirm that they have understood the nature of the study, and that they are happy to participate.
The following information should be included:

- Details of who will be conducting the study.
- Details about who is sponsoring the study and what the terms of the sponsorship are (i.e. who will 'own' the data and how the data will be used).
- Details about the nature, purpose and duration of the study. (Participants whose first language is NOT English may need further explanation of what is involved as their understanding of some of the terminology may be limited).
- What kinds of procedures will be used and what participant will be asked to do.
- Details about any hazards, inconveniences and risks associated with the study.
- What procedures will be followed if a participant is injured. (only needed if risk of injury has been identified)
- What benefits (payments, expenses etc) are attached to the study.
- What they need to do in order to receive the payments described above.
- What procedures will be employed to maintain confidentiality and anonymity (e.g. removing personal details from data/reports, keeping data in locked files)
- What will happen to the data (how it will be used, how it will be stored, in what form it will be disseminated and if it is likely to be used for further analysis).
- How you will use photographs or video records (data analysis, illustration purposes, displayed to sponsors/ non-public academic audiences, printed in public domain documents etc).
- Details about who to contact if questions or problems arise.
- ALL participants must be told that any involvement in the study is voluntary and they are free to withdraw at any time. You should also explain any consequences for the participant of withdrawing from the study and indicate what will be done with the participant's data if they withdraw.

# Faculty of Engineering
# Application for approval of research study involving human participants

**ALL applicants must provide the following information**

The applicant must be the person who will conduct the investigations; each application must be made by one applicant:

- usually the student in the case of taught or research courses,
- usually the researcher (the member of university research or academic staff) who will conduct the study in the case of funded research projects,
- usually the principal investigator in the case of applications for ethics approval in advance of submission of a research proposal

**If the applicant is an Undergraduate or Postgraduate taught or research student please complete the information below. The application must be approved by a Supervisor.**

| | | | |
|---|---|---|---|
| Name of student: | David Jung | Student No: | 4202060 |
| Course of study: | PhD, EEE | Email address: | eexdsj@notthingham.ac.uk |
| Supervisor: | Chung See | | |

**If the applicant is a member of university research or academic staff, please complete the information below: For research staff, the application must be approved by the Principal Investigator**

| | | | |
|---|---|---|---|
| Name: | | Principal Investigator (Budget Holder) | |
| Email address: | | PI Signature: …… | |

**Title of investigation** : Skin reflectance measurement under influence of temperature

**Planned date for study to begin:** 1st March 2016 **Duration of Study:** 1 Month (until end of March 2016)

**Please state whether this application is:**

☒ New ☐ Revised ☐ A renewal ☐ For a continuation study

**Selection of review process**

Please indicate whether the application is required to go forward to the ethics committee for formal review, or, in the case of projects completed by ***taught undergraduate and postgraduate students only***, whether the application can be approved by the supervisor under the expedited review process.

☒ Formal review, application will be submitted to ethics committee

☐ Expedited review, application is approved by supervisor

**Approval by supervisor: expedited review**

I approve the application as supervisor of this project, under the expedited review procedure.

Name of supervisor…… Signature…… Date……

Office use only

**Date form received:**

**Passed to reviewers:** 1. Name…… Date……..

**(formal review only)** 2. Name…… Date……..

**Date decision returned to applicant:**

## Ethical Issues Checklist

The purpose of this Checklist is to facilitate the review process and to identify any ethical issues that may concern the Committee. It is meant to be an aid to both the researcher and the Committee. Listed below are areas which require some justification and attention on your part in specifying your study protocol. Please answer each question honestly, giving full details where required. Answering "YES" to any of the questions will not necessarily lead to a negative response to your application but it will draw issues to your attention and give the reviewers the opportunity to ensure appropriate steps are being taken. In expedited review, supervisors should ensure that for any questions where the answer "YES" has been given, appropriate measures have been taken to maintain ethical compliance.

Applicant's full name: David Jung

**You must complete ALL of this section before submitting your application**

**1** Who is the population to be studied?

*Humans, 18+ years old, white skin colour.*

**2** Please give details of how the participants will be identified, approached and recruited. (Include any relationship between the investigator and participants e.g. instructor-student).

*Posters will be put up in the department. The information sheet will be send to interested individuals via email.*

**3** Will the population studied include any vulnerable members of the public? **YES** ☐ **NO** ☒
Note: for the purpose of ethics approval this includes participants who are under 18, people who are disabled or in poor health, and also those who are non-English speakers and may not be able to understand the consent forms. (If YES, please give further details)

……

**4** Will it be possible to associate specific information in your records with specific participants on the basis of name, position or other identifying information contained in your records? **YES** ☐ **NO** ☒

**5** What steps have you taken to ensure confidentiality of personal information and anonymity of data both during the study and in the release of its findings?

*No personal data will be collected. Each participant will be given a unique 3 digit number. This number will be connected to the data, but not to the consent form. Their name will be only connected to the consent form but not the data. The participant will not be identifiable.*

**6** Describe what data will be stored, where, for what period of time, the measures that will be put in place to ensure security of the data, who will have access to the data, and the method and timing of disposal of the data.

*The data to be stored are skin reflectance measurements and photographs of the hand.*
*The original photographs will be stored on a removable SD card on the camera. This data will be transferred to the University network (Z: drive) and the original data on the SD card deleted. The measurement data will be stored on the University network directly. The data will be accessible by the student conducting the study only, using their username and password.*
*The participant may request deletion of the data quoting their unique ID number, before publication of the data. All paper documents (consent form and data collection sheet) will be stored securely within the University.*
*All data will be kept for 7 years after date of publication.*

**7** Will persons participating in the study be subjected to physical or psychological discomfort, pain or aversive stimuli which is more than expected from everyday life? (If YES, please give further details) **YES** ☒ **NO** ☐

*Exposure of one hand to cold (~6°C) and hot (~47°C) water for 5 minutes each.*

| | | | |
|---|---|---|---|
| **8** | Will participants engage in strenuous or unaccustomed physical activity? (If YES, please give further details) ..... | **YES** ☐ | **NO** ☒ |
| **9** | Will the investigation use procedures designed to induce participants to act contrary to their wishes? (If YES, please give further details) ..... | **YES** ☐ | **NO** ☒ |
| **10** | Will the investigation use procedures designed to induce embarrassment, humiliation, lowered self esteem, guilt, conflict, anger, discouragement or other emotional reactions? (If YES, please give further details) ..... | **YES** ☐ | **NO** ☒ |
| **11** | Will participants be induced to disclose information of an intimate or otherwise sensitive nature? (If YES, please give further details) ..... | **YES** ☐ | **NO** ☒ |
| **12** | Will participants be deceived or actively misled in any manner? (If YES, please give further details) ..... | **YES** ☐ | **NO** ☒ |
| **13** | Will information be withheld from participants that they might reasonably expect to receive? (If YES, please give further details) ..... | **YES** ☐ | **NO** ☒ |
| **14** | Will the research involve potentially sensitive topics? (If YES, please give further details) ..... | **YES** ☐ | **NO** ☒ |

If you require space for additional information, please add it here and identify the question to which it refers:

**Checklist of information to include with your application:**
Please tick the boxes below to confirm that you have included the following information with your submission. Failure to include the required information may result in your ethics application and approval for start of your research to be delayed.

☒ A brief description of the study design:
- number and type of participants
- number and duration of activities participants will be involved in
- equipment and procedures to be applied
- information about how participants will be recruited
- whether participants will be paid (state how this will be done)
- plans to ensure participant confidentiality and anonymity
- plans for storage and handling of data
- information about what will happen to the data after the study
- information about how any data and images may be used
- state whether it will be possible to identify any individuals.

☒ Copies of any information sheets to be given to participants (include recruitment information (e.g. adverts, posters, letters, etc)

☒ A copy of the participant consent form

☒ Copies of data collection sheets, questionnaires, etc

*I confirm that all of the above is included in the application:*

*As the applicant I confirm that I have read and understand the Ethical requirements for my study and have read and complied with the University of Nottingham Code of Research Conduct and Research Ethics.*

**Signature of applicant** …… Date ……

*As supervisor, I confirm that I have checked the details of this application.*

**Signature of supervisor** …… Date ……

**NB The signature of the supervisor on this part of the application DOES NOT indicate supervisor approval for expedited review. If supervisor approval is granted then the front page of the application MUST be signed for approval to be confirmed.**

## Ethics Committee Reviewer Decision

This form must be completed by each reviewer. Each application will be reviewed by two members of the ethics committee. Reviews may be completed electronically and sent to the Faculty ethics administrator (Dina Martin) from a University of Nottingham email address, or may be completed in paper form and delivered to the Faculty of Engineering Research Office.

Applicant full name ……

**Reviewed by:**

Name ……

Signature (paper based only) ……

Date ……

- ☐ Approval awarded - no changes required
- ☐ Approval awarded - subject to required changes (see comments below)
- ☐ Approval pending - further information & resubmission required (see comments)
- ☐ Approval declined – reasons given below

Comments:

……

……

……

……

……

……

……

……

……

……

**Please note:**

1. The approval only covers the participants and trials specified on the form and further approval must be requested for any repetition or extension to the investigation.
2. The approval covers the ethical requirements for the techniques and procedures described in the protocol but does not replace a safety or risk assessment.
3. Approval is not intended to convey any judgement on the quality of the research, experimental design or techniques.
4. Normally, all queries raised by reviewers should be addressed. In the case of conflicting or incomplete views, the ethics committee chair will review the comments and relay these to the applicant via email. All email correspondence related to the application must be copied to the Faculty research ethics administrator.

**Any problems which arise during the course of the investigation must be reported to the Faculty Research Ethics Committee**

# Study Design

## Skin Reflectance Measurement

**Summary:**

During the experiment, the participant will submerge their hand in cold and hot water for a period of 5 minutes in order to change the blood flow in the hand. This will change the colour of the skin. Camera recordings as well as reflection measurements with a custom build optical setup will be taken. The safety of the custom build optical system is has been checked with the safety office and supervisors.

**Details:**

| | |
|---|---|
| Participants | 3, white skin colour, no preference for age or gender |
| Activities | 1. The participant will be asked to stay at room temperature for 10 minutes.<br>2. Measurement of the skin reflectance: The hand will be placed on a sample stage, illuminated with laser and the reflectance measured. A measurement will take less than one minute. Photographs of the hand will be taken to document the skin appearance.<br>3. The participant will be asked to submerge their hand in cold (6°C) water for 5 minutes.<br>4. Measurement of the skin reflectance.<br>5. Wait for 30mins, to reach normal skin temperature.<br>6. Measurement of the skin reflectance.<br>7. The participant will be asked to submerge their hand in hot (47°C) water for 5 minutes.<br>8. Measurement of the skin reflectance. |
| Equipment and Procedures | - Hot and cold water, thermometer<br>- Custom optics<br>- Photo Camera |
| Recruiting | Poster |
| Pay | No |
| Data, Confidentiality and Anonymity | No personal data will be collected. Each participant will be given a unique 3 digit number. This number will be connected to the data, but not to the consent form. Their name will be only connected to the consent form but not the data. The participant will not be identifiable.<br>The data to be stored are skin reflectance measurements and photographs of the hand. The original photographs will be stored on a removable SD card on the camera. This data will be transferred to the University network (Z: drive) and the original data on the SD card deleted. The measurement data will be stored on the University network directly. The data will be accessible by the student conducting the study only, using their username and password.<br>The participant may request deletion of the data quoting their unique ID number, before publication of the data. All paper documents (consent form and data collection sheet) will be stored securely within the University.<br>All data will be kept for 7 years after date of publication. |

# Participants Needed

## Skin reflectance measurement under influence of temperature

The University of Nottingham
UNITED KINGDOM · CHINA · MALAYSIA

Study running from 1st March 2016 to 1st April 2016

---

### Background

Inflammation in tissue is to be detected. Inflammation results in a higher blood flow in the diseased tissue causing a red appearance. For this, a spectroscopy based optical system has been developed and needs to be validated. Instead of inducing inflammation, the blood flow will be altered by immersing a hand in hot and cold water. This will change the skin colour and different reflection spectra can be measured.

### What will I need to do?

In order to change the blood flow in a hand you will be asked to immerse one hand in hot/cold water for 5 minutes and reflectance measurements and photographs will be taken before and after. The study consists of the following steps:

1. The participant will be asked to stay inside (room temperature) for 10 minutes.
2. Measurement of the skin reflectance: The hand will be placed on a holder, illuminated with a laser and the reflectance measured. A measurement will take less than one minute. Photographs of the hand will be taken to document the skin appearance.
3. The participant will be asked to submerge their hand in cold (6°C) water for 5 minutes.
4. Measurement of the skin reflectance.
5. Wait for 30mins, to reach normal skin temperature.
6. Measurement of the skin reflectance.
7. The participant will be asked to submerge their hand in hot (47°C) water for 5 minutes.
8. Measurement of the skin reflectance.

### Who can apply?

This study is looking for willing participants with white skin colour of eighteen years or older.

### Additional information:

This study is entirely voluntary. No reimbursement will be provided. All collected data will be stored securely within the University of Nottingham and might be used in publications.

### Interested?

If you would like to take part or want more information about this study please contact

David Jung (PhD Student) david.jung@nottingham.ac.uk

# Information for Participant

## Skin Reflectance Measurement

Participant ID: ☐☐☐

**Study will be conducted by**

**David Jung**, PhD student at the University of Nottingham and Nottingham Hearing Biomedical Research Unit
His research focussed on the assessment of inflammation in the middle ear. This study is part of his research.

**Background**

Inflammation in the middle ear is to be detected. Inflammation results in a higher blood flow in the diseased tissue causing a red appearance. For this, a spectroscopy based optical system has been developed and needs to be validated.
Instead of inducing inflammation in the ear, the blood flow in a hand will be altered by immersing a hand in hot and cold water. This will change the skin colour and different reflection spectra can be measured. This will validate the system design and show its ability to detect differences in blood flow based on the measured reflection spectra.

**Procedures**

In order to change the blood flow the hand has to be placed in hot and cold water and reflection measurements and photographs are taken. The whole process will last about 60minutes (including breaks) and involves the following steps:

1. The participant will be asked to stay inside (room temperature) for 10 minutes.
2. Measurement of the skin reflectance: The hand will be placed on a sample stage, illuminated with red and NIR laser and the reflectance measured. A measurement will take less than one minute. Photographs of the hand will be taken to document the skin appearance.
3. The participant will be asked to submerge their hand in cold (6°C) water for 5 minutes.
4. Measurement of the skin reflectance.
5. Wait for 30mins, to reach normal skin temperature.
6. Measurement of the skin reflectance.
7. The participant will be asked to submerge their hand in hot (47°C) water for 5 minutes.
8. Measurement of the skin reflectance.

**Discomfort & Risk**

It will be uncomfortable to keep the hand in the cold/hot water for 5 minutes. But no risks are involved in this. The participant may withdraw from the study at any time due to discomfort or for any other reason.

**Payment**

None

**Collected Data & Data Storage**

No personal data (such as name, age, or sex) will be recorded so that the participant cannot be identified. Photographs of the hand and experimental data will be stored securely within the University of Nottingham and are not

connected to your name. You can request deletion of the data quoting the ID number given on the top of this form. This is only possible before publication of the data.
The collected data will primarily be used to validate the developed optical system. It might also be used in publications and for further research.


**Contact**

| | |
|---|---|
| Student (conducting the study) | David Jung<br>Email: david.jung@nottingham.ac.uk<br>Phone: 0115 8468848 |
| Supervisor | John Crowe<br>Email: John.Crowe@nottingham.ac.uk<br>Phone: 0115 9515590 |


*Involvement in this study is voluntary and the participant is free to withdraw at any time without giving reasons. There are no consequences for the participant of withdrawing from the study. All data will be deleted in case of withdrawing from the study.*

*You may contact the conductor of the study (see above) and request for your data to be removed from the study. You will need your identification number that was given to you during the data acquisition in order to do this (see top of this form).* ***Note:*** *Once your data has been used in a publication (including thesis submission) the elements that appear in the results cannot be deleted or removed.*

## Participant Consent Form

The University of Nottingham
UNITED KINGDOM · CHINA · MALAYSIA

### Skin Reflectance Measurement

Please tick box

1. I confirm that I have read and understand the information sheet explaining the above research project and I have had the opportunity to ask questions about the project and had these answered satisfactorily. ☐

2. I understand that my participation is voluntary and that I am free to withdraw at any time without giving any reason and without there being any negative consequences. ☐

3. I understand that my name will not be linked with the research materials, and I will not be identified or identifiable from the data or in reports that result from the research. ☐

4. I agree for the anonymised data may be used in publications. ☐

5. I agree to take part in the above study. ☐

| _____ | _____ | _____ |
|---|---|---|
| Name | Date | Signature |

## Data Collection Sheet

The University of Nottingham
UNITED KINGDOM · CHINA · MALAYSIA

### Skin Reflectance Measurement

| No | Participant ID | Water Temperature [°C] | | | | Date |
|---|---|---|---|---|---|---|
| | | Cold Start | Cold End | Warm Start | Warm End | |
| *Example* | *123* | *6* | *7* | *47* | *43* | *11/02/16* |
| 1 | | | | | | |
| 2 | | | | | | |
| 3 | | | | | | |
| 4 | | | | | | |
| 5 | | | | | | |
| | | | | | | |
| | | | | | | |
| | | | | | | |

## Jung David

**From:** Deeley Joanne
**Sent:** 04 March 2016 14:50
**To:** Jung David
**Subject:** Ethics Application
**Attachments:** Jung_BR_Reviewer Decision.docx; Reviewer Decision - DM.docx

**Categories:** Important

Dear David

Please find attached the final decision on your recent ethics application.

**The decision was: Approval Awarded – subject to required changes (see comments).**

Please ensure that these changes are made and approved by your supervisor(s).

Best of luck with your study.

Best wishes,

Jo Deeley
Research Administrator
Engineering Faculty Research Office
University of Nottingham
University Park
Nottingham
NG7 2RD

Tel: 0115 74 84583

## Ethics Committee Reviewer Decision

This form must be completed by each reviewer. Each application will be reviewed by two members of the ethics committee. Reviews may be completed electronically and sent to the Faculty ethics administrator (Jo Deeley) from a University of Nottingham email address, or may be completed in paper form and delivered to the Faculty of Engineering Research Office.

Applicant full name David Jung

**Reviewed by: Brendan Ryan**

Name
Signature (paper based only) ……

Date ……4 March 2016……

- ☐ Approval awarded - no changes required
- ☐ Approval awarded - subject to required changes (see comments below)
- ☐ Approval pending - further information & resubmission required (see comments)
- ☐ Approval declined – reasons given below

taken. The safety of the custom build optical system is has been checked with the safety office and supervisors.

Comments:

…See above extract from the Study design document. This is approved on the basis that this has been checked by the safety office and supervisor and does not present a risk to participants. It may be advisable to point this out to participants if this has been approved.

……
……
……
……
……
……

**Please note:**

1. The approval only covers the participants and trials specified on the form and further approval must be requested for any repetition or extension to the investigation.
2. The approval covers the ethical requirements for the techniques and procedures described in the protocol but does not replace a safety or risk assessment.
3. Approval is not intended to convey any judgement on the quality of the research, experimental design or techniques.
4. Normally, all queries raised by reviewers should be addressed. In the case of conflicting or incomplete views, the ethics committee chair will review the comments and relay these to the applicant via email. All email correspondence related to the application must be copied to the Faculty research ethics administrator.

**Any problems which arise during the course of the investigation must be reported to the Faculty Research Ethics Committee**

## Ethics Committee Reviewer Decision

This form must be completed by each reviewer. Each application will be reviewed by two members of the ethics committee. Reviews may be completed electronically and sent to the Faculty ethics administrator (Jo Deeley) from a University of Nottingham email address, or may be completed in paper form and delivered to the Faculty of Engineering Research Office.

Applicant full name David Jung

**Reviewed by:**

Name David Morris
Signature (paper based only) ……

Date ……1 Mar 2016……

- ■ Approval awarded - no changes required
- ☐ Approval awarded - subject to required changes (see comments below)
- ☐ Approval pending - further information & resubmission required (see comments)
- ☐ Approval declined – reasons given below

Comments:

I am happy for this study to proceed as is.

**Please note:**

1. The approval only covers the participants and trials specified on the form and further approval must be requested for any repetition or extension to the investigation.
2. The approval covers the ethical requirements for the techniques and procedures described in the protocol but does not replace a safety or risk assessment.
3. Approval is not intended to convey any judgement on the quality of the research, experimental design or techniques.
4. Normally, all queries raised by reviewers should be addressed. In the case of conflicting or incomplete views, the ethics committee chair will review the comments and relay these to the applicant via email. All email correspondence related to the application must be copied to the Faculty research ethics administrator.

**Any problems which arise during the course of the investigation must be reported to the Faculty Research Ethics Committee**

# Appendix F

# Measurement on Human Volunteers

The system cannot be tested on the middle ear in the clinical setting as no hand-held system is available yet and the experiments would require a more complicated ethics application procedure to be followed. Instead, experiments on human volunteers are conducted in order to validate the model for absorption of blood in the mucosa phantoms and show that the system is able to measure blood concentration in living tissue. For this the blood level in a human volunteer is altered and the inflammation index measured. First several options to alter the blood flow are presented and the most suitable one selected.

**Occlusion of limbs:** The first option is to alternate the blood flow in a limb by a pressure cuff as in [122]. A pressure of 50 mmHg allows blood flow into the tissue while the blood flow out of the tissue is blocked. This causes the total blood level to increase while the pressure is applied. A pressure of 250 mmHg stops both blood flows. This causes a need for oxygenated blood and a release of the pressure causes more blood to flow into the limb (reactive hyperemia) in order to supply the needed blood and the blood concentration is increased directly after pressure release. The oxygenation is also altered during these experiments.

**Histamine:** Histamine has an important role in the immune response and inflammation, it causes the local blood vessels to dilate and increase in permeability to allow more blood to reach the tissue [229]. It is commonly used in allergy skin tests to validate the normal response of skin [230], in animal models to trigger inflammation [120,231], and in human studies [121,232]. This could be used to induce inflammation and alter the blood flow in a local area but would require a trained person to apply histamine.

**Exposure to cold and heat:** Warming of tissue causes assimilation (expansion of the blood vessels) while exposure to cold causes vasoconstriction (decrease in vessel diameter) and can decrease blood flow to essential zero [233]. For example Stephen et al. [234] use exposure of a hand to 45-50 deg hot water for 2 minutes to increase the blood flow and to measure the skin colour.

**Scratching:** Another option would be to scratch the skin and measure the resulting increase in blood flow. The skin might be injured and the amount of scratching is hard to measure and cannot be easily reproduced.

The exposure to cold and heat is chosen as method as it is least invasive, allows a reproducible protocol, and changes the blood flow relatively quickly to allow comparable measurements at the same area.

## F.1 Protocol

Approval for these experiments was obtained at on the 04/03/2016, the relevant documentation and communications are printed in Appendix E. Four healthy volunteers were recruited between the 08/03/2016 and 18/03/2016. Only volunteers with white skin colour were selected to avoid high melanin concentrations in the skin that may to influence measurements. This is appropriate as no melanin is present in the middle ear mucosa.

After waiting at room temperature for more than half an hour to avoid influences of extreme temperatures outside the volunteer submerged a hand in cold water (temperature about 5 °C) for 5 minutes. The hand is then dried and a photograph taken. Then the hand is placed on the sample holder presented in Figure 3.29 at the position of the mucosa phantom (as shown in Figure 2 of the attached safety documentation Appendix D). The 1500 grid diffuser is placed in front to simulate the eardrum. The green and NIR reflectance signals are then recorded over a time course of 4 minutes, with one measurement taken every minute. The hand is kept on the sample stage during the measurements to ensure sampling of the same area. After the measurement series another photograph of the hand is taken. The photograph is taken with a flash, in a room without windows and the room light on and a defined distance between hand and camera of about 20 cm in order to ensure constant lighting. The protocol of the measurement is illustrated in Figure F.1.

A safety data sheet of the system is produced and shown in Appendix D in order to show the safety of the optical system and acquire permission to conduct the experiments.

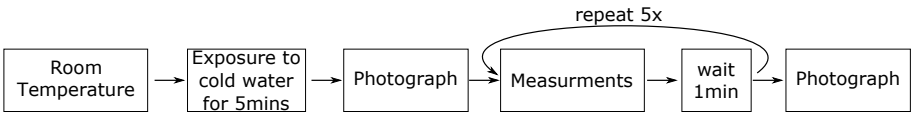


Figure F.1: Protocol of the experiments on human hands.

## F.2 Results

The exposure to cold water causes the blood content in the hand to increase in order to increase the temperature of the hand. This is in contrast to [233] reporting a decrease in blood flow during exposure to cold. It is assumed that the increase in blood flow observed here is due to the fact that only one hand is exposed to cold and the body does not need to protect the body to become hypothermic. Further, the measurements are made when the hand is exposed to air at room temperature and the temperature of the skin is rising again. Over the time course of 4 minutes the hand warms up and the blood flow is reduced. This is visible in the photographs that show a reddening of the hand directly after exposure to cold water in Figure F.2 (a), indicating a high blood volume. After 4 minutes, the hand is less red indicating a normal blood level as seen in Figure F.2 (b).

The measured inflammation index for the 4 volunteers is shown in Figure F.2 (c) and shows a highest value directly after the exposure to cold water ($t = 0\,\text{min}$) and lowest value after 4 minutes. The markers indicate measurements and the lines are exponential interpolations $II_{\text{fit}} = a \cdot \exp(b \cdot t) + c$ with the $R^2$ values of 0.89, 0.66, 0.96, and 0.95. The difference between the measured index for the volunteers can be explained by any of the following reasons: differences in the thickness of skin (up to 1.5 mm on the palm [235]) with no blood perfusion in the top layer (epidermis) [235], different levels of blood perfusion, or different reactions of the blood circulation to exposure to cold. Still, all cases show an increase of the measured inflammation index with blood concentration. Volunteer 2 shows a very small change in measured inflammation index, but this was expected as the hand did not show a change in colour and it is assumed that the blood content did not change.

The change in inflammation index seen here corresponds to a change from mucosa phantom 2 to phantom 1 equivalent to a change of 8 % to 2 % blood concentration. This comparison does not consider the skin with a thickness up to 1.5 mm. A more accurate phantom model would be necessary for correct calibration.

(a) Photograph of the hand at the start of measurement ($t = 0\,\text{min}$)

(b) Photograph of the hand at the end of measurement ($t = 4\,\text{min}$)

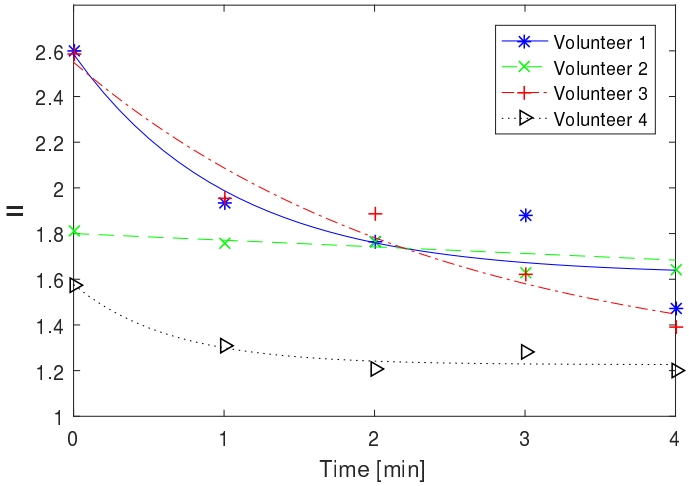


(c) Time course of the inflammation index. Markers indicate measurements and lines indicate exponential fitted curves.

Figure F.2: Inflammation index measured on human volunteers. The photographs show the hand of volunteer 2 before and after the measurement series.

# Appendix G

# Publications

The publications resulting from this project are attached below. First, a paper presenting the anti-confocal system and simulations was submitted to "OSA - Optics in the Life Sciences" conference held in Vancouver, Canada from the $12^{th}$ to $15^{th}$ of April 2015. The paper was accepted as poster presentation and the poster is printed as well. Second, a more detailed description of the simulations and change of parameters of the optical system and tissue was accepted for publication in the "Biomedical Optics Express", Volume 6, Issue 10, published 2015.

NHS National Institute for Health Research

# Monte Carlo Photon Simulation of an Anti-Confocal System to Monitor Middle Ear Inflammation

The University of Nottingham
UNITED KINGDOM · CHINA · MALAYSIA

David S. Jung[1,3], John P. Birchall[1,2], John A. Crowe[3], Chung W. See[3], Michael G. Somekh[3,4]

## 1. Motivation

[1]

**Medical Background:**
Chronic Middle Ear Inflammation is characterized by **inflammation of the middle ear mucosa** and secretion of a liquid causing **hearing loss**. The only effective treatment is surgically draining the liquid and placing a ventilation tube through the eardrum. This is one of the **most common surgeries** in children in the developed world [2]. In 25% of the cases the symptoms recur [3] and there is **no way of predicting the recurrence**. It is hypothesised that a recurrence is linked to a persistent inflammation after surgery.

**Aim of the project:**
This project aims to develop a medical device that will be able to determine whether the middle ear mucosa is still inflamed or has returned to normal in order to **improve diagnosis**. Direct view of the mucosa is obscured by the eardrum. Consequently, an optical method must be implemented to allow measurements through the eardrum by **maximising the signal** detected from the mucosa and **minimising background reflections** from the eardrum. The ratio of the detected signal at two wavelengths will allow **assessment of the inflammation** similar to haemoglobin concentration measurements. The use of confocal and anti-confocal systems is investigated here.

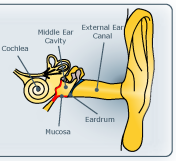


## 2. The Anti-Confocal System

**Conventional Confocal System:**

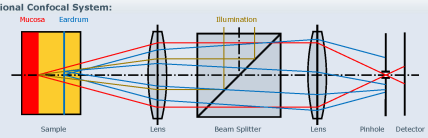


- Illumination focused on the mucosa
- Pinhole placed in the image plane of the mucosa blocks out-of-focus light
- High resolution
- Small sampling volume

**Anti-Confocal System:**

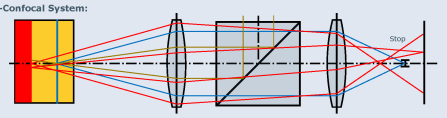


- Illumination focused on the eardrum
- Stop placed in the image plane of the eardrum blocks in-focus light
- Low resolution
- Big sampling volume

## 3. Monte Carlo Simulation

Monte Carlo methods are used to **simulate light propagation** in the ear and anti-confocal system in order to study the influence of different design parameters on the system performance.
A **random path of a photon** in the tissue is simulated and then propagated through the optical system to the detector. **Multiple paths** are added in order to achieve a representable distribution. Tissue parameters are approximated from literature and measurements on animal models.

**Inputs:** Numerical Aperture (NA), geometry, tissue properties, photon weight and direction.

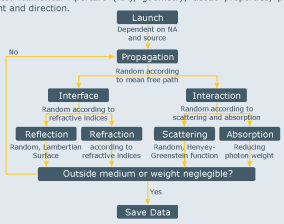


**Outputs:** photon path and position.

## 4. Results

**Sample path of a single photon:**
(1) Launched into the tissue
(2) Passes eardrum and tympanic cavity
(3) Scattered several times inside the mucosa
(4) Propagated to detector

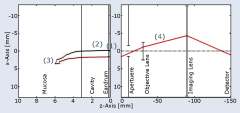


**Addition of 10,000 paths to distribution:**

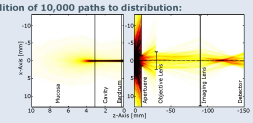


Knowing the photon path **signal, background,** and **signal-to-background ratio (SBR)** can be defined as follows:

| | |
|---|---|
| Signal | Number of photons reaching the mucosa, thus carrying information about inflammation |
| Background | Number of photons blocked by the eardrum thus no information about inflammation |
| SBR | Signal divided by Background |

**Simulated signal and SBR** vs. radius of pinhole or stop:

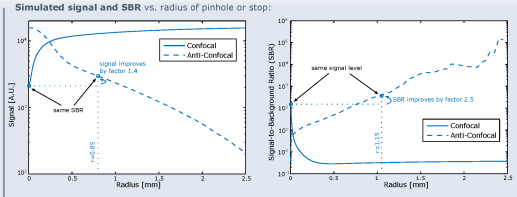


Confocal System:
- Increasing signal but decreasing SBR with increasing diameter

Anti-Confocal System:
- Increasing SBR but decreasing signal for increasing radius
- **2.5x better SBR** at 1.15mm radius for same signal level compared to confocal system or
- **1.4x higher signal** level at 0.85mm radius for same SBR compared to confocal system

**Variations** of the system:

| | |
|---|---|
| Focus of the illumination | Slightly improved SBR when focused on mucosa |
| Combination of pinhole and stop | No improvement |
| NA | SBR increases for confocal and stronger for anti-confocal |
| Scattering of the eardrum | SBR decreases for confocal but increases in some cases for anti-confocal |
| Distance between eardrum and mucosa | Improvement of the SBR for confocal but no significant change for anti-confocal |

## 5. Preliminary Experiments

Preliminary experiments **confirm** that the anti-confocal system is working.

Recovering the signal (black) reflected off the target (reflective bars on non-reflective background) hidden behind a guinea pig eardrum. The contrast is better using anti-confocal system (red) compared to the confocal system (yellow).

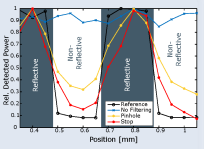


## 6. Conclusion

Both the confocal and anti-confocal systems have their merits.
The **anti-confocal system is superior** in this special case as:
- Easier to focus
- Bigger sampling volume in tissue
- Higher SBR and signal power possible
- More photons penetrating deeper into the tissue carrying 'more' information of the inflammation are detected

But it **cannot replace the confocal system** as:
- Low spatial resolution
- Not applicable when single layer to be imaged is embedded in scattering sample.

**Future tasks:**
- Experimental characterisation and validation of the anti-confocal system using tissue simulating targets.
- Implementation of spectroscopic measurements making use of the absorption spectra of blood.

**References:**
[1] NHS choices, Online. http://www.nhs.uk/conditions/Otitis-media/Pages/Introduction.aspx, Accessed 06/01/13.
[2] J. Rimmer, C. E. B. Giddings, and N. Weir (2007). History of myringotomy and grommets. The Journal of Laryngology & Otology, 121, pp 911-916.
[3] M. Daniel, Otitis Media with Effusion: Current Treatment, New Understanding of its Aetiopathogenesis, and a Novel Therapeutic Approach. PhD thesis, University of Nottingham, 2012.

iBIOS Institute of Biophotonics, Imaging and Optical Science
Applied Optics Group http://opticseee.nottingham.ac.uk
Nottingham Hearing Biomedical Research Unit

David.Jung@Nottingham.ac.uk

1 National Institute for Health Research (NIHR) Nottingham Hearing Biomedical Research Unit, 113 The Ropewalk Nottingham NG1 5DU, UK
2 Otology and Hearing group, Division of Clinical Neuroscience, School of Medicine, University of Nottingham, Nottingham, NG7 2UH, UK
3 Faculty of Engineering, University of Nottingham, University Park, University of Nottingham, NG7 2RD, UK
4 Department of Electronic and Information Engineering, The Hong Kong Polytechnic University, Hung Hom, Kowloon, Hong Kong

# Bibliography


[1] A. R. Moller, *Hearing: Anatomy, Physiology and Disorders of the Auditory System*. Burlington, MA, USA: Academic Press, 2006.

[2] A. Kavakli, M. Ogeturk, H. Yildirim, S. Karakas, T. Karlidag, and M. Sarsilmaz, "Volume assessment of age-related conversion of the tympanic cavity by helical computerized tomography scanning," *Saudi Medical Journal*, p. 4, 2004.

[3] H. Gray, *Anatomy of the Human Body*. Philadelphia: Lea & Febiger, 1918.

[4] B. Ars, *Chronic Otitis Media: Pathogenesis-Oriented Therapeutic Management*. The Hauge, NLD: Kugler Publications, 2008.

[5] S. Van der Jeught, J. J. Dirckx, J. R. Aerts, A. Bradu, A. Podoleanu, and J. Buytaert, "Full-field thickness distribution of human tympanic membrane obtained with optical coherence tomography," *Journal of the Association for Research in Otolaryngology*, pp. 1–12, 2013.

[6] H. Kubba, J. Pearson, and J. Birchall, "The aetiology of otitis media with effusion: a review," *Clinical Otolaryngology & Allied Sciences*, vol. 25, no. 3, pp. 181–194, 2000.

[7] M. Daniel, S. Imtiaz-Umer, N. Fergie, J. Birchall, and R. Bayston, "Bacterial involvement in otitis media with effusion," *International Journal of Pediatric Otorhinolaryngology*, vol. 76, no. 10, pp. 1416–1422, 2012.

[8] "Surgical management of otitis media with effusion in children," tech. rep., NICE, 2008. www.nice.org/cg60.

[9] M. Daniel, *Otitis Media with Effusion: Current Treatment, New Understanding of its Aetiopathogenesis, and a Novel Therapeutic Approach*. PhD thesis, University of Nottingham, 2012.

[10] M. Daniel, R. Chessman, S. Al-Zahid, B. Richards, C. Rahman, W. Ashraf, J. McLaren, H. Cox, O. Qutachi, H. Fortnum, N. Fergie, K. Shakesheff, J. P. Birchall, and R. R. Bayston,

"Biofilm eradication with biodegradable modified-release antibiotic pellets: A potential treatment for glue ear," *Archives of Otolaryngology-Head & Neck Surgery*, vol. 138, no. 10, pp. 942–949, 2012.

[11] H. Yaman, S. Yilmaz, N. Alkan, B. Subasi, E. Guclu, and O. Ozturk, "Shepard grommet tympanostomy tube complications in children with chronic otitis media with effusion," *European Archives of Oto-Rhino-Laryngology*, vol. 267, no. 8, pp. 1221–1224, 2010.

[12] T. Saito, E. Iwaki, Y. Kohno, T. Ohtsubo, I. Noda, S. Mori, T. Yamamoto, Y. Shibamori, and H. Saito, "Prevention of persistent ear drum perforation after long-term ventilation tube treatment for otitis media with effusion in children," *International Journal of Pediatric Otorhinolaryngology*, vol. 38, no. 1, pp. 31–39, 1996.

[13] N. Freemantle, E. L. Harvey, F. Wolf, J. M. Grimshaw, R. Grilli, and L. A. Bero, "Printed educational materials: effects on professional practice and health care outcomes," *Cochrane Database Syst Rev*, no. 2, p. CD000172, 2000.

[14] S. Keyhani, L. C. Kleinman, M. Rothschild, J. M. Bernstein, R. Anderson, and M. Chassin, "Overuse of tympanostomy tubes in new york metropolitan area: evidence from five hospital cohort," *BMJ*, vol. 337, 2008.

[15] P. Chandrasoma and C. Taylor, *Concise pathology*. Appleton & Lange, 1998.

[16] A. Kuruvilla, J. Li, P. Yeomans, P. Quelhas, N. Shaikh, A. Hoberman, and J. Kovacevic, "Otitis media vocabulary and grammar," in *Image Processing (ICIP), 2012 19th IEEE International Conference on*, pp. 2845–2848, 2012.

[17] P. Wormald and G. Browning, *Otoscopy: A Structured Approach*. Singular Publishing Group, 1996.

[18] D. J. Price, "Abc of ear, nose and throat," *The Journal of the Royal College of General Practitioners*, vol. 32, no. 241, pp. 507–507, 1982. J R Coll Gen Pract.

[19] Riester GmbH & Co. KG, P.O. Box 35, DE-72417 Jungingen, Germany, *Pocket instruments*, March 2007.

[20] W. Allyn, "Welch allyn digital macroview otoscope." Online. http://www.welchallyn.com/promotions/digitalmacroview/specs.htm, [Accessed: 18/09/2015].

[21] P. K. Harris, K. M. Hutchinson, and J. Moravec, "The use of tympanometry and pneumatic otoscopy for predicting middle ear disease," *Am J Audiol*, vol. 14, no. 1, pp. 3–13, 2005.

[22] H. Lindén, H. Teppo, and M. Revonta, "Spectral gradient acoustic reflectometry in the diagnosis of middle-ear fluid in children," *European Archives of Oto-Rhino-Laryngology*, vol. 264, no. 5, pp. 477–481, 2007.

[23] T. Venema, "Continuing education: Tympanometry," tech. rep., International Hearing Society, 2012.

[24] C. Vertan, D. Gheorghe, and B. Ionescu, "Eardrum color content analysis in video-otoscopy images for the diagnosis support of pediatric otitis," in *Signals, Circuits and Systems (ISSCS), 2011 10th International Symposium on*, pp. 1–4, 2011.

[25] I. Mironica, C. Vertan, and D. Gheorghe, "Automatic pediatric otitis detection by classification of global image features," in *E-Health and Bioengineering Conference (EHB), 2011*, pp. 1–4, 2011.

[26] A. Kuruvilla, N. Shaikh, A. Hoberman, and J. Kovačević, "Automated diagnosis of otitis media: Vocabulary and grammar," *International Journal of Biomedical Imaging*, vol. 2013, p. 15, 2013.

[27] L. Cheng, J. Liu, C. Roehm, and T. Valdez, "Enhanced video images for tympanic membrane characterization," in *Engineering in Medicine and Biology Society,EMBC, 2011 Annual International Conference of the IEEE*, pp. 4002–4005, 2011.

[28] A.-S. Shiao and Y.-C. Guo, "A comparison assessment of videotelescopy for diagnosis of pediatric otitis media with effusion," *International Journal of Pediatric Otorhinolaryngology*, vol. 69, no. 11, pp. 1497–1502, 2005.

[29] T. A. Valdez, N. Spegazzini, R. Pandey, K. Longo, C. Grindle, D. Peterson, and I. Barman, "Multi-color reflectance imaging of middle ear pathology in vivo," *Anal Bioanal Chem*, vol. 407, no. 12, pp. 3277–83, 2015.

[30] M. Sundberg, M. Peebo, Å. Öberg, P.-G. Lundquist, and T. Strömberg, "Diffuse reflectance spectroscopy of the human tympanic membrane in otitis media," *Physiological Measurement*, vol. 25, no. 6, pp. 1473–1483, 2004.

[31] M. Sundberg, *Optical Methods for Tympanic Membrane Characterisation : Towards Objective Otoscopy in Otitis Media*. PhD thesis, Linköping University, Biomedical Instrumentation, The Institute of Technology, 2008.

[32] L. Hall-Stoodley, F. Z. Hu, A. Gieseke, L. Nistico, D. Nguyen, J. Hayes, M. Forbes, D. P. Greenberg, B. Dice, A. Burrows, P. A. Wackym, P. Stoodley, J. C. Post, G. D. Ehrlich, and

J. E. Kerschner, "Direct detection of bacterial biofilms on the middle-ear mucosa of children with chronic otitis media," *JAMA*, vol. 296, no. 2, pp. 202–211, 2006.

[33] G. D. Ehrlich, R. Veeh, X. Wang, J. W. Costerton, J. D. Hayes, F. Z. Hu, B. J. Daigle, M. D. Ehrlich, and J. C. Post, "Mucosal biofilm formation on middle-ear mucosa in the chinchilla model of otitis media," *JAMA*, vol. 287, no. 13, pp. 1710–5, 2002.

[34] J. A. Werkhaven, L. Reinisch, M. Sorrell, J. Tribble, and R. H. Ossoff, "Noninvasive optical diagnosis of bacteria causing otitis media," *The Laryngoscope*, vol. 104, no. 3, pp. 264–268, 1994.

[35] B. C. Spector, L. Reinisch, D. Smith, and J. A. Werkhaven, "Noninvasive fluorescent identification of bacteria causing acute otitis media in a chinchilla model," *The Laryngoscope*, vol. 110, no. 7, pp. 1119–1123, 2000.

[36] T. A. Valdez, R. Pandey, N. Spegazzini, K. Longo, C. Roehm, R. R. Dasari, and I. Barman, "Multiwavelength fluorescence otoscope for video-rate chemical imaging of middle ear pathology," *Analytical Chemistry*, vol. 86, no. 20, pp. 10454–10460, 2014.

[37] N. Bedard, I. Tošić, L. Meng, A. Hoberman, J. Kovačević, and K. Berkner, "In vivo middle ear imaging with a light field otoscope," in *Optics in the Life Sciences*, p. BW3A.3, Optical Society of America, 2015.

[38] *A compact structured light based otoscope for three dimensional imaging of the tympanic membrane*, vol. 9303, 2015.

[39] M. d. S. Hernández-Montes, C. Furlong, J. J. Rosowski, N. Hulli, E. Harrington, J. T. Cheng, M. E. Ravicz, and F. M. Santoyo, "Optoelectronic holographic otoscope for measurement of nano-displacements in tympanic membranes," *Journal of biomedical optics*, vol. 14, no. 3, p. 034023, 2009.

[40] N.-H. Cho, U.-S. Jung, H.-I. Kwon, H.-S. Jeong, and J.-H. Kim, "Development of sd-oct for imaging the in vivo human tympanic membrane," *J. Opt. Soc. Korea*, vol. 15, pp. 74–77, Mar 2011.

[41] N. H. Cho, S. H. Lee, W. Jung, J. H. Jang, and J. Kim, "Optical coherence tomography for the diagnosis and evaluation of human otitis media," *J Korean Med Sci*, vol. 30, no. 3, pp. 328–35, 2015.

[42] G. L. Monroy, R. L. Shelton, R. M. Nolan, C. T. Nguyen, M. A. Novak, M. C. Hill, D. T. McCormick, and S. A. Boppart, "Noninvasive depth-resolved optical measurements of the tympanic membrane and middle ear for differentiating otitis media," *The Laryngoscope*, 2015.

[43] H. R. Djalilian, J. Ridgway, M. Tam, A. Sepehr, Z. Chen, and B. J. Wong, "Imaging the human tympanic membrane using optical coherence tomography in vivo," *Otology & neurotology : official publication of the American Otological Society, American Neurotology Society [and] European Academy of Otology and Neurotology*, vol. 29, no. 8, pp. 1091–1094, 2008.

[44] C. Pitris, K. Saunders, J. Fujimoto, and M. Brezinski, "High-resolution imaging of the middle ear with optical coherence tomography: A feasibility study," *Archives of Otolaryngology-Head & Neck Surgery*, vol. 127, no. 6, pp. 637–642, 2001.

[45] C. T. Nguyen, W. Jung, J. Kim, E. J. Chaney, M. Novak, C. N. Stewart, and S. A. Boppart, "Noninvasive in vivo optical detection of biofilm in the human middle ear," *Proceedings of the National Academy of Sciences*, 2012.

[46] S. Boppart, "Visualizing middle-ear biofilms in otitis media: a new benchmark for successful treatment," *ENT and Audiology News*, vol. 21, pp. 94–95, 2012.

[47] Z. Hubler, N. D. Shemonski, R. L. Shelton, G. L. Monroy, R. M. Nolan, and S. A. Boppart, "Real-time automated thickness measurement of the in vivo human tympanic membrane using optical coherence tomography," *Quantitative Imaging in Medicine and Surgery*, vol. 5, no. 1, 2015.

[48] M. E. Pawlowski, S. Shrestha, J. Park, B. E. Applegate, J. S. Oghalai, and T. S. Tkaczyk, "Miniature, minimally invasive, tunable endoscope for investigation of the middle ear," *Biomed. Opt. Express*, vol. 6, pp. 2246–2257, Jun 2015.

[49] R. Seth, C. M. Discolo, G. M. Palczewska, J. J. Lewandowski, and P. R. Krakovitz, "Ultrasound characterization of middle ear effusion," *American Journal of Otolaryngology*, vol. 34, no. 1, pp. 44–50, 2013.

[50] C. Discolo, M. Byrd, T. Bates, D. Hazony, J. Lewandowski, and P. J. Koltai, "Ultrasonic detection of middle ear effusion: A preliminary study," *Archives of Otolaryngology-Head & Neck Surgery*, vol. 130, no. 12, pp. 1407–1410, 2004.

[51] D. Abramson, A. Abramson, and D. Coleman, "Ultrasonics in otolaryngology: An aid in the diagnosis of middle ear fluid," *Archives of Otolaryngology*, vol. 96, no. 2, pp. 146–150, 1972.

[52] T. G. Landry, J. W. Rainsbury, R. B. Adamson, M. L. Bance, and J. A. Brown, "Real-time imaging of in-vitro human middle ear using high frequency ultrasound," *Hearing Research*, vol. 326, pp. 1–7, 2015.

[53] J. Song and K. Hynynen, "Accurate assessment of middle ear effusion by monitoring ultrasound reflections from a tympanic membrane," in *Ultrasonics Symposium (IUS), 2009 IEEE International*, pp. 193–195, Sept 2009.

[54] A. DeRowe, E. Ophir, S. Sade, G. Fishman, D. Ophir, M. Grankin, and A. Katzir, "Optical-fiber-coupled inferometric measurement of tympanic membrane temperature: a new diagnostic tool for acute otitis media," in *Lasers in Surgery: Advanced Characterization, Therapeutics, and Systems VIII*, vol. 3245 of *Society of Photo-Optical Instrumentation Engineers (SPIE) Conference Series*, pp. 227–233, Jul 1998.

[55] G. Fishman, A. DeRowe, E. Ophir, V. Scharf, A. Shabtai, D. Ophir, and A. Katzir, "Improved tympanic thermometer based on a fiber optic infrared radiometer and an otoscope and its use as a new diagnostic tool for acute otitis media," in *BiOS'99 International Biomedical Optics Symposium*, pp. 278–286, International Society for Optics and Photonics, 1999.

[56] E. Dvir, R. M. Kirberger, and A. G. Terblanche, "Magnetic resonance imaging of otitis media in a dog," *Vet Radiol Ultrasound*, vol. 41, no. 1, pp. 46–9, 2000.

[57] N. E. Love, R. W. Kramer, G. J. Spodnick, and D. E. Thrall, "Radiographic and computed tomographic evaluation of otitis media in the dog," *Veterinary Radiology & Ultrasound*, vol. 36, no. 5, pp. 375–379, 1995.

[58] R. N. Pittman, "Regulation of tissue oxygenation," in *Colloquium Series on Integrated Systems Physiology: From Molecule to Function*, vol. 3, pp. 1–100, Morgan & Claypool Life Sciences, 2011.

[59] "Understanding continous mixed venous oxygen saturation monitoring with the swan-ganz oximetry td system," *Edwards Lifesciences LLC*, vol. 2, no. 6, 2002.

[60] Q.-B. Li, X.-J. Sun, Y.-Z. Xu, L.-M. Yang, Y.-F. Zhang, S.-F. Weng, J.-S. Shi, and J.-G. Wu, "Diagnosis of gastric inflammation and malignancy in endoscopic biopsies based on fourier transform infrared spectroscopy," *Clinical Chemistry*, vol. 51, no. 2, pp. 346–350, 2005.

[61] V. K. Katukuri, J. Hargrove, S. J. Miller, K. Rahal, J. Y. Kao, R. Wolters, E. M. Zimmermann, and T. D. Wang, "Detection of colonic inflammation with fourier transform infrared spectroscopy using a flexible silver halide fiber," *Biomed. Opt. Express*, vol. 1, pp. 1014–1025, Oct 2010.

[62] R. A. Shaw, H. H. Mantsch, and J. E. Anderson, "Infrared spectroscopy of dystrophic mdx mouse muscle tissue distinguishes among treatment groups," *Journal of Applied Physiology*, vol. 81, no. 5, p. 2328, 1996.

[63] D. C. de Veld, M. Skurichina, M. J. Witjes, R. P. Duin, H. J. Sterenborg, and J. L. Roodenburg, "Autofluorescence and diffuse reflectance spectroscopy for oral oncology," *Lasers in Surgery and Medicine*, vol. 36, no. 5, pp. 356–364, 2005.

[64] V. D. Lernia, "Targeting the ifn-$\gamma$/cxcl10 pathway in lichen planus," *Medical Hypotheses*, vol. 92, pp. 60–61, 2016.

[65] K. Z. Liu, X. M. Xiang, A. Man, M. G. Sowa, A. Cholakis, E. Ghiabi, D. L. Singer, and D. A. Scott, "In vivo determination of multiple indices of periodontal inflammation by optical spectroscopy," *J Periodontal Res*, vol. 44, no. 1, pp. 117–24, 2009.

[66] H.-C. Wang, Y.-T. Chen, J.-T. Lin, C.-P. Chiang, and F.-H. Cheng, "Enhanced visualization of oral cavity for early inflamed tissue detection," *Opt. Express*, vol. 18, pp. 11800–11809, May 2010.

[67] H.-C. Wang and Y.-T. Chen, "Optimal lighting of rgb leds for oral cavity detection," *Opt. Express*, vol. 20, pp. 10186–10199, Apr 2012.

[68] C. Wang, J. Kim, C. T. Jin, P. H. Leong, and A. McEwan, "Near infrared spectroscopy in optical coherence tomography," *J. Near Infrared Spectrosc*, vol. 20, pp. 237–247, 2012.

[69] F. Leung, "Endoscopic reflectance spectrophotometry and visible light spectroscopy in clinical gastrointestinal studies," *Digestive Diseases and Sciences*, vol. 53, no. 6, pp. 1669–1677, 2008.

[70] H. Wang, G. Li, Z. Zhao, and L. Lin, "Non-invasive measurement of haemoglobin based on dynamic spectrum method," *Transactions of the Institute of Measurement and Control*, vol. 35, no. 1, pp. 16–24, 2013.

[71] T. O. McBride, B. W. Pogue, E. D. Gerety, S. B. Poplack, U. L. Osterberg, and K. D. Paulsen, "Spectroscopic diffuse optical tomography for the quantitative assessment of hemoglobin concentration and oxygen saturation in breast tissue," *Appl. Opt.*, vol. 38, pp. 5480–5490, Sep 1999.

[72] K.-Z. Liu, A. Cholakis, M. G. Sowa, and X. Xiang, *Diagnosis and Monitoring of Gingivitis in vivo Using Non-Invasive Technology-Infrared Spectroscopy*. INTECH Open Access Publisher, 2011.

[73] L. Persson, K. Svanberg, and S. Svanberg, "On the potential of human sinus cavity diagnostics using diode laser gas spectroscopy," *Applied Physics B*, vol. 82, no. 2, pp. 313–317, 2006.

[74] Q. J. Milner and G. R. Mathews, "An assessment of the accuracy of pulse oximeters," *Anaesthesia*, vol. 67, no. 4, pp. 396–401, 2012.

[75] J. E. Sinex, "Pulse oximetry: Principles and limitations," *The American Journal of Emergency Medicine*, vol. 17, no. 1, pp. 59 – 66, 1999.

[76] J. Das, A. Aggarwal, and N. K. Aggarwal, "Pulse oximeter accuracy and precision at five different sensor locations in infants and children with cyanotic heart disease," *Indian J Anaesth*, vol. 54, no. 6, pp. 531–4, 2010.

[77] J. W. Berkenbosch and J. D. Tobias, "Comparison of a new forehead reflectance pulse oximeter sensor with a conventional digit sensor in pediatric patients," *Respiratory Care*, vol. 51, no. 7, pp. 726–731, 2006.

[78] L. Schallom, C. Sona, M. McSweeney, and J. Mazuski, "Comparison of forehead and digit oximetry in surgical/trauma patients at risk for decreased peripheral perfusion," *Heart & Lung: The Journal of Acute and Critical Care*, vol. 36, no. 3, pp. 188–194, 2007.

[79] F. C. Setzer, S. H. Kataoka, F. Natrielli, E. Gondim-Junior, and C. L. Caldeira, "Clinical diagnosis of pulp inflammation based on pulp oxygenation rates measured by pulse oximetry," *J Endod*, vol. 38, no. 7, pp. 880–3, 2012.

[80] "Accuracy of noninvasive and continuous hemoglobin measurement by pulse co-oximetry," tech. rep., Masimo Corporation, 2010.

[81] Masimo, "Masimo - rainbow set pulse co-oximetry." Online. http://www.masimo.co.uk/rainbow/about.htm, [Accessed: 23/02/2016].

[82] S. H. Hardarson, A. Harris, R. A. Karlsson, G. H. Halldorsson, L. Kagemann, E. Rechtman, G. M. Zoega, T. Eysteinsson, J. A. Benediktsson, A. Thorsteinsson, P. K. Jensen, J. Beach, and E. Stefánsson, "Automatic retinal oximetry," *Investigative Ophthalmology & Visual Science*, vol. 47, no. 11, pp. 5011–5016, 2006.

[83] B. Shen, G. Z. Jr, T. L. Gramlich, N. Gladkova, P. Trolli, M. Kareta, C. P. Delaney, J. T. Connor, B. A. Lashner, C. L. Bevins, F. Feldchtein, F. H. Remzi, M. L. Bambrick, and V. W. Fazio, "In vivo colonoscopic optical coherence tomography for transmural inflammation

in inflammatory bowel disease," *Clinical Gastroenterology and Hepatology*, vol. 2, no. 12, pp. 1080–1087, 2004.

[84] R. Leitgeb, M. Wojtkowski, A. Kowalczyk, C. K. Hitzenberger, M. Sticker, and A. F. Fercher, "Spectral measurement of absorption by spectroscopic frequency-domain optical coherence tomography," *Opt. Lett.*, vol. 25, pp. 820–822, Jun 2000.

[85] O. Faix, *Methods in Lignin Chemistry*, ch. Fourier Transform Infrared Spectroscopy, pp. 83–109. Berlin, Heidelberg: Springer Berlin Heidelberg, 1992.

[86] L. Kagemann, G. Wollstein, M. Wojtkowski, H. Ishikawa, K. A. Townsend, M. L. Gabriele, V. J. Srinivasan, J. G. Fujimoto, and J. S. Schuman, "Spectral oximetry assessed with high-speed ultra-high-resolution optical coherence tomography," *J Biomed Opt*, vol. 12, no. 4, p. 041212, 2007.

[87] M. E. van Velthoven, D. J. Faber, F. D. Verbraak, T. G. van Leeuwen, and M. D. de Smet, "Recent developments in optical coherence tomography for imaging the retina," *Progress in Retinal and Eye Research*, vol. 26, no. 1, pp. 57–77, 2007.

[88] X. Liu and J. U. Kang, "Depth-resolved blood oxygen saturation assessment using spectroscopic common-path fourier domain optical coherence tomography," *IEEE Trans Biomed Eng*, vol. 57, no. 10, pp. 2572–5, 2010.

[89] D. J. Faber and T. G. van Leeuwen, "Are quantitative attenuation measurements of blood by optical coherence tomography feasible?," *Opt. Lett.*, vol. 34, pp. 1435–1437, May 2009.

[90] J. Yi and X. Li, "Estimation of oxygen saturation from erythrocytes by high-resolution spectroscopic optical coherence tomography," *Opt. Lett.*, vol. 35, pp. 2094–2096, Jun 2010.

[91] C. A. Lieber, S. K. Majumder, D. L. Ellis, D. D. Billheimer, and A. Mahadevan-Jansen, "In vivo nonmelanoma skin cancer diagnosis using raman microspectroscopy," *Lasers in surgery and medicine*, vol. 40, no. 7, pp. 461–467, 2008. Research Support, N.I.H., Extramural.

[92] D. A. Baab and P. Å. Öberg, "Laser doppler measurement of gingival blood flow in dogs with increasing and decreasing inflammation," *Archives of Oral Biology*, vol. 32, no. 8, pp. 551–555, 1987.

[93] A. G. Quinn, J. McLelland, T. Essex, and P. M. Farr, "Quantification of contact allergic inflammation: a comparison of existing methods with a scanning laser doppler velocimeter," *Acta Derm Venereol*, vol. 73, no. 1, pp. 21–5, 1993.

[94] C. Gleissner, O. Kempski, S. Peylo, J. H. Glatzel, and B. Willershausen, "Local gingival blood flow at healthy and inflamed sites measured by laser doppler flowmetry," *J Periodontol*, vol. 77, no. 10, pp. 1762–71, 2006.

[95] B. Yuan, S. A. Burgess, A. Iranmahboob, M. B. Bouchard, N. Lehrer, C. Bordier, and E. M. Hillman, "A system for high-resolution depth-resolved optical imaging of fluorescence and absorption contrast," *Rev Sci Instrum*, vol. 80, no. 4, p. 043706, 2009.

[96] D. A. Boas, D. H. Brooks, E. L. Miller, C. A. DiMarzio, M. Kilmer, R. J. Gaudette, and Q. Zhang, "Imaging the body with diffuse optical tomography," *Signal Processing Magazine, IEEE*, vol. 18, no. 6, pp. 57–75, 2001.

[97] Y. L. Kim, Y. Liu, V. M. Turzhitsky, R. K. Wali, H. K. Roy, and V. Backman, "Depth-resolved low-coherence enhanced backscattering," *Opt. Lett.*, vol. 30, pp. 741–743, Apr 2005.

[98] Y. L. Kim, V. M. Turzhitsky, Y. Liu, H. K. Roy, R. K. Wali, H. Subramanian, P. Pradhan, and V. Backman, "Low-coherence enhanced backscattering: review of principles and applications for colon cancer screening," *J Biomed Opt*, vol. 11, no. 4, p. 041125, 2006.

[99] V. Ntziachristos, "Going deeper than microscopy: the optical imaging frontier in biology," *Nat Meth*, vol. 7, no. 8, pp. 603–614, 2010.

[100] K. B. Dunbar and M. I. Canto, "Confocal endomicroscopy," *Techniques in Gastrointestinal Endoscopy*, vol. 12, no. 2, pp. 90–99, 2010.

[101] J. Shah, S. Park, S. Aglyamov, T. Larson, L. Ma, K. Sokolov, K. Johnston, T. Milner, and S. Y. Emelianov, "Photoacoustic imaging and temperature measurement for photothermal cancer therapy," *J Biomed Opt*, vol. 13, no. 3, p. 034024, 2008.

[102] L. V. Wang and S. Hu, "Photoacoustic tomography: in vivo imaging from organelles to organs," *Science*, vol. 335, no. 6075, pp. 1458–62, 2012.

[103] E. Z. Zhang, B. Povazay, J. Laufer, A. Alex, B. Hofer, B. Pedley, C. Glittenberg, B. Treeby, B. Cox, P. Beard, and W. Drexler, "Multimodal photoacoustic and optical coherence tomography scanner using an all optical detection scheme for 3d morphological skin imaging," *Biomed Opt Express*, vol. 2, no. 8, pp. 2202–15, 2011.

[104] G. Rousseau, A. Blouin, and J.-P. Monchalin, "Non-contact photoacoustic tomography and ultrasonography for tissue imaging," *Biomed. Opt. Express*, vol. 3, pp. 16–25, Jan 2012.

[105] Y. Wang, C. Li, and R. K. Wang, "Noncontact photoacoustic imaging achieved by using a low-coherence interferometer as the acoustic detector," *Opt. Lett.*, vol. 36, pp. 3975–3977, Oct 2011.

[106] J. Selb, S. Lévêque-Fort, L. Pottier, and A. C. Boccara, "3d acousto-optic modulated-speckle imaging in biological tissues," *Comptes Rendus de l'Académie des Sciences-Series IV-Physics*, vol. 2, no. 8, pp. 1213–1225, 2001.

[107] K. R. Mathura, K. C. Vollebregt, K. Boer, J. C. De Graaff, D. T. Ubbink, and C. Ince, "Comparison of ops imaging and conventional capillary microscopy to study the human microcirculation," *Journal of Applied Physiology*, vol. 91, no. 1, pp. 74–78, 2001.

[108] W. Groner, J. W. Winkelman, A. G. Harris, C. Ince, G. J. Bouma, K. Messmer, and R. G. Nadeau, "Orthogonal polarization spectral imaging: A new method for study of the microcirculation," *Nat Med*, vol. 5, no. 10, pp. 1209–1212, 1999.

[109] C. M. Treu, O. Lupi, D. A. Bottino, and E. Bouskela, "Sidestream dark field imaging: the evolution of real-time visualization of cutaneous microcirculation and its potential application in dermatology," *Arch Dermatol Res*, vol. 303, no. 2, pp. 69–78, 2011.

[110] P. T. Goedhart, M. Khalilzada, R. Bezemer, J. Merza, and C. Ince, "Sidestream dark field (sdf) imaging: a novel stroboscopic led ring-based imaging modality for clinical assessment of the microcirculation," *Opt. Express*, vol. 15, pp. 15101–15114, Nov 2007.

[111] I. Itzkan, L. Qiu, H. Fang, M. M. Zaman, E. Vitkin, I. C. Ghiran, S. Salahuddin, M. Modell, C. Andersson, L. M. Kimerer, P. B. Cipolloni, K.-H. Lim, S. D. Freedman, I. Bigio, B. P. Sachs, E. B. Hanlon, and L. T. Perelman, "Confocal light absorption and scattering spectroscopic microscopy monitors organelles in live cells with no exogenous labels," *Proceedings of the National Academy of Sciences*, vol. 104, no. 44, pp. 17255–17260, 2007.

[112] F. Reinholz, R. A. Ashman, and R. H. Eikelboom, "Simultaneous three wavelength imaging with a scanning laser ophthalmoscope," *Cytometry*, vol. 37, no. 3, pp. 165–170, 1999.

[113] T. Hanioka, S. Shizukuishi, and A. Tsunemitsu, "Hemoglobin concentration and oxygen saturation of clinically healthy and inflamed gingiva in human subjects," *J Periodontal Res*, vol. 25, no. 2, pp. 93–8, 1990.

[114] G. Lohmann, S. Bohn, K. MÃ$\frac{1}{4}$ller, R. Trampel, and R. Turner, "Image restoration and spatial resolution in 7-tesla magnetic resonance imaging," *Magnetic Resonance in Medicine*, vol. 64, no. 1, pp. 15–22, 2010.

[115] A. Goel and et al., "High resolution ct — radiology reference article — radiopaedia.org." Online. http://radiopaedia.org/articles/high-resolution-ct, [Accessed: 31/03/2016].

[116] A. G. Quinn, J. McLelland, T. Essex, and P. M. Farr, "Measurement of cutaneous inflammatory reactions using a scanning laser-doppler velocimeter," *Br J Dermatol*, vol. 125, no. 1, pp. 30–7, 1991.

[117] W. Xia, D. Piras, J. C. G. van Hespen, S. van Veldhoven, C. Prins, T. G. van Leeuwen, W. Steenbergen, and S. Manohar, "An optimized ultrasound detector for photoacoustic breast tomography," *Medical Physics*, vol. 40, no. 3, p. 032901, 2013.

[118] A. Ar, P. Herman, E. Lecain, M. Wassef, P. T. B. Huy, and R. E. Kania, "Middle ear gas loss in inflammatory conditions: The role of mucosa thickness and blood flow," *Respiratory Physiology & Neurobiology*, vol. 155, no. 2, pp. 167–176, 2007.

[119] A. Florea, J. E. Zwart, C. W. Lee, A. Depew, S. K. Park, J. Inman, R. Wareham, K. Johnson, E. John, G. M. Wall, and T. Jung, "Effect of topical dexamethasone versus rimexolone on middle ear inflammation in experimental otitis media with effusion," *Acta Otolaryngol*, vol. 126, no. 9, pp. 910–5, 2006.

[120] P. Borissova, S. Valcheva, and A. Belcheva, "Antiinflammatory effect of flavonoids in the natural juice from aronia melanocarpa, rutin and rutin-magnesium complex on an experimental model of inflammation induced by histamine and serotonin," *Acta physiologica et pharmacologica Bulgarica*, vol. 20, no. 1, pp. 25–30, 1994.

[121] O. Holm, E. Lindell, and L. Malm, "Colour change in the human histamine wheal made visible by lyyn: a technique to enhance colour differences," *Skin Research and Technology*, vol. 16, no. 4, pp. 385–389, 2010.

[122] I. Nishidate, N. Tanaka, T. Kawase, T. Maeda, T. Yuasa, Y. Aizu, T. Yuasa, and K. Niizeki, "Noninvasive imaging of human skin hemodynamics using a digital red-green-blue camera," *Journal of Biomedical Optics*, vol. 16, no. 8, pp. 086012–086012–14, 2011.

[123] R. Long, T. King, T. Akl, M. N. Ericson, M. Wilson, G. L. Coté, and M. J. McShane, "Optofluidic phantom mimicking optical properties of porcine livers," *Biomed. Opt. Express*, vol. 2, pp. 1877–1892, Jul 2011.

[124] V. V. Tuchin and V. Tuchin, *Tissue optics: light scattering methods and instruments for medical diagnosis*, vol. 13. SPIE press Bellingham, 2007.

[125] J. Crowe and D. Morris, "Biomedical optics." Lecture Notes, Feb 2012.

[126] E. M. Hillman, "Optical brain imaging in vivo: techniques and applications from animal to man," *J Biomed Opt*, vol. 12, no. 5, p. 051402, 2007.

[127] S. L. Jacques and J. C. Ramella-Roman, "Polarized light imaging of tissues," in *Lasers and Current Optical Techniques in Biology* (P. R. Palumbo G, ed.), vol. 4 of *Comprehensive series in photochemistry and photobiology*, ch. 19, pp. 592–607, The Royal Society of Chemistry, 2004.

[128] S. L. Jacques, "Probing nanoscale tissue structure using light scattering," in *Optics in the Life Sciences*, p. NW3C.2, Optical Society of America, 2015.

[129] A. Kienle, F. K. Forster, and R. Hibst, "Anisotropy of light propagation in biological tissue," *Opt. Lett.*, vol. 29, pp. 2617–2619, Nov 2004.

[130] C. F. Bohren and D. R. Huffman, *Absorption and Scattering of Light by Small Particles*. Wiley-VCH Verlag GmbH, 2007.

[131] I. S. Saidi, S. L. Jacques, and F. K. Tittel, "Mie and rayleigh modeling of visible-light scattering in neonatal skin," *Appl. Opt.*, vol. 34, pp. 7410–7418, Nov 1995.

[132] J. F. N. Júnior, M. J. B. Martins, C. V. Aguiar, and A. I. Pinheiro, "Fully endoscopic stapes surgery (stapedotomy): technique and preliminary results," *Brazilian Journal of Otorhinolaryngology*, vol. 77, pp. 721–727, Dec 2011.

[133] J. L. Sandell and T. C. Zhu, "A review of in-vivo optical properties of human tissues and its impact on pdt," *Journal of Biophotonics*, vol. 4, no. 11-12, pp. 773–787, 2011.

[134] A. N. Bashkatov, E. A. Genina, V. I. Kochubey, V. Rubtsov, E. A. Kolesnikova, and V. V. Tuchin, "Optical properties of human colon tissues in the 355-2500 nm spectral range," *Quantum Electronics*, vol. 44, no. 8, pp. 779–784, 2014.

[135] A. Bashkatov, É. Genina, V. Kochubey, V. Tuchin, E. Chikina, A. Knyazev, and O. Mareev, "Optical properties of mucous membrane in the spectral range 350-2000 nm," *Optics and Spectroscopy*, vol. 97, no. 6, pp. 978–983, 2004.

[136] A. N. Bashkatov, E. A. Genina, V. I. Kochubey, and V. V. Tuchin, "Optical properties of human skin, subcutaneous and mucous tissues in the wavelength range from 400 to 2000 nm," *Journal of Physics D: Applied Physics*, vol. 38, no. 15, p. 2543, 2005.

[137] A. N. Bashkatov, E. A. Genina, V. I. Kochubey, A. A. Gavrilova, S. V. Kapralov, V. A. Grishaev, and V. V. Tuchin, "Optical properties of human stomach mucosa in the spectral

range from 400 to 2000 nm prognosis for gastroenterology," *Medical Laser Application*, vol. 22, no. 2, pp. 95–104, 2007.

[138] G. Zonios, L. T. Perelman, V. Backman, R. Manoharan, M. Fitzmaurice, J. Van Dam, and M. S. Feld, "Diffuse reflectance spectroscopy of human adenomatous colon polyps in vivo," *Appl. Opt.*, vol. 38, no. 31, pp. 6628–37, 1999.

[139] D. Hidovic-Rowe and E. Claridge, "Modelling and validation of spectral reflectance for the colon," *Phys Med Biol*, vol. 50, no. 6, pp. 1071–93, 2005.

[140] R. K. Shah, B. Nemati, L. V. Wang, and S. M. Shapshay, "Optical-thermal simulation of tonsillar tissue irradiation," *Lasers in Surgery and Medicine*, vol. 28, no. 4, pp. 313–319, 2001.

[141] H. J. Wei, D. Xing, J. J. Lu, H. M. Gu, G. Y. Wu, and Y. Jin, "Determination of optical properties of normal and adenomatous human colon tissues in vitro using integrating sphere techniques," *World . Gastroenterol*, vol. 11, no. 16, pp. 2413–9, 2005.

[142] A. L. Clark, A. Gillenwater, R. Alizadeh-Naderi, A. K. El-Naggar, and R. Richards-Kortum, "Detection and diagnosis of oral neoplasia with an optical coherence microscope," *J. Biomed. Opt.*, vol. 9, no. 6, pp. 1271–80, 2004.

[143] H. W. Wang, T. C. Zhu, M. E. Putt, M. Solonenko, J. Metz, A. Dimofte, J. Miles, D. L. Fraker, E. Glatstein, S. M. Hahn, and A. G. Yodh, "Broadband reflectance measurements of light penetration, blood oxygenation, hemoglobin concentration, and drug concentration in human intraperitoneal tissues before and after photodynamic therapy," *J Biomed Opt*, vol. 10, no. 1, p. 14004, 2005.

[144] A. N. Bashkatov, E. A. Genina, and V. V. Tuchin, "Optical properties of skin, subcutaneous, and muscle tissues: A review," *Journal of Innovative Optical Health Sciences*, vol. 04, no. 01, pp. 9–38, 2011.

[145] A. Amelink, O. Kaspers, H. Sterenborg, J. van der Wal, J. Roodenburg, and M. Witjes, "Non-invasive measurement of the morphology and physiology of oral mucosa by use of optical spectroscopy," *Oral Oncology*, vol. 44, no. 1, pp. 65–71, 2008.

[146] R. Matanda, P. Van De Heyning, J. Bogers, and B. Ars, "Behaviour of middle ear cleft mucosa during inflammation: Histo- morphometric study," *Acta Oto-laryngologica*, vol. 126, no. 9, pp. 905–909, 2006.

[147] M. Sambongi, M. Igarashi, T. Obi, M. Yamaguchi, N. Oyama, M. Kobayashi, Y. Sano, S. Yoshida, and K. Gono, "Analysis of spectral reflectance of mucous membrane for endoscopic diagnosis," in *Engineering in Medicine and Biology Society, 2000. Proceedings of the 22nd Annual International Conference of the IEEE*, vol. 2, pp. 1026–1029, 2000.

[148] M. Sambongi, M. Igarashi, T. Obi, M. Yamaguchi, N. Ohyama, M. Kobayashi, Y. Sano, S. Yoshida, and K. Gono, "Analysis of spectral reflectance using normalization method from endoscopic spectroscopy system," *Optical Review*, vol. 9, no. 6, pp. 238–243, 2002.

[149] J. L. Jayanthi, G. U. Nisha, S. Manju, E. K. Philip, P. Jeemon, K. V. Baiju, V. T. Beena, and N. Subhash, "Diffuse reflectance spectroscopy: diagnostic accuracy of a non-invasive screening technique for early detection of malignant changes in the oral cavity," *BMJ Open*, vol. 1, no. 1, 2011.

[150] D. Hidović-Rowea, E. Claridgea, T. Ismailb, and P. Taniereb, "Analysis of multispectral images of the colon to reveal histological changes characteristic of cancer," *Medical Image Understanding Analysis MIUA*, vol. 1, pp. 66–70, 2006.

[151] A. Sakudo, K. Baba, and K. Ikuta, "Analysis of vis-nir spectra changes to measure the inflammatory response in the nasal mucosal region of influenza a and b virus-infected patients," *Journal of Clinical Virology*, vol. 55, no. 4, pp. 334–338, 2012.

[152] Y. Liu, R. E. Brand, V. Turzhitsky, Y. L. Kim, H. K. Roy, N. Hasabou, C. Sturgis, D. Shah, C. Hall, and V. Backman, "Optical markers in duodenal mucosa predict the presence of pancreatic cancer," *Clinical Cancer Research*, vol. 13, no. 15, pp. 4392–4399, 2007.

[153] D. Hidovic-Rowe and E. Claridge, "Model-based recovery of histological parameters from multispectral images of the colon," vol. 5745, pp. 127–137, 2005.

[154] K. C. Su, F. W. Leung, and P. H. Guth, "Assessment of mucosal hemodynamics in normal human colon and patients with inflammatory bowel disease," *Gastrointest Endosc*, vol. 35, no. 1, pp. 22–7, 1989.

[155] M. Tsujij, S. Kawano, S. Tsuji, I. Kobayashi, Y. Takei, K. Nagano, H. Fusamoto, T. Kamada, T. Ogihara, and N. Sato, "Colonic mucosal hemodynamics and tissue oxygenation in patients with ulcerative colitis: Investigation by organ reflectance spectrophotometry," *Journal of Gastroenterology*, vol. 30, no. 2, pp. 183–188, 1995.

[156] S. Prahl, "Optical absorption of hemoglobin." Online, 1999. http://omlc.org/spectra/hemoglobin/index.html, [Accessed: 16/01/2015].

[157] S. A. Lisenko and M. M. Kugeiko, "Online determination of biophysical parameters of mucous membranes of a human body," *Quantum Electronics*, vol. 43, no. 7, p. 683, 2013.

[158] D. Yudovsky and L. Pilon, "Rapid and accurate estimation of blood saturation, melanin content, and epidermis thickness from spectral diffuse reflectance," *Appl Opt*, vol. 49, no. 10, pp. 1707–19, 2010.

[159] S. Prahl, "Mie scattering calculator." Online, 1999. http://omlc.org/calc/mie_calc.html, [Accessed: 16/01/2015].

[160] K. Markowicz, "Matlab code for mie scattering on spheres." Online, 2005. http://scatterlib.googlecode.com/files/bhmie-matlab.zip, [Accessed: 16/01/2015].

[161] S. Prahl, "Mie theory model for tissue optical properties." Online, 1998. http://omlc.org/education/ece532/class3/mie.html, [Accessed: 16/01/2015].

[162] K. F. Palmer and D. Williams, "Optical properties of water in the near infrared," *J. Opt. Soc. Am.*, vol. 64, pp. 1107–1110, Aug 1974.

[163] M. Doladov, V. Kazakevich, I. Kalashnikov, V. Kupaeva, and V. Shcherbakov, "Optical reflection spectrum of the human tympanic membrane," *Journal of Applied Spectroscopy*, vol. 68, no. 4, pp. 708–710, 2001.

[164] D. MacDougall, J. Rainsbury, J. Brown, M. Bance, and R. Adamson, "Optical coherence tomography system requirements for clinical diagnostic middle ear imaging," *J Biomed Opt*, vol. 20, no. 5, p. 56008, 2015.

[165] H.-J. Foth, S. Färber, A. Gauer, and R. Wagner, "Thermal damage threshold at 633 nm of tympanic membrane of pig," *Hearing Research*, vol. 142, no. 1-2, pp. 71–78, 2000.

[166] G. Alzbutiene, A. Hermansson, P. Caye-Thomasen, and V. Kinduris, "Tympanic membrane changes in experimental acute otitis media and myringotomy," *Medicina (Kaunas)*, vol. 44, no. 4, pp. 313–21, 2008.

[167] G. Volandri, F. D. Puccio, P. Forte, and C. Carmignani, "Biomechanics of the tympanic membrane," *Journal of Biomechanics*, vol. 44, no. 7, pp. 1219–1236, 2011.

[168] E. R. Rasmussen, P. L. Larsen, K. Andersen, M. Larsen, K. Qvortrup, and H. P. Hougen, "Petechial hemorrhages of the tympanic membrane in attempted suicide by hanging: A case report," *Journal of Forensic and Legal Medicine*, vol. 20, no. 2, pp. 119–121, 2013.

[169] S. Merchant and J. Nadol, *Schuknecht's Pathology of the Ear*. Pmph USA Ltd Series, People's Medical Publishing House-USA, 2010.

[170] J. Fay, S. Puria, W. F. Decraemer, and C. Steele, "Three approaches for estimating the elastic modulus of the tympanic membrane," *Journal of biomechanics*, vol. 38, no. 9, pp. 1807–1815, 2005.

[171] C. Rutledge, M. Thyden, C. Furlong, J. Rosowski, and J. Cheng, "Mapping the histology of the human tympanic membrane by spatial domain optical coherence tomography," in *MEMS and Nanotechnology, Volume 6* (G. A. Shaw, B. C. Prorok, and L. A. Starman, eds.), Conference Proceedings of the Society for Experimental Mechanics Series, pp. 125–129, Springer New York, 2013.

[172] A. Sanli, S. Aydin, and R. Ozturk, "Microscopic guide to the middle ear anatomy in guinea pigs," *Kulak Burun Bogaz Ihtis Derg*, vol. 19, no. 2, pp. 87–94, 2009.

[173] W. R. Funnell and C. A. Laszlo, "A critical review of experimental observations on ear-drum structure and function," *ORL J Otorhinolaryngol Relat Spec*, vol. 44, no. 4, pp. 181–205, 1982.

[174] Y. Uno, "The attachment structure of the guinea pig tympanic membrane," *Auris Nasus Larynx*, vol. 27, no. 1, pp. 45–50, 2000.

[175] F. T. Kayhan and Z. Algun, "A histologic study on the temporal bone of guinea pigs," *Kulak Burun Bogaz Ihtis Derg*, vol. 10, no. 2, pp. 51–7, 2003.

[176] L. C. Kuypers, J. J. Dirckx, W. F. Decraemer, and J.-P. Timmermans, "Thickness of the gerbil tympanic membrane measured with confocal microscopy," *Hearing research*, vol. 209, no. 1, pp. 42–52, 2005.

[177] M. Von Unge, J. A. Buytaert, and J. J. Dirckx, "Anatomical boundary of the tympanic membrane pars flaccida of the meriones unguiculatus (mongolian gerbil)," *Anat Rec (Hoboken)*, vol. 294, no. 6, pp. 987–95, 2011.

[178] M. von Unge, W. F. Decraemer, J. J. Dirckx, and D. Bagger-Sjoback, "Shape and displacement patterns of the gerbil tympanic membrane in experimental otitis media with effusion," *Hear Res*, vol. 82, no. 2, pp. 184–96, 1995.

[179] J. P. Tuck-Lee, P. M. Pinsky, C. R. Steele, and S. Puria, "Finite element modeling of acousto-mechanical coupling in the cat middle ear," *J Acoust Soc Am*, vol. 124, no. 1, pp. 348–62, 2008.

[180] H. B. Soares and L. Lavinsky, "Histology of sheep temporal bone," *Braz J Otorhinolaryngol*, vol. 77, no. 3, pp. 285–92, 2011.

[181] G. Park, T. S. Aum, J. H. Kwon, J. H. Park, B. K. Kim, and J. K. Shin, "Characterization and modeling light scattering in diffuser sheets," *Journal of Korean Physical Society*, vol. 54, p. 44, Jan. 2009.

[182] Thorlabs, "Unmounted n-bk7 ground glass diffusers." Online. http://www.thorlabs.de/newgrouppage9.cfm?objectgroup_id=1132, [Accessed: 24/09/2015].

[183] B. W. Pogue and M. S. Patterson, "Review of tissue simulating phantoms for optical spectroscopy, imaging and dosimetry," *J Biomed Opt*, vol. 11, no. 4, p. 041102, 2006.

[184] M. Firbank, M. Oda, and D. T. Delpy, "An improved design for a stable and reproducible phantom material for use in near-infrared spectroscopy and imaging," *Physics in Medicine and Biology*, vol. 40, no. 5, p. 955, 1995.

[185] M. Firbank and D. T. Delpy, "A design for a stable and reproducible phantom for use in near infra-red imaging and spectroscopy," *Physics in Medicine and Biology*, vol. 38, no. 6, p. 847, 1993.

[186] A. McNaughtion, "Measuring surface roughness using confocal microscopy and imagej (or fiji variant)." Online, 2012. http://occm.otago.ac.nz/resources/Surface-Roughness-Ra-Using-Confocal.pdf, [Accessed: 08/09/2015].

[187] Biomedical Imaging Group, École Polytechnique Fédérale de Lausanne, "Extended depth of field." Online, 2011. http://bigwww.epfl.ch/demo/edf/index.html, [Accessed: 08/09/2015].

[188] B. Forster, D. Van De Ville, J. Berent, D. Sage, and M. Unser, "Complex wavelets for extended depth-of-field: A new method for the fusion of multichannel microscopy images," *Microscopy Research and Technique*, vol. 65, pp. 33–42, September 2004.

[189] GCH, "Gcsca." Online, 2009. http://www.gcsca.net/IJ/SurfCharJ.html, [Accessed: 08/09/2015].

[190] G. Chinga, P. O. Johnsen, R. Dougherty, E. L. Berli, and J. Walter, "Quantification of the 3d microstructure of sc surfaces," *Journal of Microscopy*, vol. 227, no. 3, pp. 254–265, 2007.

[191] J. Laufer, E. Zhang, and P. Beard, "Selected topics in quantum electronics, ieee journal of," *Evaluation of Absorbing Chromophores Used in Tissue Phantoms for Quantitative Photoacoustic Spectroscopy and Imaging*, vol. 16, pp. 600–607, May 2010.

[192] Pace Technologies, "Abrasive grinding paper." Online. http://www.metallographic.com/Brochures/SiCpaper.pdf, [Accessed: 04/04/2016].

[193] M. A. Nyc, S. G. Kim, A. Kapoor, and T. Jung, "Measuring thickness of middle ear mucosa using mri and ct imaging versus histopathology," *International Journal of Otolaryngology*, vol. 2012, 2012.

[194] J.-A. Conchello and J. W. Lichtman, "Optical sectioning microscopy," *Nat Meth*, vol. 2, no. 12, pp. 920–931, 2005.

[195] R. H. Webb, "Confocal optical microscopy," *Reports on Progress in Physics*, vol. 59, no. 3, p. 427, 1996.

[196] K. R. Spring, T. J. Fellers, and M. W. Davidson, "Theory of confocal microscopy, signal-to-noise considerations." Online. http://www.olympusconfocal.com/theory/signaltonoise.html, [Accessed: 22/09/2015].

[197] L. Stender, "Confocal laser scanning microscopy," tech. rep., Carl Zeiss Advanced Imaging Microscopy, 07740 Jena, Germany, 12 2008.

[198] L. Arend, "Luminance contrast." Online. https://colorusage.arc.nasa.gov/luminance_cont.php, [Accessed: 19/10/2016].

[199] V. V. Belov and B. D. Borisov, "T-effect and shower curtain effect," in *Selected Research Paper on Wave Propagation in the Atmosphere and Adaptive Optics*, pp. 8–16, International Society for Optics and Photonics, 2000.

[200] A. E. Elsner, S. A. Burns, J. J. Weiter, and F. C. Delori, "Infrared imaging of sub-retinal structures in the human ocular fundus," *Vision Research*, vol. 36, no. 1, pp. 191–205, 1996.

[201] A. E. Elsner, S. A. Burns, G. W. Hughes, and R. H. Webb, "Reflectometry with a scanning laser ophthalmoscope," *Appl Opt*, vol. 31, no. 19, pp. 3697–710, 1992.

[202] M. Smith, L. Hillman, K. Denninghoff, and R. Chipman, "Optical scanning spectroscopic apparatus and associated method," Jun 2001. US Patent 6,244,712.

[203] M. Smith, A. Lompado, K. Denninghoff, and L. Hillman, "Method and apparatus for measuring blood oxygen saturation in a retinal vessel by separately detecting single pass optical signals," Dec 2002.

[204] L. Wang and S. Jaques, *Monte Carlo Modeling Of Light Transport in Multi-layered Tissues in Standard C*. University of Texas M. D. Anderson Cancer Center, 1992.

[205] S. A. Prahl, M. Keijzer, S. L. Jacques, and A. J. Welch, "A monte carlo model of light propagation in tissue," in *SPIE Proceedings of Dosimetry of Laser Radiation in Medicine and Biology*, pp. 102–111, Press, 1989.

[206] L. Wang and S. L. Jacques, "Mcml source code in ascii." Online. http://omlc.org/software/mc/mcml-src/index.html, [Accessed 16/07/2014].

[207] E. Alerstam, S. Andersson-Engels, and T. Svensson, "White monte carlo for time-resolved photon migration," *Journal of Biomedical Optics*, vol. 13, no. 4, pp. 041304–041304–10, 2008.

[208] Q. Liu and N. Ramanujam, "Scaling method for fast monte carlo simulation of diffuse reflectance spectra from multilayered turbid media," *J. Opt. Soc. Am. A*, vol. 24, pp. 1011–1025, Apr 2007.

[209] R. Graaff, M. H. Koelink, F. F. M. de Mul, W. G. Zijlstra, A. C. M. Dassel, and J. G. Aarnoudse, "Condensed monte carlo simulations for the description of light transport," *Appl. Opt.*, vol. 32, pp. 426–434, Feb 1993.

[210] A. K. Dunn, C. Smithpeter, A. J. Welch, and R. Richards-Kortum, "Sources of contrast in confocal reflectance imaging," *Appl. Opt.*, vol. 35, pp. 3441–3446, Jul 1996.

[211] B. Yang, K. Chao, and J. Tsai, "Modeling of micro cat's eye retroreflectors using a matrix-based three-dimensional ray tracing technique," *Appl. Opt.*, vol. 51, pp. 6020–6030, Sep 2012.

[212] A. Nussbaum, "Modernizing the teaching of advanced geometric optics," vol. 1603, pp. 389–400, 1992.

[213] A. E. Feiguin, "Monte carlo error analysis." Online, Aug. 2012. http://www.northeastern.edu/afeiguin/phys5870/phys5870/node71.html, [Accessed: 25/10/2016].

[214] J. M. Beach, K. J. Schwenzer, S. Srinivas, D. Kim, and J. S. Tiedeman, "Oximetry of retinal vessels by dual-wavelength imaging: calibration and influence of pigmentation," *Journal of Applied Physiology*, vol. 86, no. 2, pp. 748–758, 1999.

[215] D. Myers, M. McGraw, M. George, K. Mulier, and G. Beilman, "Tissue hemoglobin index: a non-invasive optical measure of total tissue hemoglobin," *Crit Care*, vol. 13 Suppl 5, p. S2, 2009.

[216] G. Cicco, D. F. Bruley, and M. Ferrari, *Oxygen Transport to Tissue XXVII*, vol. 578. Springer Science & Business Media, 2006.

[217] N. Yoshizawa, Y. Ueda, H. Nasu, H. Ogura, E. Ohmae, K. Yoshimoto, Y. Takehara, Y. Yamashita, and H. Sakahara, "Effect of the chest wall on the measurement of hemoglobin concentrations by near-infrared time-resolved spectroscopy in normal breast and cancer," *Breast Cancer*, pp. 1–7, 2015.

[218] J. Laufer, D. Delpy, C. Elwell, and P. Beard, "Quantitative spatially resolved measurement of tissue chromophore concentrations using photoacoustic spectroscopy: application to the measurement of blood oxygenation and haemoglobin concentration," *Physics in Medicine and Biology*, vol. 52, no. 1, p. 141, 2007.

[219] G. Kumar and J. M. Schmitt, "Optimum wavelengths for measurement of blood hemoglobin content and tissue hydration by nir spectrophotometry," vol. 2678, pp. 442–453, 1996.

[220] H. Takiwaki, "Measurement of skin color: practical application and theoretical considerations," *J Med Invest*, vol. 44, no. 3-4, pp. 121–6, 1998.

[221] J. Ruckman, *A Comparative Study of Total Hemoglobin Measurement Technology: Noninvasive Pulse Co-oximetry and Conventional Methods.* University of Connecticut, 2011.

[222] J. J. Carr and J. M. Brown, "Sensor terminology - national instruments." Online, Sept. 2013. http://www.ni.com/white-paper/14860/en/, [Accessed: 19/10/2016].

[223] A. Lisk, *WS-1 Reflectance Standard Operating Instructions.* Ocean Optics, 830 Douglas Ave., Dunedin, FL 34698, USA, 07 2011.

[224] J. P. Landry, "Optical oblique-incidence reflectivity difference microscopy: Application to label-free detection of reactions in biomolecular microarrays," 2008.

[225] R. Paschotta, "Encyclopedia of laser physics and technology - gaussian beams, laser beam, fundamental transverse modes." Online. https://www.rp-photonics.com/gaussian_beams.html, [Accessed: 21/03/2016].

[226] Andor.com, "Ccd sensor architectures - architectures commonly used for high performance cameras." Online. http://www.andor.com/learning-academy/ccd-sensor-architectures-architectures-commonly-used-for-high-performance-cameras, [Accessed: 24/05/2016].

[227] J. Bancroft and H. Cook, *Manual of histological techniques and their diagnostic application.* Churchill Livingstone, 1994.

[228] Thorlabs, "Resolution test targets, test targets, calibration targets, and reticles." Online. http://www.thorlabs.de/newgrouppage9.cfm?objectgroup_id=4338, [Accessed: 07/12/2015].

[229] Encyclopædia Britannica Online, "Histamine." Online, 5 2015. http://www.britannica.com/science/histamine, [Accessed: 17/09/2015].

[230] Mayo Foundation for Medical Education and Research, "Allergy skin tests." Online, 2014. http://www.mayoclinic.org/tests-procedures/allergy-tests/basics/what-you-can-expect/prc-20014505, [Accessed: 17/09/2015].

[231] A. B. Montanher, S. M. Zucolotto, E. P. Schenkel, and T. S. Fröde, "Evidence of anti-inflammatory effects of passiflora edulis in an inflammation model," *Journal of Ethnopharmacology*, vol. 109, no. 2, pp. 281–288, 2007.

[232] M. Grossmann, M. J. Jamieson, and W. Kirch, "Histamine response and local cooling in the human skin: involvement of h1- and h2-receptors," *British Journal of Clinical Pharmacology*, vol. 48, no. 2, pp. 216–222, 1999.

[233] N. Charkoudian, "Skin blood flow in adult human thermoregulation: How it works, when it does not, and why," *Mayo Clinic Proceedings*, vol. 78, no. 5, pp. 603–612, 2003.

[234] I. D. Stephen, V. Coetzee, M. Law Smith, and D. I. Perrett, "Skin blood perfusion and oxygenation colour affect perceived human health," *PLoS ONE*, vol. 4, p. e5083, 04 2009.

[235] B. Amirlak, "Skin anatomy: Overview, epidermis, dermis." Online, Jul 2015. http://emedicine.medscape.com/article/1294744-overview [Accessed: 04/04/2016].